Expedient Synthesis and Antitumor Evaluation of Novel Azaheterocycles from Thiazolylenaminone

Samir Bondock, Omeer Albormani & Ahmed M. Fouda

Published online: 12 Feb 2022.

Submit your article to this journal ☞

Article views: 9

View related articles ☞

View Crossmark data ☞

Taylor & Francis
Taylor & Francis Group

Check for updates

Expedient Synthesis and Antitumor Evaluation of Novel Azaheterocycles from Thiazolylenaminone

Samir Bondock[a,b] ![ORCID], Omeer Albormani[a], and Ahmed M. Fouda[a]

[a]Chemistry Department, Faculty of Science, King Khalid University, Abha, Saudi Arabia; [b]Chemistry Department, Faculty of Science, Mansoura University, Mansoura, Egypt

ABSTRACT

Thiazole is a functional group used in cancer treatment modalities in synthetic and natural antitumor medications. In this context, convenient synthesis of new 5-heteroaryl-thiazoles is described *via* reactions of thiazolylenaminone with sulfanilamide, sulfathiazole, hydrazine hydrate, phenylhydrazine, hydroxylamine, guanidine, aminoazoles, β-dicarbonyl compounds, and diazotized aminoazoles. The constitution of the constructed thiazoles was avowed by elemental analyses and spectral data as well as alternative syntheses wherever possible. Thiazoles were also tested for their antitumor activity toward human cancer cell lines (MCF-7, HCT-116, and HepG-2) and one normal cell line (REP1). Among the synthesized thiazoles, compounds **6**, **19**, and **23a** showed high potent antitumor profiles toward cancer cell lines and found no evidence of human toxicity.

Introduction

Cancer remains one of the utmost dangerous diseases to human health. It is also the world's top cause of death. As a result, the principal objective of synthetic organic chemists and drug experts is to construct and develop more effective anticancer drugs for the treatment of cancer. 5-Acetylthiazoles are a versatile class of bioactive heterocycles owing to their chemical reactivity and diverse medical applications.[1,2] Literature reports reveal that many synthetic thiazoles have exhibited a diverse set of biological functions such as anticancer,[3,4] antimicrobial,[5–7] antioxidant,[8] anti-inflammatory,[9] analgesic,[10] antiviral,[11] antihypertensive,[12] and antimalarial.[13] The thiazole nucleus was found in over 18 FDA-approved drugs as well as over 70 drugs are under study.[14] On the other hand, tertiary enaminones (Ar–CO–CH $=$ CH–NR$_2$) are versatile substances and efficiently employed for transamination reactions and the construction of numerous biologically active azoles, azines, and their fused analogs.[15–20] Enaminones are also structurally appealing intermediates that integrate the ambient behavior of electrophilicity and nucleophilicity of enones simultaneously and have also long been utilized as acceptors in 1,2- and 1,4-addition reactions that make them versatile synthon to create a diverse type of heterocycles.[21] These discoveries inspired us to construct a new family of 5-(hetaryl)thiazoles for antitumor evaluation. In continuation of our previous studies on 2-allylamino-4-methyl-5-acetylthiazole,[22] we present herein the construction and transformations of thiazolylenamnione with some nitrogen and carbon nucleophiles, as well as, certain nitrogen electrophiles, for antitumor activity evaluation.

Results and discussion

Chemistry

5-Acetyl-2-allylamino-4-methylthiazole (**3**) was initially created *via* the interaction of allylthiourea (**1**) with α-chloroacetylacetone (**2**) in boiling ethyl alcohol comprising one drop of triethylamine following a procedure described earlier by us.[22] Heating **3** with *N,N*-dimethylformamide–dineopentylacetal (DMF-DNpA) in dry toluene gave a sole substance documented as 1-(2-allylamino-4-methylthiazol-5-yl)-3-(dimethylamino)-2-propen-1-one (**4**) (Scheme 1).

The structure of enaminone **4** has been verified based on analytical and spectroscopic data. The absorption bands at 3198, 1644, 1638 cm^{-1} in the infrared spectrum were ascribed to NH, conjugated C=O, and C=C functions, respectively. Enaminone **4** showed in ^{1}H NMR spectrum two singlets at δ_{ppm} 2.41, 3.36 assignable to CH$_3$, N(CH$_3$)$_2$ protons, and two triplet signals at δ_{ppm} 3.85, 8.14 specific for (NCH$_2$) and NH protons, respectively. It also revealed two doublet signals at δ_{ppm} 5.20 and 7.51 with an equal value of coupling constant ($J = 12$ Hz) owing to –CH=CH– protons. The J value of the ethylenic protons indicates that the structure of the enaminone **4** has the *E*-configuration. The ^{13}C NMR spectrum of **4** revealed eleven carbon signals. The aliphatic carbons resonate at δ 18.2, 39.8, 46.3 ppm assignable for the carbons of CH$_3$, N(CH$_3$)$_2$, and NCH$_2$ groups, respectively. The signals resonate at δ 121.6, 152.7, 167.8, 179.2 ppm assignable to (C-5, C-4, C-2) of a thiazole ring residue, and the carbon of carbonyl group, respectively. Furthermore, a molecular formula (C$_{12}$H$_{17}$N$_3$OS) was deduced for compound **4** by the appearance of the molecular ion peak at $m/z = 251$ (M$^+$) in its mass spectrum.

Scheme 2 illustrates a suggested mechanism for the construction of enaminone. DMF-DNpA exists in equilibrium with its stabilized carbenium ion and neopentoxide ion. The neopentoxide ion, a strong base, attacks the active hydrogen of the methylketone **3** and gives the non-isolable vinylenolate intermediate **3A** and neopentyl alcohol. Then, the nucleophilic addition of the vinyl enolate **3A** to carbenium ion affords the intermediate **3B** which also exists in equilibrium with intermediate **3C** and neopentoxide ion. Finally, the neopentoxide ion abstracts *in situ* an active α-hydrogen atom of the intermediate **3C** and affords thiazolylenaminone **4** and neopentyl alcohol.

The reactivity of **4** is ascribed to the existence of two electron-deficient sites on carbon-1 and carbon-3, as well as one electron-donating site on carbon-2 due to the delocalization of the nonbonding electrons on the N atom beside conjugation with the carbonyl function. Thiazolylenaminone **4** can behave as an electrophilic and nucleophilic reagent. Distinctive electrophilic locations are carbon-3 (N(CH$_3$)$_2$ group) and carbon-1 (C=O group). These chemical
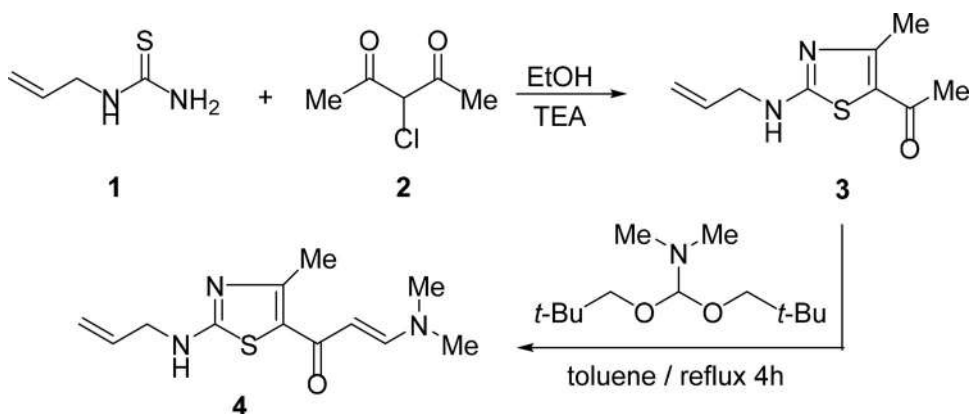
Scheme 1. Synthesis of thiazolylenaminone **4**.
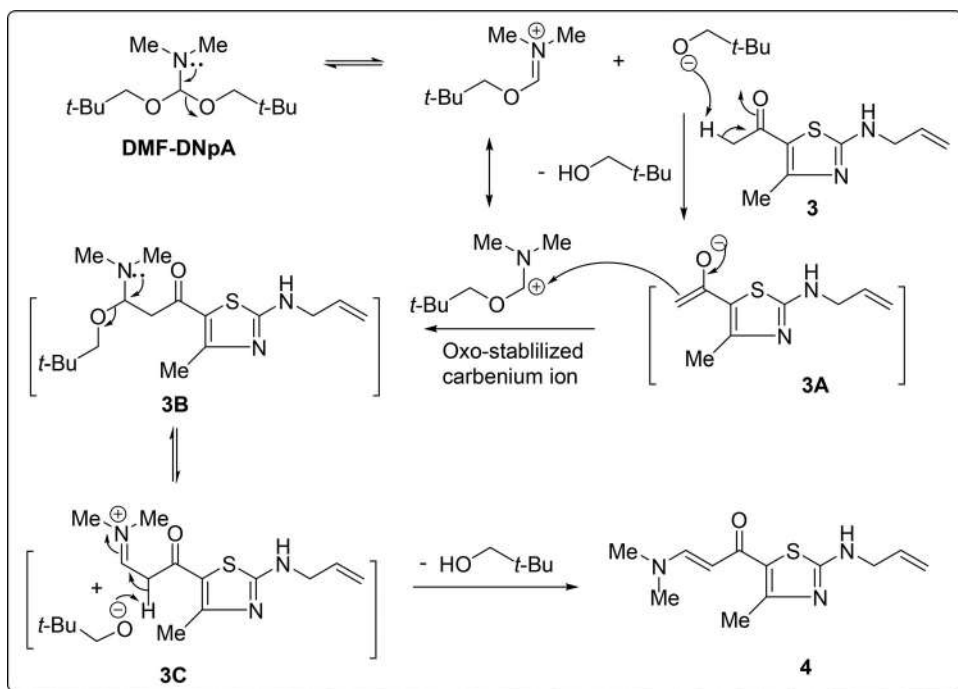
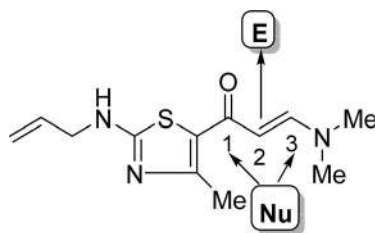**Scheme 2.** Mechanism of the creation of thiazolylenaminone **4**.

Figure 1. Chemical reactivity of thiazolylenaminone **4**.

features have been exploited to displace the dimethylamino function with amines as nucleophiles without impacting other functions. A reaction involving the keto and dimethylamino functions can occur with binucleophiles, resulting in heterocyclic compounds. Furthermore, thiazolylenaminone exhibits a nucleophilic behavior at carbon-2. It can be coupled with diazotized aromatic and/or heterocyclic amines to afford cyclic products (Figure 1).

The transamination reaction of tertiary enaminones with bioactive primary aromatic amines was efficiently used as a method to obtain compounds with good pharmacological properties.[23] Sulfonamides are an important class of drugs that have exhibited diverse types of pharmacological properties.[24] A vast variety of structurally unique sulfonamides have been found to have promised *in vitro* and i*n vivo* anticancer activity.[25] In this context, transamination reactions of thiazolylenaminone **4** with sulfanilamide and sulfathiazole aiming to reach new anticancer agent was investigated in this work. Thus, the interaction of thiazolylenaminone **4** with each of sulfanilamide and sulfathiazole, as a nitrogen mono-nucleophile, in boiling acetic acid afforded a sole substance, in each instance, as demonstrated by thin layer chromatography, identified as 4-([3-(2-(prop-2-enylamino)-4-methylthiazol-5-yl)-3-oxo-1-propen-1-yl]amino)benzen-esulfonamide (**5**) and 4-([3-(2-(prop-2-enylamino)-4-methylthiazol-5-yl)-3-oxo-1-propen-1-yl]amino)-N-(thiazol-2-yl)-benzene-sulfonamide (**6**), respectively (Scheme 3).
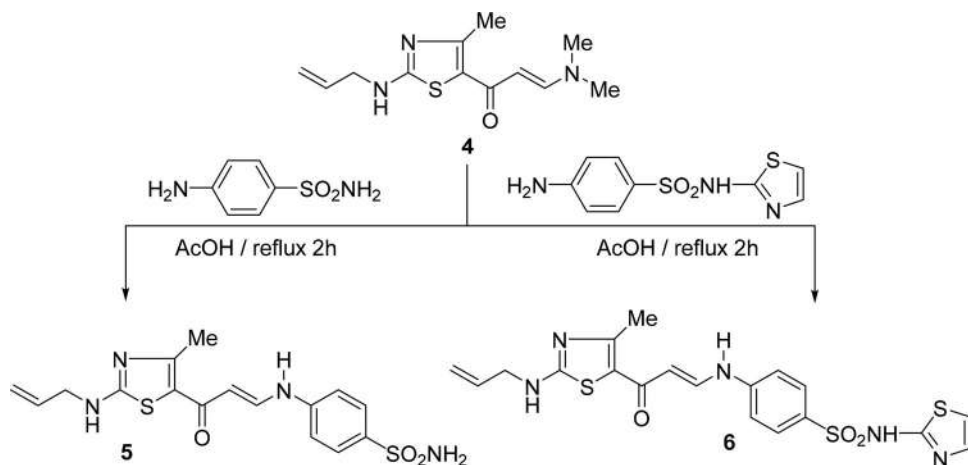
**Scheme 3.** Synthesis of secondary enaminones **5** and **6**.

The constructions of thiazoles **5** and **6** were presumed from their spectral data and microanalyses. Compound **5** showed, in its IR spectrum, stretching vibrations at 3470, 3366, 3252, 3196, 1633 cm^{-1} due to NH (enamine), NH$_2$ (sulfonamide), NH (allyl), and C=O (conjugated) functionalities, respectively. The relative configuration of compound **5** was assigned as E-configuration, as proved from the proton NMR spectrum which shows two downfield doublet signals with high coupling constant value ($J = 14.0$ Hz) resonate at δ_{ppm} 10.12 and 11.70 owing to (CH=CH). Compound **5** exhibited also 14 carbon types, in the ^{13}C NMR spectrum; the most important signals include methyl, methylene, and carbonyl carbons, which appeared at δ_{ppm} 18.9, 46.8, and 180.2, respectively. The MS spectrum of **5** disclosed a parent ion peak at $m/z = 378$ (M$^+$) and the base peak at $m/z = 172$ (100%) due to the sulfanilamide fragment ion peak. Notably, the diastereoselective formation of E-isomer for compounds **5** and **6** is also consistent with the configuration of enaminones analog confirmed by single crystal X-ray diffraction techniques.[26]

The reaction of enaminone with nitrogen binucleophiles represents the easiest route to synthesize pyrazole, isoxazole, pyridine, pyrimidine, pyrazolopyrimidine, triazolopyrimidine, and imidazopyrimidine derivatives. In this connection, the reactivity of thiazolylenaminone **4** toward several types of nitrogen binucleophiles was investigated.

When thiazolylenaminone **4** was refluxed with hydroxylamine in ethyl alcohol containing water free potassium carbonate, it produced 2-(prop-2-enylamino)-4-methyl-5-(isoxazol-3-yl)thiazole (**8**) rather than 2-(prop-2-enylamino)-4-methyl-5-(isoxazol-5-yl)thiazole (**10**) (Scheme 4). Compound **8** was also deduced by another creation. Thus, the reaction of thiazolyloxime **11**, prepared from the interaction of 5-acetylthiazole **3** with hydroxylamine hydrochloride in refluxing pyridine,[27] with DMF-DNpA in boiling toluene, furnished a substance that was identical to **8** obtained from **4** with hydroxylamine. Based on this result, the other isomer **10** was excluded. The structure of product **8** was further elucidated by its spectral data. Its ^{1}H NMR spectrum revealed two doublets at δ_{ppm} 6.95 and 7.52 with $J = 4.4$ Hz due to H-4 and H-5 of the isoxazole ring residue. There are 10 carbon peaks in the ^{13}C NMR spectrum of compound **8**. The two Sp^3 hybridized carbon atoms display at δ_{ppm} 19.2 and 46.5 due to CH$_3$ and CH$_2$N. In addition, the rest eight peaks displayed at δ_{ppm} 94.1, 116.9, 120.4, 134.4, 152.8, 153.2, 159.1, and 168.3 characteristic for thiazole-C$_5$, CH$_2$=, isoxazole-C$_4$, CH=, thiazole-C$_4$, isoxazole-C$_3$, isoxazole-C$_5$, and thiazole-C$_2$, respectively. To account for the construction of product **8**, as drawn in Scheme 4, the interaction of enaminone **4** with hydroxylamine begins with a loss of water to afford intermediate **7**, which tends to cyclization via exclusion of dimethylamine to afford **8**. It is worthwhile to
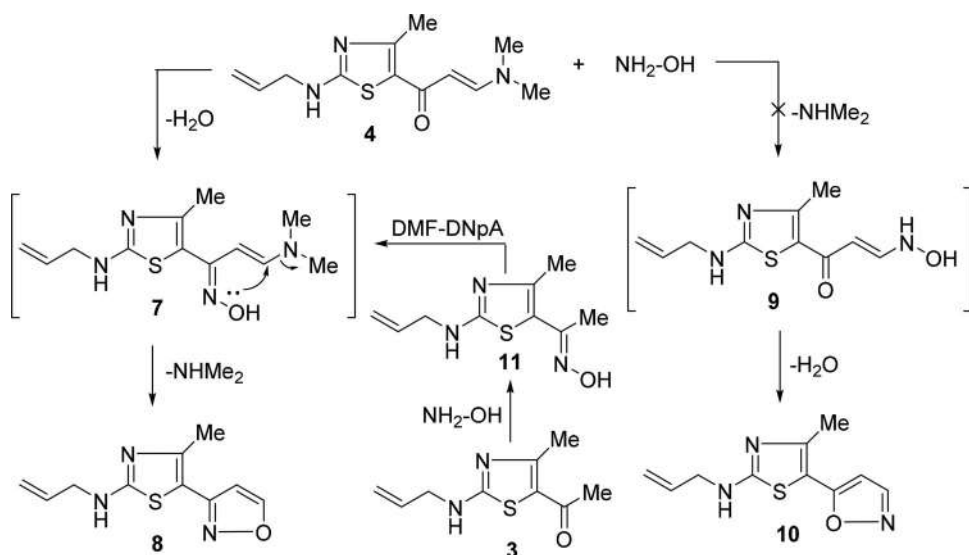
Scheme 4. Regioselective synthesis of 5-(isoxazol-3-yl)thiazole **8**.
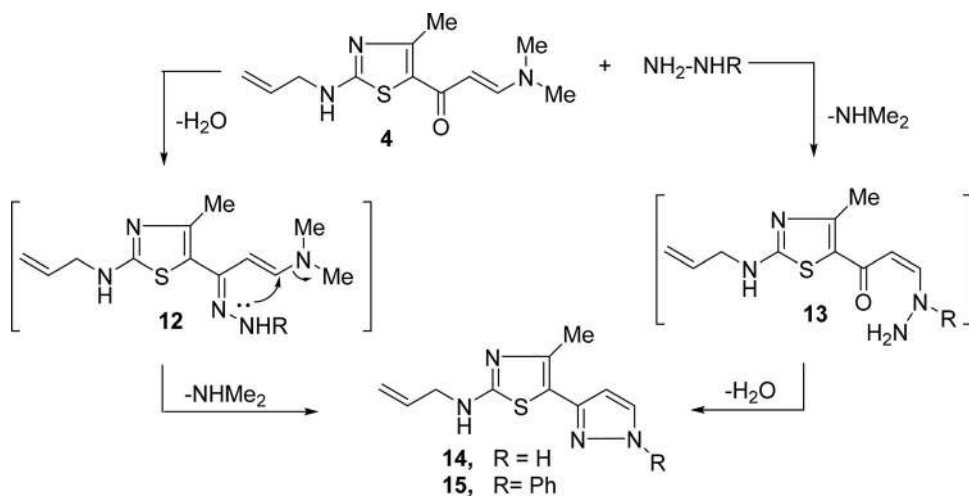

Scheme 5. Synthesis of 5-(pyrazol-3-yl)thiazoles **14** and **15**.

mention that the formation of isoxazole derivative **8** from the interaction of enaminone **4** with hydroxylamine is also consistent with previous work reported by Shawali and Haboub.[28]

Similar action of enaminone **4** with hydrazine and phenylhydrazine in boiling ethyl alcohol produced 4-methyl-2-(prop-2-enylamino)-5-(1*H*-pyrazol-3-yl)thiazole (**14**) and 4-methyl-2-(prop-2-enylamino)-5-(1-phenyl-1*H*-pyrazol-3-yl)thiazole (**15**), respectively (Scheme 5).

The constructions of the latter molecules **14** and **15** were established based on their microanalyses and spectral information. The IR spectrum of **14** exposed absorption bands at 3204, 3104, 1618 cm^{-1} distinctive for two broad NH and C=C functions. Also, the proton NMR spectrum of **14**, demonstrated two doublet signals at δ_{ppm} 6.32 and 7.67 with $J = 2.2$ Hz due to the pyrazole protons H-4 and H-5, respectively. Further, there are two singlets resonating at δ_{ppm} 2.26 and 12.73 due to CH$_3$ and pyrazole NH protons, besides two triplet signals appearing at 3.85 and 7.71 ppm characteristic for NCH$_2$ and NH protons. Ten types of carbon peaks were displayed in
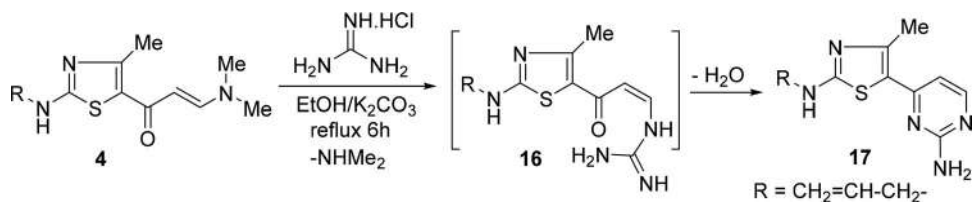
**Scheme 6.** Synthesis of 2-amino-4-(2-allylamino-4-methylthiazol-5-yl)pyrimidine (**17**).

^{13}C NMR spectrum of **14**, the most significant peaks resonate at 112.2, 130.0, 144.6 ppm due to C-3, C-4, and C-5 of pyrazole unit, respectively. The mass spectrum revealed a parent peak at 220 (M[+]).

The recommended mechanism for the creation of pyrazoles **14** and **15** is depicted in Scheme 5. There are two plausible intermediates, **12** and **13** were assumed to explain the construction of substances **14** and **15**. The intermediate **12** was created *via* the initial nucleophilic addition of the NH$_2$ function of hydrazine derivative to the keto function of the enaminone **4** followed by a loss of water. The other intermediate **13** was produced *via* the addition of hydrazine derivative to the C-3 of the enaminone **4** followed by the abolition of dimethylamine. Then, both intermediates **12** and **13** were *in situ* cyclized into the same pyrazoles **14** and **15** *via* elimination of dimethylamine or water molecule.

Interaction of thiazolylenaminone **4** with guanidine hydrochloride in boiling ethyl alcohol comprising dry K$_2$CO$_3$ as a base produced 2-amino-4-(4-methyl-2-(prop-2-enylamino)thiazol-5-yl)pyrimidine (**17**) in a good profit (Scheme 6). The IR spectrum of product **17** was free of the carbonyl function and demonstrated broad absorption peaks for NH$_2$ and NH functions at range 3191–3087 cm^{−1}. There are two singlet peaks, exchangeable with D$_2$O, displayed in ^{1}H NMR spectrum, at δ_{ppm} 2.81 and 8.14 due to NH$_2$ and NH protons. Besides, two doublets resonating at δ_{ppm} 7.49 and 8.45 assignable to the two pyrimidine protons (H-5) and (H-6), respectively. A parent ion peak (M[+]) showed in the MS spectrum at $m/z = 247$ due to a molecular formula (C$_{10}$H$_{13}$N$_5$S). The formation of **17** seemed to begin with the addition of the NH$_2$ function of guanidine to the β-carbon of enamine followed by exclusion of dimethylamine to afford intermediate **16** which undergoes tandem cyclization with a loss of water molecule.

Next, the reactivity of **4** toward 3-amino-1,2,4-triazole was studied to determine its site selectivity. Theoretically, this reaction can produce two isomeric structures, namely, 1,2,4-triazolo[1,5-a]pyrimidine or 1,2,4-triazolo[4,3-a]pyrimidine. Thus, a reaction of **4** with aminotriazole in ethanol under reflux was performed to isolate the reaction intermediate. The IR spectrum of isolated product showed distinctive bands at 3508, 3362, 3219 cm^{−1} owed to three NH functions and confirms the 1-(2-allylamino-4-methylthiazol-5-yl)-3-(4H-1,2,4-triazol-3-ylamino)-2-propen-1-one (**18**) as a product. Heating **18** in acetic acid afforded 2-allylamino-4-methyl-5-([1,2,4]triazolo[1,5-a]pyrimidin-7-yl)thiazole (**19**) (Scheme 7). The ^{1}H NMR spectrum of **19** revealed two doublets near δ_{ppm} 7.48 and 8.81 with $J = 4.68$ Hz conveyable to H-6 and H-7 protons of the pyrimidine nucleus, in addition to, a single peak at δ_{ppm} 8.65 ppm owed to the triazole H-2 proton. Such assignment is compatible with published studies on ^{1}H NMR data of 1,2,4-triazolo[1,5-a]pyrimidine derivatives.[29] Its ^{13}C NMR spectrum demonstrated peaks at δ_{ppm} 20.3, 46.8, 105.7, 116.7, 134.5, 155.8, and 172.3 diagnostics for the carbons of CH$_3$, CH$_2$N, thiazole-C$_5$, CH$_2$=, CH=, thiazole-C$_4$, and thiazole-C$_2$, successively. The MS spectrum displayed a parent ion peak at 272 amu confirming the molecular formula of **19** to be C$_{12}$H$_{12}$N$_6$S.

Similarly the interaction of **4** with each of 5-amino-3-phenylpyrazole and 2-aminobenzimidazole in ethanoic acid, under reflux, produced the derivatives of pyrazolo[1,5-a]pyrimidine and benzimidazo[1,2-a]pyrimidine **21** and **23**, successively (Scheme 7). The ^{1}H NMR spectrum of products **21** and **23** displayed pair of doublets peaks around δ_{ppm} 7.12–7.33 and 7.99–8.12 with
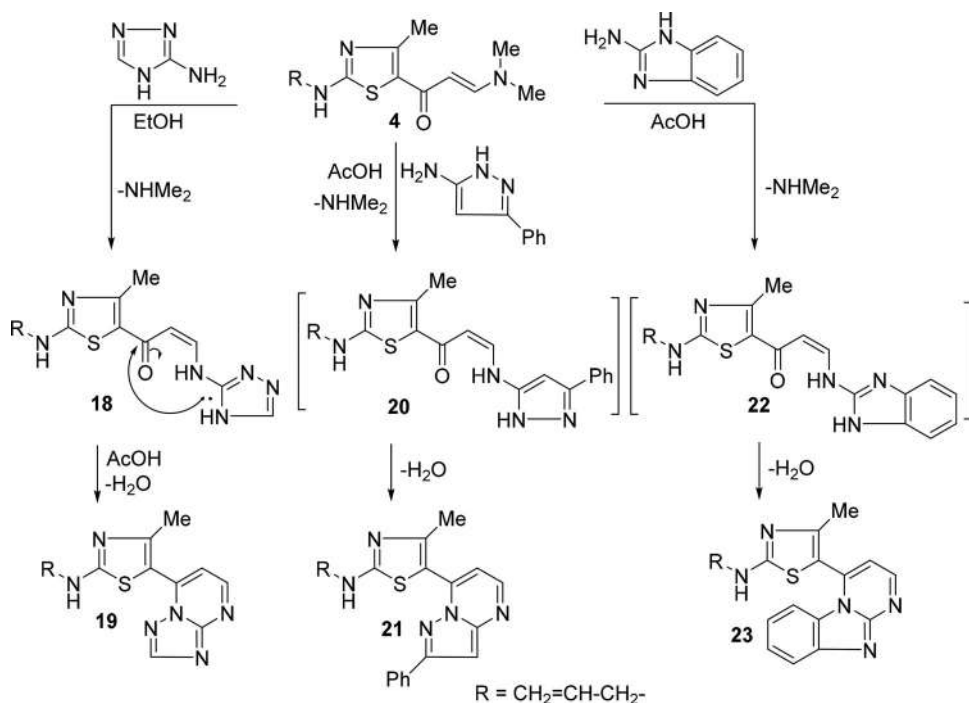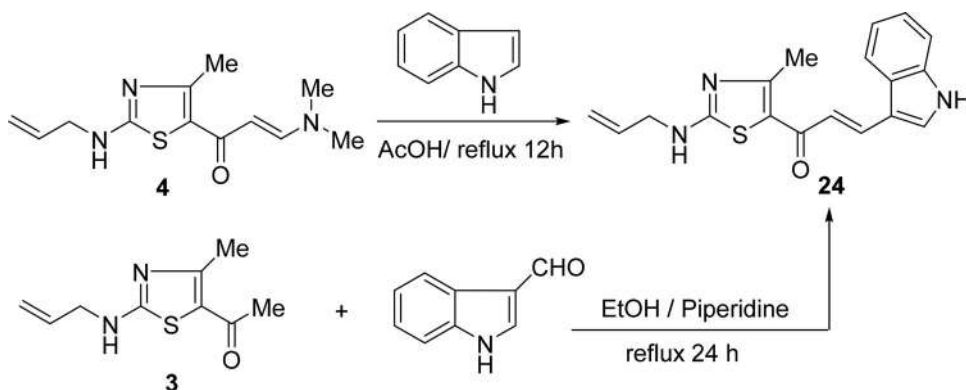
Scheme 7. Reactions of enaminone **4** with aminoazoles.

$J = 5\,\text{Hz}$ attributable to the two sequential protons of pyrimidine unit. It is proposed that the examined reactions began with the Michael addition of the NH_2 group of aminoazoles to the active C-3 of **4** followed by ring closure *via* loss of $(CH_3)_2NH$ and H_2O to produce the products **19**, **21**, and **23** (Scheme 7). It is worthy to mention that the regioselective formation of azoloazines **19**, **21**, and **23** is also in the line with similar compounds secured by single crystal X-ray analyses and published earlier by Farghaly and coworkers.[30]

We further investigated the reactivity of **4** to carbon nucleophiles. Thus, the interaction of **4** with indole, as a carbon nucleophile, in ethanoic acid, under reflux, afforded 1-(4-methyl-2-(prop-2-enylamino)thiazol-5-yl)-3-(1H-indol-3-yl)-2-prop-1one (**24**) (Scheme 8). The latter product was elucidated by elemental and spectral analyses, as well as chemically established by the Claisen–Schmidt reaction of **3** with 3-formylindole in ethyl alcohol, under reflux, including one drop of piperidine (Scheme 8). Diagnostic bands appearing in the IR spectrum of **24** at 3204, 3178, 1635, 1621 cm^{-1} owed to two NH, conjugated C=O, and C=C functionalities, successively. Its ^{1}H NMR spectrum disclosed five singlets at δ_{ppm} 2.58, 3.93, 8.00, 8.60, and 11.90 ppm assignable to CH_3, NCH_2, indole-H-2, and 2 NH protons, consecutively. The *E*-configuration of **24** was assigned based on the determination of coupling constant value ($J = 15.3\,\text{Hz}$) between the ethylenic protons appearing at δ_{ppm} 7.13 and 7.83. Eighteen carbon peaks were recognized in the ^{13}C NMR spectrum of **24**, the diagnostic carbon peaks appeared at δ_{ppm} 18.8, 46.4, and 180.3 due to CH_3, NCH_2, and C=O, successively. Moreover, its MS spectrum exhibited a molecular ion peak at 323 amu supporting a molecular formula ($C_{18}H_{17}N_3OS$).

Next, the reactions of the thiazolylenaminone **4** with certain 1,3-dicarbonyl compounds, like *C,O*-binucleophile, were studied. Thus, the interaction of **4** with 2,4-pentandione, ethyl 2-oxobutanoate, and ethyl benzoyl ethanoate in refluxing ethanoic acid comprising ammonium ethanoate afforded 2-(2-allylamino-4-methylthiazol-5-yl)pyridine derivatives **26a–c** (Scheme 9). As illustrated in Scheme 9, the formation of **26** seems to start with Michael addition of the active $-CH_2-$ group of β-dicarbonyl reagents to the C-3 of enaminone **4**, then loss of $(CH_3)_2NH$ to give the

Scheme 8. Reaction of enaminone **4** with indole.
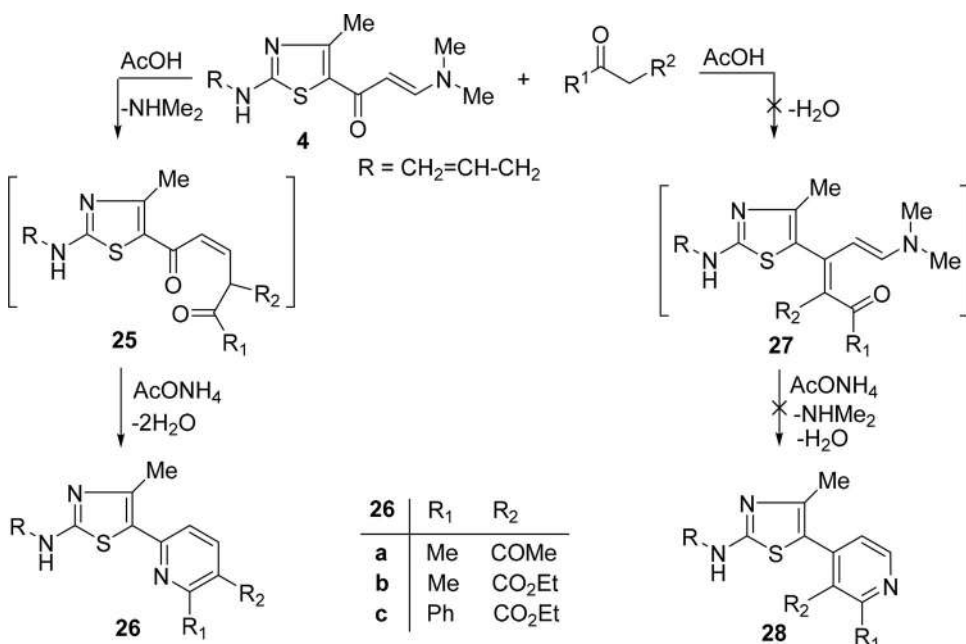
Scheme 9. Synthesis of 2-(thiazol-5-yl)pyridine derivatives **26a–c**.

intermediate **25** which concurrently reacts with ammonium ethanoate to furnish **26**. The other possible regioisomeric product **28** was excluded based on spectral information. Compound **26a**, as an example, shows two doublet peaks ($J = 8.36$ Hz) at δ_{ppm} 7.42 and 8.19 due to the H-3 and H-4 of the pyridine unit in its ^{1}H NMR spectrum. It is valuable to note that the coupling constant for the vicinal protons of pyridine H-2 and H-3 in excluded structure **28** was reported with a lower value ($J = 4$–6 Hz).[31] Also, five singlet signals were detected in the ^{1}H NMR spectrum of **26a** at δ_{ppm} 1.91, 2.68, 2.76, 3.90, 8.14 confirming the presence of three CH_3 groups, CH_2N, and NH proton, successively. The ^{13}C NMR spectrum of **26a** revealed 15 distinct carbon peaks. The most typical peaks resonate at δ_{ppm} 18.9, 25.4, 29.6, 46.8, 199.6 due to the three carbons of methyl functions, methylene carbon, and a carbonyl carbon, respectively.

The reaction of thiazolylenaminone **4** with ethyl cyanoacetate in boiling ethanolic sodium ethoxide solution produced a single substance that formulated as 6-(4-methyl-2-(prop-2-enylamino)-thiazol-5-yl)-3-ethoxycarbonyl-2-oxo-1,2-dihydropyridine (**31**) (Scheme 10). The structure of the
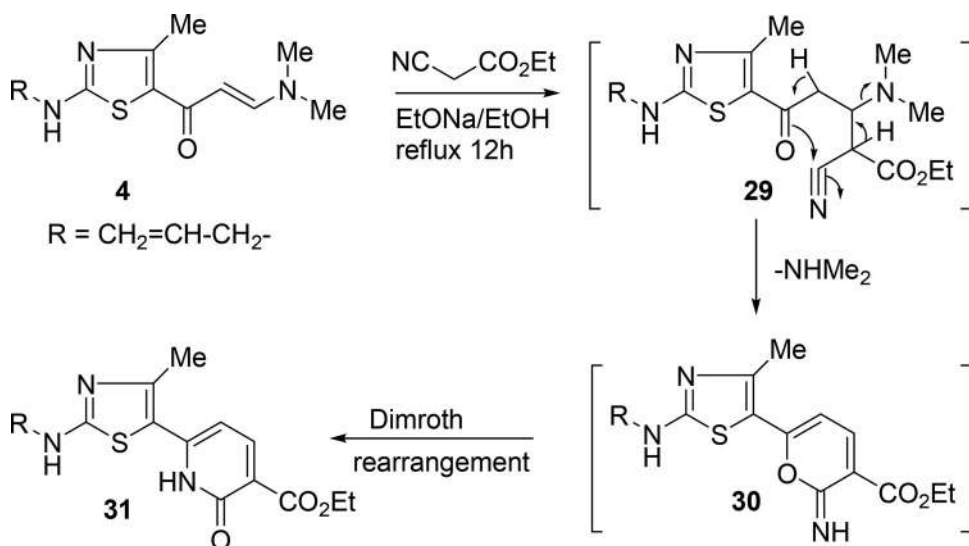
Scheme 10. Synthesis of ethyl 6-(thiazol-5-yl)-2-oxo-1,2-dihydropyridine carboxylate **31**.

final product was well-matched with its spectral results. Thus, its IR spectrum disclosed appearing of two NH and two CO groups bands around 3310, 3200, 1720, and 1640 cm^{-1}. The ^{1}H NMR spectrum revealed signals at δ_{ppm} 1.20, 4.13 due to the ethoxy group, and two doublet signals near δ 8.17 (pyridine-H-5) and 8.32 (pyridine-H-4). The construction of **31** was rationalized by the first addition of –CH$_2$– group of ethyl cyano ethanoate to C-3 of enaminone, as a typical Michael addition reaction, followed by removal of (CH$_3$)$_2$NH to form intermediate **29**. Then, the enol form of carbonyl group adds to a nitrile function *via* 6-*exo-trig* ring cyclization to afford iminopyran **30** that convert *in situ* to pyridone **31** *via* Dimroth rearrangement (Scheme 10).

The hydrogen atom at C-2 of enaminone is known to have a nucleophilic nature and can be substituted by electrophilic reagents. In this context, the reaction of thiazolylenaminone **4** toward some diazotized heterocyclic amines was examined to attain bridged head nitrogen heterocyclic compounds with potential pharmacological activity. Thus, interaction of **4** with 1,2,4-triazolyl diazonium nitrate in pyridine at 0–5 °C gave (4-methyl-2-(prop-2-enylamino)thiazol-5-yl)([1,2,4]triazolo[3,4-*c*][1,2,4]triazin-6-yl)methanone (**33**).

The chemical structure of **33** was deduced from the IR spectrum which displayed distinctive bands at 3198, 1632, 1620 cm^{-1} for NH, conjugated C=O, and C=C functions, consecutively. The ^{1}H NMR spectrum confirmed the construction of triazolo[3,4-*c*]triazine system by appearing two singlets at δ_{ppm} 6.81 and 7.98 due to the protons of triazole-H$_3$ and triazine-H$_5$. The ^{13}C NMR spectrum of **33** disclosed the existence of 12 carbon peaks, and the MS spectrum showed ion peak at 301 (M$^+$), confirming a molecular formula (C$_{12}$H$_{11}$N$_7$OS). The distinctive carbon peaks detected at δ_{ppm} 19.6, 46.3, and 178.2 owing to CH$_3$, NCH$_2$, and C=O carbons, respectively.

Similarly, the interaction of enaminone **4** with each of 5-phenylpyrazol-3-yl diazonium chloride and benzimidazol-2-yl diazonium nitrate gave (7-phenylpyrazolo[5,1-*c*][1,2,4]triazin-3-yl)(4-methyl-2-(prop-2-enylamino)thiazol-5-yl) methanone (**35**) and (benzimidazo[2,1-c][1,2,4]triazin-3-yl)(4-methyl-2-(prop-2-enylamino)thiazol-5-yl)methanone (**37**), respectively (Scheme 11).

The creation of heterocycles **33**, **35**, and **37** appears to commence with the displacement of a hydrogen atom at C-2 of enaminone **4** by the azo group to give intermediates **32**, **34**, and **36** that then undergo intramolecular 6-*exo-trig* cyclization with the removal of dimethylamine. The elemental and spectral investigations of heterocycles **33**, **35**, and **37** confirmed their molecular structures (see Experimental part).
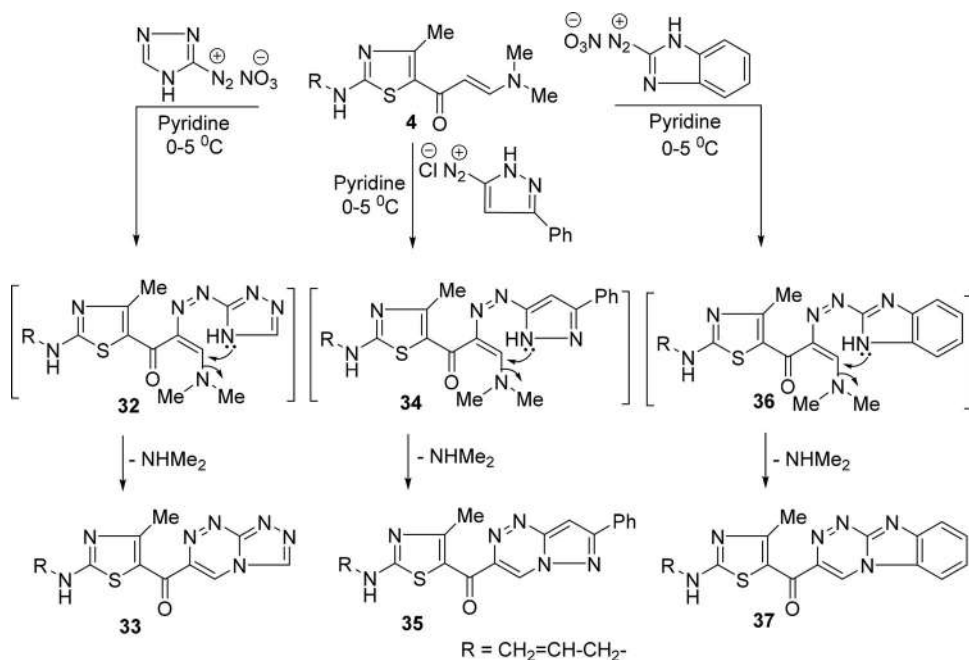
Scheme 11. Reactions of enaminone **4** with diazotized heterocyclic amines.

Antitumor evaluation

Thirteen thiazoles out of the created substances have been analyzed for their antitumor profiles toward MCF-7 (breast cancer), HCT-116 (colon carcinoma), and HepG-2 (hepatocellular carcinoma). To check the safety of thiazoles in typical cells, they were further screened on a normal epithelial cell line (RPE1). The antitumor activity of some newly selected thiazoles was determined using a standard methodology for the Sulforhodamine B (SRB) cytotoxicity assay.[32,33] The information gathered was utilized to calculate IC_{50} (µM) values. The anticancer drug doxorubicin was utilized as a standard reference.

The data of the antiproliferative activity presented in Table 1 show that compounds **4–26a,b** displayed varying degrees of inhibition against the examined tumor cells. Compounds **6**, **19**, and **23** exerted moderate cytotoxic effects against breast cancer cells (MCF-7), with IC_{50} values of 15.50, 18.26, and 16.78 µM, respectively, as compared to doxorubicin (IC_{50} 6.77 µM). Unpredictably, the remaining chemicals tested had low or no growth inhibitory effects. Among the investigated compounds, compounds **19** and **6** demonstrated the highest potency against colon cancer cells, with IC_{50} values of 7.99 and 17.57 µM, respectively. Moreover, compounds **6**, **17**, **19**, and **23** exhibited considerable antiproliferative potential against the hepatic cancer cell line, with IC_{50} values of 26.02, 24.33, 21.55, and 14.89 µM, respectively. The remaining compounds displayed only a minor inhibitory effect (Table 1). It is notable to mention that compounds **6**, **19**, and **23** demonstrated high antiproliferative activity against the three examined cancer cell lines. Compound **19** displays also selectively toward the HCT-116 cell line. Furthermore, except for compounds **8** and **14**, none of the compounds presented in Table 1 exerted toxicity toward the normal cell line (RPE1). These results suggest that the examined compounds could be considered as scaffolds for the synthesis of potential anticancer agents.

Structure–activity relationship

The following structural activity relationships (SAR) were proposed by linking the data of cytotoxic action of substances to their structures.

Table 1. Antitumor profile (IC_{50}) of the assayed substances.

Compd #	IC_{50}^{a} values (µM)[b]			
	MCF-7	HCT-116	HepG-2	RPE1
4	>100	95.36 ± 4.80	>100	>100
5	50.23 ± 3.45	91.41 ± 7.11	>100	>100
6	15.40 ± 1.28	17.57 ± 1.36	26.02 ± 1.80	>100
8	>100	>100	>100	78.16 ± 3.15
14	>100	>100	>100	70.24 ± 2.38
15	>100	>100	>100	>100
17	83.07 ± 3.26	>100	24.33 ± 2.96	>100
19	18.26 ± 1.58	7.99 ± 0.18	21.55 ± 1.98	>100
21	>100	>100	>100	>100
23	16.78 ± 1.66	80.52 ± 6.93	14.89 ± 1.45	>100
24	>100	>100	>100	>100
26a	95.50 ± 4.48	>100	>100	>100
26b	>100	>100	>100	>100
Doxorubicin	6.77 ± 0.25	1.69 ± 0.14	3.21 ± 0.17	10.45 ± 1.18

[a]IC_{50} is the 50% concentration of compound to impede cell growth at 48 h.
[b]The results were obtained by three times experiments.

- A basic skeleton thiazole is required for a broad spectrum of cytotoxic action against cancer cells (MCF-7, HCT 116, and HepG2).
- As with compound **6**, transamination of thiazolylenaminone **4** with sulfathiazole improved the cytotoxic action.
- The anticancer activity of thiazolylenaminone **4** was boosted by converting it to thiazolyl pyrimidine **17**.
- The cytotoxic action of thiazolylenaminone **4** was increased by heterocyclization to triazolo[1,5-*a*]pyrimidine **19** and benzo[*d*]imidazo[1,2-*a*]pyrimidine **23**.

Conclusion

We have reported the facile synthesis and structural characterization of some new functionalized 5-hetaroylthiazoles for antitumor activity evaluation. The synthetic approach was dependent upon the reaction of thiazolylenaminone with a variety of nitrogen and carbon mono and binucleophilic reagents and some *N*-electrophilic reagents. The results of antitumor activity evaluation revealed that compounds **6**, **19**, and **23** have displayed high potency antiproliferative action to the appraised cancer cells (MCF-7, HCT-116, and HepG-2) with no toxicity against normal human cell line (RPE1).

Experimental

The melting points were measured using Stuart, model SMP11, melting point equipment. The FTIR Jasco spectrophotometer was used to record infrared spectra in KBr disks. The (^{1}H and ^{13}C NMR) spectra were measured in deuterated dimethyl sulfoxide at 400 and 850 MHZ on an AvanceCore-Brucker spectrometer. A Shimadzu GC/MS-QP5, mass spectrometer, was employed to record mass spectra at 70 eV. A Perkin-Elmer 240, micro-analyzer, was used to record elemental analyses.

Synthesis of 1-(4-methyl-2-(prop-2-enylamino)thiazol-5-yl)-3-(N,N-dimethylamino)-2-propen-1-one (4)

Compound **3** (1.24 g, 0.006 mol) and *N,N*-dimethylformamide dineopentyl acetal (5.3 mL, 0.04 mol) were refluxed in 15 mL toluene for 4 h. The formed substance on cold was filtered of, laved with methyl alcohol to give pure compound **4**.

Light yellow powder; Yield 65%; mp 176–177 °C; IR(KBr) v_{max}/cm^{-1} = 3198 (NH), 3085 (=C–H, sp^2), 2990 (C–H, sp^3), 1644 (C=O), 1638 (C=C); ^{1}H NMR (850 MHz, DMSO-d$_6$): δ_{ppm} = 2.41(s, 3H, CH$_3$), 3.36 (s, 6H, (CH$_3$)$_2$N), 3.85 (t, J = 5.95 Hz, 2H, NCH$_2$), 5.12 (dd, J = 10.2, 1.7 Hz, 1H, CH=), 5.20 (d, J = 12 Hz, 1H, CH=), 5.24 (dd, J = 12.75, 1.7 Hz, 1H, CH=), 5.87 (m, 1H, CH=), 7.51 (d, J = 12Hz, 1H, CH=), 8.41 (t, J = 5.95 Hz, 1H, NH); ^{13}C NMR (212.5 MHz, DMSO-d$_6$): δ_{ppm} = 18.24 (CH$_3$), 39.85 (NCH$_3$), 46.35 (NCH$_2$), 95.64 (CH=), 116.0 (CH$_2$=), 121.67 (thiazole-C$_5$), 134.43 (CH=), 152.33 (NCH=), 152.71 (thiazole-C$_4$), 167.81 (thiazole-C$_2$), 179.82 (C=O); MS m/z (%): 252 (M$^+$, 8.93), 246 (18.84), 231 (7.16), 228 (7.87), 220 (14.46), 216 (22.51), 203 (43.44), 195 (7.51), 185 (10.14), 154 (30.39), 146 (15.34), 130 (12.25), 126 (38.18), 119 (12.44), 111 (59.07), 110 (26.23), 108 (27.16), 104 (50.99), 101 (30.87), 92 (65.25), 90 (43.80), 78 (34.99), 70 (29.18), 66 (18.13), 64 (59.11), 63 (32.03), 62 (51.35), 58 (16.89), 55 (26.49), 41 (100). Anal. Calcd. For C$_9$H$_{12}$N$_2$OS (251.11): C, 57.34; H, 6.82; N, 16.72%, Found: C, 57.31; H, 6.83; N, 16.74%.

Synthesis of 4-([3-(4-methyl-2-(prop-2-enylamino)thiazol-5-yl)-3-oxo-1-propen-1-yl]amino)-benzene-sulfonamide (5)

Enaminone **4** (0.8 g, 0.003 mol) and sulfanilamide (0.55 g, 0.003 mol) were heated for 2 h, under reflux, in 20 mL ethanoic acid. The mixture was then cold and diluted with 50 mL of ice water. The obtained compound was isolated by filtration, dried, and crystallized from methyl alcohol to get compound **5**.

Orange crystals; Yield 76%; mp. 200–201 °C; IR (KBr) v_{max}/cm^{-1} = 3470 (NH enamine), 3366, 3252 (NH$_2$), 3196 (NH allyl), 3009 (C–H, sp^2), 2938 (C–H, sp^3), 1633 (C=O), 1630 (C=C), 1593 (C=N); ^{1}H NMR (400 MHz, DMSO-d$_6$): δ_{ppm} = 2.49 (s, 3H, CH$_3$), 3.90 (s, 2H, NCH$_2$), 5.14 (dd, J = 10.2, 1.7 Hz, 1H, CH=), 5.27 (dd, J = 17.2, 1.7 Hz, 1H, CH=), 5.91 (m, 1H, CH=), 7.24 (d, J = 8.24 Hz, 2H, Ar–H$_{3,5}$), 7.72 (d, J = 8.24 Hz, 2H, Ar–H$_{2,6}$), 7.95 (t, J = 5.8 Hz, 1H, NH), 8.40 (d, J = 6.0 Hz, 1H, NH), 10.12 (d, J = 14.0 Hz, 1H, CH=), 11.70 (d, J = 14.0 Hz, 1H, CH=), 11.73 (s, 2H, NH$_2$SO$_2$); ^{13}C NMR (100 MHz, DMSO-d$_6$): δ_{ppm} = 18.99 (CH$_3$), 46.89 (NCH$_2$), 98.18 (C=C–CO), 103.07 (thiazole-C$_5$), 114.98 (Ar–C$_5$), 115.85 (Ar–C$_3$), 116.75 (CH$_2$=), 127.14 (Ar–C$_2$), 127.94 (Ar–C$_6$), 128.13 (Ar–C$_1$), 134.56 (CH=), 143.64 (C–NH), 144.58 (Ar–C$_4$), 169.50 (thiazole-C$_4$), 169.14 (thiazole-C$_2$), 183.32 (C=O); MS m/z (%): 363 (M$^+$, 80.59), 360 (3.51), 342 (1.07), 327 (1.27), 320 (1.19), 304 (2.11), 284 (1.27), 275 (4.04), 258 (4.50), 246 (2.64), 234 (1.66), 207 (8.64), 196 (5.74), 181 (19.45), 172 (100), 156 (90.62), 154 (32.85), 139 (27.49), 126 (17.09), 108 (57.77), 92 (89.91), 80 (20.34), 65 (56), 41 (16.02). Anal. Calcd. For C$_{16}$H$_{18}$N$_4$O$_3$S$_2$ (378.08); C, 50.78; H, 4.79; N, 14.80%, Found: C, 50.80; H, 4.78; N, 14.78%.

Synthesis of 4-([3-(4-methyl-2-(prop-2-enylamino)thiazol-5-yl)-3-oxo-1-propen-1-yl]amino)-N-(thiazol-2-yl)-benzene-sulfonamide (6)

Enaminone **4** (0.8 g, 0.003 mol) and sulfathiazole (0.81 g, 0.003 mol) were mixed in ethanoic acid (10 mL) and then refluxed for 3 h. The reaction content was quenched by pouring to 20 mL cold water with shaking. The formed precipitate was collected, dried and cleaned from ethyl alcohol to give compound **6**.

Yellow crystals; Yield 68%; mp. 174–175 °C; IR (KBr) v_{max}/cm^{-1} = 3528 (NH), 3210 (b, 2 NH), 3105 (C–H, sp^2), 2978 (C–H, sp^3), 1633 (C=O conjugated), 1594 (C=C), 1585 (C=N), 1135 (SO$_2$); ^{1}H NMR (400 MHz, DMSO-d$_6$): δ_{ppm} = 2.48 (s, 3H, CH$_3$), 3.89 (s, 2H, NCH$_2$), 5.14 (dd, J = 10.20, 1.80 Hz, 1H, CH=), 5.26 (dd, J = 17.17, 1.8 Hz, 1H, CH=), 5.91 (m, 1H, CH=), 6.87 (d, J = 2.6 Hz, IH, thiazole-H$_5$), 7.24 (d, J = 8.24 Hz, 2H, Ar–H$_{3,5}$), 7.34 (d, J = 2.6 Hz, 1H, thiazole-H$_4$), 7.72 (d, J = 8.24 Hz, 2H, Ar–H$_{2,6}$), 7.94 (t, J = 6.0 Hz, 1H, NH), 8.42 (bs, 1H, NH), 10.15 (d, J = 12.64 Hz, 1H, CH=), 11.71 (d, J = 12.64 Hz, 1H, CH=), 12.65 (s, 1H, NHSO$_2$); ^{13}C

NMR (100 MHz, DMSO-d_6): δ_{ppm} = 18.91 (CH$_3$), 46.89 (NCH$_2$), 98.24 (CH$=$C), 114.98 (thiazole-C$_5$), 115.89 (thiazole-C$_5$), 116.75 (CH$_2=$), 118.88 (Ar–C$_{3,5}$), 120.63 (CH$_{Ar}$), 121.85 (CH$_{Ar}$), 128.09 (Ar–C$_{2,6}$), 128.30 (CH$=$), 134.55 (thiazole-C$_4$), 135.06 (C$_{Ar}$), 142.83 (C$_{Ar}$), 155.75 (NCH$=$), 156.45 (thiazole-C$_4$), 169.01 (thaizole-C$_2$), 169.5 (thiazole-C$_2$), 183.35 (C$=$O); MS m/z (%): 461 (M$^+$, 2.0), 378 (3.22), 368 (10.71), 321 (9.64), 283 (28.89), 271 (16.18), 255 (14.84), 230 (24.54), 206 (13.09), 176 (16.26), 158 (22.57), 148 (24.45), 140 (31.30), 123 (31.49), 121 (18.09), 85 (100), 83 (77.49), 73 (46.79), 55 (54.95), 43 (64.14). Anal. Calcd. For C$_{19}$H$_{19}$N$_5$O$_3$S$_3$ (461.07); C, 49.44; H, 4.15; N, 15.17%, Found: C, 49.42; H, 4.16; N, 15.18%.

Synthesis of 4-methyl-2-(prop-2-enylamino)-5-(isoxazole-3-yl)thiazole (8)

Method A: Enaminone 4 (0.8 g, 0.003 mol) was dissolved in 5 mL ethanol and then added to a mixture of hydroxyl amine hydrochloride (0.22 g, 0.003 mol) and K$_2$CO$_3$ (0.88 g, 0.006 mol) in 30 mL dry ethanol. The mixture has been boiled for 3 h and slaked by adding cold water (50 mL). The created substance was collected, dried, and cleaned from ethyl alcohol to get thiazole 8.

Method B: The thiazolyl oxime 11[27] (2.11 g, 0.01 mol) and N,N-dimethyl formamide dineopentyl acetal (5.3 mL, 0.04 mol) was refluxed in 15 mL toluene for 8 h. The cold-formed solid was filtered and washed with ether to afford a compound that was consistent with compound 8.

Yellow crystals; Yield 92%; mp. 190–191 °C; IR(KBr)v_{max}/cm^{-1} = 3198 (NH), 3087 (C–H, sp^2), 2982 (C–H, sp^3), 1636 (C$=$C), 1586 (C$=$N); ^{1}H NMR (400 MHz, DMSO-d_6): δ_{ppm} = 2.45 (s, 3H, CH$_3$), 3.90 (s, 2H, NCH$_2$), 5.13 (dd, $J=10.20$, 1.8 Hz, 1H, CH$=$), 5.25 (dd, $J=17.16$, 1.8 Hz, 1H, CH$=$), 5.86 (m, 1H, $=$CH), 6.95 (d, $J=4.4$ Hz, 1H, isoxazole-H$_4$), 7.52 (d, $J=4.4$ Hz, 1H, isoxazole-H$_5$), 8.70 (bs, 1H, NH); ^{13}C NMR (100 MHz, DMSO-d_6): δ_{ppm} = 19.20 (CH$_3$), 46.50 (NCH$_2$), 94.16 (thiazole-C$_5$), 116.96 (CH$_2=$), 120.40 (isoxazole-C$_3$), 134.41 (CH$=$), 152.88 (thiazole-C$_4$), 153.29 (isoxazole-C$_4$), 159.16 (isoxazole-C$_5$), 168.37 (thiazole-C$_2$). Anal. Calcd. For C$_{10}$H$_{11}$N$_3$OS (221.06); C, 54.28; H, 5.01; N, 18.99%, Found: C, 54.26; H, 5.03; N, 18.97%.

Synthesis of 4-methyl-2-(prop-2-enylamino)5-(1H-pyrazol-3-yl)thiazole (14)

Hydrazine hydrate (0.2 mL) and enaminone 4 (0.8 g, 0.003 mol) were heated in 20 mL dry ethyl alcohol for 5 h. The cold-achieved precipitate was picked up, dried, and cleaned from ethyl alcohol to afford compound 14.

Pale yellow crystals; Yield 87%; mp. 128–129 °C; IR(KBr) v_{max}/cm^{-1} = 3204, 3104 (2NH), 3033 (C–H, sp^2), 2973 (C–H, sp^3), 1618 (C$=$C), 1581 (C$=$N); ^{1}H NMR (400 MHz, DMSO-d_6): δ_{ppm} = 2.26 (s, 3H, CH$_3$), 3.85 (s, 2H, NCH$_2$), 5.12 (dd, $J=10.24$, 1.25 Hz, 1H, CH$=$), 5.25 (dd, $J=17.16$, 1.25, 1H, CH$=$), 5.87 (m, 1H, $=$CH), 6.32 (d, $J=2.2$ Hz, 1H, pyrazole-H$_4$), 7.67 (d, $J=2.2$ Hz, 1H, pyrazole-H$_5$), 7.71 (bs, 1H, NH), 12.73 (s, 1H, pyrazole-NH); ^{13}C NMR (100 MHz, DMSO-d_6): δ_{ppm} = 17.20 (CH$_3$), 46.86 (NCH$_2$), 102.79 (thiazole-C$_5$), 112.20 (pyrazole-C$_3$), 116.26 (CH$_2=$), 130.0 (pyrazole-C$_4$), 132.31 (CH$=$), 144.6 (pyrazole-C$_5$), 145.31 (thiazole-C$_4$), 166.06 (thiazole-C$_2$); MS m/z (%): 220 (M$^+$, 100), 205 (47.58), 193 (27.68), 179 (33.66), 162 (9.64), 152 (37.89), 137 (35.12), 125 (9.09), 111 (40.50), 106 (16.94), 93 (47.02), 82 (8.58), 67 (11.4), 41(10.6). Anal. Calcd. For C$_{10}$H$_{12}$N$_4$S (220.08); C, 54.52; H, 5.49; N, 25.43%, Found: C, 54.51; H, 5.47; N, 25.40%.

Synthesis of 4-methyl-2-(prop-2-enylamino)-5-(1-phenyl-1H-pyrazol-3-yl)thiazole (15)

Phenyl hydrazine (0.32 mL, 0.003 mol) and enaminone 4 (0.8 g, 0.003 mol) were boiled for 8 h in 30 mL dry ethanol. The cold-formed yellow precipitate was taken up, dried, and got pure from ethyl alcohol to furnish compound 15.

Yellow powder; Yield 95%; mp. 230–231 °C; IR(KBr) v_{max}/cm^{-1} = 3262 (NH), 3069 (C–H, sp^2), 2932 (C–H, sp^3), 1630 (C=C), 1580 (C=N); ^{1}H NMR (400 MHz, DMSO-d$_6$): δ_{ppm} = 2.62 (s, 3H, CH$_3$), 3.45 (s, 2H, NCH$_2$), 5.12 (dd, J = 10.24, 1.25 Hz, 1H, CH=), 5.25 (dd, 1H, J = 17.16, 1.25, 1H, CH=), 5.88 (m, 1H, =CH), 6.70 (d, J = 2.6 Hz, 1H, pyrazole-H$_4$), 6.98 (d, J = 2.6 Hz, 1H, pyrazole-H$_5$), 7.10–7.86 (m, 6H, Ar–H + NH); ^{13}C NMR (100 MHz, DMSO-d$_6$): δ_{ppm} = 17.5 (CH$_3$), 46.89 (NCH$_2$), 102.68 (thiazole-C$_5$), 112.8 (pyrazole-C$_3$), 130.46 (pyrazole-C$_4$), 116.19 (CH$_2$=), 121.01 (Ar–C$_{2,6}$), 126.9 (Ar–C$_4$), 129.8 (Ar–C$_{3,5}$), 132.19 (CH=), 138.8 (Ar–C$_1$), 144.75 (pyrazole-C$_5$), 146.02 (thiazole-C$_4$), 165.49 (thiazole-C$_2$); MS m/z (%): 296 (M$^+$, 2.43), 272 (2.43), 266 (11.89), 254 (3.16), 236 (8.05), 205 (3.66), 191(0.86), 187 (15.79), 181 (36.32), 172 (29.62), 155 (49.47), 119 (11.56), 92 (45.69), 77 (100), 65 (32.07), 51 (10.03), 40 (22.98). Anal. Calcd For C$_{16}$H$_{16}$N$_4$S (296.11); C, 64.84; H, 5.44; N, 18.90%, Found: C, 64.83; H, 5.45; N, 18.93%.

Synthesis of 2-amino-4-(4-methyl-2-(prop-2-enylamino)thiazol-5-yl)pyrimidine (17)

Compound **4** (0.8 g, 0.003 mol), guanidine hydrochloride (0.3 g, 0.003 mol), and dry potassium carbonate (0.88 g, 0.006 mol) were mixed and refluxed in ethyl alcohol for 6 h. The solution was put into 20 mL cold water and left for 0.5 h. The formed substance was separated, washed with water, and sintered from methyl alcohol to provide pyrimidine **17**.

Orange powder; Yield 94%; mp. 164–165 °C; IR(KBr) v_{max}/cm^{-1} = 3191–3087 (NH$_2$, NH), 1636 (C=C),1586 (C=N); ^{1}H NMR (400 MHz, DMSO-d$_6$): δ_{ppm} = 2.41 (s, 3H, CH$_3$), 2.81 (s, 2H, NH$_2$), 3.85 (s, 2H, NCH$_2$), 5.13 (dd, J = 10.20, 1.25 Hz, 1H, CH=), 5.22 (dd, J = 17.16, 1.25 Hz, 1H, CH=), 5.86 (m, 1H, CH=), 7.49 (d, J = 6.8 Hz, 1H, pyrimidine-H$_5$), 8.14 (s, 1H, NH), 8.45 (d, J = 6.8 Hz, 1H, pyrimidine-H$_6$); ^{13}C NMR (100 MHz, DMSO-d$_6$): δ_{ppm} = 18.8 (CH$_3$), 46.95 (NCH$_2$), 94.18 (pyrimidine-C$_5$), 116.56 (thiazole-C$_5$), 122.26 (CH$_2$=), 135.01 (CH=), 144.01 (thiazole-C$_4$), 152.87 (pyrimidine-C$_6$), 153.3 (pyrimidine-C$_4$), 168.39 (thiazole-C$_2$), 179.79 (pyrimidine-C$_2$); MS m/z (%): 257 (M$^+$, 9.33), 206 (19.46), 194 (2.29), 181 (5.07), 152 (7.44), 151 (44.61), 141 (1.31), 138 (4.14), 137 (37.30), 136 (21.90), 134 (13.49), 127 (3.28), 125 (2.38), 123 (2.01), 113 (2.29), 111 (5.81), 100 (3.50), 99 (6.10), 97 (100), 70 (9.01), 69 (17.88), 68 (9.17), 66 (6.46), 64 (1.05), 57 (8.79), 55 (5.39), 54 (25.25), 52 (3.50), 44 (4.33), 42 (4.19), 41 (16.91), 40 (20.62). Anal. Calcd. For C$_{11}$H$_{13}$N$_5$S (247.09); C, 53.42; H, 5.30; N, 28.32%, Found: C, 53.43; H, 5.32; N, 28.31%.

Synthesis of 1-(4-methyl-2-(prop-2-enylamino)thiazol-5-yl)-3-(4H-1,2,4-triazol-3-ylamino)-2-propen-1-one (18)

A mixture of enaminone **4** (0.8 g, 0.003 mol) and 2-aminotriazole (0.27 g, 0.003 mol) was heated in ethyl alcohol (15 mL) for 8 h. The deposited substance was collected by filtration to provide pure compound **18**.

Pale green powder; Yield 92%; mp. 168–169 °C; IR(KBr) v_{max}/cm^{-1} = 3508, 3362, 3219 (3NH), 3081 (C–H, sp^2), 2936 (C–H, sp^3), 1645 (C=O), 1630 (C=C), 1584 (C=N); ^{1}H NMR (400 MHz, DMSO-d$_6$): δ_{ppm} = 2.51 (s, 3H, CH$_3$), 3.98 (s, 2H, NCH$_2$), 5.16 (dd, J = 10.24, 1.25 Hz, 1H, CH=), 5.27 (dd, J = 17.17, 1.25 Hz, 1H, CH=), 5.94 (m, 1H, CH=), 8.62 (bs, 1H, NH), 8.66 (s, 1H, triazole-H$_3$), 9.25 (s, 1H, triazole-H$_4$), 10.13 (s, 1H, NH), 10.16 (d, J = 14.0 Hz, 1H, CH=), 11.73 (d, J = 14.0 Hz, 1H, CH=); ^{13}C NMR (100 MHz, DMSO-d$_6$): δ_{ppm} = 17.7 (CH$_3$), 46.6 (NCH$_2$), 98.21 (CH=C), 110.6 (thiazole-C$_5$), 116.2 (CH$_2$=), 134.8 (CH=), 152.9 (thiazole-C$_4$), 155.65 (NCH=), 157.4 (thiazole-C$_3$), 159.5 (thiazole-C$_5$), 167.0 (thiazole-C$_2$), 183.31(C=O); Anal. Calcd. For C$_{12}$H$_{14}$N$_6$OS (290.35); C, 49.64; H, 4.86; N, 28.95%, Found: C, 49.63; H, 4.84; N, 28.93%.

General procedure for interaction of enaminone with aminoazoles

Enaminone **4** (0.63 g, 0.0025 mol) and the appropriate aminoazoles (1,2,4-triazole-3-amine (0.21 g, 0.0025 mol), 5-amino-3-phenyl-1*H*-pyrazole (0.4 g, 0.0025 mol), 2-aminobenzimidazole (0.33 g, 0.0025 mol)) were refluxed in 15 mL ethanoic acid 12 h and then left to cool down to room temperature. The deposited substances were taken up, dried, and sintered from a mixture of MeOH:DMF (1:1) to afford compounds **19**, **21**, and **23**.

4-Methyl-2-(prop-2-enylamino)-5-([1,2,4]triazolo[1,5-a]pyrimidin-7-yl) thiazole (19)

Green crystals; Yield 90%; mp. 176–177 °C; IR (KBr) v_{max}/cm^{-1} = 3195 (NH), 3080 (C–H, sp^2), 2934 (C–H, sp^3), 1633 (C=C), 1583 (C=N); ^{1}H NMR (400 MHz, DMSO-d$_6$): δ_{ppm} = 2.59 (s, 3H, CH$_3$), 4.05 (s, 2H, NCH$_2$), 5.16 (dd, J = 10.24, 1.25 Hz, 1H, CH=), 5.30 (dd, J = 17.16, 1.25 Hz, 1H, CH=), 5.89 (m, 1H, =CH), 7.48 (d, J = 4.68 Hz, 1H, pyrimidine-H$_6$), 8.62 (bs, 1H, NH), 8.65 (s, 1H, triazole-H$_3$), 8.81 (d, J = 4.68 Hz, 1H, pyrimidine-H$_7$); ^{13}C NMR (100 MHz, DMSO-d$_6$): δ_{ppm} = 20.3 (CH$_3$), 46.84 (NCH$_2$), 105.73 (thiazole-C$_5$), 107.45 (pyrimidine-C$_5$), 116.70 (CH$_2$=), 134.56 (CH=), 142.35 (pyrimidine-C$_6$), 154.10 (pyrimidine-C$_5$), 154.82 (pyrimidine-C$_4$), 155.81 (thiazole-C$_4$), 158.54 (pyrimidine-C$_2$), 172.36 (thiazole-C$_2$); MS *m/z* (%): 272 (M$^+$,100), 257 (38.40), 245 (11.56), 244 (16.46), 231 (14.26), 230 (23.23), 204 (29.47), 198 (7.61), 191 (7.86), 190 (9.74), 189 (11.40), 162 (17.49), 158 (12.97), 107 (6.74), 105 (1.71), 103 (2.50), 98 (1.19), 95 (2.22), 94 (11.04), 78 (1.57), 76 (3.28), 75 (1.82), 69 (3.41), 68 (4.72), 67 (6.68), 64 (6.17), 56 (3.11), 41 (8.82). Anal. Calcd. For C$_{12}$H$_{12}$N$_6$S (272.08); C, 52.92; H, 4.44; N, 30.86%, Found: C, 52.95; H, 4.43; N, 30.88%.

4-Methyl-2-(prop-2-enylamino)-5-(2-phenyl-pyrazolo[1,5-a]pyrimidin-7-yl)thiazole (21)

Orange crystals; Yield 89%; mp. 130–131 °C; IR (KBr) v_{max}/cm^{-1} = 3200 (NH), 3083 (C–H, sp^2), 2958 (C–H, sp^3), 1625 (C=C), 1559 (C=N); ^{1}H NMR (400 MHz, DMSO-d$_6$): δ_{ppm} = 2.47 (s, 3H, CH$_3$), 3.89 (s, 2H, NCH$_2$), 5.15-5.26 (m, 2H, CH$_2$=), 5.90 (m, 1H, CH=), 6.25 (s, 1H, pyrazole-H$_4$), 7.12 (d, J = 5 Hz, 1H, pyrimidine-H$_5$), 7.15-7.90 (m, 5H, Ar–H), 7.99 (d, J = 5 Hz, 1H, pyrimidine-H$_4$), 8.51 (bs, 1H, NH); ^{13}C NMR (100 MHz, DMSO-d$_6$): δ_{ppm} = 20.01 (CH$_3$), 46.7 (NCH$_2$), 93.37 (pyrazole-C$_4$), 105.87 (pyrimidine-C$_5$), 106.17 (thiazole-C$_5$), 116.76 (CH$_2$=), 126.59 (2CH–Ar), 129.34 (2CH–Ar), 129.54 (CH=), 132.90 (CH–Ar), 134.92 (Cq–Ar), 140.29 (pyrazole-C$_5$), 149.29 (pyrimidine-C$_6$), 150.73 (thiazole-C$_4$), 153.95 (pyrimidine-C$_4$), 156.87 (pyrimidine-C$_2$), 171.59 (thiazole-C$_2$); MS *m/z* (%): 321 (M$^+$, 100), 320 (M$^+$ − H, 32.02), 306 (26.61), 280 (14.79), 238 (22.98), 213 (15.81), 207 (36.01), 196 (35.03), 181 (64.71), 168 (26.55), 154 (21.76), 133 (61.11), 114 (11.77), 105 (23.43), 90 (32.76), 85 (9.90), 71 (19.16), 41 (19.54). Anal. Calcd. For C$_{19}$H$_{17}$N$_5$S (347.12); C, 65.68; H, 4.93; N, 20.16%, Found: C, 65.70; H, 4.94; N, 20.17%.

5-(Benzo[d]imidazo[1,2-a]pyrimidin-4-yl)-4-methyl-2-(prop-2-enylamino) thiazole (23)

Orange powder; Yield 85%; mp. 130–131 °C; IR (KBr) v_{max}/cm^{-1} = 3200 (NH), 3083 (C–H, sp^2), 2958 (C–H, sp^3), 1625 (C=C), 1559 (C=N); ^{1}H NMR (400 MHz, DMSO-d$_6$): δ_{ppm} = 2.47 (s, 3H, CH$_3$), 3.89 (s, 2H, NCH$_2$), 5.15-5.13 (m, 2H, CH$_2$=), 5.90 (m, 1H, CH=), 7.12 (d, J = 5.0 Hz, 1H, pyrimidine-H$_5$), 7.15–7.90 (m, 4H, Ar-H), 7.99 (d, J = 5.0 Hz, 1H, pyrimidine-H$_4$), 8.51 (bs, 1H, NH); ^{13}C NMR (100 MHz, DMSO-d$_6$): δ_{ppm} = 19.0 (CH$_3$), 46.89 (NCH$_2$), 99.69 (thiazole-C$_5$), 111.81 (Ar–C$_{3,5}$), 116.81 (CH$_2$=), 120.26 (pyrimidine-C$_5$), 121.43 (Ar–C$_{4,5}$), 123.50 (Ar–CH), 130.18 (imidazole-C$_5$), 134.31 (imidazole-C$_4$), 134.50 (CH=), 134.62 (pyrimidine-C$_2$), 141.31 (pyrimidine-C$_4$), 141.69 (thiazole-C$_4$), 156.16 (pyrimidine-C$_6$),170.36 (thiazole-C$_2$); MS *m/z* (%): 321 (M$^+$, 100), 320 (32.02), 306 (26.61), 280 (14.79), 238 (22.98), 213 (15.81), 207 (36.01), 196

(35.03), 181 (64.71), 168 (26.55), 154 (21.76), 133 (61.11), 114 (11.77), 105 (23.43), 90 (32.76), 85 (9.90), 71 (19.16), 41 (19.54). Anal. Calcd. For $C_{17}H_{15}N_5S$ (321.1); C, 63.53; H, 4.70; N, 21.79%, Found: C, 63.55; H, 4.68; N, 21.78%.

Synthesis of 3-(1H-indol-3-yl)-1-(4-methyl-2-(prop-2-enylamino)thiazol-5-yl)-2-propen-1one (24)

Method A: Indole (0.37 g, 0.003 mol) and enaminone **4** (0.8 g, 0.003 mmol) were heated, for 12 h, in 15 mL ethanoic acid. The cold-separated solid was taken up by filtration, and sintered from ethyl alcohol to deliver compound **24**.

Method B: Thiazole **3** (0.2 g, 0.001 mol) was boiled for 48 h with 3-formylindole (0.15 g, 0.001 mol) in dry ethanol (10 mL) comprising 0.1 mL piperidine. The deposited substance on cold was picked up to deliver **24**.

Yellow crystals; Yield 77%; mp. >300 °C; IR (KBr) υ_{max}/cm^{-1} = 3204, 3178 (2NH), 3088 (C–H, sp^2), 2980 (C–H, sp^3), 1635 (conjugated C=O), 1621 (conjugated C=C); ^{1}H NMR: (850 MHz, DMSO-d$_6$): δ_{ppm} = 2.58 (s, 3H, CH$_3$), 3.93 (s, 2H, NCH$_2$), 5.16 (dd, J = 17.0, 1.7 Hz, 1H, CH=), 5.26 (dd, J = 10.2, 1.7 Hz, 1H, CH=), 5.91 (m, 1H, =CH), 7.13 (d, J = 15.3 Hz, 1H, CH=), 7.23–7.81 (m, 4H, Ar–H), 7.83 (d, J = 15.3 Hz, 1H, CH=), 8.00 (s, 1H, Indole-H$_2$), 8.60 (bs, 1H, NH), 11.90 (s, 1H, NH indole); ^{13}C NMR (212.5 MHz, DMSO-d$_6$): δ_{ppm} = 18.85 (CH$_3$), 46.45 (NCH$_2$), 112.37 (indole-C$_8$), 116.28 (CH$_2$=), 118.46 (CH–CO), 119.00 (indole-C$_6$), 121.10 (indole-C$_5$), 121.41 (thiazole-C$_5$), 122.5 (indole-C$_7$), 122.59,(indole-C$_3$), 124.95 (indole-C$_4$), 132.66 (CH=), 134.08 (indole-C$_9$), 136.31 (indole-C$_2$), 137.55 (CH-indole), 156.90 (thiazole-C$_4$), 169.44 (thiazole-C$_2$), 180.37 (C=O); MS m/z (%): 323 (M$^+$, 15.85), 315 (12.19), 304 (12.17), 278 (19.83), 263 (3.92), 259 (11.00), 240 (8.95), 220 (5.41), 212 (14.59), 190 (7.39), 186 (1.81), 172 (3.81), 154 (8.32), 137 (8.37), 110 (4.53), 99 (18.71), 97 (19.78), 91 (13.88), 81 (10.45), 77 (7.28), 67 (21.19), 56 (31.19), 51 (15.78), 43 (100). Anal. Calcd. For $C_{18}H_{17}N_3OS$ (323.11); C, 66.85; H, 5.30; N, 12.99%, Found: C, 66.84; H, 5.32; N, 13.02%.

Typical procedure for the interaction of enaminone with 1,3-dicarbonyl reagents

An equimolar amount of 1,3-dicarbonyl reagents (acetylacetone (0.33 mL, 0.003 mol), ethyl ace-toacetate (0.43 mL, 0.003 mol), and/or ethyl benzoylacetate (0.6 mL, 0.003 mol)), enaminone **4** (0.8 g, 0.003 mol) and ammonium ethanoate (0.24 g, 0.003 mol) was refluxed in ethanoic acid (25 mL) for 10 h. The created precipitate upon dilution with ice water (15 mL) was taken up by filtration, rinsed with aqueous ethanol, and sintered from mixed solvents of EtOH/DMF (1:1) to provide pyridines **26a–c**.

3-Acetyl-6-(4-methyl-2-(prop-2-enylamino)thiazol-5-yl)-2-methylpyridine (26a)

Yellow crystals; 93%; mp. 154–155 °C; IR (KBr) υ_{max}/cm^{-1} = 3204 (NH), 3070 (C–H, sp^2), 2969 (C–H, sp^3), 1666 (C=O), 1638 (C=C), 1598 (C=N); ^{1}H NMR (400 MHz, DMSO-d$_6$): δ_{ppm} = 1.91 (s, 3H, CH$_3$), 2.68 (s, 3H, CH$_3$), 2.76 (s, 3H, CH$_3$), 3.90 (s, 2H, CH$_2$N), 5.13 (dd, J = 10.16, 1.5 Hz, 1H, CH=), 5.30 (dd, J = 17.0, 1.5 Hz, 1H, CH=), 5.91 (m, 1H, CH=), 7.42 (d, J = 8.36 Hz, 1H, pyridine-H$_3$), 8.14 (bs, 1H, NH), 8.19 (d, J = 8.36 Hz, 1H, pyridine-H$_4$); ^{13}C NMR (100 MHz, DMSO-d$_6$): δ_{ppm} = 18.90 (CH$_3$), 25.40 (CH$_3$), 29.60 (CH$_3$), 46.80 (NCH$_2$), 116.44 (thiazole-C$_5$), 116.48 (CH$_2$=), 127.86 (CH=), 119.44 (pyridine-C$_3$), 135.05 (pyridine-C$_5$), 139.04 (pyridine-C$_4$), 150.25 (thiazole-C$_4$), 153.81 (pyridine-C$_2$), 157.79 (pyridine-C$_6$), 168.67 (thiazole-C$_2$), 199.65 (C=O); MS m/z (%): 287 (M$^+$, 14.49), 272 (25.77), 260 (4.45), 259 (6.58), 247 (4.82), 238 (5.82), 207 (18.75), 196 (31.49), 181 (56.89), 172 (32.24), 155 (27.30), 133 (54.33), 113 (25.72), 71

(55.10), 60 (76.30), 55 (31.3), 45 (60.8), 43 (100). Anal. Calcd. For $C_{15}H_{17}N_3OS$ (287.38); C, 62.69; H, 5.96; N, 14.62%, Found: C, 62.68; H, 5.95; N, 14.60%.

Ethyl 6-(4-methyl-2-(prop-2-enylamino)thiazol-5-yl)-2-methylnicotinate (26b)

Yellow crystals; Yield 71%; mp. 160–161 °C; IR (KBr) v_{max}/cm^{-1} = 3200 (NH), 3087 (C–H, sp^2), 2973 (C–H, sp^3), 1725 (C=O), 1625 (C=C), 1598 (C=N); ^{1}H NMR (850 MHz, DMSO-d$_6$): δ_{ppm} = 1.32 (t, J = 6.8 Hz, 3H, CH$_3$), 2.46 (s, 3H, CH$_3$), 2.75 (s, 3H, CH$_3$), 3.89 (t, J = 4.5 Hz, 2H, NCH$_2$), 4.28 (q, J = 6.8 Hz, 2H, OCH$_2$), 5.13 (dd, J = 9.0, 1.5 Hz, 1H, CH=), 5.26 (dd, J = 15.75, 1.5 Hz, 1H, CH=), 5.91 (m, 1H, CH=), 7.24 (d, J = 8.5 Hz, 1H, pyridine-H$_5$), 8.12 (d, J = 8.5 Hz, 1H, pyridine-H$_4$), 8.15 (t, J = 4.5 Hz, 1H, NH); ^{13}C NMR (212.5 MHz, DMSO-d$_6$): δ_{ppm} = 14.1 (CH$_3$), 18.5 (CH$_3$), 24.7 (CH$_3$), 46.3 (NCH$_2$), 60.6 (CH$_2$O), 115.98 (pyridine-C$_3$), 116.2 (CH$_2$=), 118.9 (pyridine-C$_5$), 119.9 (thiazole-C$_5$), 134.5 (CH=), 138.7 (pyridine-C$_4$), 150.0 (pyridine-C$_2$), 153.4 (thiazole-C$_4$), 158.6 (pyridine-C$_6$), 165.6 (thiazole-C$_2$), 168.2 (C=O); MS m/z (%): 317 (M$^+$, 14.49), 315 (12.00), 303 (75.06), 296 (19.81), 271 (10.65), 269 (13.48), 245 (15.83), 242 (17.23), 228 (19.05), 227 (15.24), 180 (61.94), 177 (19.15), 174 (22.06), 173 (32.12), 171 (26.78), 156 (20.19), 154 (24.81), 145 (15.98), 111 (16.72), 104 (18.76), 99 (32.35), 89 (31.66), 87 (23.95), 85 (61.07), 77 (22.62), 71 (21.01), 69 (29.05), 66 (20.50), 62 (15.42), 59 (24.30), 54 (100). Anal. Calcd. For $C_{16}H_{19}N_3O_2S$ (317.12); C, 60.54; H, 6.03; N, 13.24%, Found: C, 60.51; H, 6.06; N, 13.23%.

Ethyl 6-(4-methyl-2-(prop-2-enylamino)thiazol-5-yl)-2-phenylnicotinate (26c)

Yellow crystals; Yield 76%; mp. 171–172 °C; IR (KBr) v_{max}/cm^{-1} = 3202 (NH), 3082 (C–H, sp^2), 2935 (C–H, sp^3), 1717 (C=O), 1628 (C=C), 1582 (C=N); ^{1}H NMR (850 MHz, DMSO-d$_6$): δ_{ppm} = 1.33 (t, J = 6.8 Hz, 3H, CH$_3$), 2.51 (s, 3H, CH$_3$), 3.92 (t, J = 4.5 Hz, 2H, NCH$_2$), 4.29 (q, J = 6.8 Hz, 2H, OCH$_2$), 5.15 (dd, J = 9.0, 1.5 Hz, 1H, CH=), 5.27 (dd, J = 15.7, 1.5 Hz, 1H, CH=), 5.90 (m, 1H, CH=), 7.24 (d, J = 8.5 Hz, 1H, pyridine-H$_5$), 7.98–7.58 (m, 5H, Ar–H), 8.18 (d, J = 8.5 Hz, 1H, pyridine-H$_4$), 8.17 (bs, 1H, NH); ^{13}C NMR (212.5 MHz, DMSO-d$_6$): δ_{ppm} = 14.1 (CH$_3$), 18.43 (CH$_3$), 46.3 (NCH$_2$), 60.9 (CH$_2$O), 115.92 (pyridine-C$_3$), 116.5 (CH$_2$=), 119.1 (pyridine-C$_5$), 119.03 (thiazole-C$_5$), 127.9 (Ar–C$_{2,6}$), 128.3 (Ar–C$_4$), 129.1 (Ar–C$_{3,5}$), 134.5 (CH=), 136.07 (Ar–C$_1$), 138.63 (pyridine-C$_4$), 153.4 (thiazole-C$_4$), 150.1 (pyridine-C$_2$), 157.47 (pyridine-C$_6$), 163.1 (thiazole-C$_2$), 168.10 (C=O); MS m/z (%): 379 (M$^+$, 100), 378 (11.32), 376 (2.48), 366 (2.17), 365 (5.23), 364 (20.15), 353 (1.61), 352 (8.76), 351 (6.00), 350 (9.36), 346 (3.08), 339 (3.22), 338 (5.66), 337 (9.28), 336 (6.18), 334 (4.26), 324 (1.89), 322 (1.46), 319 (1.11), 317 (5.41), 311 (1.50), 310 (6.43), 308 (1.96), 306 (1.72), 104 (3.29), 76 (2.67), 42 (2.32), 41 (4.28). Anal. Calcd. For $C_{21}H_{21}N_3O_2S$ (379.14); C, 66.47; H, 5.58; N, 11.07%, Found: C, 66.45; H, 5.60; N, 11.04%.

Synthesis of ethyl 2-oxo-6-(4-methyl-2-(prop-2-enylamino)thiazol-5-yl)-1,2-dihydropyridine-3-carboxylate (31)

Enaminone **4** (1.26 g, 0.005 mol) in sodium ethoxide solution, prepared by dissolving 0.12 g Na in 20 mL dry ethanol, and ethyl cyano ethanoate (0.53 mL, 0.005 mol) was warmed for 12 h. Then, the solution was added to cold water (20 mL) containing two drops of HCl (1 M). The formed substance was collected, dried, and sintered from ethyl alcohol to furnish pyridone **31**.

Pale yellow powder; Yield 68%; mp. 185–186 °C; IR (KBr) v_{max}/cm^{-1} = 3310, 3200 (2NH), 3067 (C–H, sp^2), 2928 (C–H, sp^3), 1720, 1640 (2C=O), 1618 (C=C), 1587 (C=N); ^{1}H NMR (850 MHz, DMSO-d$_6$): δ_{ppm} = 1.20 (t, J = 6.8 Hz, 3H, CH$_2$CH$_3$), 2.40 (s, 3H, CH$_3$), 3.92 (bs, 2H, NCH$_2$), 4.13 (q, J = 6.8 Hz, 2H, OCH$_2$), 5.16 (dd, J = 10.0, 1.7 Hz, 1H, CH=), 5.24 (dd, J = 17.5,

1.7 Hz, 1H, CH=), 5.89 (m, 1H, CH=), 8.17 (d, J = 8.5 Hz, 1H, pyridine-H$_5$), 8.32 (d, J = 8.5 Hz, 1H, pyridine-H$_4$), 8.69 (bs, 1H, NH), 9.59 (bs, 1H, NH); ^{13}C NMR (212.5 MHz, DMSO-d$_6$): δ_{ppm} = 14.0 (CH$_3$), 14.05 (CH$_3$), 46.58 (NCH$_2$), 61.6 (CH$_2$O), 109.34 (thiazole-C$_5$), 116.2 (CH$_2$=), 116.49 (pyridine-C$_5$), 121.77 (CH=), 123.50 (pyridine-C$_3$), 133.77 (pyridine-C$_6$), 134.16 (pyridine-C$_4$), 149.51 (thiazole-C$_4$), 152.57 (thiazole-C$_2$), 162.87 (amidic C = O), 165.20 (ester C = O); MS m/z (%): 319 (M$^+$, 31.39), 294 (10.34), 278 (19.14), 269 (5.10), 266 (25.45), 253 (34.45), 247 (13.48), 233 (22.82), 217 (18.69), 207 (36.52), 204 (6.04), 198 (10.43), 187 (80.99), 178 (11.79), 171 (35.87), 168 (41.00), 158 (19.56), 124 (56.73), 111 (73.31), 108 (40.51), 106 (50.18), 78 (52.27), 72 (48.93), 66 (15.82), 57 (33.56), 55 (100). Anal. Calcd. For C$_{15}$H$_{17}$N$_3$O$_3$S (319.10); C, 56.41; H, 5.37; N, 13.16%, Found: C, 56.43; H, 5.36; N, 13.14%.

General procedure for the coupling reaction of enaminone 4 with diazotized heterocyclic amines

To an ice-cold solution of enaminone **4** (1.26 g, 0.005 mol) in 15 mL pyridine was added portion-wise a cold suspension of the suitable diazonium salt of the corresponding heteroaryl amine (1,2,4-triazole-3-amine (0.42 g, 0.005 mol), 5-amino-3-phenylpyrazole (0.8 g, 0.005 mol), 2-amino-benzimidazole (0.67 g, 0.005 mol)), obtained as normal by adding a solution of sodium nitrite (0.35 g, 0.005 mol) in 5 mL water to the request heteroaryl amine (0.005 mmol) in HNO$_3$ (6 M, 3.5 mL). The reaction mixture was agitated for an additional 1 h while chilling in an ice-sodium chloride bath and then refrigerated for 48 h. The formed precipitate was taken up, rinsed with ether, and sintered from equal mixed solvents of MeOH/DMF to produce compounds **33**, **35**, and **37**.

(4-Methyl-2-(prop-2-enylamino)thiazol-5-yl)([1,2,4]-triazolo[3,4-c][1,2,4] triazin-6-yl)methanone (33)

Orange powder; Yield 63%; mp. >300 °C; IR(KBr) υ_{max}/cm^{-1} = 3198 (NH), 3067 (C–H, sp^2), 2928 (C–H, sp^3), 1632 (C = O), 1620 (C = C), 1561 (C = N); ^{1}H NMR (850 MHz, DMSO-d$_6$): δ_{ppm} = 2.49 (s, 3H, CH$_3$), 3.98 (t, J = 5.0 Hz, 2H, NCH$_2$), 5.17 (dd, J = 1.5, 10.0 Hz, 1H, CH=), 5.26 (dd, J = 1.5, 15.0 Hz, 1H, CH=), 5.94 (m, 1H, CH=), 6.81 (s, 1H, triazole-H$_3$), 7.98 (s, 1H, triazine-H$_5$), 8.87 (bs, 1H, NH); ^{13}C NMR: (212.5 MHz, DMSO-d$_6$): δ_{ppm} = 19.6 (CH$_3$), 46.3 (NCH$_2$), 111.97 (thiazole-C$_5$), 116.27 (CH$_2$=), 133.9 (CH=), 138.67 (triazole-C$_3$), 146.57 (triazine-C$_5$), 149.38 (triazine-C$_3$), 150.36 (triazine-C$_6$), 169.0 (thiazole-C$_2$), 178.27 (C = O); MS m/z (%): 301 (M$^+$, 5.63), 243 (7.15), 235 (7.91), 231 (7.26), 220 (1.59), 211 (2.61), 206 (8.40), 204 (3.03), 192 (11.25), 188 (5.61), 184 (5.03), 182 (5.35), 165 (13.86), 155 (4.04), 128 (5.46), 125 (4.48), 122 (8.16), 120 (22.20), 111 (24.01), 106 (14.02), 101 (4.64), 100 (13.02), 98 (11.65), 96 (16.59), 79 (11.72), 76 (13.25), 72 (12.52), 70 (56.98), 68 (11.05), 67 (23.63), 65 (31.52), 61 (5.71), 57 (19.46), 53 (54.75), 52 (100). Anal. Calcd. For C$_{12}$H$_{11}$N$_7$OS (301.07); C, 47.83; H, 3.68; N, 32.54%, Found: C, 47.82; H, 3.66; N, 32.53%.

(4-Methyl-2-(prop-2-enylamino)thiazol-5-yl)(7-phenylpyrazolo[5,1-c][1,2,4]triazin-3-yl)methanone (35)

Red powder; Yield 68%; mp. >300 °C; IR (KBr) υ_{max}/cm^{-1} = 3200 (NH), 3069 (C–H, sp^2), 2932 (C–H, sp^3), 1638 (C = O), 1620 (C = C), 1571 (C = N); ^{1}H NMR (850 MHz, DMSO-d$_6$): δ_{ppm} = 2.50 (s, 3H, CH$_3$), 3.91 (bs, 2H, NCH$_2$), 5.16 (dd, J = 1.5, 10.0 Hz, 1H, CH=), 5.26 (dd, J = 1.5, 15.0 Hz, 1H, CH=), 5.94 (m, 1H, CH=), 6.26 (s, 1H, pyrazole-H$_4$), 7.35–7.48 (m, 5H, Ar–H), 8.22 (bs, 1H, NH), 9.59 (s, 1H, triazine-H$_5$); ^{13}C NMR (212.5 MHz, DMSO-d$_6$): 17.75 (CH$_3$), 46.41 (NCH$_2$), 71.23 (pyrazole-C$_4$), 110.35 (triazole-C$_5$), 116.26 (CH$_2$=), 126.94 (Ar–C$_{2,6}$), 128.65

(Ar–C$_4$), 129.24 (Ar–C$_{3.5}$), 133.21 (Ar–C$_1$), 134.62 (CH=), 144.3 (triazine-C$_5$), 149.5 (triazine-C$_3$), 151.7 (triazine-C$_6$), 152.5 (thiazole-C$_4$), 154.3 (pyrazole-C$_5$), 167.05 (thiazole-C$_2$), 169.35 (C=O); MS m/z (%): 376 (M$^+$,10.43), 349 (22.47), 347 (100), 336 (18.31), 335 (77.99), 334 (50.70), 333 (85.97), 322 (4.06), 321 (13.30), 320 (22.00), 315 (3.79), 309 (2.79), 308 (10.36), 307 (11.42), 305 (1.37), 302 (1.17), 295 (7.85), 294 (15.16), 292 (22.35), 291 (15.05), 77 (7.63), 70 (3.20), 68 (1.70), 66 (2.84), 52 (4.33), 50 (1.34), 41 (4.76). Anal. Calcd. For C$_{19}$H$_{16}$N$_6$OS (376.11); C, 60.62; H, 4.28; N, 22.33%, Found: C, 60.65; H, 4.26; N, 22.31%.

(Benzo[d]imidazo[2,1-c][1,2,4]triazin-3-yl)(4-Methyl-2-(prop-2-enylamino) thiazol-5-yl)methanone (37)

Yellow powder; Yield 85%; mp. 128–129 °C; IR (KBr) v_{max}/cm^{-1} = 3200 (NH), 3067 (C–H, sp^2), 2930 (C–H, sp^3), 1628 (C=O), 1620 (C=C), 1573 (C=N); ^{1}H NMR (850 MHz, DMSO-d$_6$): δ_{ppm} = 2.41 (s, 3H, CH$_3$), 3.93 (bs, 2H, NCH$_2$), 5.12 (dd, J = 10.0, 1.5 Hz, 1H, CH=), 5.24 (dd, J = 15.5, 1.5 Hz, 1H, CH=), 5.89 (m, 1H, CH=), 7.38 (t, J = 7.6 Hz, 2H, Ar–H$_{4,5}$), 7.78 (d, J = 7.6 Hz, 2H, Ar–H$_{3,6}$), 8.58 (s, 1H, triazine-H), 8.93 (s, 1H, NH); ^{13}C NMR (212.5 MHz, DMSO-d$_6$): δ_{ppm} = 19.1 (CH$_3$), 46.3 (NCH$_2$), 112.4 (thiazole-C$_5$), 113.25 (Ar–C$_3$), 116.41 (CH$_2$=), 116.5 (Ar–C$_5$), 117.21 (Ar–C$_4$), 123.29 (Ar–C$_6$), 134.29 (pyrazole-C$_5$), 134.44 (CH=), 136.16 (pyrazole-C$_4$), 136.78 (triazole-C$_5$), 149.61 (triazole-C$_6$), 152.77 (thiazole-C$_4$), 161.94 (triazole-C$_3$), 165.31 (thiazole-C$_2$), 176.5 (C=O). Anal. Calcd. For C$_{17}$H$_{14}$N$_6$OS (350.09); C, 58.27; H, 4.03; N, 23.98%, Found: C, 58.24; H, 4.04; N, 23.96%.

Cytotoxicity assay

Sulphorhodamine B (SRB) assay technique was used to assess the cytotoxicity of some new synthesized thiazoles against three tumor cells and one regular cell. The hepatocytes for breast cancer (MCF-7), colon carcinoma (HCT-116), and hepatocellular carcinoma (HepG-2) were grown in RPMI-1640 media, while the ordinary human epithelia line (RPE1) was grown in DMEM-F12. ATCC provides the cell lines through VACSERA, an organic products and vaccine holding firm based in Cairo, Egypt. All media were complemented with ten percentage of fetal bovine serum, 10^2 units per milliliter of penicillin, and 0.1 g/L streptomycin. The cells were reserved at 37 °C in a humidified environment with 5% carbon dioxide and subcultured for two to three weeks. Using 0.25% trypsin–EDTA, exponentially developing cells were removed from dishes and placed in 96-well plates at a density of about 1000 cells per well. After a 24-h incubation period, cells were treated for 48 h with varied doses of the tested substances. Cells were preserved with 10% trichloroacetic acid for 1 h at 4 °C, washed multiple times with distilled water, stained with 0.4% SRB solution for 10 min in a dark area, and finally rinsed with 1% ethanoic acid. Tris–HCl was used to dissolve the SRB-stained cells after they had dried overnight. The color intensity was assessed at 570 nm by means of a microplate reader (Anthos Zenyth-200RT, Cambridge, England). The IC$_{50}$ value, concentration that inhibits 50% of cellular development, is determined. As a positive control, doxorubicin was utilized and the bioassays were carried out in triplicate.

ORCID

Samir Bondock   http://orcid.org/0000-0003-1622-1599

References

1. Samir Bondock, Omeer Albormani, Ahmed M. Fouda, and Kayed A. Abu Safieh, "Progress in the Chemistry of 5-Acetylthiazoles," *Synthetic Communications* 46, no. 13 (2016): 1081–117.
2. Olesia G. Kulyk, Dmytro A. Biloborodov, Maksim A. Cherevatenko, Yevhen Y. Shyriakin, Alexander Yu Lyapunov, Alexander V. Mazepa, Valerii V. Vashchenko, Valeriy D. Orlov, and Maksim A. Kolosov, "Versatile Approaches to a Library of Building Blocks Based on 5-Acylthiazole Skeleton," *Synthetic Communications* 50, no. 23 (2020): 3616–28.
3. Adileh Ayati, Saeed Emami, Setareh Moghimi, and Alireza Foroumadi, "Thiazole in the Targeted Anticancer Drug Discovery," *Future Medicinal Chemistry* 11, no. 15 (2019): 1929–52.
4. Saqarkumar Patel Anuradha, Rajkumar Patle, Preethi Parameswaran, Alok Jain, and Amit Shard, "Design, Computational Studies, Synthesis and Biological Evaluation of Thiazole-Based Molecules as Anticancer Agents," *European Journal of Pharmaceutical Science* 134 (2019): 20–30.
5. Samir Bondock, and Tamer Nasr, "Synthesis and Antimicrobial Activity of New 4-Methyl-2-(3-Pyridyl)Thiazolyl Chalcones and Pyrazolines," *Russian Journal of General Chemistry* 91, no. 3 (2021): 488–94.
6. Samir Bondock, Tamer Naser, and Yousry A. Ammar, "Synthesis of Some New 2-(3-Pyridyl)-4,5-Disubstituted Thiazoles as Potent Antimicrobial Agents," *European Journal of Medicinal Chemistry* 62 (2013): 270–9.
7. Anna Biernasiuk, Magdalena Kawczyńska, Anna Berecka-Rycerz, Beata Rosada, Anna Gumieniczek, Anna Malm, Katarzyna Dzitko, and Krzysztof Z. Łączkowski, "Synthesis, Antimicrobial Activity, and Determination of the Lipophilicity of ((Cyclohex-3-Enylmethylene)Hydrazinyl) Thiazole Derivatives," *Medicinal Chemistry Research* 28, no. 11 (2019): 2023–36.
8. Dattatraya G. Raut, Sandeep B. Patil, Prafulla B. Choudhari, Vikas D. Kadu, Anjana S. Lawand, Mahesh G. Hublikar, and Raghunath B. Bhosale, "POCl$_3$ Mediated Synthesis, Pharmacological Evaluation and Molecular Docking Studies of Some Novl Benzofused Thiazole Derivatives as a Potential Antioxidant and anti-Inflammatory Agents," *Current Chemical Biology* 14, no. 1 (2020): 58–68.
9. Salah A. Abdel-Aziz, Ehab S. Taher, Ping Lan, Gihan F. Asaad, Hesham A. M. Gomaa, Nawal A. El-Koussi, and Bahaa G. M. Youssif, "Design, Synthesis, and Biological Evaluation of New Pyrimidine-5-Carbonitrile Derivatives Bearing 1,3-Thiazole Moiety as Novel Anti-Inflammatory EGFR Inhibitors with Cardiac Safety Profile," *Bioorganic Chemistry* 111 (2021): 104890.
10. Gajendra Kumar, and N. P. Singh, "Synthesis, Anti-Inflammatory and Analgesic Evaluation of Thiazole/Oxazole Substituted Benzothiazole Derivatives," *Bioorganic Chemistry* 107 (2021): 104608.
11. Inder P. Singh, Shiv Gupta, and Sanjay Kumar, "Thiazole Compounds as Antiviral Agents: An Update," *Medicinal Chemistry (Shariqah (United Arab Emirates))* 16, no. 1 (2020): 4–23.
12. Sobhi M. Gomha, Khaled Khalil, Hassan Abdel-Aziz, and Mohamed Abdalla, "Synthesis and Antihypertensive α-Blocking Activity Evaluation of Thiazole Derivatives Bearing Pyrazole Moiety," *Heterocycles* 91, no. 9 (2015): 1763–73.
13. Arpita Das, Surajit K. Ghosh, Hans R. Bhat, Junmoni Kalita, Ankita Kashyap, and Nayana Adhikari, "Docking, Synthesis and Antimalarial Evaluation of Hybrid Phenyl Thiazole 1,3,5-Triazene Derivatives," *Current Bioactive Compounds* 16, no. 5 (2020): 639–53.
14. Anthi Petrou, Maria Fesatidou, and Athina Geronikaki, "A Thiazole Ring – A Biologically Active Scaffold," *Molecules* 26, no. 11 (2021): 3166.
15. Branko Stanovnik, and Jurij Svete, "Synthesis of Heterocycles from Alkyl 3-(Dimethylamino)Propenoates and Related Enaminones," *Chemical Reviews* 104, no. 5 (2004): 2433–80.
16. Sayed M. Riyadh, "Enaminones as Building Blocks for the Synthesis of Substituted Pyrazoles with Antitumor and Antimicrobial Activities," *Molecules (Basel, Switzerland)* 16, no. 2 (2011): 1834–53.
17. Hatem M. Gaber, Mark C. Bagley, Zeinab A. Muhammad, and Sobhi M. Gomha, "Recent Developments in Chemical Reactivity of N,N-Dimethylamino Ketones as Synthons for Various Heterocycles," *RSC Advances* 7, no. 24 (2017): 14562–610.
18. Fathi A. Abu-Shanab, Sherif M. Sherif, and Sayed A. S. Mousa, "Dimethylformamide Dimethylacetal as Building Block in Heterocyclic Synthesis," *Journal of Heterocyclic Chemistry* 46, no. 5 (2009): 801–27.
19. Mariam A. Al-Shiekh, Abdellatif M. Salah El-Din, Ebtisam H. Hafez, and Mohamed H. Elnagdi, "2-Arylhydrazono-3-Oxopropanals in Heterocyclic Synthesis: Synthesis of Arylazopyrazole, Arylazoisoxazole and Dialkylpyridazine-5,6-Dicarboxylate Derivatives. New One-Step Synthesis of Arylazopyrimidines," *Journal of Heterocyclic Chemistry* 41, no. 5 (2004): 647–54.

20. Elsayed M. Afsah, El-Sayed I. El-Desoky, Hassan A. Etman, Ibrahim Youssef, and Ahbarah M. Soliman, "Mannich Reaction with Enaminones: Convenient Synthesis of Functionalized Tetrahydro-Pyrimidines, Dihydro-1,3-Oxazines, and Dihydro-1,2,4-Triazepines," *Journal of Heterocyclic Chemistry* 55, no. 12 (2018): 2959–70.

21. Thoraya A. Farghaly, Alaa M. Abo Alnaja, and Mohamed R. Shaaban, "Recent Advances in Synthesis and Reactions of β-Amino-α,β-Enones (Enaminones)," *Current Organic Synthesis* 18, no. 7 (2021): 639–84.

22. Samir Bondock, and Ahmed M. Fouda, "Synthesis and Evaluation of Some New 5-(Hetaryl)Thiazoles as Potential Antimicrobial Agents," *Synthetic Communications* 48, no. 5 (2018): 561–73.

23. Mostafa M. Ghorab, Mahmoud S. Bashandy, and Mansour S. Alsaid, "Novel Thiophene Derivatives with Sulfonamide, Isoxazole, Benzothiazole, Quinoline and Anthracene Moieties as Potential Anticancer Agents," *Acta Pharmaceutica (Zagreb, Croatia)* 64, no. 4 (2014): 419–31.

24. Angela Casini, Andrea Scozzafava, Antonio Mastrolorenzo, and Laudiu T. Supuran, "Sulfonamides and Sulfonylated Derivatives as Anticancer Agents," *Current Cancer Drug Targets* 2, no. 1 (2002): 55–75.

25. Mostafa M. Ghorab, Mansour S. Alsaid, Ghada H. Al-Ansary, Ghada A. Abdel-Latif, and Dalal A. Abou El Ella, "Analogue Based Drug Design, Synthesis, Molecular Docking and Anticancer Evaluation of Novel Chromene Sulfonamide Hybrids as Aromatase Inhibitors and Apoptosis Enhancers," *European Journal of Medicinal Chemistry* 124 (2016): 946–58.

26. Assem Barakat, Saied M. Soliman, Matti Haukka, Abdullah Mohamed Al-Majid, Mohammed Shahidul Islam, M. Ali, and Mohammed Rafi Shaik, "One-Pot Synthesis, X-Ray Single Crystal and Molecular Insight of Enaminone-Based β-Morpholino-1N-Methylpiperazinyl-/Pyrrolidinyl Propiophenone," *Crystals* 10, no. 4 (2020): 282.

27. Florian Gagiu, Gyorgy Csavassy, and Greta Todor, "Synthesis of 2-Allylaminothiazoles," *Archiv der Pharmazie* 300, no. 11 (1967): 964–8.

28. Ahmad S. Shawali, and Adel J. M. Haboub, "Convenient Synthesis of Polyaza-3,4-Bis(Heteroaryl)Pyrazoles," *Synthetic Communications* 45, no. 5 (2015): 611–24.

29. Antonio Salgado, Carmen Varela, Ana Maria Garcia Collazo, and Paolo Pevarello, "Differentiation Between [1,2,4]Triazolo[1,5-*a*]Pyrimidine and [1,2,4]Triazolo[4,3-*a*]-Pyrimidine Regioisomers by ^{1}H–^{15}N HMBC Experiments," *Magnetic Resonance in Chemistry: MRC* 48, no. 8 (2010): 614–22.

30. Thoraya A. Farghaly, Naglaa A. Abdel Hafez, Eman A. Ragab, Hanem M. Awad, and Mohamed M. Abdalla, "Synthesis, Anti-HCV, Antioxidant, and Peroxynitrite Inhibitory Activity of Fused Benzosuberone Derivatives," *European Journal of Medicinal Chemistry* 45, no. 2 (2010): 492–500.

31. Eberhard Breitmaier, *Structure Elucidation by NMR in Organic Chemistry, A Practical Guide* (Chichester, UK: John Wiley, 1993), 27.

32. Philip Skehan, Ritsa Storeng, Dominic Scudiero, Anne Monks, James McMahon, David Vistica, Jonathan T. Warren, Heidi Bokesch, Susan Kenney, and Michael R. Boyd, "New Colorimetric Cytotoxicity Assay for Anticancer-Drug Screening," *Journal of the National Cancer Institute* 82, no. 13 (1990): 1107–12.

33. Vanicha Vichai, and Kanyawim Kirtikara, "Sulforhodamine B Colorimetric Assay for Cytotoxicity Screening," *Nature Protocols* 1, no. 3 (2006): 1112–6.

Facile Synthesis and Anticancer Evaluation of Novel 1-(Thiazol-2-yl)-3-(thiazol-5-yl)-5-(thiophen-2-yl) Pyrazolines

Samir Bondock[a,b,*], **Omeer Albormani**[a], **and Ahmed M. Fouda**[a]

[a] Chemistry Department, College of Science, King Khalid University, Abha, 9004 Saudi Arabia
[b] Chemistry Department, Faculty of Science, Mansoura University, Mansoura, 35516 Egypt
*e-mail: bondock@mans.edu.eg

Abstract—Some novel pyrazoline derivatives bearing thiazole and thiophene moieties have been efficiently synthesized and characterized. The synthetic approach involves condensation of 5-acetylthiazole **1** with 2-formyl thiophene **2** followed by heterocyclization of the produced chalcone **3** with hydrazine and thiosemicarbazide under different conditions to give selectively 1-substituted-3-(thiazol-5-yl)-5-(thiophen-2-yl)pyrazolines **4–6** and **8** in high yields. Heterocyclization of 1-thicarbomylpyrazoline **8** with 3-chloro-2,4-pentanedione, phenacyl bromide and hydrazonoyl bromides in boiling ethanol and TEA results in the respective 1-(thiazol-2-yl)-3-(thiazol-5-yl)-5-(thiophen-2-yl)pyrazolines **11**, **12**, and **14a–14f**. Anticancer activity of the novel 1,3,5-trisubstituted pyrazolines has been evaluated, against breast (MCF-7), liver (HepG2), and colon (HCT-116) cancer cell lines, as well as epithelial (REP1) normal cell line. Among the synthesized pyrazolines, compounds **8**, **14a**, and **14f** demonstrate the highest anticancer activity with IC_{50} values of 1.83, 5.47, and 11.43 μM, respectively, and presenting no evidence of human toxicity.

Keywords: thiazole, thiophene, 2-pyrazoline, chalcone, anticancer activity

DOI: 10.1134/S1070363222060226

INTRODUCTION

Chalcones, 1,3-diarylprop-2-en-1-ones and their heterocyclic analogs are versatile precursors for five- and six-membered azaheterocycles such as azoles, diazoles, azines, and diazines [1]. As chalcones are easily attainable, a vast number of compounds can be constructed by substituting those with several heteroaromatic and aromatic moieties. Thienyl chalcones act as intermediates in formation of pyrazoline derivatives that act as human monoamine oxidase (hMAO) inhibitors [2]. 2-Pyrazolines produced from chalcones were characterized by a variety of biological activities including anti-inflammatory [3], antimicrobial [4, 5], antimalarial [6], and some more. 1,3,5-Trisubstitutedpyrazolines have been used as antileukemic [7], antitumor [8] and antiproliferative [9] drugs, and exceptional anticancer agents that block various types of enzymes involved in cells division [10]. Inclusion of the pyrazoline nucleus between thiophene and 1,3-thiazole rings of chalcones played an important role in supporting their cytotoxic potential [11, 12]. Since thiazole derivatives have demonstrated pronounced anticancer activity [13, 14], development of their pyrazoline hybrids could be a promising approach to potent anticancer agents. Based on these findings and in continuation of our ongoing research program in design and synthesis of novel bioactive heterocycles as effective anticancer agents [15–19], we report herein the facile synthetic approach to and anticancer activity of novel 2-pyrazolines bearing thiophene and thiazole moieties.

RESULTS AND DISCUSSION

In this study the chalcone precursor 1-(2-allylamino-4-methylthiazol-5-yl)-3-(2-thienyl)prop-2-en-1-one (**3**), was formed in 85% yield by the Claisen-Schmidt reaction of 1-(2-allylamino-4-methylthiazol-5-yl)ethanone (**1**) with 2-formylthiophene (**2**) in an aqueous methanolic

Scheme 1. Synthesis of 1-substituted-3-(thiazol-5-yl)-5-(thiophen-2-yl)pyrazoline derivatives **4–6**.
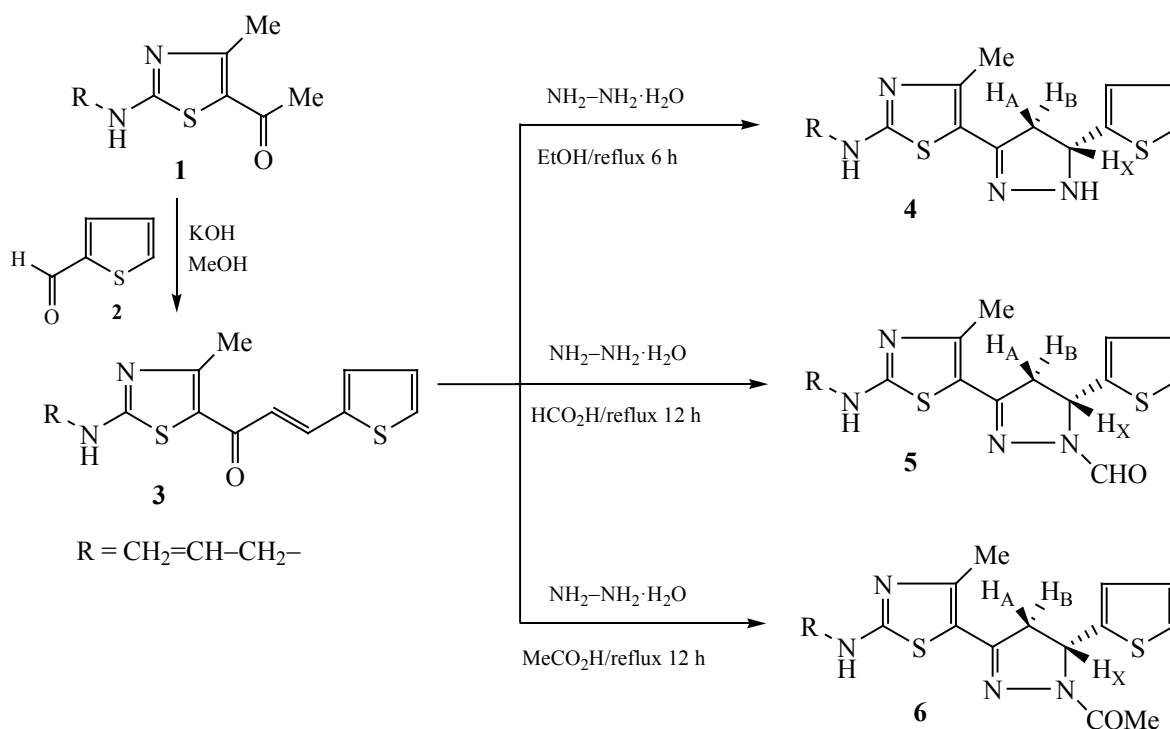
solution of potassium hydroxide at room temperature (Scheme 1). The structure of chalcone **3** was confirmed by IR, ^{1}H, and ^{13}C NMR, and mass spectra.

The α,β-unsaturated carbonyl system of thiazolylchalcone **3** containing two reactive electrophilic sites (C-1 and C-3) allowed to perform the addition reaction with *N,N*-binucleophiles via attack to the carbonyl group (1,2-addition) or involving the β-carbon (1,4-addition), leading to creation of bioactive 2-pyrazolines. Cyclocondensation reaction of equimolar amount of chalcone **3** with hydrazine hydrate in ethanol gave 2-allylamino-4-methyl-5-[5-(2-thienyl)-4,5-dihydropyrazol-3-yl]thiazole (**4**) in moderate yield (Scheme 1). Thiazolylchalcone **4,** being subjected to cycloaddition condensation with hydrazine hydrate in boiling methanoic or ethanoic acid, led to the respective derivatives of 2-pyrazoline-1-carboxaldehyde (**5**) and 1-acetyl-2-pyrazoline (**6**). Structures of pyrazoline **4–6** were deduced from spectral data and elemental analysis.

Treatment of thiazolylchalcone **3** with thiosemi-carbazide in ethanol in presence of equivalent amount of sodium hydroxide gave the only product identified as 3-(2-allylamino-4-methylthiazol-5-yl)-5-(2-thienyl)-4,5-dihydropyrazole-1-carbothioamide (**10**) (Scheme 2). Approach to 2-pyrazoline-1-thiocarbamide (**8**) started with 1,2-nucleophilic addition of a basic NH$_2$ group of thiosemicarbazide to the carbonyl group of chalcone **3**, followed by tandem elimination of water to give the non-isolable thiosemicarbazone intermediate **7,** cyclized in 2-pyrazoline **8** via addition of the secondary amino group to the activated β-carbon of thiosemicarbazone **7**. Formation of another possible regioisomeric product **10** was excluded on the basis of spectral data. IR spectrum of compound **8** exhibited bands at 3424, 3258, 3201, 1610, 1312 cm^{-1} attributed to NH, NH$_2$, C=C, and C=S groups, respectively. In its ^{1}H NMR spectrum three new doublets of doublets resonated at 3.17 (J = 18.0, 5.0 Hz), 3.93 (J = 18.0, 11.7 Hz) and 6.16 ppm (J = 11.7, 5.0 Hz) due to three protons of pyrazoline ring residue H-4A, H-4B and H-5, respectively. The primary NH$_2$ group in thiocarboxamide was recorded as two magnetically nonequivalent signals at 7.22 and 7.87 ppm. This phenomenon was also observed in ^{1}H NMR spectra of similar 1-thiocarbamoyl pyrazolines by Beloglazkina and coworkers [20]. ^{13}C NMR spectrum of **8** supported well its formation.

Scheme 2. Synthesis of 1-thiocarbamoyl-3-(thiazol-5-yl)-5-(thiophen-2-yl)pyrazoline derivative **8**.
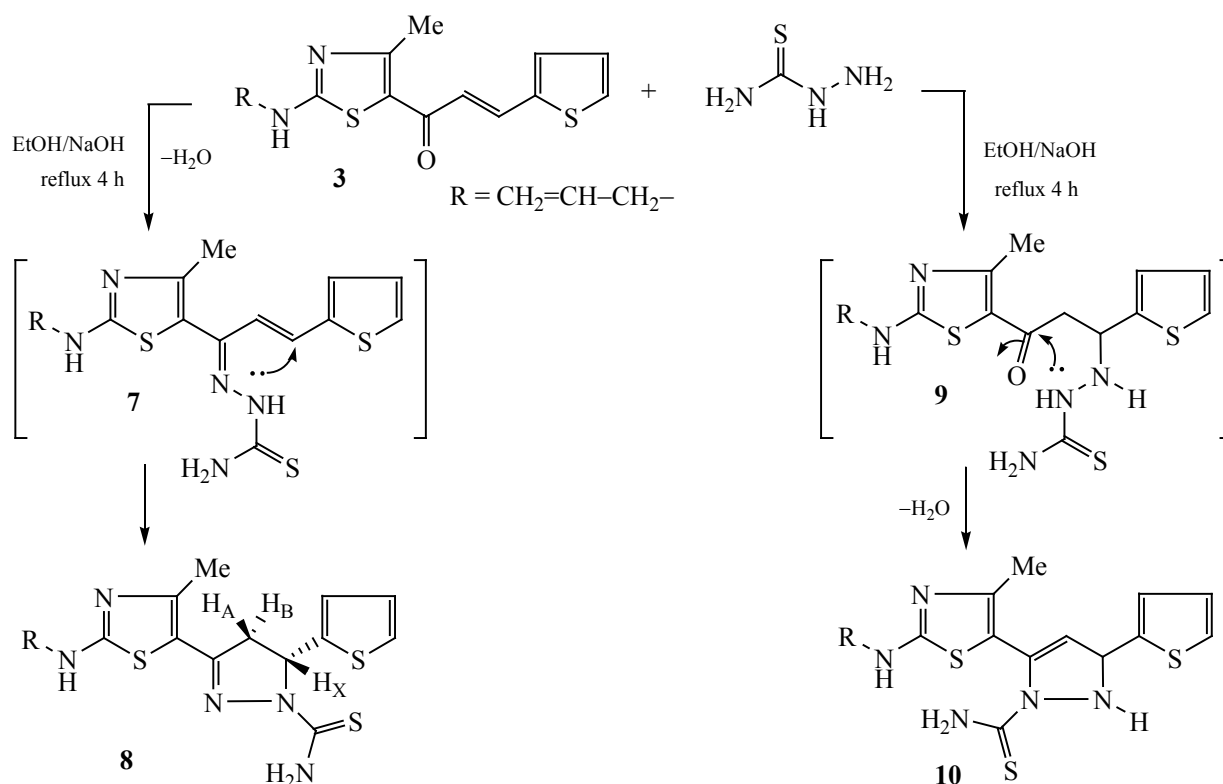
The versatile thiocarbamoyl group at position 1 of pyrazoline ring had been introduced in the process of cyclization with formation of bioactive functionalized 1-(2-thiazolyl)pyrazoline derivatives [21]. In this context, reactivity of pyrazoline-1-thiocarboxamide **8** towards some α-halo carbonyl compounds was studied targeting synthesis of new functionalized 1-thiazolylpyrazolines. Thus, refluxing of **8** with 3-chloro-2,4-pentanedione under Hantzsch thiazole reaction conditions afforded 1-{2-[3-(2-allylamino-4-methylthiazol-5-yl)-5-(2-thienyl)-4,5-dihydropyrazol-1-yl]-4-methylthiazol-2-yl}ethanone (**11**) (Scheme 3). In the similar manner, heterocyclization of compound **8** with phenacyl bromide gave 2-allylamino-4-methyl-5-[1-(4-phenylthiazol-2-yl)-5-(2-thienyl)-4,5-dihydro-1*H*-pyrazol-3-yl]thiazole (**12**). Structures of thiazolylpyrazoline **11** and **12** were deduced from spectral and microanalytical data. For example, IR spectrum of **11** displayed the absence of the bands of NH$_2$ and C=S groups characteristic to its precursor **8** and demonstrated strong absorption bands at 3200, 1648, and 1625 cm^{-1} attributed to NH, C=O and C=C groups, respectively. ^{1}H NMR spectrum of compound

11 exhibited, besides the expected signals of the protons of pyrazoline ring, thiophene ring and vinyl group, five singlets at δ 2.35, 2.37, 2.43, 3.95, 8.82 ppm assigned to the protons of three CH$_3$ groups and also CH$_2$ and NH protons, respectively.

This study was extended to reactivity of pyrazoline-1-thiocarboxamide **8** towards hydrazonoyl halides, aiming the synthesis of novel coloring materials that could be useful in medicinal chemistry [4, 21]. Interaction of pyrazoline-1-thiocarboxamide **8** with a series of *N*-aryl hydrazonoyl bromides **13** [22] in refluxing ethanol and in presence of TEA, afforded one colored product, in each case, as was evidenced by TLC. Those were identified as the corresponding 2-allylamino-4-methyl-5-{1-[5-(4-substituted phenyldiazenyl)-4-phenylthiazol-2-yl]-5-(2-thienyl)-4,5-dihydro-1*H*-pyrazol-3-yl}thiazoles **14a–14f** (Scheme 3).

Besides spectral analysis, structures of the latter adducts were confirmed by the alternative synthetic route. Thus, coupling of the active methine carbon at position 4 of thiazole derivative **12** with aromatic

Scheme 3. Synthesis of 1-(thiazol-2-yl)-3-(thiazol-5-yl)-5-(thiophen-2-yl)pyrazoline derivatives **11, 12** and **14a–14f**.
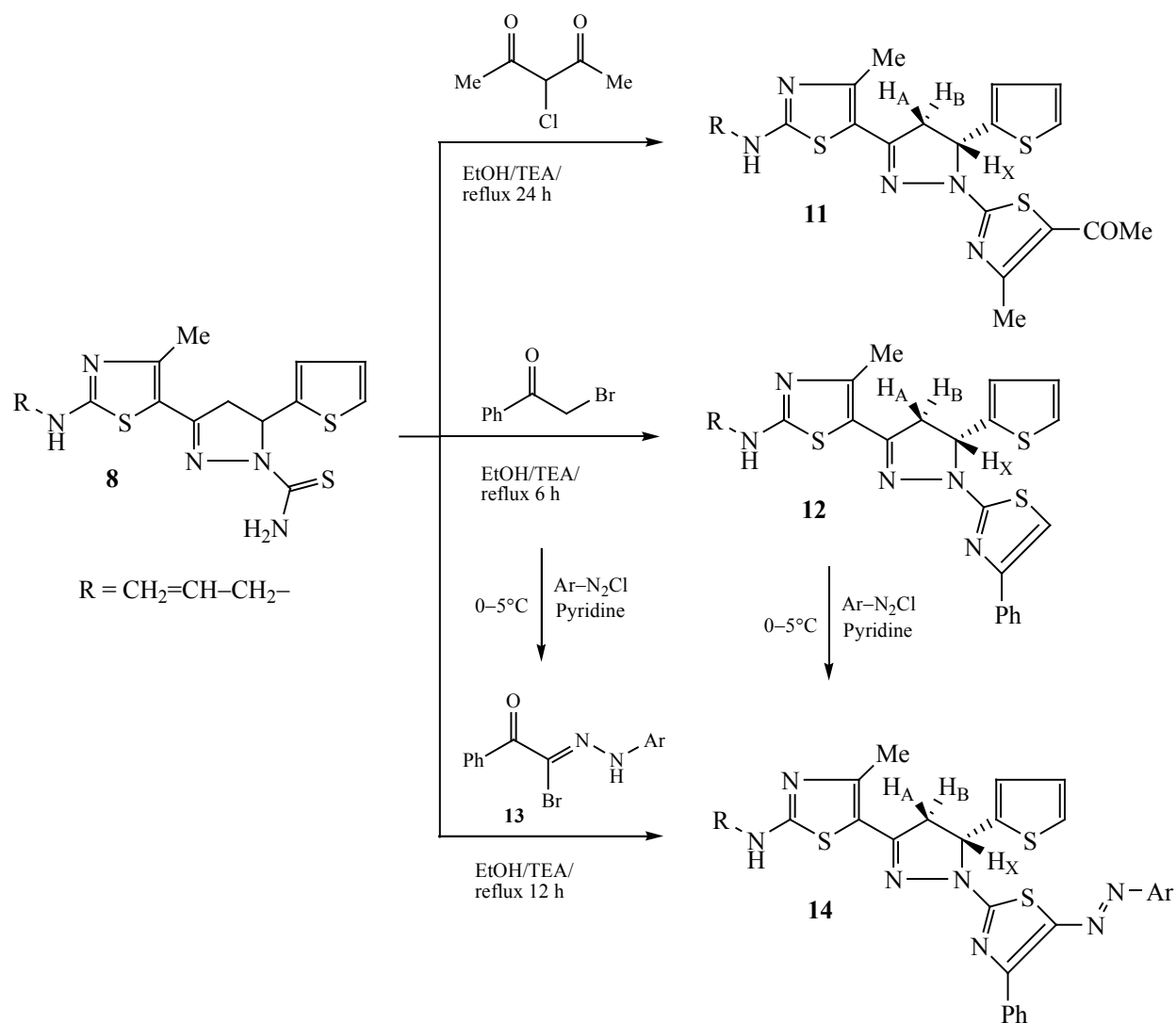
14a, Ar = C_6H_5; **14b**, Ar = 4-Me–C_6H_4; 14c, Ar = 4-MeO–C_6H_4; **14d**, Ar = 4-Cl–C_6H_4; **14e**, Ar = 4-Br–C_6H_4; **14f**, Ar = 4-NO_2–C_6H_4.

diazonium chlorides in pyridine at 0–5°C afforded, as a sole product, identical in each case, compounds **14a–14f**. These results supported the probable mechanism of formation of **14a–14f** that included the initial formation of thiohydrazonate via nucleophilic displacement of chlorine atom by the thiol group, which underwent in situ dehydrative cyclization with formation of the final products. IR and NMR spectral data supported the proposed structures of compounds **14a–14f.**

Anticancer activity. The synthesized 1,3,5-trisubstituted pyrazolines were submitted to the Bioassay-Cell Culture Laboratory at Biology Department, King Khalid University (Saudi Arabia) for in vitro anticancer evaluation. The pyrazolines bearing thiazole and thiophene moieties were assessed by the sulforhodamine B (SRB) assay against breast cancer (MCF-7), colon cancer (HCT-116), and liver carcinoma (HepG2) cell lines [22, 23]. Pyrazolines were also tested on a regular human epithelial cell line (RPE1) to determine their safety in normal cells. The well-known doxorubicin anticancer drug was used as a reference. The cytotoxic activity data expressed in terms of IC_{50} are listed in Table 1. Anticancer activity of compounds **3–14a–14f** revealed that most of these exhibited variable inhibitory effects on growth of three tested human tumor cell lines. Activity against

Table 1. Cytotoxic activity (IC$_{50}$, μM)^a of the synthesized 1,3,5-trisubstituted pyrazolines

Compound	MCF-7	HCT-116	HepG2	REP1
3	≥100	≥100	≥100	≥100
4	98.38 ± 1.84	≥100	69.68 ± 3.86	≥100
5	≥100	≥100	58.57 ± 2.98	85.12 ± 1.12
6	90.82 ± 3.44	≥100	45.66 ± 2.85	≥100
8	3.74 ± 0.14	1.46 ± 0.06	1.83 ± 0.12	≥100
11	≥100	≥100	48.37 ± 1.78	≥100
12	27.80 ± 1.86	25.13 ±2.61	35.58 ± 2.26	≥100
14a	7.52 ± 1.39	6.80 ± 0.30	5.47 ± 0.60	≥100
14b	≥100	≥100	≥100	≥100
14c	≥100	≥100	≥100	≥100
14d	≥100	≥100	≥100	≥100
14e	≥100	≥100	≥100	≥100
14f	13.54 ± 1.92	12.24 ± 1.26	11.43 ± 2.04	≥100
Doxorubicin	6.77 ± 0.25	1.69 ± 0.14	3.21 ± 0.17	10.45 ± 1.18

^{a} Data are offered as the mean ± SD of three independent experiments.

breast cancer MCF-7 was determined for compounds **8**, **14a**, and **14f**. It is noteworthy that compound **8** exhibited significantly higher antiproliferative activity (IC$_{50}$ 3.74 μM) than doxorubicin (IC$_{50}$ 6.77 μM) against MCF-7.

Compounds **8**, **12**, **14a**, and **14f** were determined to be of higher antiproliferative activity against colon cancer cell line (HCT 116) than the other products (Table 1). Compound **8** demonstrated the most potent anticancer activity nearly equipotent to doxorubicin. Most of tested products exhibited broad-spectrum of anticancer activity against hepatic carcinoma cell line (HepG2). Compounds **8, 14a** and **14f** exhibited the highest cytotoxic activity. Most of products were characterized by higher selectivity toward hepatic carcinoma cell line (HepG2) than breast cancer (MCF-7) and colon cancer (HCT 116) cell lines. Also, none of the compounds listed in Table 1, but product 5, demonstrated toxicity in the normal cell line (RPE1). These results suggested a common therapeutic index for pyrazolines **8**, **14a**, and **14f** that could be considered as promising anticancer agents.

Structure-activity relationship (SAR). The following structure-activity relationship was worked out for the compounds synthesized in this study (Scheme 4).

—The basic pyrazoline skeleton is required for the broad spectrum of cytotoxic activity against (MCF-7, HCT 116 and HepG2) cancer cell lines.

—Transformation of thiazolylchalcone **4** to thiazolylpyrazolines **5**–**8** enhanced the cytotoxic effect against HepG2 cell line.

—Insertion of the thiocarboxamide group (NH$_2$–C=S) in position 1 of pyrazoline ring, as in compound **8,** resulted in higher antitumor activity than the formyl (CH=O) and acetyl (CH$_3$–C=O) groups.

—Heterocyclization of the thiocarbomyl group at position 1 in compound **8** that led to thiazole derivative **12** characterized by lower cytotoxic activity.

—Insertion of the phenylazo (Ph–N=N–) pharmacophoric group at position 5 of the thiazole ring, as in compound **14a,** increased the antiproliferative activity.

—The electron-withdrawing nitro group at position 4 in the aryl moiety of thiazole ring boosted the cytotoxic activity.

—Presence of electron donating groups such as methyl or methoxy groups at position 4 in the aryl moiety of thiazole ring (**14b** and **14c)** diminished their cytotoxic activity.

EXPERIMENTAL

Melting points were recorded on the Stuart melting point-device and were uncorrected. IR spectra (KBr discs) were recorded on a Jasco FT/IR-460 plus spectrophotometer. ^{1}H NMR (850, 500 MHz) and ^{13}C NMR (212.5, 125 MHz) spectra were measured on a Bruker Avance NMR spectrometer using DMSO-d_6 as

Scheme 4. Influence of substituents on anticancer activity of pyrazoline derivatives.
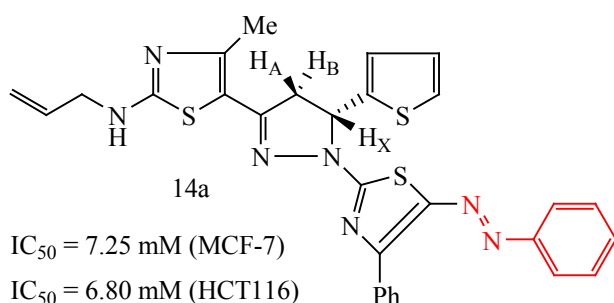

8
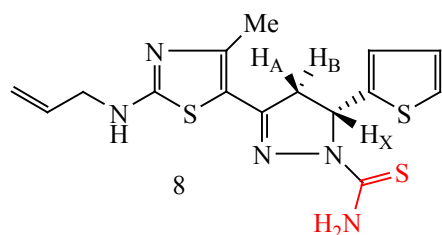
IC_{50} = 3.74 mM (MCF-7)

IC_{50} = 1.46 mM (HCT116)

IC_{50} = 1.83 mM (HepG2)
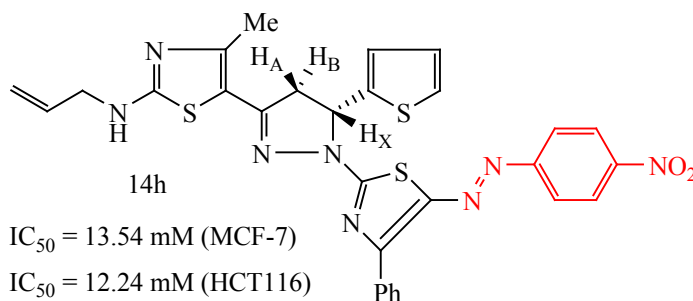
12
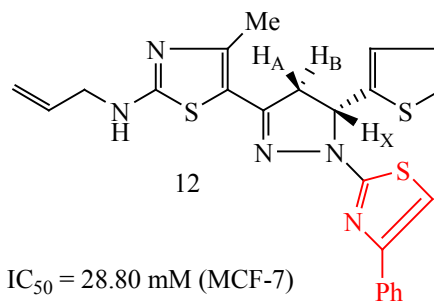
IC_{50} = 28.80 mM (MCF-7)

IC_{50} = 25.13 mM (HCT116)

14a

IC_{50} = 7.25 mM (MCF-7)

IC_{50} = 6.80 mM (HCT116)

IC_{50} = 5.47 mM (HepG2)

14h

IC_{50} = 13.54 mM (MCF-7)

IC_{50} = 12.24 mM (HCT116)

IC_{50} = 11.43 mM (HepG2)

a solvent. Mass spectra were measured on a Shimadzu GC/MS-QP5 mass spectrometer at 70 eV. Elemental analysis was carried out on a Perkin Elmer 2400 analyzer.

Synthesis of 1-(2-allylamino-4-methylthiazol-5-yl)-3-(thiophen-2-yl)prop-2-en-1-one (3). To a solution of 5-acetylthiazole **1** (1.96 g, 0.01 mol) in 20 mL methanol, potassium hydroxide (0.56 g, 0.01 mol) was added. The mixture was stirred in an ice bath for 10 min and then 2-formylthiophene **2** (0.95 mL, 0.01 mol) was added in portions. The reaction mixture was stirred for 24 h more. The resulting yellow precipitate was filtered off, washed several times with water, dried, and crystallized from ethanol to give pure compound **3**. Pale yellow crystals, yield 68%, mp 176–177°C. IR spectrum, ν, cm⁻¹: 3200 (NH), 3062 (=C–H, sp^2), 2933 (C–H, sp^3), 1643 (C=O), 1600 (C=C), 1575 (C=N). ¹H NMR spectrum, δ, ppm: 2.50 s (3H, CH₃), 3.92 br. s (2H, NCH₂), 5.17 d. d (1H, J = 1.5, 16.8 Hz, CH=), 5.27 d. d (1H, J =1.5,10.5 Hz, CH=), 5.89 m (1H, CH=), 6.95 d (1H, J =15.4 Hz, CH=), 7.16 t (1H, J = 3.68 Hz, C⁴H_thiophene), 7.56 d (1H, J = 4.00 Hz, C³H_thiophene), 7.72 d (1H, J = 1.48 Hz, C⁵H_thiophene), 7.73 d (1H, J = 15.4 Hz, CH=), 8.74 br. s

(1H, NH). ¹³C NMR spectrum, δ_C, ppm: 19.4 (CH₃), 46.5 (NCH₂), 117.0 (CH₂=), 121.5 (C⁵_thiazole), 123.7 (CH-CO), 129.2 (C⁴_thiophene), 130.1 (CH=), 132.7 (C³_thiophene), 134.4 (C⁵_thiophene), 134.5 (CH=), 140.2 (C²_thiophene), 159.5 (C⁴_thiazole), 171.1 (C²_thiazole), 180.2 (C=O). Found, %: C 57.92; H 4.84; N 9.68. C₁₄H₁₄N₂OS₂. Calculated, %: C 57.90; H 4.86; N 9.65. MS: m/z (%): 290 (M^+,100).

Synthesis of 2-allylamino-4-methyl-5-[5-(thiophen-2-yl)-4,5-dihydropyrazol-3-yl]thiazole (4). To a solution of chalcone **3** (1.45 g, 0.005 mol) in absolute ethanol (20 mL) was added hydrazine hydrate (0.25 mL, 0.005 mol). The reaction mixture was refluxed for 6 h and then cooled down to room temperature. White precipitate was filtered off and crystallized from ethanol to give pure pyrazoline **4**. Colorless crystals, yield 64%, mp >300°C. IR spectrum, ν, cm⁻¹: 3262, 3197 (2NH), 3067 (=C–H, sp^2), 2938 (C–H, sp^3), 1624 (C=C), 1594 (C=N). ¹H NMR spectrum, δ, ppm: 2.23 s (3H, CH₃), 2.84 d. d (1H, J = 14.25, 9.75 Hz, C⁴ᴬH_pyrazole), 3.46 d. d (1H, J = 14.25, 3.75 Hz, C⁴ᴮH_pyrazole), 3.84 t (2H, J = 4.5 Hz, CH₂N), 5.02 d. d (1H, J = 9.75, 3.75 Hz, C⁵ˣH_pyrazole), 5.11 d. d (1H, J = 9.0, 1.5 Hz, CH=), 5.22 d. d (1H, J = 15.75,

1.5 Hz CH=), 5.87 m (1H, CH=), 6.97 d. d (1H, $J = 4.5$, 3.0 Hz, $C^4H_{thiophene}$), 7.04 d (1H, $J = 3.0$ Hz, $C^3H_{thiophene}$), 7.25 d (1H, $J = 9.0$Hz, NH-pyrazoline), 7.40 d (1H, $J = 4.5$ Hz, $C^5H_{thiophene}$), 7.90 t (1H, $J = 4.5$Hz, NH). ^{13}C NMR spectrum, δ_C, ppm: 17.3 (CH_3), 44.0 ($C^4_{pyrazoline}$), 46.6 (NCH_2), 60.1 ($C^5_{pyrazoline}$), 113.0 ($C^5_{thiazole}$), 116.2 (CH_2=), 125.0 ($C^3_{thiophene}$), 125.1 ($C^4_{thiophene}$), 127.2, ($C^5_{thiophene}$), 135.2 (CH=), 145.7 ($C^3_{pyrazoline}$), 146.9 ($C^2_{thiophene}$), 147.2 ($C^4_{thiazole}$), 166.7 ($C^2_{thiazole}$). Found, %: C 55.21; H 5.33; N 18.37. $C_{14}H_{16}N_4S_2$. Calculated, %: C 55.23; H 5.30; N 18.40. MS: m/z (%): 304 (M^+, 92).

Synthesis of 3-[2-(allylamino)-4-methylthiazol-5-yl]-5-(thiophen-2-yl)-4,5-dihydropyrazole-1-carbaldehyde (5). To a solution of chalcone **3** (1.45 g, 0.005 mol) in methanoic acid (20 mL) was added hydrazine hydrate (1 mL, 0.02 mol). The reaction mixture was refluxed for 12 h and then cooled down to room temperature. The precipitate was crystallized from ethanol to afford pure compound **5**. Colorless crystals, yield 53%, mp 178–179°C. IR spectrum, ν, cm^{-1}: 3200 (NH), 3058 (=C–H, sp^2), 2935 (C–H, sp^3), 1642 (C=O), 1605 (C=C), 1579 (C=N). ^{1}H NMR spectrum, δ, ppm: 2.52 s (3H, CH_3), 3.28 d. d (1H, $J = 15.0$, 9.75 Hz, $C^{4A}H_{pyrazoline}$), 3.88 d. d (1H, $J = 15.0$, 3.11 Hz, $C^{4B}H_{pyrazoline}$), 3.92 t (2H, $J = 4.5$ Hz, CH_2N), 5.14 d. d (1H, $J = 8.0$, 1.5 Hz, CH=), 5.26 d. d (1H, $J = 14.5$, 1.5 Hz, CH=), 5.77 d. d (1H, $J = 9.75$, 3.11 Hz, $C^{5X}H_{pyrazoline}$), 5.89 m (1H, CH=), 6.98 d. d (1H, $J = 4.5$, 3.0 Hz, $C^4H_{thiophene}$), 7.17 d (1H, $J = 4.5$ Hz, $C^3H_{thiophene}$), 7.44 d (1H, $J = 4.5$ Hz, $C^5H_{thiophene}$), 8.30 t (1H, $J = 4.5$Hz, NH), 8.68 s (1H, CHO). ^{13}C NMR spectrum, δ_C, ppm: 17.7 (CH_3), 44.1 ($C^4_{pyrazoline}$), 46.7 (NCH_2), 54.5 ($C^5_{pyrazoline}$), 110.2 ($C^5_{thiazole}$), 116.6 (CH_2=), 123.6 ($C^3_{thiophene}$), 125.4 ($C^4_{thiophene}$), 127.2, ($C^5_{thiophene}$), 134.7 (CH=), 144.2 ($C^3_{pyrazoline}$), 151.7 ($C^2_{thiophene}$), 153.2 ($C^4_{thiazole}$), 168.3 ($C^2_{thiazole}$), 170.6 (C=O). Found, %: C 54.21; H 4.88; N 16.82. $C_{15}H_{16}N_4OS_2$. Calculated, %: C 54.19; H 4.85; N 16.85. MS: m/z (%): 332 (M^+, 9.2).

Synthesis of 1-{3-[2-(allylamino)-4-methylthiazol-5-yl]-5-(thiophen-2-yl)-4,5-dihydropyrazol-1-yl}-ethanone (6). Hydrazine hydrate (1 ml, 0.02 mol) was added to a solution of chalcone **3** (1.45 g, 5 mmol) in glacial acetic acid (20 mL), and the mixture was refluxed for 12 h, then cooled down to room temperature. The precipitate was crystallized from ethanol to afford pure compound **6**. Yellow crystals, yield 52%, mp 166–167°C. IR spectrum, ν, cm^{-1}: 3200 (NH), 3057 (=C–H, sp^2), 2934 (C–H, sp^3), 1667 (C=O), 1643 (C=C), 1598 (C=N). ^{1}H NMR spectrum, δ, ppm: 2.15 s (3H, CH_3), 2.23 s (3H,

CH_3), 3.20 d. d (1H, $J = 15.0$, 9.75 Hz, $C^{4A}H_{pyrazoline}$), 3.85 d. d (1H, $J = 15.0$, 3.75 Hz, $C^{4B}H_{pyrazoline}$), 3.89 br. s (2H, CH_2N), 5.12 d. d (1H, $J = 9.0$, 1.5 Hz, CH=), 5.24 d. d (1H, $J = 15.75$, 1.5 Hz, CH=), 5.77 d. d (1H, $J = 9.75$, 3.75 Hz, $C^{5X}H_{pyrazoline}$), 5.89 m (1H, CH=), 6.94 d. d (1H, $J = 4.5$, 3.0 Hz, $C^4H_{thiophene}$), 7.00 d (1H, $J = 4.5$ Hz, $C^3H_{thiophene}$), 7.39 d (1H, $J = 4.5$ Hz, $C^5H_{thiophene}$), 8.27 t (1H, $J = 4.5$Hz, NH). ^{13}C NMR spectrum, δ_C, ppm: 17.7 (CH_3), 21.9 (CH_3), 43.9 ($C^4_{pyrazoline}$), 46.7 (NCH_2), 55.3 ($C^5_{pyrazoline}$), 110.5 ($C^5_{thiazole}$), 116.2 (CH_2=), 124.9 ($C^3_{thiophene}$), 125.3 ($C^4_{thiophene}$), 127.1 ($C^5_{thiophene}$), 134.8 (CH=), 145.3 ($C^3_{pyrazoline}$), 150.1 ($C^2_{thiophene}$), 152.7 ($C^4_{thiazole}$), 167.0 ($C^2_{thiazole}$), 168.2 (C=O). Found, %: C 55.45; H 5.27; N 16.15. $C_{16}H_{18}N_4OS_2$. Calculated, %: C 55.47; H 5.24; N 16.17. MS: m/z (%): 347 (M^+, 20.9).

Synthesis of 3-(2-allylamino-4-methylthiazol-5-yl)-5-(thiophen-2-yl)-4,5-dihydropyrazole-1-carbothioamide (8). A mixture of chalcone **3** (1.45 g, 0.005 mol) with thiosemicarbazide (0.46 g, 0.005 mol) and sodium hydroxide (0.2 g, 0.005mol) in absolute ethanol (20 mL) was refluxed for 4h and then cooled down to room temperature. The yellow precipitate was filtered off and washed from ethanol to give pyrazoline **8**. Yellow crystals, yield 77%, mp 198–199°C. IR spectrum, ν, cm^{-1}: 3424 (NH), 3258, 3201 (NH$_2$), 3055 (=C–H, sp^2), 2936 (C–H, sp^3), 1667 (C=O), 1610 (C=C), 1598 (C=N), 1312 (C=S). ^{1}H NMR spectrum, δ, ppm: 2.31 s (3H, CH_3), 3.17 d. d (1H, $J = 18.0$, 9.75 Hz, $C^{4A}H_{pyrazoline}$), 3.89 s (2H, CH_2N), 3.93 d. d (1H, $J = 18.0$, 5.0 Hz, $C^{4B}H_{pyrazoline}$), 5.12 d. d (1H, $J = 10.6$, 1.5 Hz, CH=), 5.24 d. d (1H, $J = 16.5$, 1.5 Hz, CH=), 5.87 m (1H, CH=), 6.16 d. d (1H, $J = 11.7$, 5.0 Hz, $C^{5X}H_{pyrazoline}$), 6.95 d (1H, $J = 4.0$, 3.0 Hz, $C^4H_{thiophene}$), 6.98 d (1H, $J = 4.0$ Hz, $C^3H_{thiophene}$), 7.22 t (1H, $J = 4.5$Hz, NH), 7.37 d (1H, $J = 4.5$ Hz, $C^5H_{thiophene}$), 7.87 s (1H, NH), 8.40 s (1H, NH). ^{13}C NMR spectrum, δ_C, ppm: 18.1 (CH_3), 44.6 ($C^4_{pyrazoline}$), 46.5 (NCH_2), 59.2 ($C^5_{pyrazoline}$), 110.3 ($C^5_{thiazole}$), 116.6 (CH_2=), 125.1 ($C^3_{thiophene}$), 125.2 ($C^4_{thiophene}$), 127.1, ($C^5_{thiophene}$), 134.8 (CH=), 145.7 ($C^3_{pyrazoline}$), 151.7 ($C^2_{thiophene}$), 154.2 ($C^4_{thiazole}$), 169.2 ($C^2_{thiazole}$), 175.2 (C=S). Found, %: C 49.53; H 4.73; N 19.29. $C_{15}H_{17}N_5S_3$. Calculated, %: C 49.56; H 4.71; N 19.27. MS: m/z (%): 364 (M^+, 21.4).

Synthesis of 1-{2-[3-(2-allylamino-4-methylthiazol-5-yl)-5-(thiophen-2-yl)-4,5-dihydropyrazol-1-yl]-4-methyl thiazol-2-yl}ethanone (11). A mixture of thioamide **8** (0.5 g, 0.0014 mol) with 3-chloro-2,4-pentanedione (0.16 mL, 1.375 mmol) was dissolved in absolute ethanol (20 mL) containing TEA (0.1 mL)

and then refluxed for 24 h. The precipitate formed upon cooling down the mixture was filtered off and crystallized from ethanol to afford pure compound **11**. Yellow crystals, yield 75%, mp >300°C. IR spectrum, ν, cm^{-1}: 3200 (NH), 3052 (=C–H, sp^2), 2933 (C–H, sp^3), 1648 (C=O), 1625 (C=C), 1598 (C=N). ^{1}H NMR spectrum, δ, ppm: 2.35 s (3H, CH$_3$), 2.37 s (3H, CH$_3$), 2.43 s (3H, CH$_3$CO), 3.42 d. d (1H, J = 15.0, 3.75 Hz, C^{4A}H$_{pyrazoline}$), 3.95 s (2H, CH$_2$N), 4.07 d. d (1H, J = 15.0, 9.75 Hz, C^{4B}H$_{pyrazoline}$), 5.16 d. d (1H, J = 9.0, 1.5 Hz, CH=), 5.27 d. d (1H, J = 15.0, 1.5 Hz, CH=), 5.89 m (1H, CH=), 5.99 d. d (1H, J = 9.75, 3.75 Hz, C^{5X}H$_{pyrazoline}$), 6.95 d (1H, J = 4.0, 3.0 Hz, C^{4}H$_{thiophene}$), 6.98 d (1H, J = 4.0 Hz, C^{3}H$_{thiophene}$), 7.37 d (1H, J = 4.5 Hz, C^{5}H$_{thiophene}$), 8.82 br. s (1H, NH). ^{13}C NMR spectrum, δ_C, ppm: 19.1 (CH$_3$), 30.0 (CH$_3$), 31.1 (CH$_3$), 45.2 (C^4$_{pyrazoline}$), 46.9 (NCH$_2$), 59.3 (C^5$_{pyrazoline}$), 110.1 (C^5$_{thiazole}$), 116.8 (CH$_2$=), 123.9 (C$^{5'}$$_{thiazole}$), 126.0 (C^3$_{thiophene}$), 126.0 (C^4$_{thiophene}$), 127.3, (C^5$_{thiophene}$), 134.4 (CH=), 143.7 (C^3$_{pyrazoline}$), 151.2 (C^2$_{thiophene}$), 157.6 (C^4$_{thiazole}$), 158.5 (C$^{4'}$$_{thiazole}$), 164.6 (C$^{2'}$$_{thiazole}$), 168.5 (C^2$_{thiazole}$), 189.4 (C=O). Found, %: C 54.13; H 4.80; N 15.82. C$_{20}$H$_{21}$N$_5$OS$_3$. Calculated, %: C 54.15; H 4.77; N 15.79. MS: m/z (%): 443 (M^+, 17.2).

Synthesis of 2-allylamino-4-methyl-5-[1-(4-phenylthiazol-2-yl)-5-(thiophen-2-yl)-4,5-dihydro-1H-pyrazol-3-yl]thiazole (12). A mixture of thioamide **8** (0.5 g, 0.0014 mol) with phenacyl bromide (0.27 g, 0.0014 mol) was dissolved in ethanol (20 mL) containing TEA (0.1 mL), and then it was refluxed for 6 h. The formed precipitate was filtered off, washed with aqueous ethanol, dried, and crystallized from ethanol to give pure compound **12**. Yellowish green crystals, yield 79%, mp 186–187°C. IR spectrum, ν, cm^{-1}: 3198 (NH), 3053 (=C–H, sp^2), 2932 (C–H, sp^3), 1620 (C=C), 1594 (C=N). ^{1}H NMR spectrum, δ, ppm: 2.34 s (3H, CH$_3$), 3.45 d. d (1H, C^{4A}H$_{pyrazoline}$), 3.91 s (2H, CH$_2$N), 4.06 d. d (1H, J = 15.0, 5.25 Hz, C^{4B}H$_{pyrazoline}$), 5.15 d. d (1H, J = 7.5, 1.5 Hz, CH=), 5.25 d. d (1H, J = 15.0, 1.5 Hz, CH=), 5.91 m (1H, CH=), 5.99 d. d (1H, J = 7.75, 5.25 Hz, C^{5X}H$_{pyrazoline}$), 7.00 t (1H, J = 4.5 Hz, C^{4}H$_{thiophene}$), 7.24 d (1H, J = 3.0 Hz, C^{3}H$_{thiophene}$), 7.30 s (1H, C^{5}H$_{thiazole}$), 7.37 m (3H, CH$_{Ar}$), 7.44 d (1H, J = 4.5 Hz, C^{5}H$_{thiophene}$), 7.81 m (2H, CH$_{Ar}$), 8.30 br. s (1H, NH). ^{13}C NMR spectrum, δ_C, ppm: 17.8 (CH$_3$), 45.2 (C^4$_{pyrazoline}$), 46.7 (NCH$_2$), 60.3 (C^5$_{pyrazoline}$), 104.7 (C^5$_{thiazole}$), 110.5 (C$^{5'}$$_{thiazole}$), 116.4 (CH$_2$=), 125.9 (C^3$_{thiophene}$), 126.0 (C^4$_{thiophene}$), 126.2 (C^3$_{Ar}$), 127.0, (C^5$_{thiophene}$), 128.9 (2C$_{Ar}$), 134.4 (CH=), 135.0 (C$_{Ar}$), 144.5 (C^3$_{pyrazoline}$), 148.9 (C^2$_{thiophene}$),

150.9 (C^4$_{thiazole}$), 152.1 (C$^{4'}$$_{thiazole}$), 165.1 (C$^{2'}$$_{thiazole}$), 168.2 (C^2$_{thiazole}$). Found, %: C 59.61; H 4.60; N 15.13. C$_{23}$H$_{21}$N$_5$S$_3$. Calculated, %: C 59.58; H 4.57; N 15.11. MS: m/z (%): 463 (M^+, 100).

General procedure for the synthesis of 2-allylamino-4-methyl-5-{1-[5-(4-substituted phenyl diazenyl)-4-phenylthiazol-2-yl]-5-(thiophen-2-yl)-4,5-dihydro-1H-pyrazol-3-yl}thiazoles (14a–14f). To a mixture of equimolar amounts of thioamide **8** (0.36 g, 0.01 mol) with the desired hydrazonyl bromide **12a–12f** (0.01 mol) and ethanol (20 mL), TEA (0.2 mL) was added. Then the mixture was refluxed for 12 h and cooled down. The precipitated solid was filtered off, washed with aqueous ethanol, dried, and crystallized from ethanol to give the corresponding pure compound **14a–14f**.

2-Allylamino-4-methyl-5-[1-(5-phenyldiazenyl)-4-phenylthiazol-2-yl]-5-(thiophen-2-yl)-4,5-dihydro-1H-pyrazol-3-yl]thiazole (14a). Red powder, yield 89%, mp 230–231°C. IR spectrum, ν, cm^{-1}: 3200 (NH), 3053 (=C–H, sp^2), 2932 (C–H, sp^3), 1620 (C=C), 1595 (C=N), 1555 (N=N). ^{1}H NMR spectrum, δ, ppm: 2.39 s (3H, CH$_3$), 3.56 d. d (1H, J = 15.0, 3.75 Hz, C^{4A}H$_{pyrazoline}$), 3.92 s (2H, CH$_2$N), 4.14 d. d (1H, J = 15.0, 9.75 Hz, C^{4B}H$_{pyrazoline}$), 5.16 d. d (1H, J = 9.0, 1.5 Hz, CH=), 5.26 d. d (1H, J = 15.0, 1.5 Hz, CH=), 5.91 m (1H, CH=), 6.18 d. d (1H, J = 9.75, 3.75 Hz, C^{5X}H$_{pyrazoline}$), 7.02 t (1H, J = 4.5 Hz, C^{4}H$_{thiophene}$), 7.27 d (1H, J = 3.0 Hz, C^{3}H$_{thiophene}$), 7.37–7.41 m (5H, CH$_{Ar}$), 7.48 d (1H, J = 4.5 Hz, C^{5}H$_{thiophene}$), 7.47–7.54 m (5H, CH$_{Ar}$), 8.49 br. s (1H, NH). ^{13}C NMR spectrum, δ_C, ppm: 17.5 (CH$_3$), 44.4 (C^4$_{pyrazoline}$), 46.4 (NCH$_2$), 58.6 (C^5$_{pyrazoline}$), 105.5 (C^5$_{thiazole}$), 109.6 (C$^{5'}$$_{thiazole}$), 116.1 (CH$_2$=), 124.6 (C^3$_{thiophene}$), 126.0 (C^4$_{thiophene}$), 126.8 (2CH$_{Ar}$), 127.0, (C^5$_{thiophene}$), 128.9 (2CH$_{Ar}$), 133.5 (CH=), 134.2 (C$_{Ar}$), 141.4 (C$_{Ar}$), 142.4 (C^2$_{thiophene}$), 151.5 (C^3$_{pyrazoline}$), 153.6 (C^4$_{thiazole}$), 154.2 (C$^{4'}$$_{thiazole}$), 162.4 (C$^{2'}$$_{thiazole}$), 168.4 (C^2$_{thiazole}$). Found, %: C 61.33; H 4.46; N 17.30. C$_{29}$H$_{25}$N$_7$S$_3$. Calculated, %: C 61.35; H 4.44; N 17.27. MS: m/z (%): 567 (M^+, 10).

2-Allylamino-4-methyl-5-{1-[5-(4-methyl-phenyldiazenyl)-4-phenylthiazol-2-yl]-5-(thiophen-2-yl)-4,5-dihydro-1H-pyrazol-3-yl}thiazole (14b). Red powder, yield 87%, mp 234–235°C. IR spectrum, ν, cm^{-1}: 3198 (NH), 3053 (=C–H, sp^2), 2932 (C–H, sp^3), 1623 (C=C), 1594 (C=N), 1540 (N=N). ^{1}H NMR spectrum, δ, ppm: 2.37 s (3H, CH$_3$), 2.39 s (3H, CH$_3$), 3.55 d. d (1H, J = 15.0, 3.75 Hz, C^{4A}H$_{pyrazoline}$) 3.92 s (2H, CH$_2$N), 4.15 d. d (1H, J = 15.0, 9.75 Hz, C^{4B}H$_{pyrazoline}$),

5.16 d. d (1H, J = 9.75, 1.5 Hz, CH=), 5.27 d. d (1H, J = 15.0, 1.5 Hz, CH=), 5.92 m (1H, CH=), 6.17 d. d (1H, J = 9.75, 3.75 Hz, C^{5X}H$_{pyrazoline}$), 7.02 t (1H, J = 4.5 Hz, C^{4}H$_{thiophene}$), 7.11–7.24 m (5H, CH$_{Ar}$), 7.27 d (1H, J = 3.0 Hz, C^{3}H$_{thiophene}$), 7.31 d (2H, J = 7.5 Hz, CH$_{Ar}$), 7.49 d (1H, J = 4.5 Hz, C^{5}H$_{thiophene}$), 7.61 d (2H, J = 7.5 Hz, CH$_{Ar}$), 8.51 br. s (1H, NH). ^{13}C NMR spectrum, δ_C, ppm: 17.6 (CH$_3$), 20.9 (CH$_3$), 44.4 (C$^4_{pyrazoline}$), 46.4 (NCH$_2$), 58.6 (C$^5_{pyrazoline}$), 105.5 (C$^5_{thiazole}$), 109.6 (C$^{5'}_{thiazole}$), 116.1 (CH$_2$=), 121.8 (2CH$_{Ar}$), 125.9 (C$^3_{thiophene}$), 126.0 (C$^4_{thiophene}$), 126.8 (2CH$_{Ar}$), 128.5, (C$^5_{thiophene}$), 129.6 (2CH$_{Ar}$), 130.1 (CH=), 133.2 (C$_{Ar}$), 134.2 (C$_{Ar}$), 139.3 (C$_{Ar}$), 141.4 (C$_{Ar}$), 142.9 (C$^2_{thiophene}$), 150.4 (C$^3_{pyrazoline}$), 151.8 (C$^4_{thiazole}$), 153.2 (C$^{4'}_{thiazole}$), 162.1 (C$^2_{thiazole}$), 168.5 (C$^2_{thiazole}$). Found, %: C 61.95; H 4.71; N 16.82. C$_{30}$H$_{27}$N$_7$S$_3$. Calculated, %: C 61.93; H 4.68; N 16.85. MS: m/z (%): 581 (M^+, 100).

2-Allylamino-4-methyl-5-{1-[5-(4-methoxy-phenyldiazenyl)-4-phenylthiazol-2-yl]-5-(thiophen-2-yl)-4,5-dihydro-1*H*-pyrazol-3-yl}thiazole (14c). Reddish purple powder, yield 92%, mp 228–229°C. IR spectrum, ν, cm^{-1}: 3197 (NH), 3053 (=C–H, sp^2), 2932 (C–H, sp^3), 1630 (C=C), 1595 (C=N), 1543 (N=N). ^{1}H NMR spectrum, δ, ppm: 2.39 s (3H, CH$_3$), 3.54 d. d (1H, J = 15.0, 3.75 Hz, C^{4A}H$_{pyrazoline}$), 3.84 s (3H, OCH$_3$), 3.93 s (2H, CH$_2$N), 4.14 d. d (1H, J = 15.0, 3.75 Hz, C^{4B}H$_{pyrazoline}$), 5.16 d. d (1H, J = 9.0, 1.5 Hz, CH=), 5.26 d. d (1H, J = 15.0, 1.5 Hz, CH=), 5.92 m (1H, CH=), 6.15 d. d (1H, J = 9.75, 3.75, Hz C^{5X}H$_{pyrazoline}$), 7.02 t (1H, J = 4.5 Hz, C^{4}H$_{thiophene}$), 7.08 d (2H, J = 7.5 Hz, CH$_{Ar}$), 7.27 d (1H, J = 3.0 Hz, C^{3}H$_{thiophene}$), 7.28–7.45 m (5H, CH$_{Ar}$), 7.49 d (1H, J = 4.5 Hz, C^{5}H$_{thiophene}$), 7.70 d (2H, J = 7.5 Hz, CH$_{Ar}$), 8.48 br. s (1H, NH). ^{13}C NMR spectrum, δ_C, ppm: 17.7 (CH$_3$), 44.5 (C$^4_{pyrazoline}$), 46.4 (NCH$_2$), 55.6 (OCH$_3$), 58.6 (C$^5_{pyrazoline}$), 105.5 (C$^5_{thiazole}$), 109.7 (C$^{5'}_{thiazole}$), 114.8 (2CH$_{Ar}$), 116.2 (CH$_2$=), 123.6 (C$_{Ar}$), 125.9 (C$^3_{thiophene}$), 127.2 (C$^4_{thiophene}$), 128.1 (2CH$_{Ar}$), 128.8 (C$^5_{thiophene}$), 129.6 (2CH$_{Ar}$), 130.1 (CH=), 133.2 (C$_{Ar}$), 134.7 (C$_{Ar}$), 141.7 (C$^2_{thiophene}$), 143.0 (C$_{Ar}$), 146.5 (C$_{Ar}$), 151.5 (C$^3_{pyrazoline}$), 152.0 (C$^4_{thiazole}$), 153.8 (C$^{4'}_{thiazole}$), 161.8 (C$^2_{thiazole}$), 168.4 (C$^2_{thiazole}$). Found, %: C 60.25; H 4.52; N 16.43. C$_{30}$H$_{27}$N$_7$OS$_3$. Calculated, %: C 60.28; H 4.55; N 16.40. MS: m/z (%): 597 (M^+, 29).

2-Allylamino-4-methyl-5-{1-[5-(4-chloro-phenyldiazenyl)-4-phenylthiazol-2-yl]-5-(thiophen-2-yl)-4,5-dihydro-1*H*-pyrazol-3-yl}thiazole (14d). Red powder, yield 93%, mp 244–245°C. IR spectrum, ν, cm^{-1}: 3202 (NH), 3050 (=C–H, sp^2), 2947 (C–H, sp^3), 1624 (C=C), 1590 (C=N), 1532 (N=N). ^{1}H NMR spectrum, δ, ppm: 2.39 s (3H, CH$_3$), 3.56 d. d (1H, J = 15.0, 3.75 Hz, C^{4A}H$_{pyrazoline}$), 3.93 s (2H, CH$_2$N), 4.15 d. d (1H, J = 15.0, 9.75 Hz, C^{4B}H$_{pyrazoline}$), 5.16 d. d (1H, J = 9.0, 1.5 Hz, CH=), 5.26 d. d (1H, J = 15.0, 1.5 Hz, CH=), 5.93 m (1H, CH=), 6.19 d. d (1H, J = 9.75, 3.75 Hz, C^{5X}H$_{pyrazoline}$), 7.02 t (1H, J = 4.5 Hz, C^{4}H$_{thiophene}$), 7.27 d (1H, J = 3.0 Hz, C^{3}H$_{thiophene}$), 7.48 d (1H, J = 4.5 Hz, C^{5}H$_{thiophene}$), 7.49–7.56 m (5H, Ar-H), 7.69 d (2H, J = 7.5 Hz, CH$_{Ar}$), 8.24 d (2H, J = 7.5 Hz, CH$_{Ar}$), 8.56 br. s (1H, NH). ^{13}C NMR spectrum, δ_C, ppm: 17.6 (CH$_3$), 44.7 (C$^4_{pyrazoline}$), 46.4 (NCH$_2$), 58.6 (C$^5_{pyrazoline}$), 105.5 (C$^5_{thiazole}$), 109.5 (C$^{5'}_{thiazole}$), 116.2 (CH$_2$=), 123.3 (2CH$_{Ar}$), 125.8 (C$^3_{thiophene}$), 126.1 (C$^4_{thiophene}$), 126.2 (2CH$_{Ar}$), 126.9 (C), 128.5 (C), 129.9 (2CH$_{Ar}$), 130.1 (CH=), 133.2 (2C), 133.4 (C$_{Ar}$), 141.0 (C$^2_{thiophene}$), 141.2 (C$_{Ar}$), 142.7 (C$_{Ar}$), 151.1 (C$^3_{pyrazoline}$), 152.0 (C$^4_{thiazole}$), 154.5 (C$^{4'}_{thiazole}$), 162.5 (C$^2_{thiazole}$), 168.7 (C$^2_{thiazole}$). Found, %: C 57.86; H 3.99; N 16.25. C$_{29}$H$_{24}$ClN$_7$S$_3$. Calculated, %: C 57.84; H 4.02; N 16.28. MS: m/z (%): 601 (M^+, 35).

2-Allylamino-4-methyl-5-{1-[5-(4-bromo-phenyldiazenyl)-4-phenylthiazol-2-yl]-5-(thiophen-2-yl)-4,5-dihydro-1*H*-pyrazol-3-yl}thiazole (14e). Red powder, yield 90%, mp 254–255°C. IR spectrum, ν, cm^{-1}: 3200 (NH), 3052 (=C–H, sp^2), 2949 (C–H, sp^3), 1623 (C=C), 1592 (C=N), 1535 (N=N). ^{1}H NMR spectrum, δ, ppm: 2.40 s (3H, CH$_3$), 3.56 d. d (1H, J = 15.0, 3.75 Hz, C^{4A}H$_{pyrazoline}$), 3.94 s (2H, CH$_2$N), 4.14 d. d (1H, J = 15.0, 9.75 Hz, C^{4B}H$_{pyrazoline}$), 5.16 d. d (1H, J = 9.0, 1.5 Hz, CH=), 5.26 d. d (1H, J = 15.0, 1.5 Hz, CH=), 5.91 m (1H, CH=), 6.20 d. d (1H, J = 9.75, 3.75 Hz, C^{5X}H$_{pyrazoline}$), 7.02 t (1H, J = 4.5 Hz, C^{4}H$_{thiophene}$), 7.28 d (1H, J = 3.0 Hz, C^{3}H$_{thiophene}$), 7.49 d (1H, J = 4.5 Hz, C^{5}H$_{thiophene}$), 7.44–7.54 m (5H, Ar-H), 7.70 d (2H, J = 7.5 Hz, CH$_{Ar}$), 8.25 d (2H, J = 7.5 Hz, CH$_{Ar}$), 8.52 br. s (1H, NH). ^{13}C NMR spectrum, δ_C, ppm: 17.6 (CH$_3$), 44.7 (C$^4_{pyrazoline}$), 46.4 (NCH$_2$), 58.7 (C$^5_{pyrazoline}$), 106.5 (C$^5_{thiazole}$), 109.7 (C$^{5'}_{thiazole}$), 116.2 (CH$_2$=), 121.9 (2CH$_{Ar}$), 125.7 (C$^3_{thiophene}$), 126.1 (C$^4_{thiophene}$), 126.4 (2CH$_{Ar}$), 126.9 (C), 128.6 (C), 129.9 (2CH$_{Ar}$), 130.1 (CH=), 133.4 (2C), 134.2 (C$_{Ar}$), 141.0 (C$^2_{thiophene}$), 141.3 (C$_{Ar}$), 142.7 (C$_{Ar}$), 151.1 (C$^3_{pyrazoline}$), 152.5 (C$^4_{thiazole}$), 154.5 (C$^{4'}_{thiazole}$), 162.6 (C$^2_{thiazole}$), 165.3 (C$^2_{thiazole}$). Found, %: C 53.88; H 3.73; N 15.14. C$_{29}$H$_{24}$BrN$_7$S$_3$. Calculated, %: C 53.86; H 3.74; N 15.16. MS: m/z (%): 645 (M^+, 40).

2-Allylamino-4-methyl-5-{1-[5-(4-nitro-phenyldiazenyl)-4-phenylthiazol-2-yl]-5-(thiophen-2-yl)-4,5-dihydro-1*H*-pyrazol-3-yl}thiazole (14f). Blue

powder, yield 95%, mp 242–243°C. IR spectrum, ν, cm⁻¹: 3200 (NH), 3052 (=C–H, sp^2), 2949 (C–H, sp^3), 1628 (C=C), 1597 (C=N), 1597 (N=N), 1537, 1358 (NO₂). ¹H NMR spectrum, δ, ppm: 2.49 s (3H, CH₃), 3.63 d. d (1H, J = 15.0, 3.75 Hz, C⁴ᴬH$_{pyrazoline}$), 3.95 s (2H, CH₂N), 4.19 d. d (1H, J = 15.0, 9.75 Hz, C⁴ᴮH$_{pyrazoline}$), 5.17 d. d (1H, J = 9.0, 1.5 Hz, CH=), 5.26 d. d (1H, CH=, J = 15.0, 1.5 Hz), 5.92 m (1H, CH=), 6.27 d. d (1H, J = 9.75, 3.75 Hz, C⁵ˣH$_{pyrazoline}$), 7.03 t (1H, J = 4.5 Hz, C⁴H$_{thiophene}$), 7.29 d (1H, J = 3.0 Hz, C³H$_{thiophene}$), 7.51 d (1H, J = 4.5 Hz, C⁵H$_{thiophene}$), 7.54–7.59 m (5H, Ar-H), 7.72 d (2H, J = 7.5 Hz, CH$_{Ar}$), 8.31 d (2H, J = 7.5 Hz, CH$_{Ar}$), 8.61 br. s (1H, NH). ¹³C NMR spectrum, δ$_C$, ppm: 17.7 (CH₃), 44.5 (C⁴$_{pyrazoline}$), 46.5 (NCH₂), 58.7 (C⁵$_{pyrazoline}$), 105.9 (C⁵$_{thiazole}$), 109.7 (C⁵′$_{thiazole}$), 116.2 (CH₂=), 121.9 (2CH$_{Ar}$), 125.7 (C³$_{thiophene}$), 126.1 (C⁴$_{thiophene}$), 126.4 (2CH$_{Ar}$), 126.9 (C), 128.6 (C), 129.9 (2CH$_{Ar}$), 130.2 (CH=), 133.4 (2C), 133.9 (C$_{Ar}$), 141.7 (C²$_{thiophene}$), 143.3 (C$_{Ar}$), 142.7 (C$_{Ar}$), 153.6 (C³$_{pyrazoline}$), 154.8 (C⁴$_{thiazole}$), 155.3 (C⁴′$_{thiazole}$), 162.9 (C²′$_{thiazole}$), 169.4 (C²$_{thiazole}$). Found, %: C 56.87; H 3.97; N 18.32. C₂₉H₂₄rN₈O₂S₃. Calculated, %: C 56.84; H 3.95; N 18.29. MS: m/z (%): 612 (M^+, 25).

Cytotoxicity assay. Sulforhodamine B (SRB) assay [23, 24] was used to evaluate the in vitro cytotoxicity of the new 1,3,5-trisubstituted pyrazolines against breast cancer (MCF-7), colon cancer (HCT-116) and liver carcinoma (HepG2) cell lines. The cancer cells were cultured in RPMI media supplemented with 100 μg/mL streptomycin, 100 units/mL penicillin, and 10% heat-inactivated fetal bovine serum in a humidified, 5% (v/v) CO₂ atmosphere at 37ºC. Using 0.25% trypsin–EDTA, exponentially developing cells were removed from dishes and plated in 96-well plates at a density of about 1000 cells per well. After a 24 h incubation period, cells were treated for 48 h with different doses of the tested substances. Cells were fixed with 10% TCA for 1 h at 4°C, washed repeatedly with distilled water, stained with 0.4% SRB solution for 10 min in darkness, and rinsed with 1% ethanoic acid at the end of the treatment period. Tris–HCl was used to dissolving the SRB-stained cells after they had been dried overnight, and the color intensity was assessed at 570 nm using a microplate reader (Anthos Zenyth-200RT, Cambridge, England). The IC₅₀ value, was determined. Doxorubicin was as used as a positive control, and the bioassays were carried out in triplicates.

CONCLUSIONS

A novel series of trisubstituted pyrazolines bearing thiophene and thiazole moieties have been synthesized, characterized and evaluated for their in vitro anticancer activity against three panels of cancer cell lines and one regular line. The tests have indicated that the insertion of a substituent at position 1 of 2-pyrazoline skeleton such as thioamide group, 4-phenylazothiazole and 4-nitrophenylthiazole have led to compounds with potent anticancer activity and no evidence of human toxicity. Most of the synthesized 1-substituted-3-(thiazol-5-yl)-5-(thiophen-2-yl)pyrazolines have demonstrated high selectivity toward hepatic carcinoma cell line (HepG2) in comparison with breast cancer (MCF-7) and colon cancer (HCT 116) cell lines.

FUNDING

CONFLICT OF INTEREST

No conflict of interest was declared by the authors.

REFERENCES

1. Albuquerque, H.M.T., Santos, C.M.M., Cavaleiro, J.A.S., and Silva, A.M.S., *Curr. Org. Chem.,* 2014, vol. 18, p. 2750.
https://doi.org/10.2174/1385272819666141013224253

2. Mathew, B., Haridas, A., Ucar, G., Baysal, I., Jay, M., Mathew, G.E., Lakshmanan, B., and Jayaprakash, V., *ChemMedChem.,* 2016, vol. 11, p.1161.
https://doi.org/10.1002/cmdc.201600122

3. Rathish, I.G., Javed, K., Ahmad, S., Bano, S., Alam, M.S., Pillai, K.K., Singh, S., and Bagchi, V., *Bioorg. Med. Chem. Lett.*, 2009, vol.19, p. 255.
https://doi.org/10.1016/j.bmcl.2008.10.105

4. Bondock, S. and Fouda, A.M., *Synth. Commun.,* 2018, vol. 48, p. 561.
https://doi.org/10.1080/00397911.2017.1412465

5. Bondock, S. and Nasr, T., *Russ. J. Gen. Chem.,* 2021, vol. 91, p. 488.
https://doi.org/10.1134/S1070363221030178

6. Aggarwal, S., Paliwal, D., Kaushik, D., Gupta, G.K., and Kumar, A., *Lett. Org. Chem.,* 2019, vol. 16, p. 807.
https://doi.org/10.2174/1570178616666190212145754

7. Manetti, F., Brullo, C., Magnani, M., Mosci, F., Chelli, B., Crespan, E., Schenone, S., Naldini, A., Bruno, O., Trincavelli, M. L., Maga, G., Carraro, F., Martini, C., Bondavalli, F., and Botta, M., *J. Med. Chem.,* 2008, vol. 51, p. 1252.
https://doi.org/10.1021/jm701240c

8. Rostom, S.A.F., Badr, M.H., Abd El Razik, H.A., Ashour, H.M.A., and Abdel Wahab, A.E, *Arch. Pharm. Chem. Life Sci.*, 2011, vol. 344, p. 572.
https://doi.org/10.1002/ardp.201100077

9. Schenone, S., Bruno, O., Ranise, A., Bondavalli, F., Brullo, C., Fossa, P., Mosti, L., Menozzi, G., Carraro, F., Naldini, A., Bernini, C., Manetti, F., and Botta, M., *Bioorg. Med. Chem. Lett.,* 2004, vol. 14, p. 2511.
https://doi.org/10.1016/j.bmcl.2004.03.013

10. Zhu, G.D., Gong, J., Gandhi, V.B., Woods, K., Luo, Y., Liu, X., Guan, R., Kinghofer, V., Johson, E.F., Stoll, V.S., Mamo, M., Li, Q., Rosenberg, S.H., and Giranda, V.L., *Bioorg. Med. Chem.,* 2007, vol. 15, p. 2441.
https://doi.org/10.1016/j.bmc.2007.01.010

11. Bhat, B.A., Dhar, K.L., Puri, S.C., Saxena, A.K., Shanmugavel, M., and Qazi, G.N., *Bioorg. Med. Chem. Lett.,* 2005, vol. 15, p. 3177.
https://doi.org/10.1016/j.bmcl.2005.03.121

12. Matiadis, D. and Sagnou, M., *Int. J. Mol. Sci.,* 2020, vol. 21, p. 5507.
https://doi.org/10.3390/ijms21155507

13. Morigi, R., Locatelli, A., Leoni, A., and Rambaldi, M., *Recent Pat. Anticancer Drug Discov.*, 2015, vol. 10, p. 280.
https://doi.org/10.2174/1574892810666150708110432

14. Lu, Y., Li, C.-M., Wang, Z., Ross, C.R., Chen, J., Dalton, J.T., Li, W., and Miller, D.D., *J. Med. Chem.*, 2009, vol. 52, p. 1701.
https://doi.org/10.1021/jm801449a

15. Bondock, S., Alqahtani, S., and Fouda, A.M., *J. Heterocycl. Chem.,* 2021, vol. 58, p. 56.
https://doi.org/10.1002/jhet.4148

16. Ramadan, A.M., Elsamra, R.M.I., and Bondock, S., *Appl. Organometal. Chem.,* 2021, vol. 35, p. e6102.
https://doi.org/10.1002/aoc.6102

17. Bondock, S., Nasr, T., and Alqahtani, S., *Chemistry Select*, 2020, vol. 5, p. 12087.
https://doi.org/10.1002/slct.202002912

18. Bondock, S., Alqahtani, S., and Fouda, A.M., *Synth. Commun.,* 2019, vol. 49, p. 2188.
https://doi.org/10.1080/00397911.2019.1616759

19. Bondock, S. and Gieman, H., *Res. Chem. Intermed.,* 2015, vol. 41, p. 8381.
https://doi.org/10.1007/s11164-014-1899-8

20. Beloglazkina, E.K., Korablina, D.D., Vorozhtsov, N.I., Sviridova, L.A., Moiseeva, A.A., Skvortsov, D.A., Rybakov, V.B., Majouga, A.G., and Zyk, N.V., *Arab. J. Chem.,* 2019, vol. 12, p. 1050.
https://doi.org/10.1016/j.arabjc.2017.01.005

21. Mansour, E., Aboelnaga, A.; Nassar, E.M., and Elewa, S.I., *Synth. Commun.,* 2020, vol. 50, p. 368.
https://doi.org/10.1080/00397911.2019.1695839

22. Shawali, A.S. and Abdelhamid, A.O., *Bull. Chem. Soc. Jpn.,* 1976, vol. 49, p. 321.
https://doi.org/10.1246/bcsj.49.321

23. Skehan, P., Storeng, R., Scudiero, D., Monks, A., McMahon, J., Vistica, D., Warren, J.T., Bokesch, H., Kenney, S., and Boyd, M.R., *J. Natl. Cancer Inst.*, 1990, vol. 82, p. 1107.
https://doi.org/10.1093/jnci/82.13.1107

24. Vichai, V. and Kirtikara, K., *Nat. Protoc.,* 2006, vol. 1, p. 1112.
https://doi.org/10.1038/nprot.2006.179

EFFECT OF STABILIZER ON OPTICAL BAND GAP OF ZnO AND THEIR PERFORMANCE IN DYE-SENSITIZED SOLAR CELLS

A. Kalam[1,2*], S.A.S. Allami[1], A.G. Al-Sehemi[1,2], M.A. Assiri[1] and P. Yadav[3]

[1]Department of Chemistry, Faculty of Science, King Khalid University, P.O. Box 9004, Abha 61413, Saudi Arabia
[2]Research Center for Advanced Materials Science (RCAMS), King Khalid University, P.O. Box 9004, Abha 61413, Saudi Arabia
[3]Department of Solar Energy, School of Technology, Pandit Deendayal Petroleum University, Gujarat, India

ABSTRACT. In dye-sensitized solar cells, transparent metal oxide working electrodes play a vital role in defining the power conversion efficiency. It was found that the size of nanoparticles influences the electrical, optical properties of these electrodes. Herein, we describe the synthesis of ZnO with zinc acetate dihydrate and different stabilizers (diethylamine and triethylamine) by using a modified solvothermal process. The obtained materials were characterized by XRD, SEM, EDX, TEM, HRTEM, UV-visible, FTIR, and Raman methods. The crystallite sizes for ZnO-1 and ZnO-2 samples were indexed as 39.0 and 40.5 nm for the highest peak intensity with diethylamine and triethylamine stabilizer, respectively. We examine the effect of stabilizers on the morphology, optical band gap, and photovoltaic performance of the prepared ZnO. We found that ZnO prepared using diethylamine stabilizer exhibiting significant efficiency of 1.45%, open-circuit voltage 0.454 V, short-circuit current density 2.128 mA/cm^2, and 0.66 fill factor were achieved under 44 mW/cm^2 illumination powers with dye-3.

KEY WORDS: Dye-sensitized solar cells, ZnO, Band gap, Photovoltaic performance

INTRODUCTION

Semiconductor nanoparticles have received much attention from researchers in multidisciplinary fields such as nanoscale electronic devices, solar cells, light-emitting nanodevices due to exceptional advantages like the optical band gap and size. The optical band gap is directly related to the photo ability of the material, and nanoscale size can impact the physicochemical properties of a material yielding unique properties owing to their large surface area or quantum size effect, such as the optical properties.

Among semiconductor materials, zinc oxide semiconductor (ZnO) has many specific properties such as a wide band gap in the near-UV spectral region with band gap energy of 3.37 eV at room temperature (R.T.), good transparency, considerable free-exciton binding energy (60 meV), high electron mobility (200-1000 cm^2 V^{-1} s^{-1}) and strong room-temperature luminescence as compared to TiO$_2$ nanomaterials. The wide band gap and considerable excitonic binding energy have highly valued zinc oxide in industrial and scientific circles [1].

Lately, ZnO has become a topic to study for applications such as solar cells [2], memory devices [3], sensors [4], concrete [5], etc. One-dimensional nanostructures seem like an attractive research topic for their great features and applications in nanodevices in the last few years. ZnO's bandgap energy and conduction band are analogous to the anatase TiO$_2$ materials (3.17–3.28 eV); therefore, it is an alternate working electrode for dye-sensitized solar cell (DSSC) applications [6-9]. But the conversion efficiency confirmed by ZnO is lower than TiO$_2$ materials based DSSC in which maximum efficiency reached ~13% is achieved [10]. The device performance of ZnO-based DSSC can be improved by setting its morphology, surface area, and size. Several

_____

*Corresponding author. E-mail: abul_k33@yahoo.com

preparation methods have been defined in the literature for preparation of ZnO nanostructures like sol-gel method [11], laser ablation [12], green synthesis [13], co-precipitation [14], electrophoretic deposition [15], sonochemical method [16], hydrothermal method [17], and solvothermal processes [18]. The ordered nanowire DSSC was presented that be very efficient for the excitonic photovoltaic devices [19]. The atomic layer deposition was used to coat arrays of ZnO nanowires with thin shells of amorphous Al_2O_3 or anatase TiO_2 [20]. The dendritic ZnO nanowires were reported with efficiencies of about 0.5% by using the chemical vapor deposition method (CVD) [21-22]. The ZnO nano-flower was prepared through a hydrothermal method and showed an efficiency of up to 1.9% [23]. The ZnO prepared by the solvothermal method exhibited ~2.6% of PCE in DSSC [24]. Remarkably, the hierarchically assembled ZnO nanostructure in a DSSC fabrication gave a high-efficiency reach of ~7.5 [25]. Hence, it is important to synthesize the ZnO nanoparticles with desired crystal structures and controlled particle size.

In the present work, we present a simple, economical, and effective modified solvothermal method to synthesize ZnO nanoparticles using zinc acetate precursor with diethylamine and triethylamine as a stabilizer. The effect of diethylamine and triethylamine on ZnO nanoparticles morphology and optical property will be discussed. In addition, we also discussed the efficiency of ZnO nanoparticles toward dye-sensitized solar cells (DSSCs). In continuation of our previous work, we used 2-cyano-N′-[(2-hydroxynaphthalene-1-yl)methylene]acetohydrazide (CHMA; dye-1), 2-cyano-N′-[(4-dimethylamino)benzylidene]acetohydrazide (CDBA; dye-2) and 2-cyano-N'-[(anthracene-9-yl)methylene]-acetohydrazide (AMCH; dye-3) dyes for this work [26].

EXPERIMENTAL

Synthesis of zinc oxide nanoparticle (ZnO-1)

The standard synthetic procedure to prepare ZnO was as follows: 25 mL of zinc acetate (0.2 N) solution was mixed with 5 mL of diethylamine (drop-wise) in a round bottom flask and stirred at least 30 min. 25 mL of ethanol was added to make the azeotropic mixture and heated at a temperature of 80 °C for 12 h under vigorous stirring, producing white precipitate. The centrifugation was used to separate the precipitate, washed with distilled water and acetone. The residue was heated in an oven at 100 °C for overnight.

Synthesis of zinc oxide nanoparticle (ZnO-2)

Follow the same procedure as mentioned above for ZnO-1, but we used triethylamine instead of diethylamine in the present case.

Preparation of dye

In continuation of our previous work, we prepared and used 2-cyano-N′-[(2-hydroxy naphthalene-1-yl)methylene]acetohydrazide (CHMA; dye-1), 2-cyano-N′-[(4-dimethylamino)benzylidene]-acetohydrazide (CDBA; dye-2) and 2-cyano-N'-[(anthracene-9-yl)methylene]-acetohydrazide (AMCH; dye-3) dyes for this work [26].

Preparation of zinc oxide working electrode and platinum counter electrode by doctor blade method

The as-prepared ZnO was blended with a small volume of acetylacetone, distilled water, and triton X-100 in a conical flask and stirred overnight at 350 rpm to get a colloidal suspension. The paste preparation was done in ambient air at room temperature. An evaporator concentrated the contents in the dispersion at 40 °C. The ultra-sonication was performed for 30 min to homogenize ZnO

paste. The glass substrates were cut to 2 cm x 2 cm and washed ultrasonically in ethanol for 20 min. Additionally, using the doctor blade method, the ZnO pastes were extended on conducting surface of the glass substrate and became dry in the open air to prepare the working electrode. The film was heated at 400 °C for 30 min in the high-temperature furnace. The working electrodes dip in CHMA, CDBA, and AMCH solution for 24 h and are washed with ethanol to eradicate excess dyes from the film's surface. The doctor blade method prepared the platinum counter electrodes and annealed them at 400 °C for 30 min.

Assembling of DSSC

The Pt-coated substrate was generally employed on top of the ZnO-coated substrate and made a sandwich-type device. Therefore, the conductive side of the counter electrode faced the dye-coated ZnO layer. The electrolyte solution (Iodolyte HI-30, iodide/tri-iodide redox couple) was filled in between the working electrode and the counter electrodes, and the complete solar cells were assembled. The conducting side of both electrodes was painted using silver paste and fixed the copper wire used Araldite for getting electrical contact.

Materials characterization and measurement

Different techniques were utilized for the analysis of photoanode, such as X-ray diffractometer (XRD) (Shimadzu Lab X-6000) with Cu-Kα radiation (λ = 1.5406 Å). The samples peaks were observed at room temperature in the range of 2θ from 20° to 80°. The scanning electron microscopy (JSM 6360 SEM/EDX) was employed to study the surface morphologies of the photoanode. The energy dispersive spectroscopy (EDX) is usually fixed with a scanning electron microscope to analyze the elements present in the sample. The JEOL 2100F transmission electron microscopy (TEM) and high-resolution transmission electron microscopy (HR-TEM), operating at 200 kV, were employed to study the photoanode's grain size and morphology. We used PG UV-Vis double-beam spectrophotometer to examine the absorption spectra in the wavelength ranging from 250-to 700 nm. FTIR spectra were examined on a JASCO 460 plus FTIR spectrometer using the KBr pellet technique at room temperature. Raman spectroscopy (XDR, Thermo Fisher Scientific Inc.) was used to find out the vibrational modes of ZnO at an excitation of 532 nm. Keithley 2400 source meters were used to measure the fabricated device's current density-voltage (J-V) at 44 mW cm^{-2} AM 1.5 G of solar spectrum illumination.

RESULTS AND DISCUSSION

Powder X-ray diffraction (XRD) analysis

Figure 1 shows the X-ray diffraction patterns of the samples (ZnO-1 and ZnO-2), which also confirmed the purity of the samples. Our results exhibit sharp and strong reflections, which could be indexed as a pure wurtzite phase of ZnO nanoparticles with a hexagonal structure. The ZnO nanoparticles planes with Miller indices (hkl) values of (100), (002), (101), (102), (110), (103), (200) (112), (201), (004) and (202) for a series of characteristic peaks centered almost 2θ = 31.6°, 34.3°, 36.1°, 47.4°, 56.4°, 62.4°, 66.2°, 67.8°, 69.0°, 72.4°, and 76.8° can be agreed very well with the standard X-ray diffraction pattern of monophasic ZnO nanoparticles (JCPDS card no. 36-1451 [27]. The highest peak intensity is observed with triethylamine than that of diethylamine, which could be due to a better crystalline structure. This preferred orientation (101) is achieved because of covering of progress of certain crystal planes and stimulating the progress of the 101 planes by stabilizers. Miller indices (hkl) and crystallite size (d) of the samples were played a meaningful role to conclude the electrical properties, which can be calculated from the most intense peak signal (101) by applying the Debye–Scherrer formula, d = 0.9 λ/β cos θ. Here, λ

represents the wavelength of X-ray (Cu K$_a$ = 0.154 nm), d represents the size of crystallite (nm), β represents the full width at half maximum (FWHM) of prominent intense peak measured in radians, and θ is the peak angle.
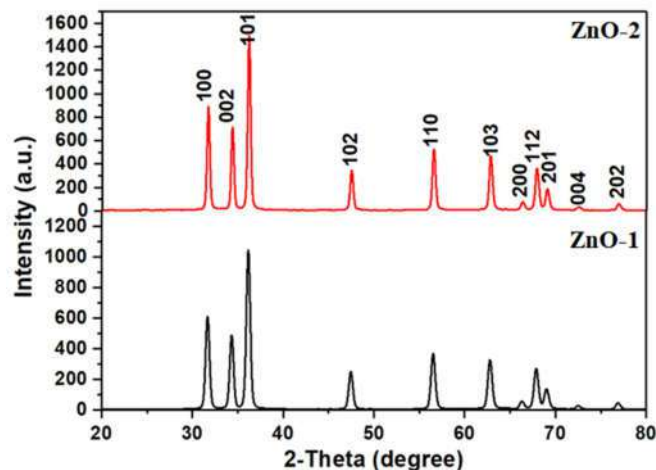

Figure 1. X-ray diffraction pattern of ZnO-1 and ZnO-2 nanoparticles.

Scanning electron microscopy (SEM)

Figure 2 shows the SEM images of ZnO-1 and ZnO-2 nanoparticles formed using diethylamine and triethylamine as stabilizers. The SEM image of ZnO-1 clearly showed a hexagonal crystal structure with a porous texture, whereas the sample ZnO-2 shows nearly spherical particles with low agglomeration. The SEM investigation exhibits that both (diethylamine and triethylamine) have a very significant role in finding the porous hexagonal and spherical morphologies of the ZnO nanoparticles. Yoshida *et al.* [28] have been reported that porous ZnO materials boosted the dye loading and PCE values.

The compositions of nanoparticles in the samples (ZnO-1 and ZnO-2) were determined by EDX analysis (Figure 2), which confirms the presence of Zn and O. Thus, it is also established from EDX analysis that ZnO nanoparticles were formed without any impurities.

Transmission electron microscopy (TEM)

TEM studies were also carried out on ZnO nanoparticles to investigate grain size, morphology, and size distribution. The relevant TEM micrographs are depicted in Figure 3 to conform almost hexagonal for ZnO-1 and spherical for ZnO-2 and uniform as observed by SEM studies. The average particle sizes of ZnO-1 and ZnO-2 samples are in the range of 255 nm to 15.5 nm, respectively, which revealed that by using triethylamine, the grain size decreases from 255 nm to 15.5 nm. The high-resolution transmission electron microscope (HRTEM) shows the spacing between the successive planes of 0.272 nm and 0.252 nm, matching the (101) reflection of pure ZnO nanoparticles. The fringe in the TEM image is linked to a transmitted wave exiting a crystal and a diffracted wave from one lattice plane of the crystal.
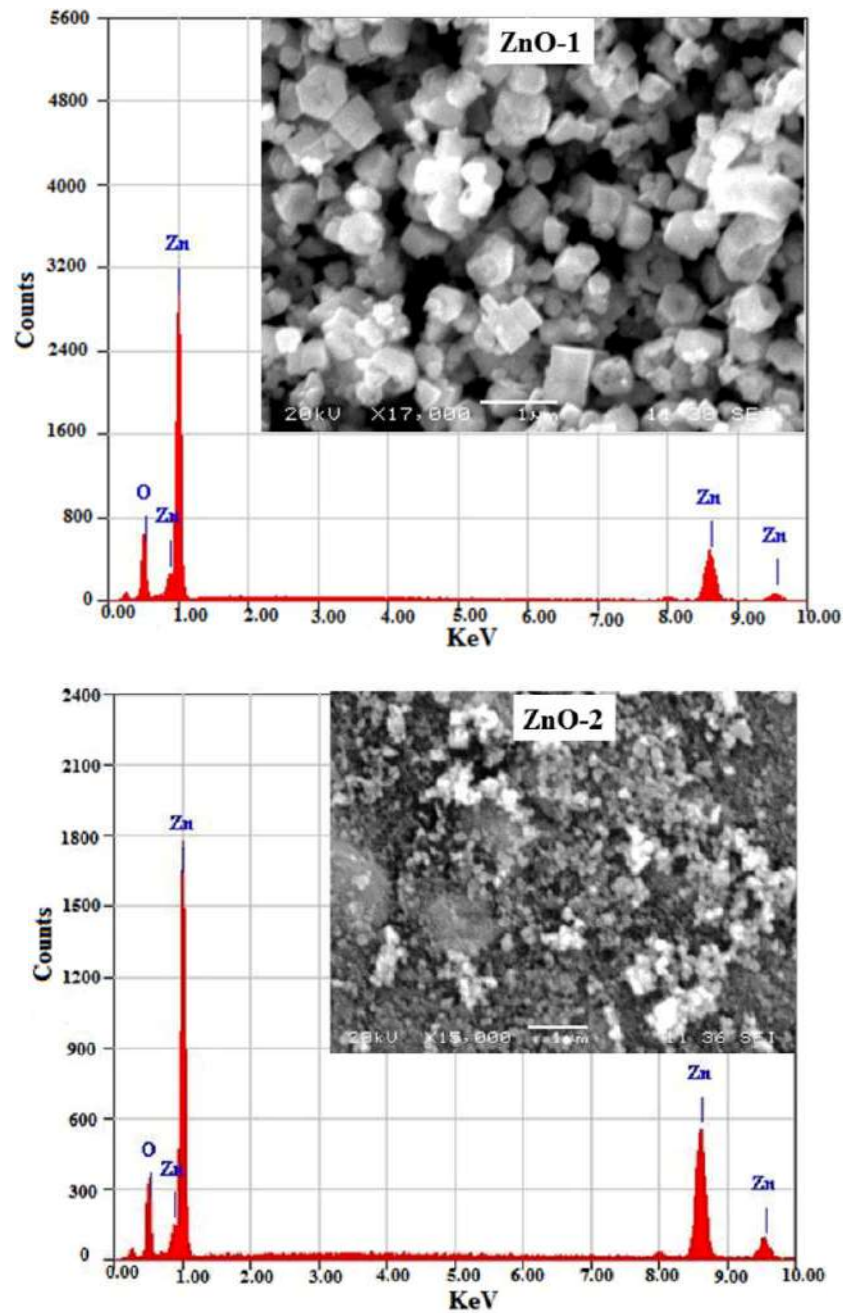
Figure 2. Scanning electron microscopy (SEM) and EDX images of ZnO-1 and ZnO-2 nanoparticles.
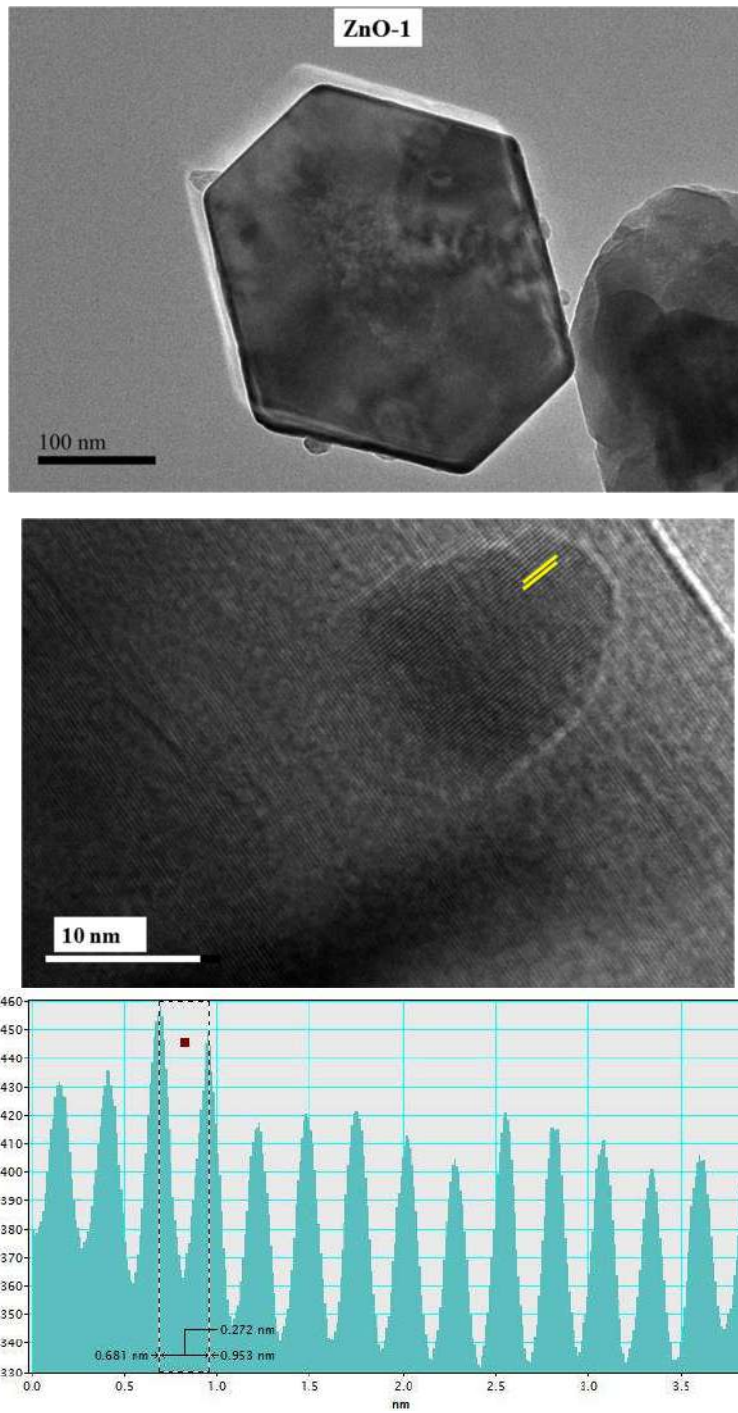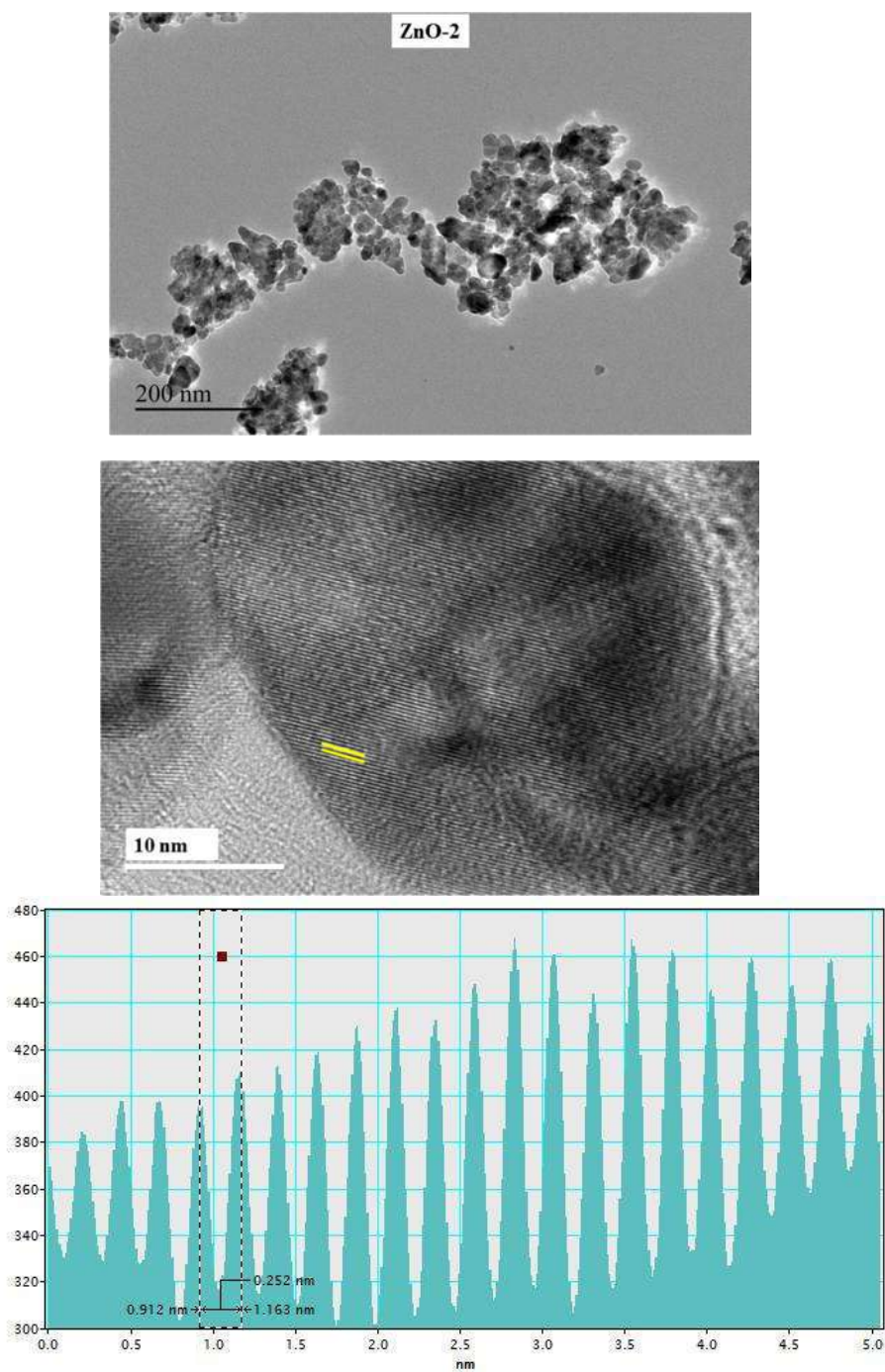
Figure 3. TEM and HRTEM images of ZnO-1 and ZnO-2 nanoparticles.

Fourier transform infra-red spectroscopy (FTIR) analysis

The FTIR spectra of the prepared ZnO nanoparticles are presented in Figure 4. The broadband obtained in the range of 3389-3422 cm^{-1} corresponds to the presence of hydrogen-bonded hydroxide (O-H) stretching mode of vibration from water to the ZnO nanoparticles. The Zn–O stretching mode of vibration shows bands in the range from 600 to 400 cm^{-1}; in consequence, the band at 473 and 481 cm^{-1} confirms the formation of ZnO nanoparticles [27, 29]. The bands obtained at 1591 cm^{-1} and 1398 cm^{-1} are associated with water molecules O–H bending modes [27, 29].
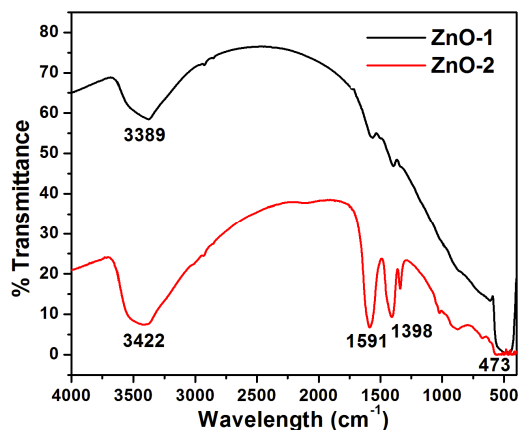
Figure 4. FTIR spectra of ZnO-1 and ZnO-2 nanoparticles.
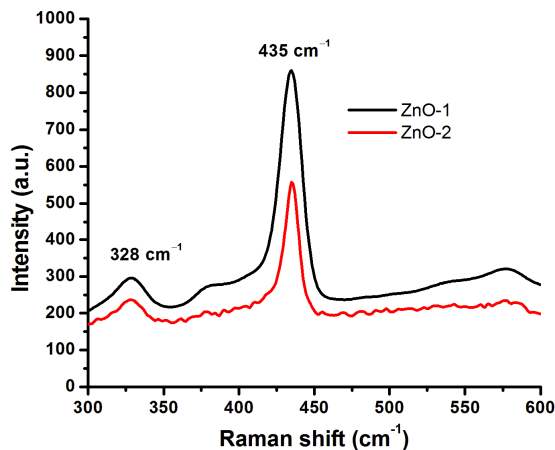
Figure 5. Raman spectra of ZnO-1 and ZnO-2 nanoparticles.

Raman analysis

The crystallinity and structural ailment in micro and nanostructured materials are studied by the Raman spectroscopy and shown in Figure 5. The space group of ZnO nanoparticles with hexagonal wurtzite structure is *P*63*mc*. As observed in Figure 5, two peaks are obtained at 435 cm^{-1} (strong) and 328 cm^{-1}. The peak at 435 cm^{-1} represented the E$_2$ (high) mode of Raman active,

which is a typical peak for the ZnO hexagonal wurtzite structure. The E_2 mode point toward high crystallinity and very low oxygen vacancy in ZnO nanoparticles. Peak 328 cm^{-1} represents to the E_{2H}–E_{2L} (multi-phonon process) mode, and it can form only a single-crystal ZnO [29-31]. No specific influence of stabilizing agent is perceived on the method of ZnO nanoparticles except peak intensity ratio. The reported results are in good agreement with the Raman spectrum of ZnO described by Yousefi *et al.* [32].

Optical properties

The UV-Vis spectra of ZnO-1 and ZnO-2 nanoparticles are shown in Figure 6. Strong absorption bands are obtained at 458 nm for ZnO-1 and 418 nm for ZnO-2 nanoparticles, which are associated with the absorption bands of ZnO. Further, the nature of the optical band gap will be preserved when the absorption spectrum moves to longer wavelengths along with the electron excitation from the valance band to the conduction band. The following equation is used to calculate the optical band gap (Eg):

$$(Ah\nu)^n = B(h\nu – Eg)$$

where $h\nu$ is the photon energy; *A* represents absorbance, *B* represents constant linked to the material; and *n* refers to either 2 or ½ for direct and indirect transitions, respectively. Therefore, the optical band gap for the absorption peak is gained by extending the linear portion of the $(Ah\nu)^n$ -$h\nu$ curve to zero, as presented in Figure 6.

In literature, the band gap energy of the bulk ZnO is found to be 3.37 eV, but in the present work, the band gap of ZnO-1 and ZnO-2 nanoparticles are found to be 2.9 and 3.0 eV, which is smaller than that of the bulk ZnO. This might be due to the existence of hydroxyl group (-OH) adsorbed on the surface of ZnO nanoparticles which is evidenced by FTIR analysis and might reduce the band gap energy [33]. The band gap of materials is not significantly changed with diethylamine and triethylamine. On the other hand, the changes in their morphologies, particle size, and surface microstructures affect the redshift of the spectral lines, which will lead to better crystallinity [34-35]. In addition, it is found that the band gap of the transport layer has a crucial role in defining the performance of dye-sensitized solar cells [36].

Table 1. Photovoltaic performance of ZnO-1 based device with (a) dye-1, (b) dye-2 and (c) dye-3.

Dye	V_{oc} (V)	J_{sc} (mA/cm^2)	Fill factor (ff)	η Efficiency (%)
dye-1	0.31	1.709	0.59	0.73
dye-2	0.41	1.647	0.58	0.90
dye-3	0.45	2.128	0.66	1.45

Photovoltaic performance

Figure 7 shows the J-V curves of DSSC prepared by ZnO-1 nanoparticle to see their applicability. We selected the ZnO-1 nanoparticle due to the porosity and wide-band gap. We also tried with ZnO-2, but unfortunately, the results were inappropriate; therefore, we did not mention it in the current report. The short-circuit density (J_{sc}), the open-circuit voltage (V_{oc}), and the fill factor (*FF*) parameters for the solar cells are measured and shown in Table 1. The best photovoltaic performance of the ZnO-1 was obtained with dye 3 with PCE of 1.45%, the open-circuit voltage of 0.454 V, short-circuit current density of 2.128 mA/cm^2, and 0.66 fill factor. This enhancement in efficiency has been attributed to the small energy band gap of dye-3 and better energy alignment with ZnO-1 nanoparticles, which could provide better charge transport. The achieved photovoltaic parameters are précised in Table 1. The results obtained from the current study are lower than the efficiencies reported in the literature. Keis *et al.* [37] reported that ZnO nanoparticle film with N719 dye showed 5% efficiency, whereas Chang *et al.* [38] reported 5.6% efficiencies with

similar properties. As far as nano wire-based DSSCs are concerned, Law *et al.* [19] reported up to 1.5% efficiency, but Xu *et al.* [39] have attained 2.1% efficiency by optimized ZnO NWs with a length of up to 30 μm. Even though some DSSCs based on ZnO showed lower efficiencies than those stated in the current study. The reasons behind the low efficiency or performance of ZnO-based DSSCs are not exclusively implicit. But, the nanoparticles of larger size and narrow optical band gap were found less suitable for dye loading. They increased the charge recombination as they could not provide continuous pathways to the electrons. On the other hand, the decrease in the photocurrent efficiency of dye-1 and dye-2 sensitized devices is attributed to the blue-shifted dyes with a greater energy band gap than the ones of the dye-3.
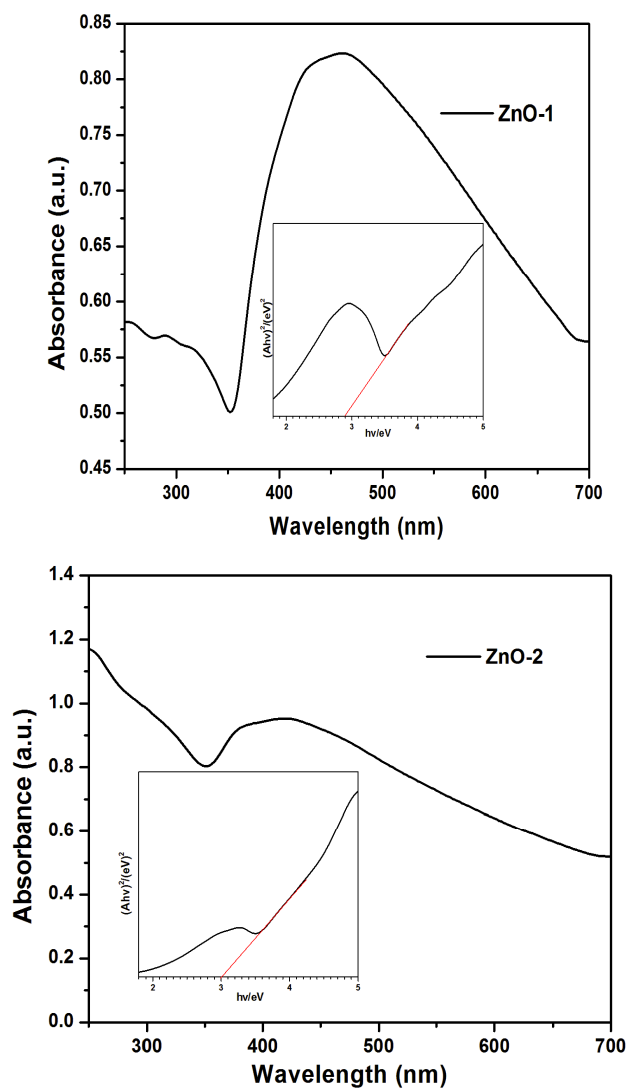
Figure 6. The UV-Vis spectra and optical band gap of ZnO-1 and ZnO-2 nanoparticles.
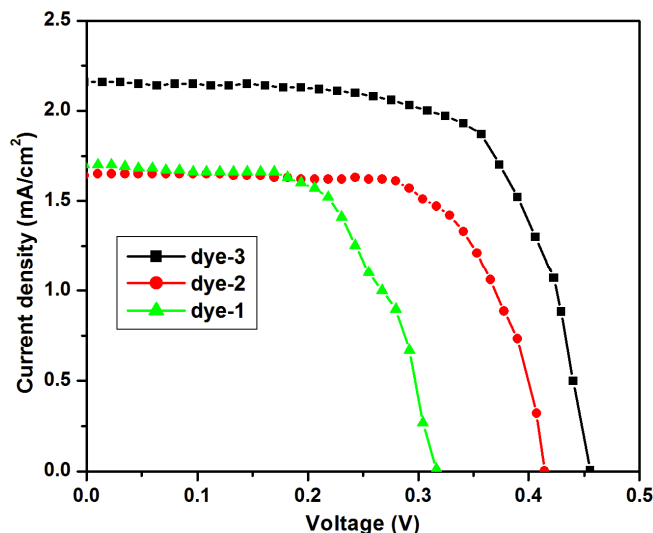
Figure 7. The current-voltage curve of ZnO-1 based device with (a) dye-1, (b) dye-2 and (c) dye-3.

CONCLUSION

The modified solvothermal method has been used to synthesize different morphologies of ZnO nanomaterials. The different morphologies and optical band gap were obtained for the ZnO by different stabilizers used in the synthesis. The band gap energy of ZnO-1 and ZnO-2 nanomaterials was 2.9 and 3.0 eV, which is smaller than that of the bulk ZnO. XRD patterns of all ZnO samples confirm the formation of a pure crystalline hexagonal phase. The photovoltaic performance of devices fabricated using ZnO-1, and dye-3 shows the highest efficiency. The difference in efficiencies with dye-1, dye-2, and dye-3 is due to their energy band gap. From the present study, we can transform the shape, size, and morphology of ZnO by changing the stabilizer and progress its performance as photoanode material in DSSCs.

ACKNOWLEDGMENT

REFERENCES

1. Ozgur, U.; Alivov, Y.I.; Liu, C.; Teke, A.; Reshchikov, M.A.; Dogan, S.; Avrutin, V.; Cho, S.J.; Morkoc, H. A comprehensive review of ZnO materials and devices. *J. Appl. Phys.* **2005**, 98, 041301.
2. Li, L.; Zhai, T.; Bando, Y.; Golberg, D. Recent progress of one-dimensional ZnO nanostructured solar cells. *Nano Energy* **2012**, 1, 91-106.
3. Zhang, F.; Li, X.; Gao, X.; Wu, L.; Zhuge, F.; Wang, Q.; He, Y. Effect of defect content on the unipolar resistive switching characteristics of ZnO thin film memory devices. *Solid State Commun.* **2012**, 152, 1630-1634.

4. Cheng, X.L.; Zhao, H.; Huo, L.H.; Gao, S.; Zhao, J.G. ZnO nanoparticulate thin film: Preparation, characterization and gas-sensing property. *Sens. Actuators B chem.* **2004**, 102, 248-252.

5. Abo-El-Enein, S.A.; El-Hosiny, F.I.; El-Gamal, S.M.A.; Amin, M.S.; Ramadan, M. Gamma radiation shielding, fire resistance and physicochemical characteristics of Portland cement pastes modified with synthesized Fe_2O_3 and ZnO nanoparticles. *Constr. Build. Mater.* **2018**, 173, 687-706.

6. Dhodamani, A.G.; More, K.V.; Mullani, S.B.; Deshmukh, S.P.; Koli, V.B.; Panda, D.K; Delekar, S.D. Structural refinement and optoelectronic properties of $(Mo_xTi_{1-2x}O_{2-\delta})_{1-y}(RGO)_y$ nanocomposites and their photovoltaic studies with natural pigments as sensitizers. *Chem. Select* **2020**, 5, 218-230.

7. Delekar, S.D.; Dhodamani, A.G.; More, K.V.; Dongale, T.D.; Kamat, R.K.; Acquah, S.F.; Dalal, N.S.; Panda, D.K. Structural and optical properties of nanocrystalline TiO_2 with multiwalled carbon nanotubes and its photovoltaic studies using Ru(II) sensitizers. *ACS Omega* **2018**, 3, 3, 2743-2756

8. Dhodamani, A.G.; More, K.V.; Patil, S.M.; Shelke, A.R.; Shinde, S.K.; Kim, D.Y.; Delekar, S.D. Synergistics of Cr(III) doping in TiO_2/MWCNTs nanocomposites: Their enhanced physicochemical properties in relation to photovoltaic studies. *Solar Energy* **2020**, 201, 398-408.

9. Dhodamani, A.G.; More, K.V.; Koli, V.B.; Shelke, A.R; Deshpande, N.G.; Panda, D.K.; Delekar, S.D. Compositional dependent physicochemical and photovoltaic properties of the $(TiO_2)_{1-x}(RGO)_x$ nanocomposites for sensitized solar cells using Ru(II) dyes. *Chem. Select* **2019**, 4, 1055-1068.

10. Mathew, S.; Yella, A.; Gao, P.; Humphry-Baker, R.; Curchod-Basile, F.E.; Ashari-Astani, N.; Tavernelli, I.; Rothlisberger, U.; Nazeeruddin, K.; Grätzel, M. Dye-sensitized solar cells with 13% efficiency achieved through the molecular engineering of porphyrin sensitizers. *Nat. Chem.* **2014**, 6, 242-247.

11. Alwin, S.; Shajan, X.S. Facile synthesis of 3-D nanostructured zinc oxide aerogel and its application as photoanode material for dye-sensitized solar cells. *Surf. Interfaces* **2017**, 7, 14-19.

12. Sima, C.; Grigoriu, C.; Toma, O.; Antohe, S. Study of dye-sensitized solar cells based on ZnO photoelectrodes deposited by laser ablation and doctor blade methods. *Thin Solid Films* **2015**, 597, 206-211.

13. Aldeen, T.S.; Mohamed, H.E.A.; Maaza, M. ZnO nanoparticles prepared via a green synthesis approach: Physical properties, photocatalytic and antibacterial activity. *J. Phys. Chem. Solids* **2022**, 160, 110313.

14. Kotresh, M.G.; Patil, M.K.; Inamdar, S.R. Reaction temperature based synthesis of ZnO nanoparticles using co-precipitation method: Detailed structural and optical characterization. *Optik* **2021**, 243, 167506.

15. Vázquez, A.; López, I.A.; Gómez, I. Growth mechanism of one-dimensional zinc sulfide nanostructures through electrophoretic deposition. *J. Mater. Sci.* **2013**, 48, 2701-2704.

16. Adedokun, O.; Bello, I.T.; Sanusi, Y.K.; Awodugba, A.O. Effect of precipitating agents on the performance of ZnO nanoparticles based photo-anodes in dye-sensitized solar cells. *Surf. Interfaces* **2020**, 21, 100656-100663.

17. Samaneh, G.; Mohammad, A.; Mohammad, I. Simple mass production of zinc oxide nanostructures via low-temperature hydrothermal synthesis. *Mater. Res. Express* **2017**, 4, 035010.

18. Xu, L.; Hu, Y.-L.; Pelligra, C.; Chen, C.-H.; Jin, L.; Huang, H.; Sithambaram, S.; Aindow, M.; Joesten, R.; Suib, S. L. ZnO with different morphologies synthesized by solvothermal methods for enhanced photocatalytic activity. *Chem. Mater.* **2009**, 21, 2875-2885.

19. Law, M.; Greene, L.E.; Johnson, J.C.; Saykally, R.; Yang, P. Nanowire dye-sensitized solar cells. *Nat. Mater.* **2005**, 4, 455.
20. Law, M.; Greene, L.E.; Radenovic, A.; Kuykendall, T.; Liphardt, J.; Yang, P. ZnO−Al$_2$O$_3$ and ZnO−TiO$_2$ core-shell nanowire dye-sensitized solar cells. *J. Phys. Chem.* B **2006**, 110, 22652-22663.
21. Suh, D.I.; Lee, S.Y.; Kim, T.H.; Chun, J.M.; Suh, E.K.; Yang, O.B.; Lee, S.K. The fabrication and characterization of dye-sensitized solar cells with a branched structure of ZnO nanowires. *Chem. Phys. Lett.* **2007**, 442, 348-353.
22. Baxter, J.B.; Aydil, E.S. Dye-sensitized solar cells based on semiconductor morphologies with ZnO nanowires. *Sol. Energy Mater. Sol. Cells* **2006**, 90, 607-622.
23. Jiang, C.Y.; Sun, X.W.; Lo, G.Q.; Kwong, D.L.; Wang, J.X. Improved dye-sensitized solar cells with a ZnO-nanoflower photoanode. *Appl. Phys. Lett.* **2007**, 90, 263501.
24. Li, J.; Sang, X.; Chen, W.; Qin, C.; Wang, S.; Su, Z.; Wang, E. The application of ZnO nanoparticles containing polyoxometalates in dye-sensitized solar cells. *Eur. J. Inorg. Chem.* **2013**, 2013, 1951-1959.
25. Memarian, N.; Concina, I.; Braga, A.; Rozati, S.M., Vomiero, A.; Sberveglieri, G. Hierarchically assembled ZnO nanocrystallites for high-efficiency dye-sensitized solar cells. *Angew. Chem. Int. Ed. Engl.* **2011**, 50, 12321-12325.
26. Al-Sehemi, A.G.; Allami, S.A.S.; Kalam, A. Design and synthesis of organic dyes with various donor groups: promising dyes for dye-sensitized solar cells. *Bull. Mater. Sci.* **2020**, 43, 224-233.
27. Dinesh, V.P.; Biji, P.; Ashok, A.; Dhara, S.K.; Kamaruddin, M.; Tyagi, A.K., Raj, B. Plasmon-mediated highly enhanced photocatalytic degradation of industrial textile effluent dyes using hybrid ZnO@Ag core-shell nanorods. *RSC Adv.* **2014**, 4, 58930-58940.
28. Yoshida, T.; Terada, K.; Schlettwein, D.; Oekermann, T.; Sugiura, T.; Minoura, H. Electrochemical self-assembly of nanoporous ZnO/Eosin Y thin films and their sensitized photoelectrochemical performance. *Adv. Mater.* **2000**, 12, 1214-1217.
29. Kutty, R.G.; Seery, M.K.; Pillai, S.C. A highly efficient Ag-ZnO photocatalyst: Synthesis, properties, and mechanism. *J. Phys. Chem.* C **2008**, 112, 13563-13570**.**
30. Umar, A.; Hahn, Y.B. Aligned hexagonal coaxial-shaped ZnO nanocolumns on steel alloy by thermal evaporation. *Appl. Phys. Lett.* **2006**, 88, 173120.
31. Wu, J.J.; Liu, S.C. Catalyst-free growth and characterization of ZnO nanorods. *J. Phys. Chem.* B **2002**, 106, 9546-9551.
32. Yousefi, R.; Jamali-Sheini, F.; Cheraghizade, M.N; Khosravi-Gandomani, S.; Sáaedi, A.; Huang, N.M.; Basirun, W.J.; Azarang, M. Enhanced visible-light photocatalytic activity of strontium-doped zinc oxide nanoparticles. *Mater. Sci. Semicond. Process.* **2015**, 32, 152-159.
33. Subalakshmi, K.; Senthilselvan, J.; Kumar, K.A.; Kumar, S.A.; Pandurangan, A. Solvothermal synthesis of hexagonal pyramidal and bifrustum shaped ZnO nanocrystals: Natural betacyanin dye and organic Eosin Y dye-sensitized DSSC efficiency, electron transport, recombination dynamics, and solar photodegradation investigations. *J. Mater. Sci. Mater. Electron.* **2017**, 28, 15565-15595.
34. Babikier, M.; Wang, D.; Wang, J.; Li, Q.; Sun, J.; Yan, Y.; Jiao, S. Cu-doped ZnO nanorod arrays: the effects of copper precursor and concentration. *Nanoscale Res. Lett.* **2014**, 9, 199.
35. Ungula, J.; Dejene, B.F.; Swart, H.C. Effect of annealing on the structural, morphological and optical properties of Ga-doped ZnO nanoparticles by reflux precipitation method. *Results Phys.* **2017**, 7, 2022-2027.
36. Dubey, R.S.; Jadkar, S.R.; Bhorde, A.B. Synthesis, and characterization of various doped TiO$_2$ nanocrystals for dye-sensitized solar cells. *ACS Omega* **2021**, 6, 3470-3482.
37. Keis, K.; Magnusson, E.; Lindström, H.; Lindquist, S.; Hagfeldt, A. A 5% efficient photoelectrochemical solar cell based on nanostructured ZnO electrodes. *Sol. Energy Mater. Sol. Cells* **2002**, 73, 51-58.

38. Chang, W.; Lee, C.; Yu, W.; Lin, C. Optimization of dye adsorption time and film thickness for efficient ZnO dye-sensitized solar cells with high at-rest stability. *Nanoscale Res. Lett.* **2012**, 7, 688.
39. Xu, C.K.; Shin, P.; Cao, L.L.; Gao, D. Preferential growth of long ZnO nanowire array and its application in dye-sensitized solar cells. *J. Phys. Chem.* C **2010**, 114, 125-129.
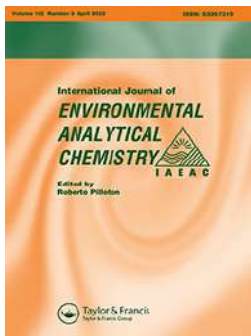
Fast removal of methylene blue by modified sorel cement using manganese(VII) as an additive: kinetics, thermodynamics, and equilibrium studies

Majed M. Alghamdi, Eman Y. Alhomod, Nasser S. Awwad, Abubakr M. Idris & Adel A. El-Zahhar

Published online: 05 Apr 2022.

Submit your article to this journal

View related articles

View Crossmark data

Taylor & Francis
Taylor & Francis Group

Check for updates

Fast removal of methylene blue by modified sorel cement using manganese(VII) as an additive: kinetics, thermodynamics, and equilibrium studies

Majed M. Alghamdi, Eman Y. Alhomod, Nasser S. Awwad, Abubakr M. Idris and Adel A. El-Zahhar

Department of Chemistry, College of Science, King Khalid University, Abha, Saudi Arabia

ABSTRACT

In this study, Sorel cement (SC) was doped with Mn^{7+} to develop a cost-effective adsorbent that can quickly remove methylene blue (MB) dye from aqueous solutions. The characteristics of the prepared adsorbents were examined using X-ray diffraction, atomic force microscopy, scanning electron microscopy, Fourier-transform infrared spectroscopy, and thermogravimetric analysis. The examinations confirmed the formation of SC and the successful doping of manganese. Batch adsorption experiments were also performed to investigate and to optimise the operational parameters such as Mn^{7+} ion concentration, contact time, dosage, MB concentration, pH, and temperature. The modified adsorbent revealed a significant adsorption improvement when compared with pure SC. A small addition of 0.01 g of Mn^{7+} exhibited 100% removal efficiency up to a dye concentration of about 100 mg/L, whereas about 64% removal efficiency was obtained with pure SC using 36.5 mg/L of the MB solution. Furthermore, the modified adsorbent revealed rapid equilibrium times of around 1 and 3 minutes using 36.5 and 100 mg/L of the MB solution, respectively. An experimental adsorption capacity of up to 246 mg/g was obtained, and the equilibrium data were consistent with the Freundlich isotherm and were well fitted with a pseudo-second-order kinetic model. The thermodynamic values indicated a physisorption, exothermic ($\Delta H° = -7.7$ kJ/mol), and spontaneous ($\Delta G° = -9.4$ kJ/mol) nature of the adsorption process with enhanced feasibility and comparable regeneration efficiency for up to five cycles. Therefore, the results indicate that the modified sorbent can possibly be utilised as a potential fast method for the removal of MB dye from wastewater.

1. Introduction

The increased use of dyes in industries is alarming because of their toxicity and tendency towards bioaccumulation in living beings, their wide range of applications, and the high rate at which they can be discharged [1]. For example, dye pollutants have been found in wastewater in various industries, primarily those producing textiles, cosmetics, papers, and carpets. The hazards related to dye pollution can be primarily attributed to the

chemical origin or aromatic composition of dyes, which makes them non-biodegradable, causing various health and environmental problems [2]. Moreover, the chemical origins and stability of dyes become even more potentially hazardous with the use of inefficient wastewater treatment processes [3]. This results in substantial health concerns associated with residual dye content [4], and meeting the dye requirements related to treated and discharged effluents remains a challenge [5].

Azo dyes deserve serious attention because they are the most marketed and carcinogenic. In addition, the by-products caused by the breakdown of toxic amines contained in these dyes have other potentially serious health effects [6,7]. Primarily, methylene blue (MB) is an inexpensive dye that has extensive applications in dying procedures but has a harmful impact on human health [8]. In terms of environmental impacts, ecotoxicological studies have revealed that dyes substantially inhibit respiration in wastewater bacteria [9] and can affect the reoxygenation process and sunlight penetration, thus disturbing the biological activity of aquatic life and the process of algae photosynthesis [10].

In response to these concerns, various approaches have been designed to remove organic compounds from polluted water and sewage. These include filtration, precipitation, ozonation, adsorption, catalytic degradation, ion exchange, reverse osmosis, and advanced oxidation processes [11–15]. Adsorption, which is only one possible water treatment procedure, has established itself as one of the most highly efficient approaches to treat and eliminate organic contaminants from wastewater. As such, the search for economical adsorbents with active binding capabilities has increased in the past few years [16]. Locally accessible materials such as natural materials and agricultural or industrial wastes can be exploited as low-cost adsorbents. Some common adsorbents generated from agriculture and industrial waste materials include activated carbon, chitosan, aluminium waste, and insecticide cans [11,17–20]; however, their use may still be limited because of the high costs of generation and regeneration [21]. Likewise, magnesium oxychloride, known as Sorel cement (SC), has also been used as an industrial waste adsorbent. It can be formed in different phases, depending on the molar ratio of $MgO/MgCl_2$. However, phases 3 and 5 are the only stable phases at temperatures of up to 100°C. The benefits of using SC include ease of preparation, mechanical properties, non-toxicity, and low-cost [22]. In addition to its major commercial uses, SC has also been used to remove the Cr^{6+} [23], U^{6+} ions [24], and to eliminate some reactive textile wastewater dyes [21,25]. El-Gamal et al. investigated the removal of the methyl orange and bromophenol blue dyes from aqueous solution using nanoparticles of SC and obtained maximum adsorption capacities of 23.21 and 4.88 mg/g, respectively [21]. SC was also effectively used for the removal of RY-145, RR-194, and RB-B dyes from textile effluents [25]. Furthermore, the enhancement of SC adsorption capacity by varied SC compositions using $FeCl_3$ was also reported by Bhaskaran et al. for the removal of Reactive Black 5 dye [26].

Given the beneficial properties of SC and its possible removal performance enhancement by its varied compositions, the aim of this study was to modify SC with Mn^{7+} adoption and to investigate its adsorption performance, isotherms, kinetics, and thermodynamic parameters in removing MB dye from aqueous solutions. In fact, modified SC using Mn^{7+} as an additive has not been studied before and could provide a potential alternative to conventional dye treatment. Mn^{7+} was proposed to

promote oxygen mobility between surface-adsorbed and lattice oxygen atoms and to provide sites that could lead to a more efficient and high level of scavenging for dyes [27].

2. Materials and methods

2.1. Materials

MgO and $MgCl_2$ were purchased from Sigma-Aldrich, US, which also provided methylene blue, $KMnO_4$, ethanol, NaCl, and NaOH. All chemicals used in this research were of analytical reagent grade. Additionally, changes in pH were regulated using 0.1 M NaOH and 0.1 M HCl solutions.

2.2. Preparation of adsorbent

Sorel cement (Phase 3) was synthesised using MgO and $MgCl_2$ [23]. In 8 ml of an aqueous 1.78 M $MgCl_2$ solution, MgO (2.4 g) was dissolved at 75°C. Different weights of Mn^{7+} salt (0.01, 0.10, 0.50, 1.00, 2.40 g) were added, and the mixture was agitated for 10 min. A precipitate was extracted by centrifugation and thoroughly washed with ethanol. The solid material was treated at 75°C to preserve phase 3 of SC and deposited in a desiccator for 4 h. Afterwards, the dry solid was ground and sieved to a 35-mesh particle size.

2.3. Characterisation

X-ray diffraction (XRD) was performed using a Shimadzu X-ray diffractometer and CuK α radiation. The XRD patterns were registered at a 10° to 80° diffraction angle with a 0.03° step and 4 sec of integration time per step. A KBr system with a NICOLET 6700 FT-IR Scientific was employed to acquire the IR spectra of the sorbent materials between 4000 and 400 cm^{-1}. Using a Philips XL 30, we conducted scanning electron microscopy (SEM) to take micrographs of the sorbent materials. In addition, atomic force microscopy (AFM) (Solver Next Russia) was used to study the material's surface. A thermal stability analysis of the prepared materials was conducted using Shimadzu TGA 51 thermal analysers with a temperature range of 25–600°C and a 15°C/min heating rate under N_2 with a flow rate of 20 cm^3/min.

2.4. Batch adsorption experiments

Batch experiments were conducted using 250 ml stopped bottles, containing 0.1 g of Mn^{7+}/SC at a pH of 5.5 with 100 ml of a 36.5 mg/L MB solution, except when examining the pH, dosage, and initial dye concentration effects. The mixture was shaken at 25 ± 0.1°C (except when examining the effect of temperature) by a mechanical water shaker thermostat. The solid product was isolated from the solution, and the dyes' concentrations were determined in the solution using a UV-visible spectrophotometer (Shimadzu, 1800 model, Japan) at a wavelength of 664 nm. The parameters influencing the sorption process were also studied by changing one parameter at a time while

keeping all other parameters constant. The effects of parameters such as shaking time, pH, Mn^{7+} ion concentration, dosage, temperature, agitation speed, and the concentration of the dye were investigated.

The adsorption capacity and the amount of MB adsorbed at time t were calculated using Equations 1 and 2, respectively [28]:

$$q_e = \frac{(C_0 - C_e)V}{m} \tag{1}$$

$$q_t = \frac{(C_0 - C_t)V}{m} \tag{2}$$

where C_0, C_e, and C_t (mg/L) are the initial, equilibrium, and after time concentrations of MB, respectively. V (L) and m (g) are the solution volume and the amount of the adsorbent, respectively. The removal uptake percentage was calculated using Equation 3:

$$Removal\% = \frac{C_0 - C_e}{C_0} \times 100 \tag{3}$$

3. Results and discussion

3.1. Materials characterisation

3.1.1. X-ray diffraction (XRD) measurements

The prepared sorbents were characterised using XRD in a region of $2\theta = 10–80°$, as shown in Figure 1. The XRD results revealed little changes in the diffraction patterns of SC after the addition of the Mn^{7+}. In the case of pure SC, several peaks appeared at $2\theta = 18.6, 32.8, 38.01, 50.8, 58.6, 62.07, 68.3$, and 72.03. These peaks agree with
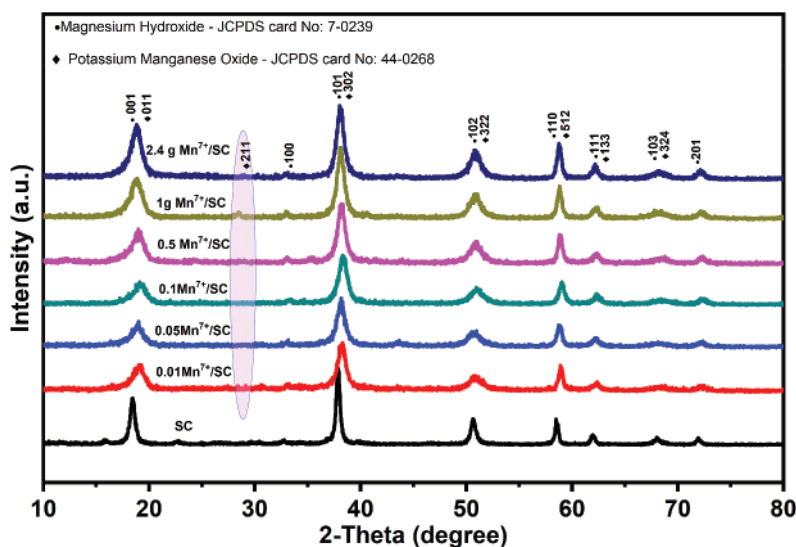
Figure 1. X-ray diffraction of the synthesised SC and Mn^{7+}/SC.

the JCPDS card # 7–0239 for SC and can be attributed to the following respective planes (001), (100), (101), (102), (110), (111), (103), and (201). Also, the JCPDS card for KMnO$_4$ (# 44–0268) was examined for peaks that could be related to the addition of Mn^{7+}. Peaks with sharp patterns were observed, indicating that the prepared SC is a crystalline material. Although small shifts towards higher 2θ took place, these results simply confirmed that SC is the only dominant materials; however, a small new peak was detected at 2θ = 27.7 for the Mn^{7+}/SC material, which corresponds to the (211) plane. This could also suggest a decrease in the crystallinity of the SC, which could be an important factor in the improved performance of Mn^{7+}/SC in removing MB. Moreover, the crystallite sizes estimated from the peak at 2θ = 38 were of around 17 nm and 8 nm for SC and Mn^{7+}/SC, respectively. The sizes were determined using Scherrer's equation with the following formula [29]:

$$D_c = \frac{K\lambda}{\beta \, cos\theta} \tag{4}$$

where D$_c$ (nm), λ (0.154056 nm), and β are the crystallite size, the wavelength, and the full width at half maximum (FWHM), respectively; K is the so-called shape factor = 0.89, and θ is the diffraction angle.

3.1.2. Scanning electron microscopy (SEM) measurements

As shown in the scanning electron micrograph images in Figure 2a, we can see a surface with a needle-like crystalline morphology appearing at a size of 0.5 μm [30]. The micrograph also showed an analysis of the materials after the sorption experiments, which revealed differences in the structure of the surface. After sorption, there were large numbers of floccules and spots due to the adsorption of MB onto the surface of the Mn^{7+}/SC, leading in turn to a rougher appearance. This heterogeneous and rough surface was an effect of MB binding to the nanowires on the surface of the material.

3.1.3. Atomic force microscope (AFM) measurements

The surface microstructure of Mn^{7+}/SC was also studied using atomic force microscopy (AFM). The results are shown in both 2D and 3D images in Figure 2b. The images indicate a smooth surface with nano-size materials distributed across the surface in homogeneous spherical shapes. The measured values for the films' grain size and roughness were 19.7 nm and 30.9, respectively. These results provide evidence of the presence of Mn^{7+} in the form of nanostructure materials being distributed across its surface. Figure 2b also shows the AFM images of Mn^{7+}/SC after MB adsorption. The images reveal an increase in the grain size and roughness (to 34.29 nm and 36.6 nm, respectively), which could be ascribed to the adsorption of dyes onto the surface of the sorbent material.

3.1.4. Fourier transform infrared (FTIR) measurements

The FT-IR spectra of the prepared materials along with MB dye are shown in Figure 3a. There were sharp absorption peaks at around 3694 cm^{-1}, which could be due to the stretching vibrations of Mg–OH [31]. The medium peaks in the range of 1420–1536 cm^{-1} could be attributed to the bending vibrations of OH and the
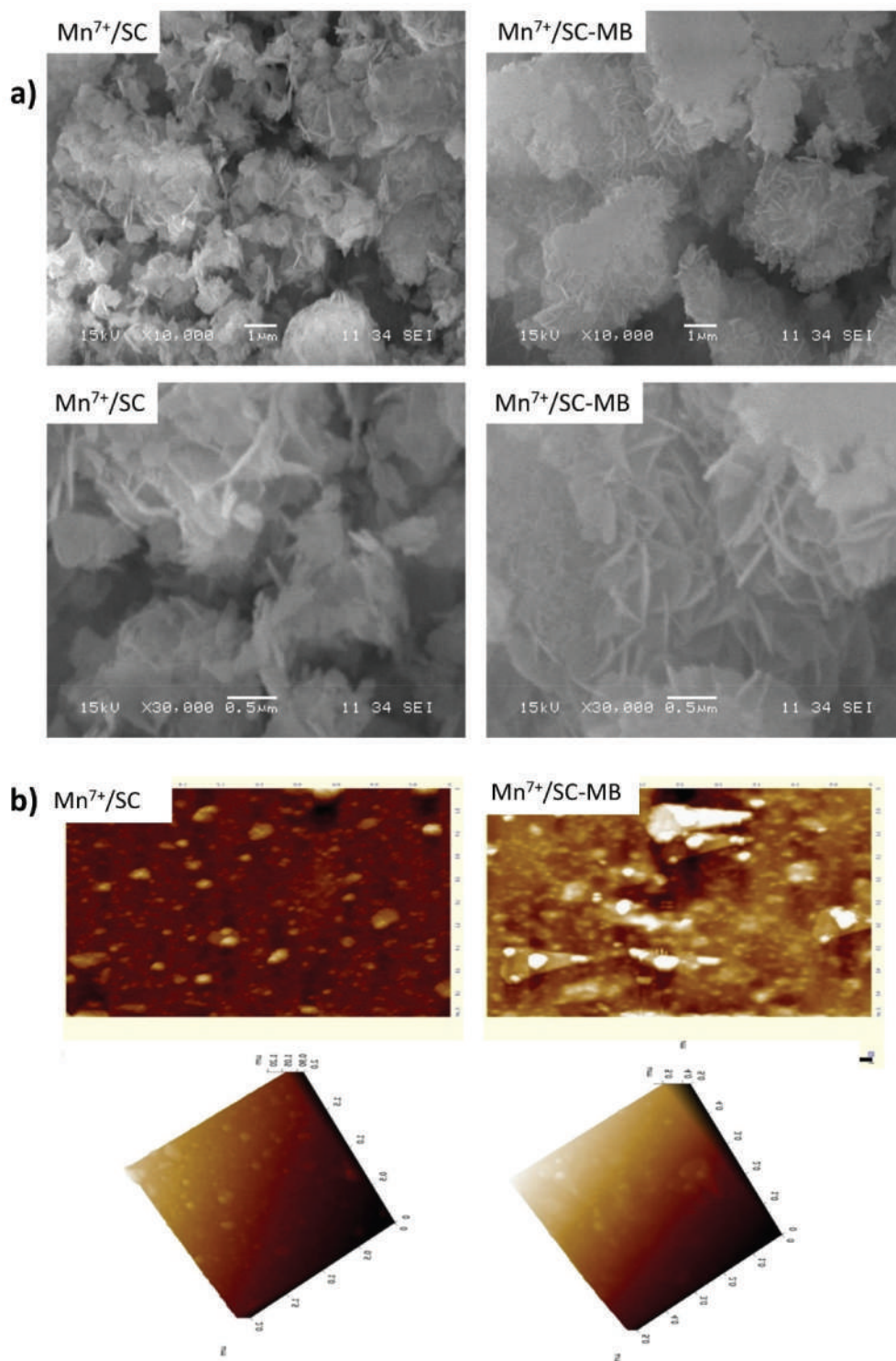
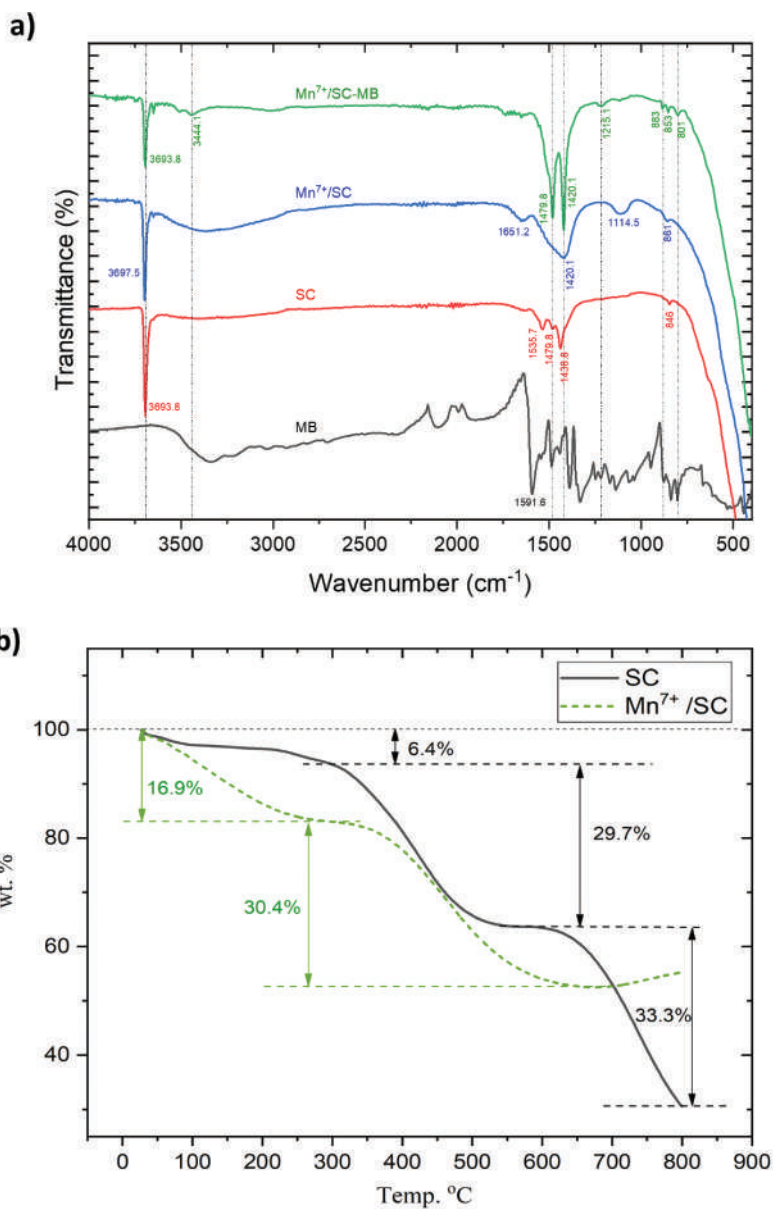**Figure 2. (a)** SEM micrographs for Mn^{7+}(0.01)/SC and Mn^{7+}/SC-MB at different magnifications; and **(b)** AFM images of the same materials.

Figure 3. (a) Infrared spectra of the synthesised $Mn^{7+}(0.01)/SC$ and $Mn^{7+}/SC-MB$; and **(b)** Thermogravimetric analyses of the synthesised SC and $Mn^{7+}(0.01)/SC$.

stretching vibrations of Mg–O in $MgCl_2.8H_2O$ [32]. The peak at 845 cm^{-1} represents the stretching vibrations of the Mg–O cubic structure [32]. Despite the similarity of the spectra of the prepared materials, Mn^{7+}/SC showed a broad peak at 1420 cm^{-1} along with a new weak band at 1114 cm^{-1}, which was assigned to the vibration mode of Mn–OH [33,34]. The band at 1651 cm^{-1} was assigned to the bending vibrations of H_2O. Moreover, the spectrum of Mn^{7+}/SC after the dye removal

experiments revealed some new peaks that can be related to MB dye, such as the peaks at 801 and 883 cm^{-1}, which arose from the aromatic peaks of MB. These results suggest the successful adoption of Mn^{7+} and adsorption of MB on the sorbent material surface.

3.1.5. Thermogravimetric analysis (TGA) measurements

The thermal stability of the prepared materials was also investigated. The TGA results for pure SC (Figure 3b) revealed two major stages of decomposition. At the beginning of the heating process (up to 350°C), dehydration caused a smaller degree of weight loss at about 6.4%. Rapid weight loss began at temperatures of up to 500°C, reaching about 29.7%. This latter number is very close to theoretical weight loss of Phase 3 (34.8%), which is related to the loss of eight water molecules. After the complete loss of water molecules, the material decomposed into MgO due to a loss of structural water and HCl, as observed at temperatures higher than 600°C. By comparison, the TGA result for Mn^{7+}/SC composite demonstrated a similar thermal behaviour with two major stages of decomposition. However, accelerated decompositions at lower temperatures were observed. The results revealed early weight loss of about 16.9% for the Mn^{7+}/SC composites, which might indicate weaker crystalline water tightness within the Mn^{7+}/SC composites. Second stage decomposition of the Mn^{7+}/SC composites also began at lower temperatures around 350°C, suggesting that the chemical structure of SC may have been changed with the addition of Mn^{7+}.

3.2. Methylene blue (MB) dye adsorption

3.2.1. Effect of shaking time

We investigated the effect of shaking time on the removal of MB dye in a time range of 1–60 minutes. As shown in Figure 4a, the use of Mn^{7+}/SC resulted in a 100% removal efficiency of MB with an equilibrium time of about one minute. In contrast, only 64% MB removal efficiency was reached for pure SC, and a plateau was attained after three minutes of equilibrium time. We therefore used a designated equilibrium time of three minutes in the subsequent experiments. Moreover, Figure 4b illustrates the uptake of MB dye from the aqueous solution. The uptake values for the two systems were around 36.5 and 23.5 mg/g for the Mn^{7+}/SC and pure SC, respectively. From the data obtained, it is clear that the modified SC that includes Mn^{7+} promises to be much more efficient in removing MB than pure SC. The high efficiency of Mn^{7+}/SC could be attributed to its Mn^{7+} newly introduced active sites. However, the results also revealed that the Mn^{7+} weight had no significant effect on the removal of MB dye in a range of 0.01–2.40 g at the specified experimental conditions. The similar values of adsorption capacity with the different Mn^{7+} ions amount might be related to the low concentration of MB dye.

3.2.2. Effect of pH on the sorption process

The results shown in Figure 5a reveal that pH significantly influenced the effectiveness of the adsorbent. Adsorption capacity was low when the pH values were very acidic and higher when using higher pH. This can be attributed to the decreased
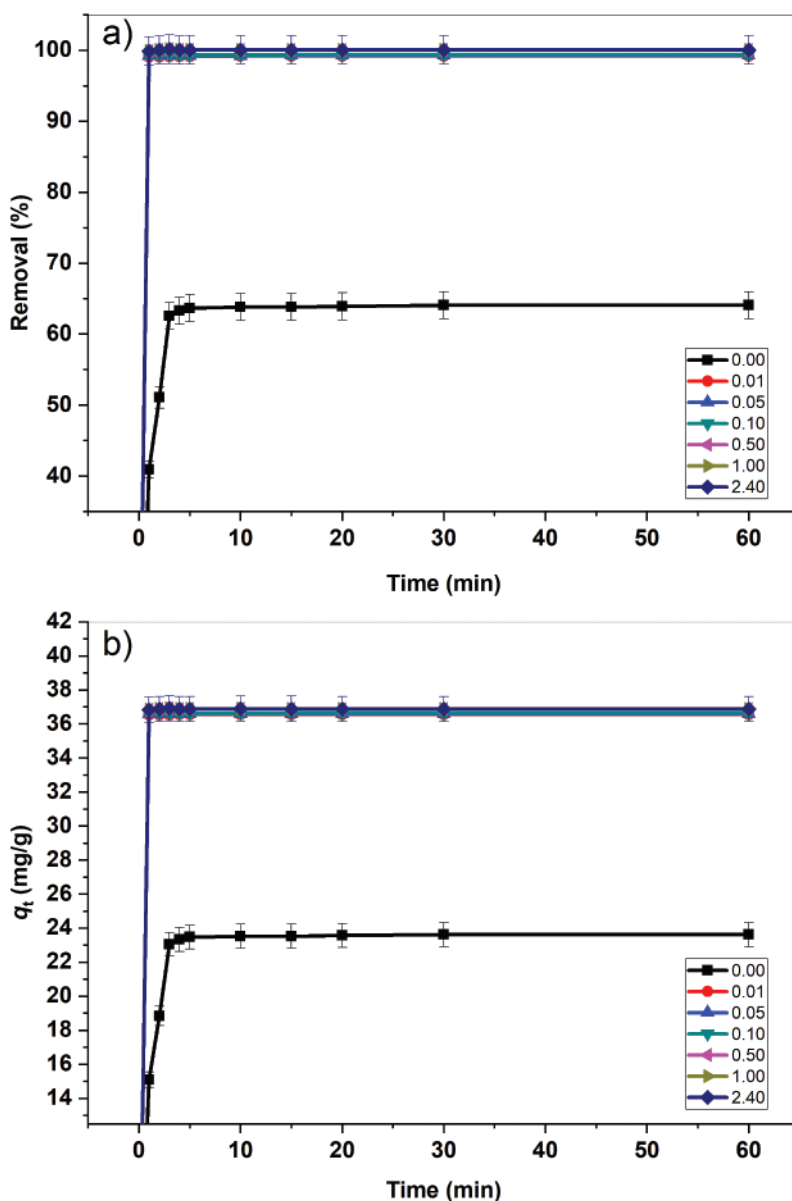
Figure 4. Effect of shaking time on **a)** removal efficiency and **b)** adsorption of MB from aqueous solutions using 0.1 g dosage of Mn^{7+}/SC, pH 5.5, 25°C, 50 rpm and with different weights of Mn^{7+}.

electrostatic forces of interaction between the surface of the sorbent and the cationic MB [35]. At lower pH values, the surface of the adsorbent became positively charged, inhibiting MB adsorption due to the electrostatic repulsion between the adsorbent and the adsorbate (Figure 5b). As pH increased, the surface of the adsorbent became less positively charged, enhancing the adsorption of the positively charged adsorbate as a result of the electrostatic force of attraction [36]. Furthermore, at low pH levels, H^+ ions may also compete for active sites with the MB dye, resulting in an increase in
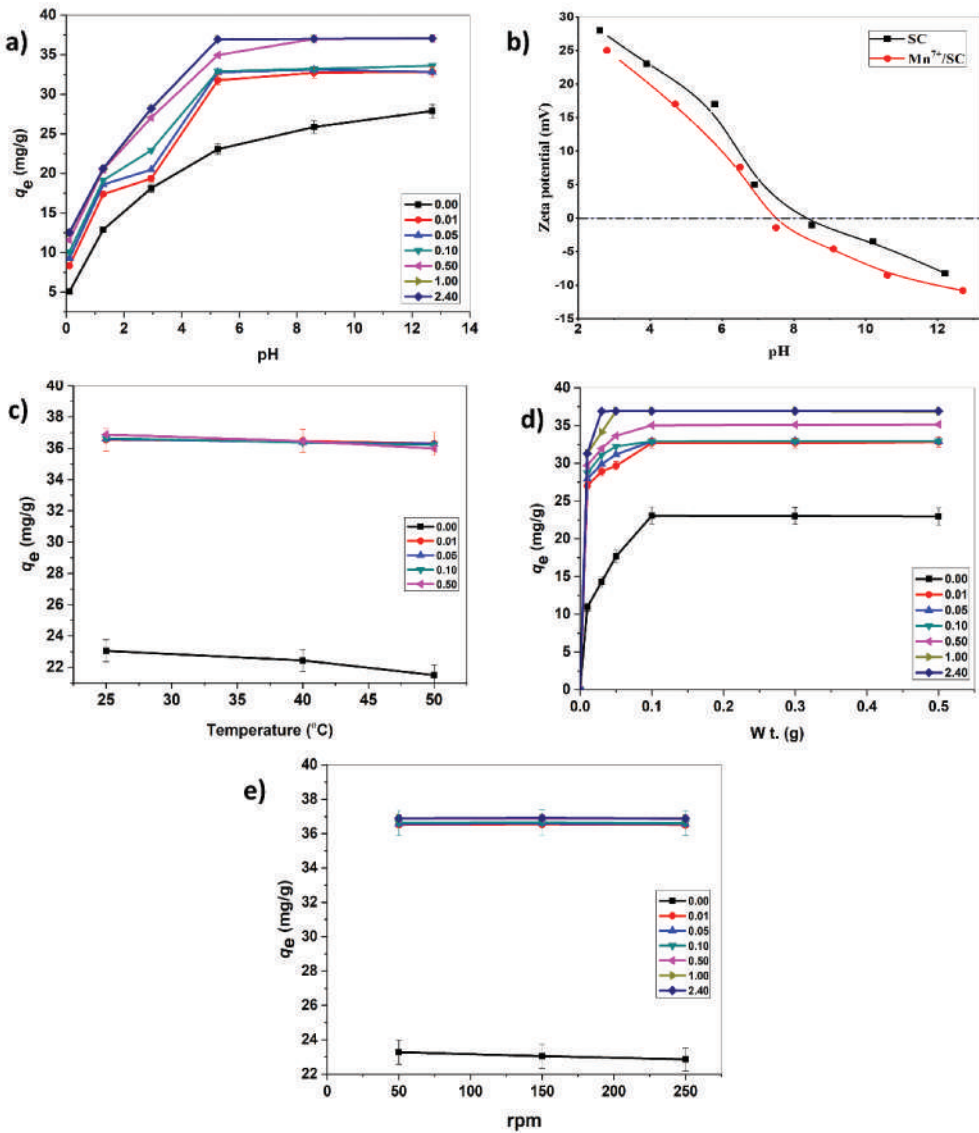
Figure 5. (a) Effects of pH, **(b)** Zeta potential (0.01 Mn^{7+}/SC and pure SC), **(c)** temperature **(d)** Mn^{7+}/SC dosage, and **e)** agitation speed (rpm) on the adsorption of 36.5 mg/L MB from an aqueous solution using Mn^{7+}/SC with different weights of Mn^{7+} as indicated.

the adsorption capacity as pH increased. In the case of Mn^{7+}/SC, sharper increases of the dye uptakes were observed as pH increased up to 5.5 with pronounce effects of the Mn^{7+} addition and weight comparing to pure SC. As illustrated in Figure 5b, this can be attributed to the clear effect of the addition of the Mn^{7+} on the surface charge, making the surface less positively charged compared to SC. At pH>5.5, no further significant change was observed and therefore a pH of 5.5 was chosen for the subsequent experiments.

3.2.3. Effect of agitation speed

Figure 5e illustrates how the agitation speed affected MB uptake. It was evident that the uptake slightly increased when agitation speed decreased. The uptake was the lowest at 250 rpm, followed by 150 and 50 rpm. Conversely, for Mn^{7+}/SC, the uptake was almost constant. This could be the result of an increase in resistance to mass transfer surrounding the sorbent particles as the agitation rate increased, thus maintaining the sorption of the dye molecules.

3.2.4. Effect of temperature

The impact of temperature on the removal efficiency of Mn^{7+}/SC was also studied at temperatures in a range of 25 – 50°C. It was noted that the uptake of MB dye decreased as the temperature increased (Figure 5c). This decrease indicated an exothermic nature of the sorption process. This behaviour in sorption uptake may be due to the weakening of adsorptive forces between the MB dye molecules and the active sites of the Mn^{7+}/SC and also between adjacent molecules during the adsorbed phase.

3.2.5. Effect of dosage

The results with respect to the effect of sorbent dosage on the removal of MB dye from an aqueous solution are shown in Figure 5d. The experiments were carried out in a range of 0.01–0.5 g/100 ml of a 36.5 mg/L MB dye solution at 25 ± 0.1°C. According to the results, as sorbent dosage increased from 0.01 to 0.1 g, adsorption of MB dye increased, while adsorption remained constant between 0.1–0.5 g. This can be attributed to greater amounts of sorbent having more surface area and therefore more available surface-active sites. Notably, the effects of the Mn^{7+} addition and weight were obvious comparing to pure SC. This might be due to the number of the available Mn^{7+} active sites. The fact that MB dye uptake was constant between 0.1–0.5 g may be related to either the complete adsorption of MB or to the possible aggregation of sorbent particles at elevated dosages, particularly when using pure SC. Such aggregation would cause a reduction in the total surface area and thus result in fewer active sites for material sorption.

3.2.6. Effect of initial MB dye concentration

The effect of the initial concentrations of MB dye on sorption was investigated by varying the initial dye concentration in a range of 3–320 mg/L. It was found that the adsorption uptake of the MB dye increased as the initial MB dye concentrations increased (Figure 6a). This is as anticipated because a larger number of MB dye molecules were present and could therefore be adsorbed onto the composite at higher concentrations. This increase could also be due to an increase in the driving force of the concentration gradient. These results, which are presented in Figure 6a, clearly establish a remarkable improvement in using the Mn^{7+}/SC composite compared with pure SC. Moreover, Figure 6b illustrates the removal efficiency of MB. In the case of pure SC, the removal percentage decreased sharply as the initial concentration of MB dye increased, whereas 100% removal efficiency was sustained for the Mn^{7+}/SC up to a dye concentration of 100 mg/L, i.e. the results revealed about a 50% enhancement of the removal efficiency of MB with a 100 mg/L concentration compared with pure SC. This could be attributed to the existence of new active sites that are able to accommodate more dye molecules at lower concentrations before they become saturated at higher concentrations.
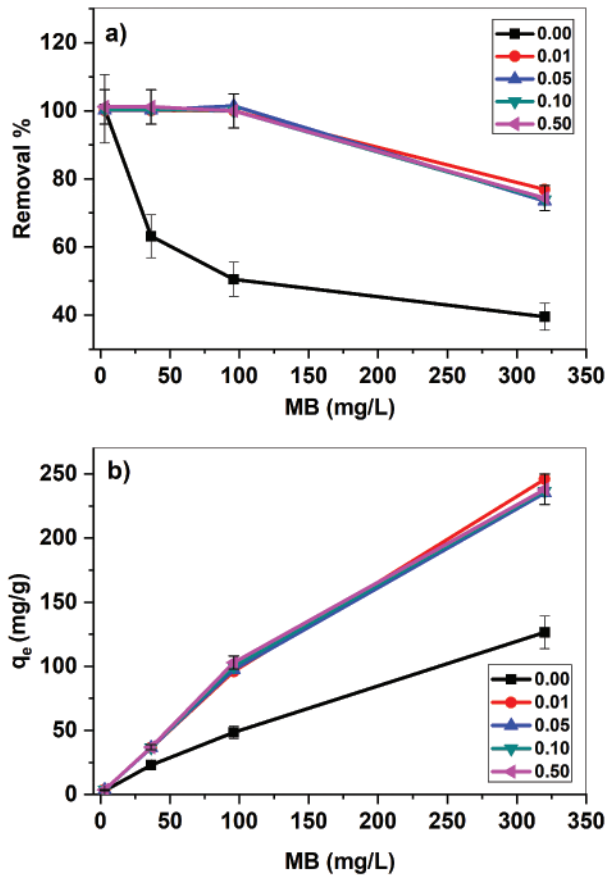
Figure 6. Effect of initial MB dye concentration on **(a)** adsorption capacity and **(b)** removal efficiency of Mn^{7+}/SC using 0.1 g dosage of Mn^{7+}/SC, pH 5.5, 25°C, 50 rpm and with different weights of Mn^{7+}.

3.2.7. Comparison with other sorbents used to remove MB dye

In addition to the Mn^{7+}/SC enhanced MB dye adsorption performance when compared to pure SC, Mn^{7+}/SC also showed a significantly greater and faster adsorption performance than several other materials as illustrated in Table 1. This suggests its potential viability as an MB removal candidate substance.

3.3. Adsorption studies

3.3.1. Adsorption kinetics

To determine the adsorption mechanism, the amount of MB adsorbed onto the SC and $Mn^{7+}(0.01)/SC$ materials as a function of time was studied. Different kinetic models were applied to determine the reaction mechanisms, namely, pseudo-first- and pseudo-second-order, Elovich, and intra-particle models.

The pseudo-first-order equation was applied as follows [37]:

$$\log(q_e - q_t) = logq_e - \frac{k_1 t}{2.303} \tag{5}$$

Table 1. Comparative adsorption capacity of some selected adsorbent materials for removing MB dye.

Adsorbent	Removal property (Conditions)	Ref.
Fe_3O_4/chitosan/graphene nanocomposite	$q_{e(exp)}$ = 47.53 mg/g (1 g/L, C_0 = 50 mg /L in 23 min)	[42]
Magnetic rice husk ash	$q_{e(max)}$ = 150.5 mg/g	[36]
Magnetic activated alumina (MFMA)	$q_{e(max)}$ = 196.08 mg/g	[43]
Carboxymethyl cellulose/carboxylated graphene oxide	$q_{e(max)}$ = 180.32 mg/g	[44]
Manganese oxide-imprinted mesoporous carbons (MOPC950)	$q_{e(max)}$ = 124.1 mg/g	[45]
$MnFe_2O_4$/GO	$q_{e(max)}$ = 78.1 mg/g	[46]
$NiFe_2O_4$/GO	$q_{e(max)}$ = 42.2 mg/g	[46]
$CoFe_2O_4$/GO	$q_{e(max)}$ = 80.6 mg/g	[46]
Fe-Mn binary oxide nanoparticles	$q_{e(max)}$ = 72.32 mg/g	[35]
Fe-Mn oxides/carbon	$q_{e(max)}$ = 9.37 mg/g	[47]
MnOx impregnated cotton fibres	$q_{e(max)}$ = 46.3 mg/g	[48]
(Na, Al, K)$_{0.03}$Mn$_2$O$_4$)	$q_{e(exp)}$ = 230 mg/g (2 g/L, C_0 = 500 mg/L, in 30 min)	[49]
Manganese oxide nanocorals	$q_{e(exp)}$ = 41.26 mg/g (1.2 g/L, C_0 = 5 mg/L in 20 min)	[50]
$MnFe_2O_4$	$q_{e(max)}$ = 32.67 mg/g	[37]
$MnFe_2O_4$/GO	$q_{e(max)}$ = 89.29 mg/g	[37]
Mn^{7+}(0.01)/SC	$q_{e(exp)}$ = 36.5 mg/g (1 g/L, C_0 = 36.5 mg/L in 1 min)	This work
Mn^{7+}(0.01)/SC	$q_{e(exp)}$ = 100 mg/g (1 g/L, C_0 = 100 mg/L in 3 min)	This work
Mn^{7+}(0.01)/SC	$q_{e(exp)}$ = 246 mg/g (1 g/L, C_0 = 320 mg/L in 3 min)	This work

where q_e and q_t are the dye concentrations in its solid phase at equilibrium and at time t, respectively, and k_1 (min^{-1}) is the model rate constant. The rate constant, k_1, was determined using the plot of log (q_e – q_t) with t, while the value of q_e was determined using the intercept. The resultant kinetic parameters are given in Table 2. As illustrated in Figure 7a, linear fits with low correlation coefficients (R^2) of 0.889 and 0.622 were obtained for Mn^{7+}/SC and pure SC, respectively. Moreover, the value of the calculated adsorption capacity q_e clarified that the kinetic model used did not fit with the experimental results.

Table 2. Kinetic model parameters for the adsorption of MB onto Mn^{7+}(0.01)/SC.

Kinetic Model	SC	Mn^{7+}/SC
Experimental	C_o = 36.5 mg/L C_e = 13 mg/L $q_{e.exp}$ = 23.5 mg/g	C_o = 36.5 mg/L C_e = 0 mg/L $q_{e.exp}$ = 36.5 mg/g
Pseudo-first-order	k_1 = 0.220 min^{-1} q_e = 1.938 mg/g R^2 = 0.622	k_1 = 0.130 min^{-1} q_e = 0.025 mg/g R^2 = 0.889
Pseudo-second-order	k_2 = 0.193 g/mg.min q_e = 23.74 mg/g R^2 = 1.00	k_2 = 19.53 g/mg.min q_e = 36.57 mg/g R^2 = 1.00
Elovich	R^2 = 0.527	R^2 = 0.860
Intra-particle	$k_{id,i}$ = 10.79 mg/g.min$^{0.5}$ C_1 = 4.08 mg/g R^2 = 0.988 $k_{id,ii}$ = 0.067 mg/g.min$^{0.5}$ C_2 = 23.21 mg/g R^2 = 0.526	k_{id} = 0.005 mg/g.min$^{0.5}$ C_1 = 36.54 mg/g R^2 = 0.619

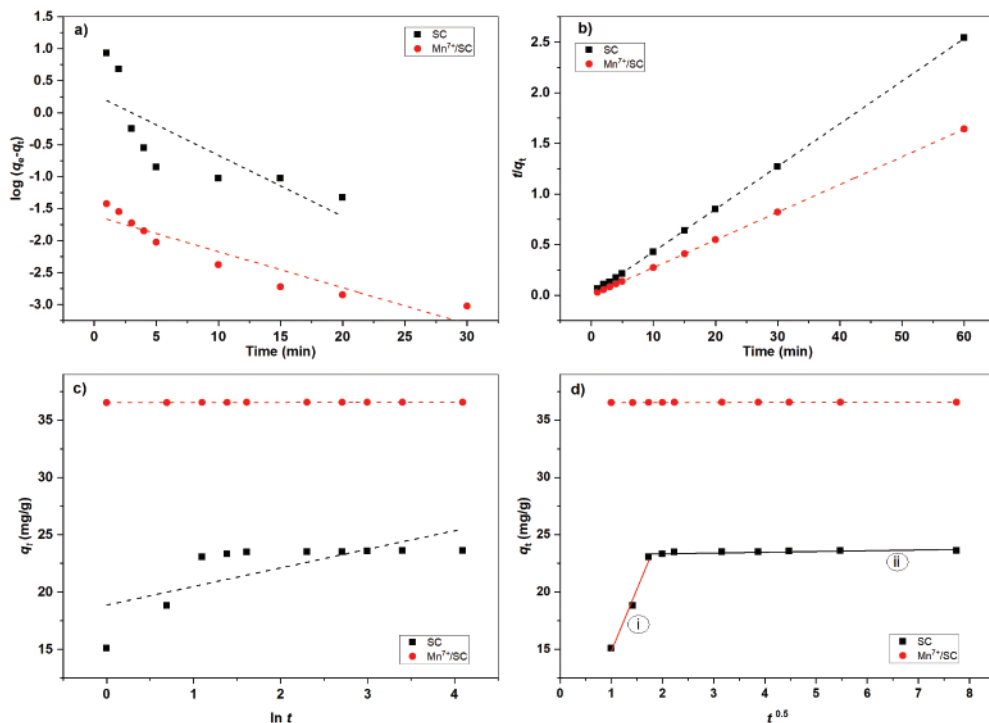**Figure 7.** Kinetic model plots for the adsorption of MB onto the synthesised $Mn^{7+}(0.01)/SC$ sorbents, dosage = 0.1 g, pH = 5.5, and T = 25°C: **(a)** pseudo-first-order plot; **(b)** pseudo-second-order plot; **(c)** Elovich plot; and **d)** intra-particle model plot.

The pseudo-second-order kinetic model is given in Equation 6 [37]:

$$\frac{t}{q_t} = \frac{1}{k_2 q_e^2} + \frac{t}{q_e} \tag{6}$$

where k_2 (g/mg.min) is the model rate constant. The model parameters were determined using the plot of t/q_t with t, as displayed in Figure 7b. The plot revealed linear relationships. The model parameters and R^2 are given in Table 2. The results demonstrated a more linear fit with the pseudo-second-order kinetic model than with the pseudo-first-order. The results also revealed a very close alignment between the calculated q_e (36.57 mg/g) and the experimental value for q_e (37 mg/g). These results together imply that the adsorption of MB can be more accurately explained with a pseudo-second-order kinetic model, which is consistent with many existing studies that report pseudo-second-order kinetics at play in the adsorption of MB dye [17,38,39].

The Elovich kinetic model was also applied, primarily to explain the process of sorption onto energetically heterogeneous solid surfaces. The Elovich model was applied as shown in Equation 7 [38]:

$$q_t = \left(\frac{1}{\beta}\right) \ln(\alpha\beta) + \left(\frac{1}{\beta}\right) \ln(t) \tag{7}$$

where α (mg/g.min) and β (g/mg) are model parameters representing the initial sorption rate and the leaching constant, respectively. The model parameters can be evaluated using the slope and intercept of the linear fit of the q_t vs. $ln(t)$ plot as illustrated in Figure 7c. The α and β values in the MB adsorption process onto Mn^{7+}/SC refer to the effect of adsorbent dosage and the possibility of performing sorption-desorption regeneration cycles; however, the R^2 values demonstrated a poor fit with the Elovich model based on our experimental results.

The intra-particle diffusion model was also used to elucidate the influence of dye that had been transferred from the solution to the solid surface of adsorbent. The adsorption reaction could be influenced by film diffusion, pore diffusion, surface diffusion, and/or adsorption on the pore surface. The Weber and Morris model was applied as described by Equation 8 [38]:

$$q_t = k_{id}t^{0.5} + C \tag{8}$$

where k_{id} is the model constant (mg/g.min$^{0.5}$), and C is a constant (mg/g) correlated with the depth of the boundary layer. The model parameters were obtained from the plot of q_t vs. $t^{1/2}$, as shown in Figure 7d. The results, which are also presented in Table 2, indicated that there was one region of the Mn^{7+}/SC, which did not pass through the origin, suggesting that intraparticle diffusion is not the rate-determining step and participation of the boundary layer effect. This finding is also supported by the SEM images and the rough surface observed in our AFM analysis. On the other hand, we observed two distinct regions in pure SC, indicating multi-stage adsorption processes. It could therefore be concluded that adsorption is controlled by multiple processes. These results demonstrate that the Mn^{7+} does indeed alter the mass transfer mechanisms at play during MB adsorption onto SC. The diffusion parameters ($k_{id,i}$, $k_{id,ii}$) of each portion for SC are also shown in Table 2.

3.3.2. Adsorption isotherm

Some common isotherm models were used to study the adsorption mechanism that controls the adsorption of MB onto the Mn^{7+}/SC. One of these was the Langmuir isotherm model, expressed as [37,40]:

$$\frac{C_e}{q_e} = \frac{1}{q_{max}K_L} + \frac{C_e}{q_{max}} \tag{9}$$

where C_e (mg/L) and q_e (mg/g) are the equilibrium concentration of the dye in the solution and on the solid materials, respectively. The q_{max} and K_L values represent the model parameters related to the maximum adsorbed amount and adsorption energy, respectively. The model parameters were determined from the plot of C_e/q_e vs. C_e, as illustrated in Figure 8. The values of the correlation coefficient (R^2), which are shown in Table 3, were found to be 0.824 and 0.904 for SC and Mn^{7+}/SC, respectively, reflecting a poor correspondence with the Langmuir isotherm model. This result proves that monolayer chemical adsorption onto a homogeneous surface is not the primary adsorption process. The equilibrium parameter, R_L, was also calculated using Equation 10, where C_0 (mg/L) is the highest initial MB concentration:
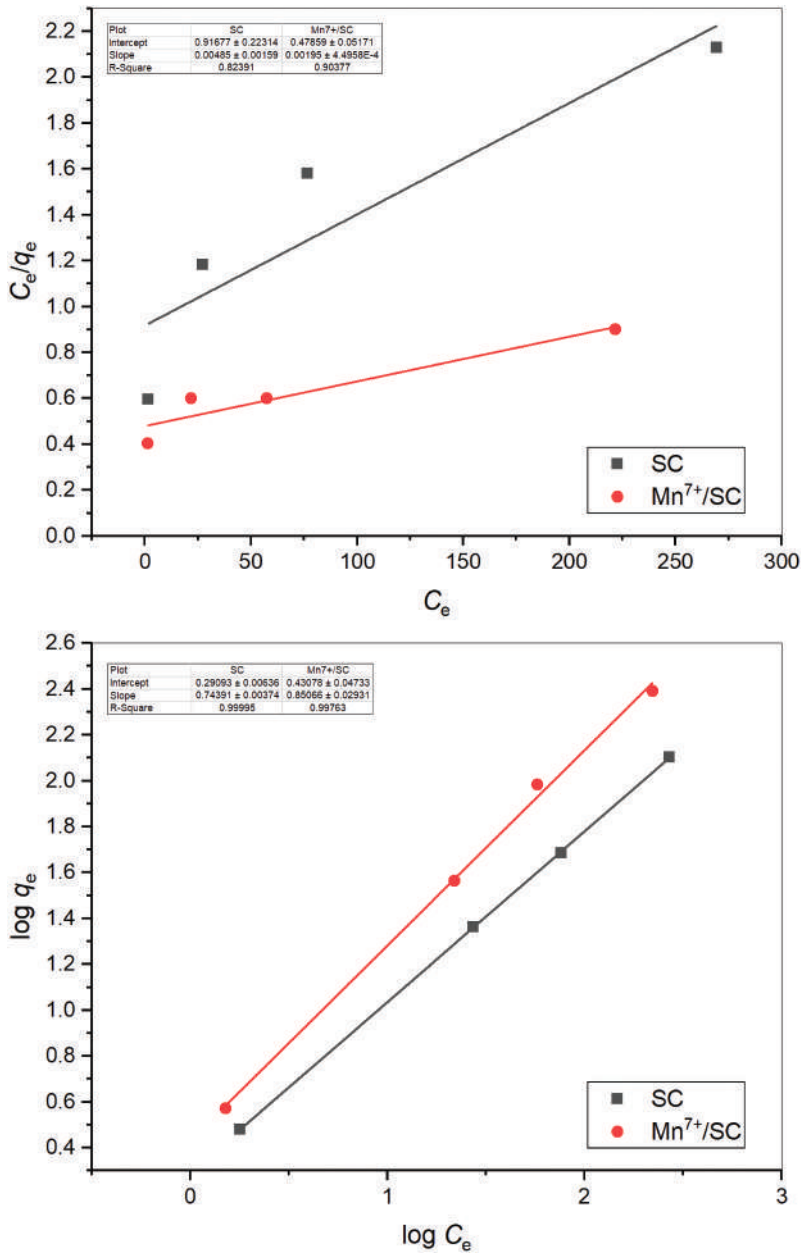
$$R_L = \frac{1}{1 + K_L C_0} \tag{10}$$

Figure 8. (a) The Langmuir isotherm plot and **(b)** the Freundlich plot for the adsorption of MB onto the synthesised SC and $Mn^{7+}(0.01)/SC$ sorbents.

The significance of the R_L value is that it can correlate with the favourability of the isotherm, where $0 < R_L < 1$ is interpreted as favourable, $R_L > 1$ as unfavourable, $R_L = 1$ as linear, and $R_L = 0$ as irreversible [41]. From the data obtained, the values of R_L for SC ($R_L = 0.371$) and Mn^{7+}/SC ($R_L = 0.434$) illustrate favourable processes.

Table 3. Adsorption isotherm model parameters for the adsorption of MB onto $Mn^{7+}(0.01)/SC$.

Model	Parameters	
	Mn^{7+}/SC	SC
Langmuir	q_{max} = 513 mg/g	q_{max} = 206 mg/g
	K_L = 0.004	K_L = 0.005
	R_L = 0.434	R_L = 0.371
	R^2 = 0.904	R^2 = 0.824
Freundlich	n = 1.18	n = 1.34
	K_f = 2.70	K_f = 1.954
	R^2 = 0.998	R^2 = 0.999

The Freundlich isotherm model, which assumes an adsorbent with a heterogeneous surface that is comprised of different adsorption energies, was also used as described in Equation 11 [37]:

$$log q_e = log K_f + \frac{1}{n} \; log C_e \tag{11}$$

where K_f ($mg^{1-1/n}.L^{1/n}/g$) and n are the model constants and indicate adsorption capacity and the degree of favourability of the adsorption process, respectively. The Freundlich model constants were assessed using the linear plot of log q_e vs. log C_e, as shown in Figure 8b, and the results are given in Table 3. The Freundlich plot (with R^2 value > 0.99) fits well with the experimental results, indicating multilayer adsorption of MB dye for both sorbents, which is in agreement with what has been reported in the literature for SC [21].

3.3.3. Adsorption thermodynamics

The Van't Hoff equation (Equation 12) was applied to estimate the thermodynamic parameters corresponding to MB dye sorption onto the prepared sorbents as follows [38]:

$$\ln K_d = \frac{\Delta S°}{R} - \frac{\Delta H°}{RT} \tag{12}$$

where K_d is the distribution coefficient of the solute dyes, $\Delta S°$(J/mol.K) is the entropy change, R (8.314 J/mol.K) is the ideal gas constant, and T (K) is the absolute temperature. The values for $\Delta H°$ and $\Delta S°$ were obtained from the slope and intercept of the plot of $ln \, K_d$ vs. 1/T (Figure 9), and the values of these parameters are listed in Table 4. The changes in free energy ($\Delta G°$) parameters were calculated at different temperatures using Equation 13; these results are also presented in Table 4.

$$\Delta G° = \Delta H° - T\Delta S° \tag{13}$$

The negative values for $\Delta G°$ and $\Delta H°$ indicate the spontaneous and exothermic nature of the adsorption process. The thermodynamics values obtained also confirm more feasibility of the adsorption process with the Mn^{7+}/SC sorbent compared with pure SC. The low enthalpy values, $\Delta H° < 20$ kJ/mol, indicate a physical adsorption process. In addition, different values for $\Delta S°$ were obtained for SC and Mn^{7+}/SC. For Mn^{7+}/SC, the positive value for $\Delta S°$ corresponds to an increase in randomness at the solid-liquid interface during the adsorption process, while the negative value for $\Delta S°$ for pure SC indicates a more ordered structure during the adsorption process, suggesting an enthalpy driven process for adsorption.
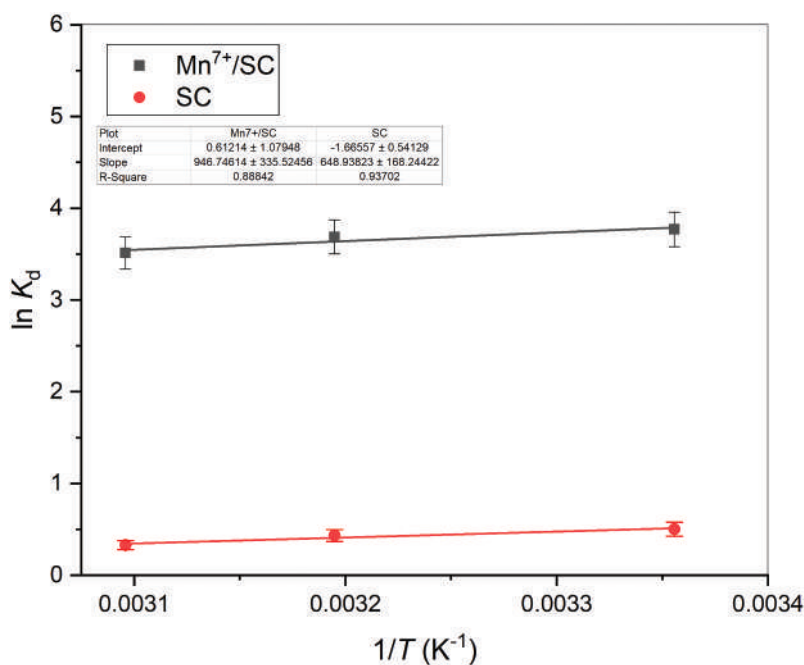
Figure 9. Effect of temperature on the adsorption of MB by the synthesised SC and Mn^{7+}(0.01)/SC sorbents.

Table 4. Thermodynamic parameters for the adsorption of MB using the synthesised SC and Mn^{7+}(0.01)/SC sorbents.

Temp. (K)	Mn^{7+}/SC			SC		
	$\Delta H°$ (kJ/mol)	$\Delta G°$ (kJ/mol)	$\Delta S°$ (J/mol.K)	$\Delta H°$ (kJ/mol)	$\Delta G°$ (kJ/mol)	$\Delta S°$ (J/mol.K)
298	−7.70	−9.38	5.63	−5.40	−1.27	−13.85
313		−9.47			−1.06	
323		−9.52			−0.92	

3.3.4. Sorbent recyclability

The regeneration efficiency of the Mn^{7+}/SC composite was studied. The process was carried out using 5 ml of ethanol (99.99%) in the presence of 0.5 ml of 0.1 M NaCl. It was found that the regeneration efficiency remained as high as 75% even after being reused five times. In addition to the use of recovered Mn^{7+}/SC for successive MB adsorption, we also inspected the recycling number of adsorbed MB in the Mn^{7+}/SC– MB complexes. As recycling dyes could also reduce industrial costs and safeguard a new reusable resource, the recycling process delivered a recycling yield of 98% of MB. However, with each additional recycling process, the MB content slightly decreased. This may be attributable to a small loss in Mn^{7+}/SC during the separation procedure. Given this potential, this practice of dye collection with its high MB yield represents a simple and inexpensive way of reusing dye and could be a promising approach for reusable resources.

4. Conclusions

This study investigated the efficiency of modified SC containing various weights of Mn^{7+} in removing MB dye from aqueous solutions. The results indicated that Mn^{7+}/SC sorbent is much more efficient in removing MB than pure SC. The addition of 0.01 g of Mn^{7+} was enough to exhibit enhanced performance. The results demonstrated a rapid removal of MB with 100% removal efficiency at MB concentrations of up to 100 mg/L and a removal enhancement of up to 50% compared with pure SC. The thermodynamic study revealed a physisorption type and the feasibility of the adsorption process. In addition to the enhanced performance of Mn^{7+}/SC, a comparable regeneration efficiency of up to five cycles was also demonstrated. The experimental results also correlated well with the Freundlich isotherm and the pseudo-second-order kinetic model. Furthermore, the study demonstrates a potential method for reclaiming MB dye from adsorbent materials after use, illustrating a simple and inexpensive procedure. Lastly, the experimental results suggest that the modified sorbent could be used as a potential approach for the removal of MB dye from wastewater.

Disclosure statement

No potential conflict of interest was reported by the author(s).

ORCID

Adel A. El-Zahar 🆔 http://orcid.org/0000-0003-2353-1480

References

[1] L. Pereira and M. Alves, Dyes—Environmental Impact and Remediation. In *Environmental Protection Strategies for Sustainable Development*, edited by Abdul Malik and Elisabeth Grohmann (Springer Netherlands, Dordrecht, 2012), p. 111.
[2] A. Tkaczyk, K. Mitrowska and A. Posyniak, Sci. Total Environ. **717**, 137222 (2020). doi:10.1016/j.scitotenv.2020.137222.
[3] H. Ali, Water Air Soil Pollut. **213**, 251 (2010). doi:10.1007/s11270-010-0382-4.
[4] F.M. Chequer, G.A. Oliveira, E.R. Ferraz, J.C. Cardoso, M.V. Zanoni and D.P. D. Oliveira, Textile Dyes: Dyeing Process and Environmental Impact. In Eco-Friendly Textile Dyeing and Finishing, edited by Melih, Günay (IntechOpen, London, 2013), p.150. doi:10.5772/53659.

[5] M. Choudhary, C.N. Peter, S.K. Shukla, P.P. Govender, G.M. Joshi and R. Wang, Environmental Issues: A Challenge for Wastewater Treatment, edited by, M. Naushad and E. Lichtfouse (Springer International Publishing, Cham, 2020), p. 1.

[6] M.A. Brown and S.C.D. Vito, Crit. Rev. Environ. Sci. Technol. **23**, 249 (1993). doi:10.1080/10643389309388453.

[7] K.-T. Chung, J. Environ. Sci. Health C **34**, 233 (2016). doi:10.1080/10590501.2016.1236602.

[8] M. Oz, D.E. Lorke, M. Hasan and G.A. Petroianu, Med. Res. Rev. **31**, 93 (2011). doi:10.1002/med.20177.

[9] T. Puzyn and A. Mostrag, *Organic Pollutants ten Years after the Stockholm Convention: Environmental and Analytical Update* (BoD–Books on Demand, IntechOpen, London, 2012). doi:10.5772/1381.

[10] G. Samchetshabam, A. Hussan, T. Gon Choudhury, S. Gita, P. Soholars and A. Hussan, Environ. Ecol. **35** (3C), 2349 (2017).

[11] K.A. Adegoke and O.S. Bello, Water Resour. Ind. **12**, 8 (2015).

[12] B. Gözmen, B. Kayan, A.M. Gizir and A. Hesenov, J. Hazard. Mater. **168**, 129 (2009). doi:10.1016/j.jhazmat.2009.02.011.

[13] T. Robinson, G. McMullan, R. Marchant and P. Nigam, Bioresour. Technol. **77**, 247 (2001). doi:10.1016/S0960-8524(00)00080-8.

[14] M. Nasrollahzadeh, M. Sajjadi, S. Iravani and R.S. Varma, Chemosphere **263**, 128005 (2021). doi:10.1016/j.chemosphere.2020.128005.

[15] E.A. Abdelrahman, D.A. Tolan and M.Y. Nassar, J. Inorg. Organomet. Polym. Mater. **29**, 229 (2019). doi:10.1007/s10904-018-0982-9.

[16] S.K. Ponnusamy, J. Joshiba, C. Femina, P. Varshini, S. Priyadharshini, A. Karthik and R. Jothirani, Desalin. Water Treat. **172**, 395 (2019). doi:10.5004/dwt.2019.24613.

[17] E. Santoso, R. Ediati, Y. Kusumawati, H. Bahruji, D.O. Sulistiono and D. Prasetyoko, Mater. Today Chem. **16**, 100233 (2020). doi:10.1016/j.mtchem.2019.100233.

[18] M. Nasrollahzadeh, M. Sajjadi, S. Iravani and R.S. Varma, Carbohydr. Polym. **251**, 116986 (2021).

[19] E.A. Abdelrahman and R.M. Hegazey, Composites, Part B **166**, 382 (2019). doi:10.1016/j.compositesb.2019.02.027.

[20] E.A. Abdelrahman and R.M. Hegazey, Microchem. J. **145**, 18 (2019). doi:10.1016/j.microc.2018.10.016.

[21] S.M.A. El-Gamal, M.S. Amin and M.A. Ahmed, J. Environ. Chem. Eng. **3**, 1702 (2015). doi:10.1016/j.jece.2015.06.022.

[22] M. Záleská, M. Pavlíková and Z. Pavlík, AIP Conf. Proc. **2170** (1), 20025 (2019).

[23] S.S.M. Hassan, N.S. Awwad and A.H.A. Aboterika, J. Radioanal. Nucl. Chem. **269**, 135 (2006). doi:10.1007/s10967-006-0242-2.

[24] N.S. Awwad and A.A.M. Daifullah, J. Radioanal. Nucl. Chem. **264**, 623 (2005). doi:10.1007/s10967-005-0762-1.

[25] S.S.M. Hassan, N.S. Awwad and A.H.A. Aboterika, J. Hazard. Mater. **162**, 994 (2009). doi:10.1016/j.jhazmat.2008.05.138.

[26] A. Bhaskaran and H. Rajagopalan, Int. J. Curr. Res. **10**, 122 (2018). doi:10.31782/IJCRR.2018.122125.

[27] D. Kiani, S. Sourav, J. Baltrusaitis and I.E. Wachs, ACS Catal. **9**, 5912 (2019). doi:10.1021/acscatal.9b01585.

[28] X. Chen, P. Li, X. Zeng, Y. Kang, J. Wang, H. Xie, Y. Liu and Y. Zhang, Int. J. Biol. Macromol. **151**, 1040 (2020). doi:10.1016/j.ijbiomac.2019.10.145.

[29] H.P. Klug and L.E. Alexander, *X-ray Diffraction Procedures: For Polycrystalline and Amorphous Materials*, 2nd ed. (John Wiley & Sons, New York, 1974).

[30] O. Jankovsky, M. Lojka, A.M. Lauermannova, F. Antoncik, M. Pavlikova, Z. Pavlik and D. Sedmidubsky, Appl. Sci.-Basel **10** (7), 2254 (2020).

[31] K. Li, Y. Wang, N. Yao and A. Zhang, Constr. Build. Mater. **255**, 119381 (2020). doi:10.1016/j.conbuildmat.2020.119381.

[32] M. Lojka, O. Jankovský, A. Jiříčková, A.-M. Lauermannová, F. Antončík, D. Sedmidubský, Z. Pavlík and M. Pavlíková, Materials (Basel, Switzerland) **13**, 767 (2020). doi:10.3390/ma13030767.

[33] G.P. Ojha, B. Pant, A. Muthurasu, S.-H. Chae, S.-J. Park, T. Kim and H.-Y. Kim, Energy **188**, 116066 (2019). doi:10.1016/j.energy.2019.116066.

[34] M. Huang, Y. Zhang, F. Li, L. Zhang, R.S. Ruoff, Z. Wen and Q. Liu, Sci. Rep. **4**, 3878 (2014). doi:10.1038/srep03878.

[35] K. Lu, T. Wang, L. Zhai, W. Wu, S. Dong, S. Gao and L. Mao, J. Colloid Interface Sci. **539**, 553 (2019). doi:10.1016/j.jcis.2018.12.094.

[36] C.P. Lawagon and R.E.C. Amon, Environ. Eng. Res. **25**, 685 (2020). doi:10.4491/eer.2019.287.

[37] L. Thi Mong Thy, N. Hoan Kiem, T. Hoang Tu, L. Minh Phu, D. Thi Yen Oanh, H. Minh Nam, M. Thanh Phong and N. H, Hieu, Chem. Phys. **533**, 110700 (2020). doi:10.1016/j.chemphys.2020.110700.

[38] F. Mashkoor and A. Nasar, J. Magn. Magn. Mater. **500**, 166408 (2020). doi:10.1016/j.jmmm.2020.166408.

[39] T.C. Andrade Siqueira, I. Zanette da Silva, A.J. Rubio, R. Bergamasco, F. Gasparotto, E. Aparecida de Souza Paccola and N. Ueda Yamaguchi, Int. J. Environ. Res. Public Health **17**, 526 (2020). doi:10.3390/ijerph17020526.

[40] I. Langmuir, J. Am. Chem. Soc. **40**, 1361 (1918). doi:10.1021/ja02242a004.

[41] S. Kocaman, Int. J. Phytorem. **22**, 885 (2020). doi:10.1080/15226514.2020.1736512.

[42] H.V. Tran, L.T. Hoang and C.D. Huynh, Chem. Phys. **535**, 110793 (2020). doi:10.1016/j.chemphys.2020.110793.

[43] H. Ebadollahzadeh and M. Zabihi, Mater. Chem. Phys. **248**, 122893 (2020). doi:10.1016/j.matchemphys.2020.122893.

[44] A.S. Eltaweil, G.S. Elgarhy, G.M. El-Subruiti and A.M. Omer, Int. J. Biol. Macromol. **154**, 307 (2020). doi:10.1016/j.ijbiomac.2020.03.122.

[45] T. Van Tran, D.T.C. Nguyen, H.T.N. Le, C.D. Duong, L.G. Bach, H.-T.-T. Nguyen and T.D. Nguyen, Chemosphere **227**, 455 (2019). doi:10.1016/j.chemosphere.2019.04.079.

[46] L.G. Bach, T. Van Tran, T.D. Nguyen, T. Van Pham and S.T. Do, Res. Chem. Intermed. **44**, 1661 (2018). doi:10.1007/s11164-017-3191-1.

[47] S.X. Ye, W.P. Jin, Q. Huang, Y. Hu, Y. Li and B. Li, Int. J. Biol. Macromol. **92**, 1169 (2016). doi:10.1016/j.ijbiomac.2016.07.106.

[48] J. Wang, L. Kou, Z. Huang and L. Zhao, RSC Adv. **8**, 21577 (2018). doi:10.1039/C8RA03924K.

[49] X. Wang, L. Mei, X. Xing, L. Liao, G. Lv, Z. Li and L. Wu, Applied Catalysis B: Environmental **160-161**, 211 (2014). doi:10.1016/j.apcatb.2014.05.009.

[50] M. Abdel Salam, Chem. Eng. J. **270**, 50 (2015). doi:10.1016/j.cej.2015.02.022.

ORIGINAL PAPER

Magnetite nanoparticles-incorporated composite thin-film nanofiltration membranes based on cellulose nitrate substrate

Majed M. Alghamdi[1] · Adel A. El-Zahhar[1] (ID) · Norah M. Alshahrani[2]

Abstract

Thin-film composite nanofiltration membranes were prepared through interfacial polymerization of trimesoyl chloride (TMC), polyvinylpyrrolidone (PVP), and magnetite nanoparticles (MNPs) on the upper surface of porous cellulose nitrate (CN) membranes. Structural and morphological properties of the prepared membranes (CN-TMC/PVP–MNP) were analyzed using FTIR, SEM, membrane contrast and AFM. The effects of reaction time, PVP concentration, and MNPs content on membrane performance were studied. Surface hydrophilicity and membrane performance were analyzed by measuring pure water contact angle, zeta potential, pure water permeation flux (PWP), and solute rejections. The CN-TMC/PVP–MNPs membranes exhibited a smooth surface and diverse surface functionalities following interfacial polymerization. The membrane surface charge was strongly affected by the presence of MNPs. Although PWP decreased with increasing MNPs content up to 0.10 wt%, Na_2SO_4 and NaCl rejections increased with increasing MNPs content, reaching, respectively, 96.8% and 76.6% at 0.1 wt% MNPs content. Moreover, the increases in steady-state flux and FRRs with increasing MNPs content, reflecting the improvement of antifouling behavior, stability, and durability, indicating their possible application for water desalination and treatment.

Keywords Thin-film composite · Nanofiltration membrane · Cellulose nitrate · Magnetite

Introduction

As a result of population growth and rapid development, freshwater scarcity has become a major current challenge. To overcome this, seawater desalination is essential in some countries as an alternative to generate freshwater (Geoffrey et al. 2010; Chung et al. 2012), and membrane filtration is an important technique to realize this. In particular, nanofiltration (NF) has found wide applications in seawater desalination and water decontamination, in addition to its industrial, pharmaceutical, and biological uses (Bai et al. 2019; Ma

et al. 2019; Kim et al. 2018; Xu et al. 2017; Ye et al. 2017; Rathore and Shirke 2011; Zhao et al. 2018). However, for their desalination application, NF membranes must possess certain properties such as high rejection, permeability, operational stability, and mechanical strength. Accordingly, the use of active separation surface thin-film nanocomposite for NF has been explored (Lau et al. 2012).

Thin-film composite (TFC) membranes with desired structural properties of the surface thin-film can be fabricated using different processes, such as interfacial polymerization, dip coating, and layer-by-layer (LbL) assembly (Wei et al. 2013; Han et al. 2014; Joseph et al. 2015). In addition, the incorporation of nanomaterials can effectively improve material properties. Therefore, TFC membranes containing different materials have been investigated. For instance, TFC membranes containing graphene oxide showed better membrane performance and higher filtration efficiency (Cheng et al. 2021; Kumar et al. 2019). Moreover, TFC membranes fabricated from polysulfone embedded with zeolite nanoparticles through interfacial polymerization of the polyamide layer showed increased surface roughness, water permeability, and membrane performance (Dong

✉ Adel A. El-Zahhar
elzahhar@kku.edu.sa

Majed M. Alghamdi
mmalghamdi@kku.edu.sa

Norah M. Alshahrani
noo0oorah2011@hotmail.com

[1] Department of Chemistry, Faculty of Science, King Khalid University, P.O. Box 9004, Abha 61413, Saudi Arabia

[2] Department of Chemistry, College of Science, Bisha University, P.O. Box 551, Bisha 61922, Saudi Arabia

et al. 2016). Likewise, NF membranes fabricated through interfacial polymerization of trimesoyl chloride (TMC) and disodium-3-3′-disulfone-4-4′-dichlorodiphenylsulfone (S-DADPS)/piperazine (PIP) on porous polysulfone showed increased flux, dye rejection, and pH and temperature resistance (Ormanci et al. 2020). Furthermore, variation of the S-DADPS/PIP ratio strongly affected membrane performance; as such, membranes with the S-DADPS/PIP ratio of 80/20 showed markedly improved water flux, although their salt or dye rejection remained unaffected. In another study, TFC membranes were fabricated via LbL interfacial polymerization of polyethyleneimine (PEI) onto the polyamide surface, followed by *N*-methylation and quaternization using 3-bromopropionic acid (Deng et al. 2021); water permeation ability of the produced membrane was improved by 11.6%, and these surface-modified membranes showed improved ion selectivity and rejection for divalent ions. TFC membranes prepared via interfacial polymerization of sericin polymer and TMC onto a commercial porous polysulfone support exhibited a smooth surface, with an isoelectric point of pH 4.1 and salt rejection of, respectively, 22.5%, 40.5%, 40.8%, and 95.4% for $MgCl_2$, $MgSO_4$, NaCl, and Na_2SO_4 at neutral pH (Zhou et al. 2014). TFC membranes with organically bridged silica deposited on a commercial polymeric membrane (NTR-7450) using low-temperature sol–gel spin-coating and curing were assessed for their vapor permeation dehydration of water-isopropanol solutions (Gong et al. 2014); the results showed a water flux of 2.3 kg/(m^2 h), with markedly enhanced separation factor of 2500. Further, interfacial polymerization of PEI and TMC onto a microporous polyethersulfone support improved membrane performance increasing salt rejection (95.1% for $MgCl_2$, 94.4% for $MgSO_4$, 85.1% for NaCl, and 80.5% for Na_2SO_4) and pure water permeation flux [24.5 L/(m^{2}h)] (Wu et al. 2014). Poly(vinyl alcohol)/poly(vinylidene fluoride) composite membranes modified with TiO_2 were prepared through dip-coating and applied for dye removal and wastewater treatment (Li et al. 2014); the membranes showed superior performance with enhanced dye removal, salt rejection, and antifouling properties.

Since nanomaterial incorporation can effectively improve the properties of materials due to their size and characteristics (Singh et al. 2013), magnetite nanoparticles (MNPs) have been explored as a potential additive in polymeric composites (Akinay et al. 2018; Zhang et al. 2012; Li et al. 2011). MNPs can enhance the properties of materials, particularly when they are well dispersed within the polymeric composite. MNPs have promising properties as developed surface area, colloidal stability and low toxicity (Kydralieva et al. 2016). The ease of synthesis of MNPs and their unique physicochemical properties (large surface area, synergistic effect on materials mechanical, thermal, magnetic properties and highly active surface groups) lead to advanced

applications. (Bustamante-Torres et al 2022). A few studies have reported that the incorporation of MNPs during membrane fabrication greatly enhanced properties desirable for various applications.

In this study, cellulose nitrate (CN) membranes were modified through interfacial surface polymerization of TMC, polyvinylpyrrolidone (PVP), and MNPs. Properties of the obtained TFC membranes (CN-TMC/PVP–MNP) were optimized in terms of reaction time, PVP concentration, and MNPs content to enhance their performance. Structural and surface properties of the produced membranes were analyzed using FTIR, SEM, Inverted phase contrast and AFM. Membrane performance was assessed based on pure water permeation (PWP), salt rejection, antifouling behavior, and surface zeta potential.

Experimental

Materials

Cellulose nitrate (CN) membranes with a diameter of 47 mm and pore size of 0.45 μm were purchased from GVS, USA. m-Phenylenediamine (m-MPD) and trimesoyl chloride (TMC) were obtained from Sigma Aldrich. Hexane and dimethylformamide (DMF) as solvents were obtained from Acros Organics.

Preparation of MNPs

MNPs were prepared as follows. Ferrous sulfate (1 g/100 mL) was slowly (1 mL/10 min) titrated with sodium hydroxide (1 mol/L) until reaching a pH of 12. The obtained black suspension was raised to 200 mL with distilled water and placed in a microwave at half power for 10 min. The obtained black MNPs were repeatedly washed with distilled water until reaching a neutral pH, separated via centrifugation, and dried to a constant weight.

Preparation of TFC membranes

CN membranes were soaked in distilled water for 5 min, followed by immersion in m-PDA solution (2 wt% in deionized) for 2 min. PVP solution (1 wt% in DMF) was mixed with various amounts of MNPs, stirred for 1 h, and sonicated for 30 min at ambient temperature (25 °C). The obtained PVP–MNPs solution was mixed with TMC solution (0.15 wt% in hexane) with continuous stirring to obtain the polymerization mixture. The polymerization mixture was dropped onto one side of the pretreated membranes and left for different reaction times (2, 4 or 6 min).

Membrane characterization

Surface structural properties of the fabricated TFC membranes were analyzed using FTIR spectroscopy (NICOLET 6700 Thermo Scientific) at wave number range of 400–4000 cm^{-1} Surface morphological properties of the thin film were analyzed using SEM (JEOL 6340) and the membrane contrast was imaged using Optika phase contrast. Surface roughness of the prepared membranes was assessed using AFM (NT-MDT, Type Next, Russia) in the non-contact mode and the attached NT-MDT software. The membrane porosity ($\varepsilon\%$), was determined using gravimetric procedure, where the ratio of voids volume to the volume of whole membrane was calculated (Ursino et al. 2019). The membrane dry weight and the membrane weight after immersion in kerosene for 24 h was measured after removing excess kerosene. The membrane porosity was calculated as follows:

$$\varepsilon\% = \left\{ \frac{(W_w - W_d)/\rho_k}{(W_w - W_d)/\rho_k + \frac{W_d}{\rho_p}} \right\} \tag{1}$$

Membrane performance

Performance of the fabricated membranes was assessed with a laboratory-designed dead-end filtration device. The effective testing membrane area was 12.56 cm^2. Firstly, the membranes were pre-stabilized for 20 min with the feed sample. Appropriate concentrations of salts (500 mg/L NaCl$_2$ and Na$_2$SO$_4$) were applied as feed solutions. These solutions were passed through the membrane at 40 psi. Permeation flux (J, L/m^2 h) and rejection (R, %) were calculated using the following equations:

$$J = \frac{V}{A\Delta t} \tag{2}$$

where V is the permeated volume, A is the effective membrane area, and Δt is the permeation time period.

$$R = \left(1 - \frac{C_p}{C_f}\right) \times 100\% \tag{3}$$

where C_f is solute concentration in the feed solution and C_p is solute concentration in the permeate solution.

Salt solution concentrations before and after permeation were measured using an electrical conductivity meter.

Antifouling experiment

Antifouling properties of the TFC membranes were studied through permeation experiments using an aqueous solution of sodium alginate (SA; 100 mg/L) as a fouling agent. The fouling results of the membranes were presented in terms of the normalized permeate fluxes J_t/J_o, where J_o and J_t are the initial water flux and water flux after time t of the fouling test, respectively. The values of the normalization flux reflected antifouling behavior of the tested membranes and the fouling agent deposition onto the membrane surface.

Furthermore, membrane antifouling and durability were determined based on fouling reversibility and washing. The removal of fouling agent depends on the weak bonding between the fouling molecules and membrane surface. Thus, to analyze membranes stability and durability, membranes are washed and re-applied in repeated fouling experiments. Accordingly, the SA solution was applied as a feed solution until reaching the steady state, followed by the washing of all permeation equipment and the used membrane with distilled water. The washed membrane was tested for pure water permeation to evaluate the pure water flux and determine the flux recovery ratio (FRR %), as below:

$$FRR\% = \left(\frac{J_{w2}}{J_{w1}}\right) \times 100 \tag{4}$$

where J_{w1} and J_{w2} are pure water fluxes before and after the fouling process, respectively.

Results and discussion

Structural and morphological characteristics of the prepared membranes

FTIR spectroscopy of the composite membrane

FTIR spectra of the unmodified CN membrane and the thin-film modified CN-TMC/PVP–MNPs membrane are shown in Fig. 1. The CN membrane spectrum (Fig. 1a) showed a peak at 3750 cm^{-1}, which was assigned to the stretching vibration of the free O–H of cellulose. The peak corresponding to CH$_2$ vibrations appeared around 3000 cm^{-1}, while the sharp peak corresponding to the H$_2$O bending mode appeared at 1635 cm^{-1}. The peaks at 2950 and 2920 cm^{-1} were assigned to symmetric and asymmetric CH$_2$ vibrations of the polymer chains. The CN-TMC/PVP–MNPs membrane spectrum (Fig. 1b) showed a wide peak at 3450 cm^{-1}, which was assigned to the stretching vibration of the O–H of cellulose, water, and PVP. The peak at 2100 cm^{-1} was assigned to the CN bond in PVP, while the peaks at 1500 and 1400 cm^{-1} were assigned to the CH$_2$ bending mode and NO$_2$, COO and C–O vibrations. The sharp peak at 570 cm^{-1} was assigned to N–C=O. The characteristic peak corresponding to Fe^{2+}–O^{2-} of MNPs was slightly shifted and appeared at 530 cm^{-1} due to bonding within the thin film (Cornwell
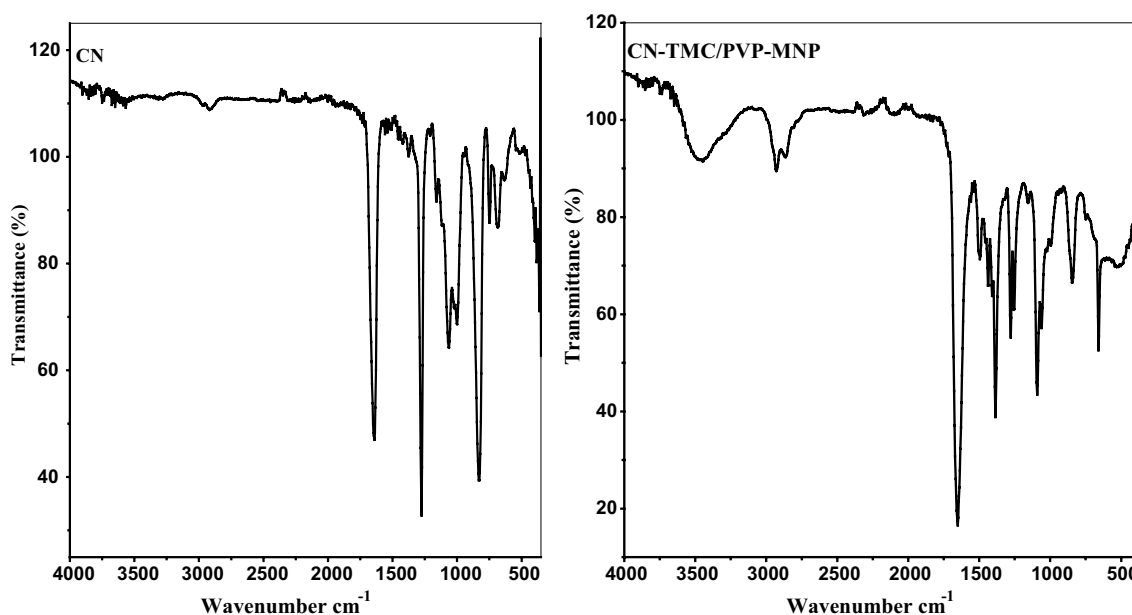
Fig. 1 FTIR spectra of the unmodified CN membrane and the modified CN-TMC/PVP–MNPs membrane with 0.1 wt% MNPs

and Schwertmann 2006; Zheng et al. 2011). The CN-TMC/PVP–MNPs membrane spectrum showed TFC formation on the surface of the supporting CN membrane.

SEM, membrane contrast and AFM of the composite membrane

Scanning electron micrographs of the modified and unmodified CN membranes are shown in Fig. 2a–d. The CN-TMC/PVP–MNPs membranes showed different characteristics from the unmodified CN membranes, as interfacial polymerization formed a coating onto the surface of the modified membranes. As shown in Fig. 2a and c, the CN membrane possesses pores on the surface, while the modified membrane with a thin surface coating (Fig. 2c and d) shows a dense, thick, and a smooth surface. As shown in Fig. 2b and d, the CN-TMC/PVP–MNPs membrane lacks agglomerates, but there is certain folding due to the high surface area of MNPs. MNPs with a large surface area, high surface energy, and high adsorption enter the pores on the surface of the support membrane and enable efficient surface coating with the co-polymer. In micrographs, the CN-TMC/PVP–MNPs membrane shows smaller pores on the surface, and the surface appears more homogeneous with a thin and smooth coating. Moreover, the micrographs of the CN-TMC/PVP–MNPs membrane showed homogeneous distribution of MNPs within the thin surface layer. Thus, MNPs strongly affected the surface properties of the membrane. The membrane contrast images for CN-TMC/PVP (Fig. 2e, f) show uniform film surface, fine structure with no defects on the surface. The images show that the interfacial polymerization

has occurred homogenously and equivalently on whole surface of the membrane with no agglomeration, folding or scalloped area.

Atomic force micrographs (AFM) (Fig. 2e and g) of the CN membrane showed symmetric morphology with clear surface roughness. Meanwhile, the micrographs of the CN-TMC/PVP–MNPs membrane (Fig. 2f, and h) showed a dense surface coat with altered roughness due to interfacial polymerization of TFC. The average root-mean-square (RMS) roughness was 258 nm for the modified membrane compared with 153 nm for the unmodified one. These results reflect the formation of a uniform and dense surface film with MNPs distributed within. Thus, interfacial polymerization provides a smooth surface with a dense and thick layer structure.

Contact angle of the composite membranes

The surface contact angles of modified TFC membranes are presented in Fig. 3. The highest pure water contact angle of 85° was obtained for the thin film lacking MNPs, while the angle decreased in the presence of MNPs, reaching 69° at 0.1 wt% MNPs. These results indicate that the inclusion of MNPs improved membrane surface hydrophilicity. This observation can be explained by the fact that the increase in MNPs content enhances PVP concentration, which elevates film thickness and, ultimately, promotes water uptake. Moreover, increasing the content of MNPs with a large surface area and high hydrophilicity nature may markedly enhance surface hydrophilicity. Thin film formation increases surface active groups and polarity, which promotes interactions

Fig. 2 Scanning electron micrographs of CN (**a**, **c**), and CN-TMC/PVP–MNPs (**b**, **d**) membranes, contrast for CN-TMC/PVP membrane (**e**, **f**) and atomic force micrographs of CN (**e**, **g**) and CN-TMC/PVP–MNPs (**f**, **h**) membranes
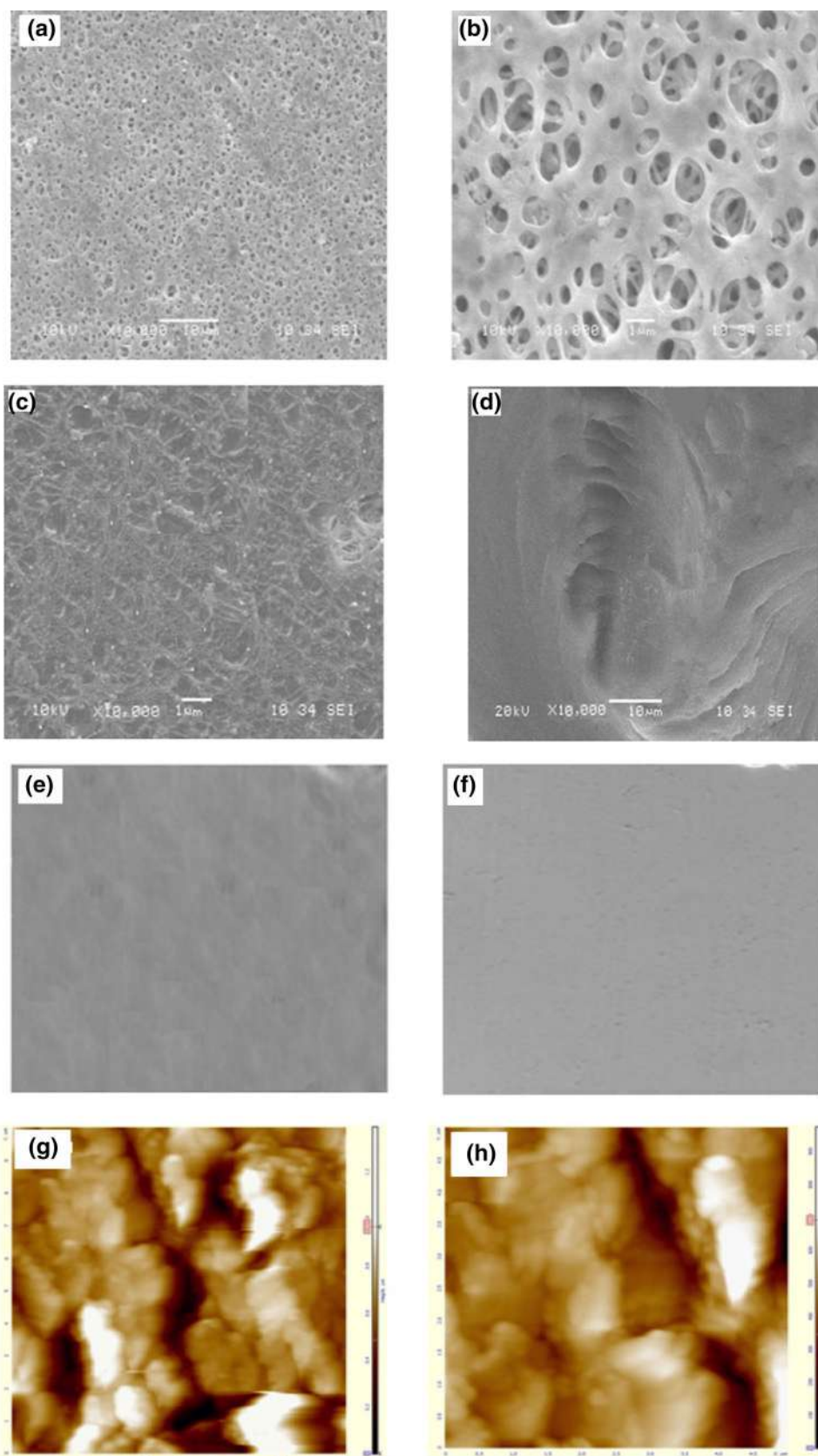
Fig. 2 (continued)
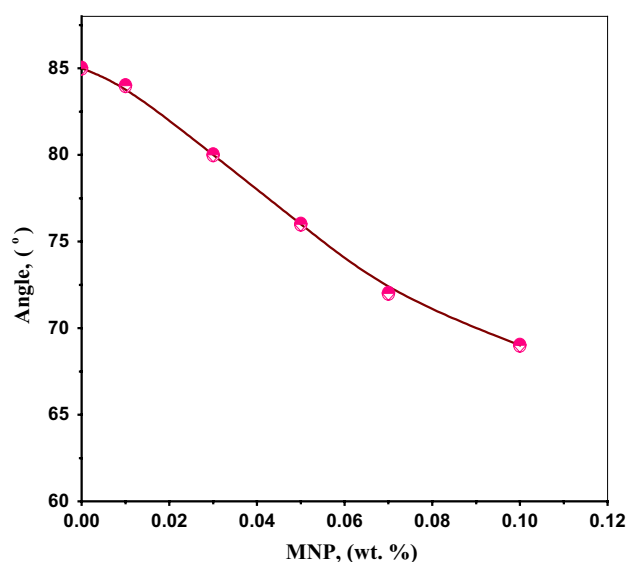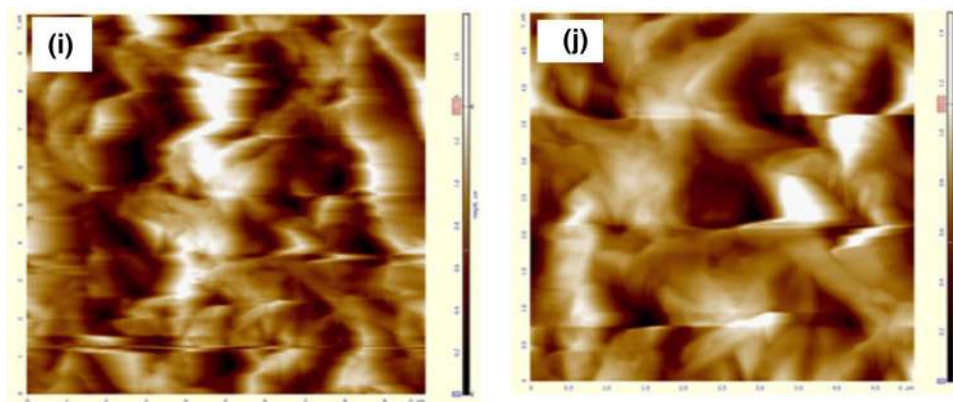
Fig. 3 Effect of MNPs content on the pure water contact angle of CN-TMC/PVP–MNPs membranes

Fig. 4 Zeta potential of the CN-TMC/PVP–MNPs membranes with different MNPs contents

with water molecules through hydrogen bonding and van der Waals forces (Pourjafar et al. 2012; Alghamdi et al. 2019). Furthermore, increased hydrophilicity may effectively improve membrane fouling behavior (Bruggen et al. 2008).

Zeta potential of the composite membrane

The surface charge of membranes strongly affects their characteristics, especially fouling behavior and adsorption properties (Kim et al. 1996; Rodemann and Staude 1995). The adsorption and fouling of materials onto the membrane surface may be affected by its electrostatic interactions with the solutes. Membrane surface charge depends on the dissociation of charged surface groups and pH of the solution (Wilbert et al. 1999). The surface charges of fabricated membranes against solution pH are presented in Fig. 4. Zeta potential decreased with increasing solution pH, which may be explained by the adsorption of OH⁻ anions and possible
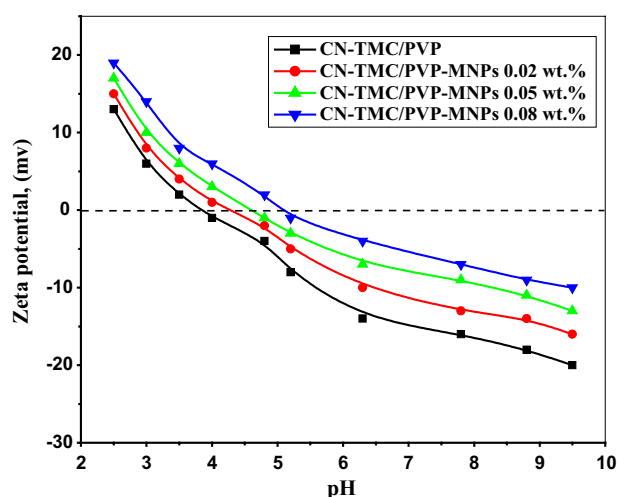
dissociation of membrane surface groups. Based on the results in Fig. 4, interfacial polymerization of TMC/PVP thin film affected the surface charge of the CN membrane. Specially, the membrane became negatively charged after a pH of 3.4, and the isoelectric point shifted to approximately 4 due to TMC/PVP polymerization. Moreover, the inclusion of MNPs markedly affected surface charge, as the point of zero charge shifted towards a higher pH value. Nitrogen atoms form quaternary nitrogen species with carboxyl groups of TMC, and the certain electrostatic interactions among surface groups attenuate the negative charge (Liu et al. 2014).

Preparation of CN-TMC/PVP–MNPs composite membranes

Improving the structural and morphological properties of membranes such as higher porosity, pore volume, and film thickness may decrease the hydraulic resistance and consequently affect water permeation. A thin layer plays an important role in the structural and morphological properties

Table 1 Effects of reaction time and PVP concentration on membrane performance

Membrane	Preparation conditions		Membrane performance	
	Reaction time (min)	PVP content (%)	PWP (L/m² h bar)	Salt rejection (%) (Na$_2$SO$_4$)
CN-NF01	2	0.5	19.6 ± 0.2	80.1 ± 0.7
CN-NF02	4	0.5	17.8 ± 0.3	81.3 ± 0.6
CN-NF03	6	0.5	16.9 ± 0.2	82.1 ± 0.5
CN-NF04	4	0.25	14.8 ± 0.3	83.9 ± 0.6
CN-NF05	4	0.5	12.8 ± 0.4	85.9 ± 0.8
CN-NF06	4	1	11.5 ± 0.3	87.5 ± 0.8

Table 2 Effect of MNPs content on the performance of modified CN membranes

Membrane	Preparation conditions			Membrane performance	
	Reaction time (min)	PVP content (%)	MNPs (%)	PWP (L/m² h.bar)	Salt rejection (%) (Na$_2$SO$_4$)
CN-NF1	6	0.5	0.02	24.6	84.3
CN-NF2	6	0.5	0.04	21.2	86.8
CN-NF3	6	0.5	0.06	19.3	89.7
CN-NF4	6	0.5	0.08	16.5	94.1
CN-NF5	6	0.5	0.10	13.6	96.8

of the membrane interface and, consequently, determines membrane performance (Ahmad and Ooi 2013). Therefore, membrane performance was assessed as a function of layer thickness. The TFC membrane was prepared through interfacial polymerization of TMC/PVP–MNPs in hexane. The film thickness was controlled by limiting the reaction time between CN and TMC/PVP–MNPs. The reaction time and MNPs content were optimized with respect to membrane performance. The effects of reaction time and PVP concentration on membrane performance were examined and the results are presented in Table 1.

Based on the results in Table 1, both reaction time and PVP concentration, strongly affected CN membrane performance. A longer reaction time affected film thickness, which significantly decreased PWP. The reaction time of 6 min was considered optimum to deliver an appropriate film thickness for providing a PWP of 16.9 L/m² h·bar. Moreover, salt rejection of the unmodified CV was clearly improved from 80.1% at a reaction time of 2 min to 82.1% at a reaction time of 6 min, indicating increased thickness of the interfacial polymerized composite film. The role of MNPs in water permeation and salt rejection improvement could be explained due to the diffusion of MNPs through the pores of porous polymeric materials (Bhattacharya 2021). Furthermore, MNPs have surface active groups and have adsorption properties for ions and molecules and which enhances solutes retention. However, higher concentrations of MNPs in the polymeric composite could increase crosslinking between polymeric moieties which provide more surface stiffness, toughness (Romero-Fierro et al. 2022).

Therefore, preparation parameters controlling membrane performance were studied at a fixed reaction time of 6 min and fixed PVP concentration of 0.5%. Moreover, the effect of MNPs content on membrane performance was studied, and the results are presented in Table 2.

Based on results in Table 2, MNPs content of the interfacial thin film significantly affected membrane performance (water flux and salt rejection). The results

demonstrate a clear improvement in membrane performance. At the same reaction time and PVP concentration, the presence of MNPs decreased the pure water flux and increased salt rejection of the CN-TMC/PVP–MNPs membrane compared with the CN-TMC/PVP membrane. Effects of MNPs inclusion on PWP are also presented in Fig. 5a. These results could be explained by the properties of MNPs. Specially, MNPs enhance surface hydrophilicity of the interfacial surface layer, consequently promoting water permeation through the thin film (Hu and Mi 2013; Stankovich et al. 2006; Lee et al. 2013). The membrane porosity (ε%), was determined for CN-NF3, CN-NF4 and CN-NF5 and found to be 62, 54 and 44%, respectively. These results reveal that the porosity decreased with increasing MNPs content in the thin-film composite deposited on CN surface, which agreed with the decreased water permeability.

The salt rejection behavior of CN-TMC/PVP–MNPs membranes with different MNPs contents was studied through flow permeation experiments with salt solutions containing NaCl and Na$_2$SO$_4$. Based on results in Fig. 5b, the salt rejection of CN-TMC/PVP–MNPs membranes improved with increasing MNPs content. These results could be due to the effect of MNPs on the membrane porosity, as it diffused through the membrane filter micro-pores (Bhattacharya 2021). MNPs additionally have highly active surface groups, which could cause solutes adsorption and increase retention. On the other hand, the presence of MNPs in the composite thin-film increases its viscosity and produces a denser layer which affects the solute rejection. Furthermore, Na$_2$SO$_4$ rejection was significantly greater than NaCl rejection. Thus, the rejection of solute ions closely depends on membrane pore size and is strongly affected by both the electrostatic properties of solute ions and membrane surface (Schaep et al. 1998; Peeters et al. 1998). Cations with greater charges show higher membrane affinity and, consequently, greater rejection.

Fig. 5 Effect of MNPs content on the pure water permeability (**a**) and salt rejection (**b**) of the modified CN membrane
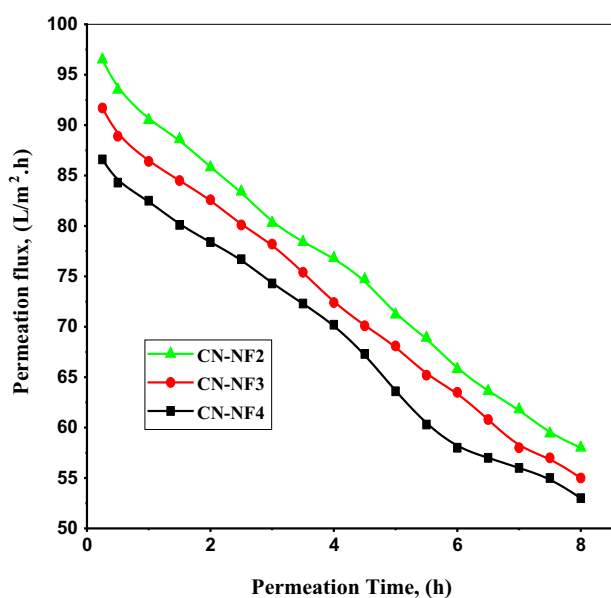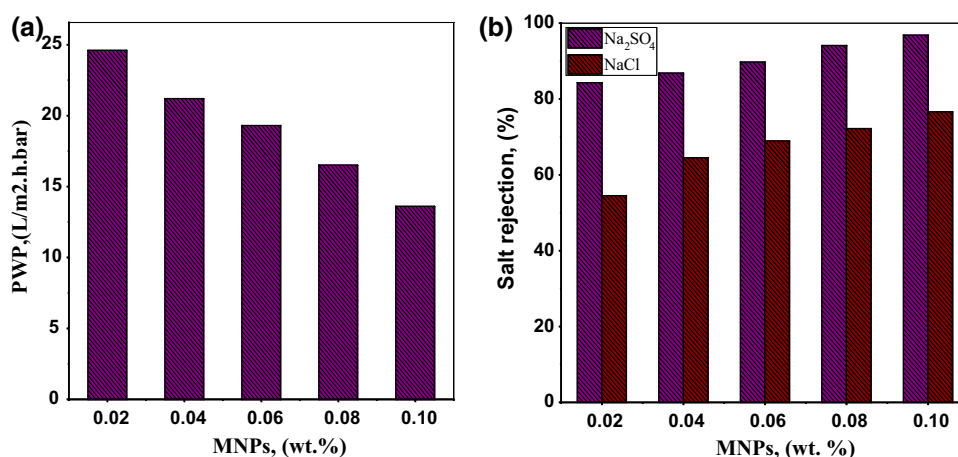

Fig. 6 Effect of permeation time on the permeation flux of Na_2SO_4 solution through CN-TMC/PVP–MNPs membranes with different MNPs contents

Table 3 Steady-state salt rejection and permeation fluxes of CN-TMC/PVP–MNPs membranes

Membrane	Steady-state flux (L/m^2 h)	Steady-state removal of Na_2SO_4 (%)
CN-NF2	53	86.7
CN-NF3	55	90.1
CN-NF4	58	94.3

application for heavy metal removal and pollutant rejection. Additionally, as shown in Table 3, salt rejection of the prepared TFC membranes was improved. These observations may be explained by the improvement of surface properties due to thin-film polymerization and MNPs addition. Moreover, under the present experimental conditions, electrostatic interaction likely produced a marked effect.

Antifouling behavior of CN-TMC/PVP–MNPs membrane

The antifouling behaviors of fabricated CN-NF3 and CN-NF4 membranes were evaluated during the permeation of 100 mg/L aqueous SA solution at pH 7.0 and of 25 °C. The molecular size of the applied fouling agent is larger than the NF membrane pore size; therefore, it cannot pass through the membrane pores during solution permeation, leading to the fouling of the membrane surface. Surface fouling was performed at a permeation flux of 80 L/m^2·h to verify the required permeation-driving hydrodynamic force. Normalized fluxes (J_t/J_o) of the studied membranes are presented in Fig. 7.

As shown in Fig. 7, membrane flux for the SA solution sharply decreased at first, followed by a slow decrease over time. These observations may be attributed to the deposition of fouling agent on the membrane surface until reaching the steady state. The steady-state flux of aqueous SA solution decreased at a rate of about 6% for the CN-NF4 membrane

Effect of permeation time on permeation flux

The salt rejection behavior for Na_2SO_4 in aqueous solution was further studied using CN-NF2, CN-NF3, and CN-NF4 membranes with different MNPs contents. The permeation of 500 mg/L of Na_2SO_4 was studied at 0.276 MPa and different permeation times, and the results are presented in Fig. 6.

As shown in Fig. 6, the solution fluxes of modified membranes with different MNPs contents gradually decreased with time up to 8 h. The steady-state flux increased with increasing MNPs content, reflecting improvement of the antifouling behavior due to the inclusion of MNPs. These results reflect the antifouling behavior of the modified TFC membrane toward salt solutions and highlight its potential

Fig. 7 Effect of filtration time on the normalized flux of SA solution through CN-TMC/PVP–MNPs membranes

Table 4 Flux recovery ratios of the CN-NF3 and CN-NF4 membranes after repeated SA fouling-washing cycles

Fouling-cleaning cycles	FRR%	
	CN-NF3 (%)	CN-NF4 (%)
1st cycle	97	98
2nd cycle	93	94
3rd cycle	89	91
4th cycle	81	83

and 8% for the CN-NF3 membrane. These findings indicate the effect of MNPs content in the interfacially polymerized thin film on the surface properties of membrane for improving its fouling behavior. The membrane with a higher MNPs content showed a better performance in fouling resistance. Fouling agents are adsorbed onto the membrane surface via hydrophobic interactions, hydrogen bonds, electrostatic interactions, and van der Waals forces. Consequently, antifouling properties can be improved by decreasing the adsorption driving forces and enhancing the repulsion effect of the membrane surface on the fouling molecules (Bruggen et al. 2008; Al-Amoudi and Lovitt 2007). Notably, at the specified testing conditions, the membrane surfaces are more negatively charged; thus, stronger electrostatic repulsive forces may act between the membrane surface and fouling agent, resulting in a weaker fouling effect.

Furthermore, to analyze flux recovery ratio (FRR %), membranes stability, and durability, membranes are washed and re-applied in repeated fouling experiments. As shown in Table 4, the inclusion of MNPs in the thin film improved antifouling properties, providing higher FRRs.

This improvement of antifouling properties may be related to the increased hydrophilic properties of the composite surface layer, which may inhibit the interaction between the fouling molecules and hydrophobic membrane surface. Surface hydrophilicity determines surface adsorption behavior (Khorshidi et al. 2016; El-Zahhar 2019). The increase in hydrophilicity by the presence of MNPs was confirmed based on the decrease in water contact angle with increasing MNPs content. Based on results in Table 4, the CN-NF3 and CN-NF4 membranes were stable until the fourth fouling-washing cycle. Overall, the CN-TMC/PVP–MNPs membranes showed increased stability, durability, and FRRs, indicating their possible application for water desalination and treatment.

Conclusion

Nanofiltration TFC membranes were fabricated via modified interfacial polymerization of TMC/PVP–MNPs on the surface of a porous CN support. The optimum preparation conditions are a reaction time of 6 min, PVP concentration of 0.5 wt%, and MNPs content of 0.1 wt%. Structural and morphological analyses revealed differences between the unmodified CN and the modified CN-TMC/PVP–MNPs membranes. The pure water contact angle of the modified membrane (with 0.1 wt% MNPs) was decreased to 69° compared with 85° of the unmodified membrane. The zeta potential of the CN-TMC/PVP–MNPs membrane significantly varied with increase in MNPs content. Although the PWP decreased with increasing MNPs content, membrane performance was superior due to enhanced salts rejection and clearly improved stability, durability, and antifouling performance.

Declarations

Conflict of interest On behalf of all authors, the corresponding author states that there is no conflict of interest.

References

Ahmad AL, Ooi BS (2013) Properties–performance of thin-film composites membrane: study on trimesoylchloride content and polymerization time. J Membr Sci 255:67–77. https://doi.org/10.1016/j.memsci.2005.01.021

Akinay Y, Hayat F, Çakir M, Akin E (2018) Magnetic and microwave absorption properties of PVB/Fe_3O_4 and PVB/$NiFe_2O_4$

composites. Polym Compos 39:3418–3423. https://doi.org/10.1002/pc.24359

Al-Amoudi A, Lovitt RW (2007) Fouling strategies and the cleaning system of NF membranes and factors affecting cleaning efficiency. J Membr Sci 303:4–28. https://doi.org/10.1016/j.memsci.2007.06.002

Alghamdi MM, El-Zahhar AA, Asiri BM (2019) Incorporation of magnetite nanoparticles in poly(vinyl chloride) microfiltration membrane for improving antifouling property and desalination performance. Desalination Water Treat 165:54–62. https://doi.org/10.5004/dwt.2019.24495

Bai L, Liu Y, Ding A, Ren N, Li G, Liang H (2019) Fabrication and characterization of thin-film composite (TFC) nanofiltration membranes incorporated with cellulose nanocrystals (CNCs) for enhanced desalination performance and dye removal. Chem Eng J 358:1519–1528. https://doi.org/10.1016/j.cej.2018.10.147

Bhattacharya S (2021) Nanostructures in gene delivery. In: Bajpai A, Saini R (eds) Advances in polymeric nanomaterials for biomedical applications, 1st edn. Elsevier Inc., Cham, pp. 101–135. ISBN 978–0–12–814657–6

Bruggen BV, Mänttäri M, Nyström M (2008) Drawbacks of applying nanofiltration and how to avoid them: a review. Sep Purif Technol 63:251–263. https://doi.org/10.1016/j.seppur.2008.05.010

Bustamante-Torres M, Romero-Fierro D, Estrella-Nuñez J, Arcentales-Vera B, Chichande-Proaño E, Bucio E (2022) Polymeric composite of magnetite iron oxide nanoparticles and their application in biomedicine: a review. Polymers 14:752. https://doi.org/10.3390/polym14040752

Cheng L, Liu G, Zhao J, Jin W (2021) Two-dimensional-material membranes: manipulating the transport pathway for molecular separation. Acc Mater Res. https://doi.org/10.1021/accountsmr.0c00092

Chung TS, Zhang S, Wang KY, Su J, Ling MM (2012) Forward osmosis processes: yesterday, today and tomorrow. Desalination 287:78–81. https://doi.org/10.1016/j.desal.2010.12.019

Cornwell RM, Schwertmann U (2006) The iron oxides structure, properties, reactions, occurrences and uses, 2nd edn. Wiley VCH Verlag GmbH & Co. KGaA, Weinheim

Deng L, Li S, Qin Y, Zhang L, Chen H, Chang Z, Hu Y (2021) Fabrication of antifouling thin-film composite nanofiltration membrane via surface grafting of polyethyleneimine followed by zwitterionic modification. J Membr Sci 619:118564. https://doi.org/10.1016/j.memsci.2020.118564

Dong L, Huang X, Wang Z, Yang Z, Wang X, Tang CY (2016) A thin-film nanocomposite nanofiltration membrane prepared on a support with in situ embedded zeolite nanoparticles. Sep Purif Technol 166:230–239. https://doi.org/10.1016/j.seppur.2016.04.043

El-Zahhar AA, Alghamdi MM, Asiri BM (2019) Poly (vinyl chloride)-MMT composite membranes with enhanced properties and separation performance. Desalination Water Treat 155:381–389. https://doi.org/10.5004/dwt.2019.24075

Geoffrey HSL, Geise M, Miller DJ, Freeman BD, Mcgrath JE, Paul DR (2010) Water purification by membranes: the role of polymer science. J Polym Sci Part B Polym Phys 48:1685–1718. https://doi.org/10.1002/polb.22037

Gong G, Wang J, Nagasawa H, Kanezashi M, Yoshioka T, Tsuru T (2014) Synthesis and characterization of a layered-hybrid membrane consisting of an organosilica separation layer on a polymeric nanofiltration membrane. J Membr Sci 472:19–28. https://doi.org/10.1016/j.memsci.2014.08.030

Han J, Yang D, Zhang S, Wang L, Jian X (2014) Preparation and performance of SPPES/PPES hollow fiber composite nanofiltration membrane with high temperature resistance. Desalination 350:95–101. https://doi.org/10.1016/j.desal.2014.06.029

Hu M, Mi B (2013) Enabling graphene oxide nanosheets as water separation membranes. Environ Sci Technol 47:3715–3723. https://doi.org/10.1021/es400571g

Joseph N, Ahmadiannamini P, Jishna PS, Volodin A, Vankelecom IFJ (2015) "Up-scaling" potential for polyelectrolyte multilayer membranes. J Membr Sci 492:271–280

Khorshidi B, Hajinasiri J, Ma G, Bhattacharjee S, Sadrzadeh M (2016) Thermally resistant and electrically conductive PES/ITO nanocomposite membrane. J Membr Sci 500:151–160. https://doi.org/10.1016/j.memsci.2015.11.015

Kim KJ, Fane AG, Nystrom M, Pihlajamaki A, Bowen WR, Mukhtar H (1996) Evaluation of electro osmosis and streaming potential for measurement of electric charges of polymeric membranes. J Membr Sci 116:149–159. https://doi.org/10.1016/0376-7388(96)00038-5

Kim S, Chu KH, Al-Hamadani YAJ, Park CM, Jang M, Kim DH, Yu M, Heo J, Yoon Y (2018) Removal of contaminants of emerging concern by membranes in water and wastewater: a review. Chem Eng J 335:896–914. https://doi.org/10.1016/j.cej.2017.11.044

Kumar S, Garg A, Chowdhuri A (2019) Sonication effect on graphene oxide (GO) membranes for water purification applications. Mater Res Express 6:085620. https://doi.org/10.1088/2053-1591/ab1ffd

Kydralieva KA, Dzhardimalieva GI, Yurishcheva AA, Jorobekova SJ (2016) Nanoparticles of magnetite in polymer matrices: synthesis and properties. J Inorg Organomet Polym 26(5):921–1106. https://doi.org/10.1007/s10904-016-0436-1

Lau WJ, Ismail AF, Misdan N, Kassim MA (2012) A recent progress in thin film composite membrane: a review. Desalination 287:190–199. https://doi.org/10.1016/j.desal.2011.04.004

Lee J, Chae HR, Won YJ, Lee K, Lee CH, Lee HH, Kim IC, Lee JM (2013) Graphene oxide nanoplatelets composite membrane with hydrophilic and antifouling properties for wastewater treatment. J Membr Sci 448:223–230. https://doi.org/10.1016/j.memsci.2013.08.017

Li XA, Zhang B, Ju CH, Han XJ, Du YC, Xu P (2011) Morphology-controlled synthesis and electromagnetic properties of porous Fe_3O_4 nanostructures from iron alkoxide precursors. J Phys Chem C 115:12350–12357. https://doi.org/10.1021/jp203147q

Li X, Chen Y, Hu X, Zhang Y, Hu L (2014) Desalination of dye solution utilizing PVA/PVDF hollow fiber composite membrane modified withTiO2 nanoparticles. J Membr Sci 471:118–129. https://doi.org/10.1016/j.memsci.2014.08.018

Liu G, Gui S, Zhou H, Zeng F, Zhou Y, Ye H (2014) A strong adsorbent for Cu^{2+}: graphene oxide odified with triethanolamine. Dalt Trans 43:6977–6980. https://doi.org/10.1039/C4DT00063C

Ma X, Yang Z, Yao Z, Guo H, Xu Z, Tang CY (2019) Tuning roughness features of thin film composite polyamide membranes for simultaneously enhanced permeability, selectivity and antifouling performance. J Colloid Interface Sci 540:382–388. https://doi.org/10.1016/j.jcis.2019.01.033

Ormanci AT, Tas CE, Keskin B, Billur E, Ozbulut S, Turker T, Imer D, Tufekci N, Menceloglu YZ, Unal S, Koyuncu I (2020) Thin-film composite nanofiltration membranes with high flux and dye rejection fabricated from disulfonated diamine monomer. J Membr Sci 60:118172. https://doi.org/10.1016/j.memsci.2020.118172

Peeters JM, Boom JP, Mulder MH, Strathmann H (1998) Retention measurements of nanofiltration membranes with electrolyte solutions. J Membr Sci 145:199–209. https://doi.org/10.1016/S0376-7388(98)00079-9

Pourjafar S, Rahimpour A, Jahanshahi M (2012) Synthesis and characterization of PVA/PES thin film composite nanofiltration membrane modified with TiO_2 nanoparticles for better performance and surface properties. J Ind Eng Chem 18:1398–1405. https://doi.org/10.1016/j.jiec.2012.01.041

Rathore AS, Shirke A (2011) Recent developments in membrane-based separations in biotechnology processes: review. Prep Biochem 41:398–421. https://doi.org/10.1080/10826068.2011.613976

Rodemann K, Staude E (1995) Electrokinetic characterization of porous membranes made from epoxidized polysulfone. J Membr Sci 104:147–155. https://doi.org/10.1016/0376-7388(95)00024-7

Romero-Fierro D, Camacho-Cruz L, Bustamante-Torres M, Hidalgo-Bonilla S, Bucio E (2022) Modification of cotton gauzes with poly(acrylic acid) and poly(methacrylic acid) using gamma radiation for drug loading studies. Radiat Phys Chem 190:109787. https://doi.org/10.1016/j.radphyschem.2021.109787

Schaep J, Van DB, Vandecasteele C, Wilms D (1998) Influence of ion size and charge in nanofiltration. Sep Purif Technol 14:155–162. https://doi.org/10.1016/S1383-5866(98)00070-7

Singh A, Shirolkar M, Limaye MV, Gokhale S, Malek CK, Kulkarni SK (2013) A magnetic nano-composite soft polymeric membrane. Microsyst Technol 19:409–418. https://doi.org/10.1007/s00542-012-1646-2

Stankovich S, Dikin DA, Dommett GH, Kohlhaas KM, Zimney EJ, Stach EA, Piner RD, Nguyen ST, Ruoff RS (2006) Graphene-based composite materials. Nature 442:282–286. https://doi.org/10.1038/nature04969

Ursino C, Di Nicolo E, Gabriele B, Criscuoli A, Figoli A (2019) Development of a novel perfluoropolyether (PFPE) hydrophobic/hydrophilic coated membranes for water treatment. J Membr Sci 581:58–71. https://doi.org/10.1016/j.memsci.2019.03.041

Wei X, Kong X, Yang J, Zhang G, Chen J, Wang J (2013) Structure influence of hyperbranched polyester on structure and properties of synthesized nanofiltration membranes. J Membr Sci 440:67–76. https://doi.org/10.1016/j.memsci.2013.03.034

Wilbert MC, Delagah S, Pellegrino J (1999) Variance of streaming potential measurements. J Membr Sci 161:247–261. https://doi.org/10.1016/S0376-7388(99)00117-9

Wu D, Huang Y, Yu S, Lawless D, Feng X (2014) Thin film composite nanofiltration membranes assembled layer-by-layer via interfacial polymerization from polyethylenimine and trimesoylchloride. J Membr Sci 472:141–153. https://doi.org/10.1016/j.memsci.2014.08.055

Xu Y, Lin J, Gao C, Bart V, Shen Q, Shao H, Shen J (2017) Preparation of high-flux nanoporous solvent resistant PAN membrane with potential fractionation of dyes and Na$_2$SO$_4$. Ind Eng Chem Res 56:11967–11976. https://doi.org/10.1021/acs.iecr.7b03409

Ye CC, Zhao FY, Wu JK, Weng XD, Zheng PY, Mi YF, An QF, Gao CJ (2017) Sulfated polyelectrolyte complex nanoparticles structured nanofiltration membrane for dye desalination. Chem Eng J 307:526–536. https://doi.org/10.1016/j.cej.2016.08.122

Zhang SJ, Liu XH, Zhou LP, Peng WJ (2012) Magnetite nanostructures: One-pot synthesis, superparamagnetic property and application in magnetic resonance imaging. Mater Lett 68:243–246. https://doi.org/10.1016/j.matlet.2011.10.070

Zhao S, Ba C, Yao Y, Zheng W, Economy J, Wang P (2018) Removal of antibiotics using polyethylenimine cross-linked nanofiltration membranes: relating membrane performance to surface charge characteristics. Chem Eng J 335:101–109. https://doi.org/10.1016/j.cej.2017.10.140

Zheng L, Su W, Qi Z, Xu Y, Zhou M, Xie Y (2011) First-order metal-insulator transition and infrared identification of shape-controlled magnetite nanocrystals. Nanotechnology 22:485706. https://doi.org/10.1088/0957-4484/22/48/485706

Zhou C, Shi Y, Sun C, Yu S, Liu M, Gao C (2014) Thin-film composite membranes formed by interfacial polymerization with natural material sericin and trimesoylchloride for nanofiltration. J Membr Sci 471:381–391. https://doi.org/10.1016/j.memsci.2014.08.033

Electrical Properties and Alkali-Pathways Simulation of New Mixed Ionic Conductor $Na_2K_2Co_{5.5}Al(AsO_4)_6$

Amira Marzouki[1,], Ameni Brahmia[2,3], Yara N. AlTherwah[2], Mutasem Z. Bani-Fwaz[2], Mohamed Hussien[2,4], Riadh Marzouki[2,5,**], Mohamed Faouzi Zid[6]*

[1] Laboratory of Signal Image and Energy Mastery, Engineering National Higher School of Tunis, Tunis, Tunisia
[2] Chemistry Department, College of Science, King Khalid University, Abha 61413, Saudi Arabia
[3] Laboratoire des Materiaux et de l'Environnement pour le Developpement Durable, LR18ES10, University of Tunis El Manar, 2092, Tunisia
[4] Pesticide Formulation Department, Central Agricultural Pesticide Laboratory, Agricultural Research Center, Dokki, Giza 12618, Egypt
[5] Chemistry Department, Faculty of Sciences of Sfax, University of Sfax, 3038, Tunisia
[6] Laboratory of Materials, Crystallochemistry and Applied Thermodynamics, Faculty of Sciences of Tunis, University of Tunis El Manar, Tunisia.
[*]E-mail : amira_marzouki@hotmail.com, rmarzouki@kku.edu.sa

A new disodium dipotassium cobalt aluminate hexaarsenate $Na_2K_2Co_{5.5}Al(AsO_4)_6$ was synthesized by solid state route at 1193 K. The crystalline structure was determined by X-ray diffraction at room temperature. The new member of β-Xenophyllite material crystallizes in the monoclinic of the C2/m space group with the unit cell parameters: a=10.738(3) Å, b= 14.793 (2) Å, c=6.723(3) Å, β = 105.365° (10), V= 1336.8(4) Å^3 and Z=4. The crystal structure validation was carried out using Bond Charge distribution (CHARDI) and Bond Valence Sum (BVS) tools. The anionic framework can be described as tridimentionnal anionic framework sowing large hexagonal tunnels along [100] direction where the sodium and potassium cations are located. The electrical property of the title material was characterized by impedance spectroscopy technique from 553 to 753K temperature range using the frequency response analyzer with 0.05V amplitude signal over the range of 13MHz-5Hz. The conductivity value of the sample at 533K is 2.06×10^{-5} S.cm^{-1}, the activation energy Ea = 0.536eV, show that the $Na_2K_2Co_{5.5}Al(AsO_4)_6$ compound is an ionicconductor. The alkali ions conduction pathways in the studied compound were simulated via the bond valence site energy model (BVSE).

1. INTRODUCTION

The crystallographic systems A–Co/Al–P/As–O (A: monovalent cation) have shown a variety of structural types in recent years, including LiCoXO_4 (X=P, As) [1, 2], $Co_xAl_{1-x}PO_4(NH_4)_x(NH_3)_{0.5-x}$ (x 0.4) [3, 4], and $Na_{0.09}(Co_{0.06}Al_{0.96})$ (PO4) [4], $Ag_{3.39}Co_2(P_2O_7)_2$ [5], triclinic form pyrophosphate in the, $A_2CoP_2O_7$, displaying bidimensional framework as mellilite structure [6, 7], $ACo_3H_2(AsO_4)_3$ (A=Na, Ag) [8, 9] alluaudites-like arsenate and $Na_4Co_{5.63}Al_{0.91}(AsO_4)_6$ [10] as Xenophellite material. In this regard, we investigated the A_2O-CoO/Al_2O_3-X_2O_5 (A = monovalent cation, X = P or As) systems, which are still understudied. Solid state reaction was used to prepared the $Na_4Co_{5.63}Al_{0.91}(AsO_4)_6$ compound in single-crystal and polycrystalline forms [11]. The structural analysis revealed that in the arsenate materials the Na^+ cations in a three-dimensional structure with hexagonal canals. The study of structural properties paves the pathways for a better understanding of electrical properties. As a result, the structural data, open framework, partial occupations, and significant agitations of Na+ ions in big tunnels indicate that these features encouraged ionic mobility.

The goal of this study is to use XRD single crystal, XRD Powder, and EDX techniques to analyze the $Na_2K_2Co_{5.5}Al(AsO_4)_6$ material. The electrical investigation was carried out via impedance spectroscopy in order to optimize the sintering conditions and microstructure. The Bond Valence Site Energy BVSE model was used to investigate the relationship between structure and ionic conductivity.

2. EXPERIMENTAL AND COMPUTATIONAL METHODS

The title material was synthesized as single crystal and polycrystalline powder using the solid-state route. Commercial chemicals were obtained and employed without additional purification. Previous works provide more information on the synthesis procedure [12]. In this work, potassium and sodium was taken in an equivalent molar ratio Na:K = 1:1. The crystallinity of the sample was first verified under polarizing microscope then by using the single crystal diffractometer.

In a platinum crucible, a mixture of high-purity reagents ($NaNO_3$, KNO_3, $Co(NO_3)_2.6H_2O$, Al_2O_5, and As_2O_5) is mixed in the stoichiometric ratios of the single crystal $Na_2K_2Co_{5.5}Al(AsO_4)_6$. The sample is progressively annealed in air to 673K for 24 hours to eliminate volatile products. Pellets-shaped samples were generated in a second step by uniaxial pressing at 2kbar and heating at 1143 K for 3 days. The material was brought to room temperature gradually. The single-crystal structure was confirmed by the powder X-ray diffraction pattern.

For the single crystal structure determination, a suitable single crystal with dimensions of 0.27×0.24×0.1 mm3 was selected. The structural data was obtained using the MoK (=0.71073) radiation on an Enraf-Nonius CAD-4 [13-14] diffractometer at room temperature. The standard corrections were used, as well as absorption through a psi-scan [15] and secondary extinction correction [16] for Lorentz and polarization effects. The SHELX-97 [16] computer programs contained in the WinGX software package [17] were used for all subsequent computations. The Diamond 3 software [18] was used to view the crystal structure.

Charge Distribution analysis CHARDI [19–20] and Bond Valence Sum BVS [21-22] were performed with the CHARDI2015 [20] and SoftBV [23] programs as validation tools, respectively.

Energy-Dispersive X-ray Spectroscopy (EDX) and microstructure control was performed by SEM using an apparatus of the type Quanta 200.

At room temperature, an X-ray powder diffraction pattern was recorded using a Philips D8 diffractometer with copper anticathode K (=1.5406) covering the range of 10° to 70°, with a step of roughly 0.02°.

The measurements were preceded by a pretreatment of the samples in order to lower the mean particle size of the generated powder to control the relative density of the ceramic for the evaluation of the electrical properties, with the goal of obtaining dense ceramic. After that, the material was ball-milled in ethanol using a FRITSCH planetary micromill pulverisette device with agate jars and agate balls. A lesser amount of powder (5 g) and six agate balls (about 10 mm diameter) are placed in the agate jars for ball milling. To prevent pollutants and unnecessary heating during the experiment, the grinding was done in ethanol. For the course of the experiment, 10 minutes milling sessions were alternated with 5 minutes stop sequences. Despite the presence of ethanol, milling is still an intense operation that results in a significant heating of the entire apparatus. Between two milling operations, the pause phase allows the system to cool down.

Pellet samples of various relative densities were compacted using a uniaxial press, followed by a sintering in air at 1143 K for 2 hours (5 K.min-1 heating and cooling rates). Utilizing a Hewlett Packard 4192A with frequency response analyser (F.R.A.) in the 13x106 Hz – 5Hz frequency range, electrical measurements were recorded in air using complex impedance spectroscopy. R.F. magnetron sputtering was used to deposit silver electrodes on the two faces of each sample. The analysis was carried out at the open circuit voltage with a 50 mV supplied AC voltage. The sample was connected to the F.R.A. by platinum grids and wires, then placed in a Pyrox furnace in a stainless steel sample holder inside an alumina tube. The relative densities of the ceramic were calculated using precise measurements of sample sizes and weights, as well as a comparison to the theoretical density derived from the crystal structure.

The sodium migration in the interlayer space was simulated using the BVSE (Bond Valence Site Energy) model [22-23]. The BVSE model is a more recent evolution of Pauling's (1929) [24] BVS model for explaining the production of inorganic compounds. Brown & Altermatt 1985 [25] and Adams 2001 [23] enhanced the BVS model, resulting in the following formula for an individual bond-valence sA-X:

$$s_{A-X} = \exp(\frac{R_0 - R_{A-X}}{b}) \quad (1)$$

The distance between counter-ions A and X is given by RA-X, and R0 and b are fitted constants, with R0 being the length of a unit valence bond.

Since 1999, the BVS model is adopted in the anionic framework to simulate cation transportation by following the valence unit as a function of migration distance [26]. Adams proposed a method for relating valence units to potential energy scales that took electrostatic interactions into account in 2011. See the references [22-23] for further information on the model. The 3DBVSMAPPER algorithm was used to calculate the BVSE using Na+ as a test ion and default parameters [26].

3. RESULTS AND DISCUSSION

3.1. Crystal structure determination and validation

The structure resolution is carried out by direct methods using the SHELXS-97 software [16]. Three peaks attributed to cobalt atoms, one to aluminum, another to arsenic, and a few oxygen atoms are located first. The obtained results are refined by the SHELXL-97 software [16]. The unit cell parameters of the title material are very close to the arsenate $Na_4Co_{5.63}Al_{0.91}(AsO_4)_6$. The structure was therefore solved based on the atomic coordinates of this isotype material. In the first step, the coordinates and thermal agitation factors of the cobalt/aluminium, arsenic and oxygen atoms were resolved. At this stage, the reliability factors are R = 0.21 and Rw (F2) = 0.42. The feasibility factors R and Rw then converge towards 0.171 and 0.372, respectively. The high agitations of the Co/Al elements prompted us to an additional refinement of their occupations. The obtained occupation is five significant peaks appearing in the Fourier-Difference synthesis were observed near Na1, Na2 and Na3 cations. These peaks were attribute to the fraction of potassium ions. Three simultaneous constraints EXYZ, EADP and SUMP are used on the Na:K sites with 0.5:0.5 occupatins. The obtained agitations are satisfactory and the final refinement of the atomic parameters in anisotropic thermal agitation mode brought these factors down to R = 0.031 and Rw (F2) = 0.094 where the empirical formula is $Na_2K_2Co_{5.5}Al(AsO_4)_6$. A summary of the crystallographic data, conditions of the data collection and the structure refinement results is given in Table 1. The atomic coordinates and the equivalent isotropic thermal factors are in Table 2.

Table 1. Summary of crystallographic data of $Na_2K_2Co_{5.5}Al(AsO_4)_6$.

Crystal data	
Empirical formula	$Na_2K_2Co_{5.5}Al(AsO_4)_6$
Crystal system ; Space group	Monoclinic; C2/m
Unit cell parameters	a = 10.7381 (3) Å; b= 14.793 (3) c = 6.723 (3) Å $\beta = 105.365 °$ (10)
Volume ; Z	1033.2(4) $Å^3$; 2
Formula weight ; $\rho_{calc.}$	1336.88 $gmol^{-1}$; 4.311 gcm^{-3}
Absorption coefficient (μ)	14.571 mm^{-1}
Crystal sharp ; color	Parallelepiped ; pink
Crystal size	$0.27 \times 0.22 \times 0.17$ mm
Data collection	
Diffractometer	Enraf-Nonius CAD-4
Wavelength ; Temperature	$\lambda_{Mo K\alpha}$=0.71073 Å ; 298(2) K
Theta range for data collection	$2.4° \leq \theta \leq 26.97°$
Limiting indices	$-13 \leq h \leq 13$; $-1 \leq k \leq 18$; $-8 \leq l \leq 1$
Scan mode	ω/2θ
Absorption correction ; T_{min} ; T_{max}	psi-scan ; 0.076; 0.054
Standards; frequency. (min); decay (%)	2 ; 120 ; 1
Reflections collected	1448

Refinement	
Refinement method	Full-matrix least-squares on F^2
Final R indices [$I > 2\sigma(I)$]	R(F)= 0.031; wR(F^2)= 0.094,
Reflections ; parameters	1146; 116
$\Delta\rho_{max}$; $\Delta\rho_{min}$ (eÅ^{-3})	0.80 ; -0.77
Goodness of fit (S)	1.103

Table 2. Atomic coordinates-and equivalent isotropic thermal factors in $Na_2K_2Co_{5.5}Al(AsO_4)_6$.

Atom	x	y	z	U_{eq}^*(Å^2)	Occ. (<1)
As1	0.598149 (5)	0.320868 (7)	0.289009 (5)	0.00696 (7)	
As2	0.821023 (3)	½	0.061819 (7)	0.00755 (10)	
Co1	0.320159 (5)	0.318455 (7)	0.180649 (3)	0.00811 (8)	0,286 (11)
Al1	0.320159 (5)	0.318455 (7)	0.180649 (3)	0.00811 (8)	0,714 (11)
Co2	0	0.664005 (7)	0	0.01241 (6)	0,607 (8)
Al2	0	0.664005 (7)	0	0.01241 (6)	0,143 (8)
Co3	½	½	0	0.00687 (8)	
O1	0.991924 (3)	0.266416 (3)	0.271529 (5)	0.01132 (6)	
O2	0.690654 (5)	0.291436 (7)	0.130191 (3)	0.01661 (8)	
O3	0.939341 (5)	½	0.277716 (5)	0.01607 (7)	
O4	0.831376 (3)	0.591728 (3)	-0.086272 (4)	0.02120 (9)	
O5	0.690296 (5)	0.349081 (7)	0.522433 (5)	0.01229 (6)	
O6	0.680672 (4)	½	0.126304 (5)	0.01064 (11)	
O7	0.487546 (7)	0.406127 (3)	0.202779 (5)	0.00942 (7)	
Na1	0.073380 (5)	0.115487 (3)	0.492822 (8)	0.02991 (11)	0..25
K1	0.073380 (5)	0.115487 (3)	0.492822 (8)	0.02991 (11)	0.25
Na2	0. 682812 (5)	½	0.423131 (9)	0.03732 (12)	0.25
K2	0.682812 (5)	½	0.423131 (9)	0.03732 (12)	0.25
Na3	0.928771 (9)	½	0.476221 (9)	0.06394 (8)	0.25
K3	0.928771 (9)	½	0.476221 (9)	0.06394 (8)	0.25
$^{(*)}$Uéq = $(1/3)\sum_i\sum_j U^{ij}a_i^*a_j^*a_i.a_j$					

Bond valence sum model BVS [21-22] and charge distribution method CHARDI [23-24] validation tools supported the proposed structural model. The formal oxidation numbers agree with the valence sums, V, calculated using the BVS model, and charges Q calculated using the CHARDI analysis. Table 4 summarises the results of the CHARDI and BVS calculations.

Table 4. CHARDI and BVS analysis of cation polyhedra in $Na_2K_2Co_{5.5}Al(AsO_4)_6$

Cation	q(i).sof(i)	Q(i)	V(i)	CN(i)	ECoN(i)
*M*1	2,714	2,810	2,701	6	5,912
*M*2	1,647	1,567	1,020	4	3,978
Co3	2,00	1,990	1,981	6	5,898
As1	5,00	5,033	5,011	4	3,990

As2	5,00	5,001	4,870	4	3,983
Na1/K1	0,50	0,498	0,471	5	4,589
Na2/K1	0,50	0,501	0,413	7	6,437
Na3/K1	0,50	0,504	0,471	6	5,970

$M1=Co_{0,286}Al_{0,714}$; $M2=Co_{0,607}Al_{0,143}\square_{0,250}$; q(i) : oxidation number;

sof(i) : taux d'occupation du site ; sodium CNs pour $d(Na–O)^{max}=3,00$ Å ;

$\sigma=[\Sigma_i(q_i-Q_i)^2/N-1]^{1/2}=0,049$.

Qualitative EDX analysis of the single crystal of $Na_2K_2Co_{5.5}Al(AsO_4)_6$ confirmed the existence of Co, As, Al, Na, K, and oxygen, confirming the presence of the previous elements. The sample holder produced a carbon peak (Figure 3).
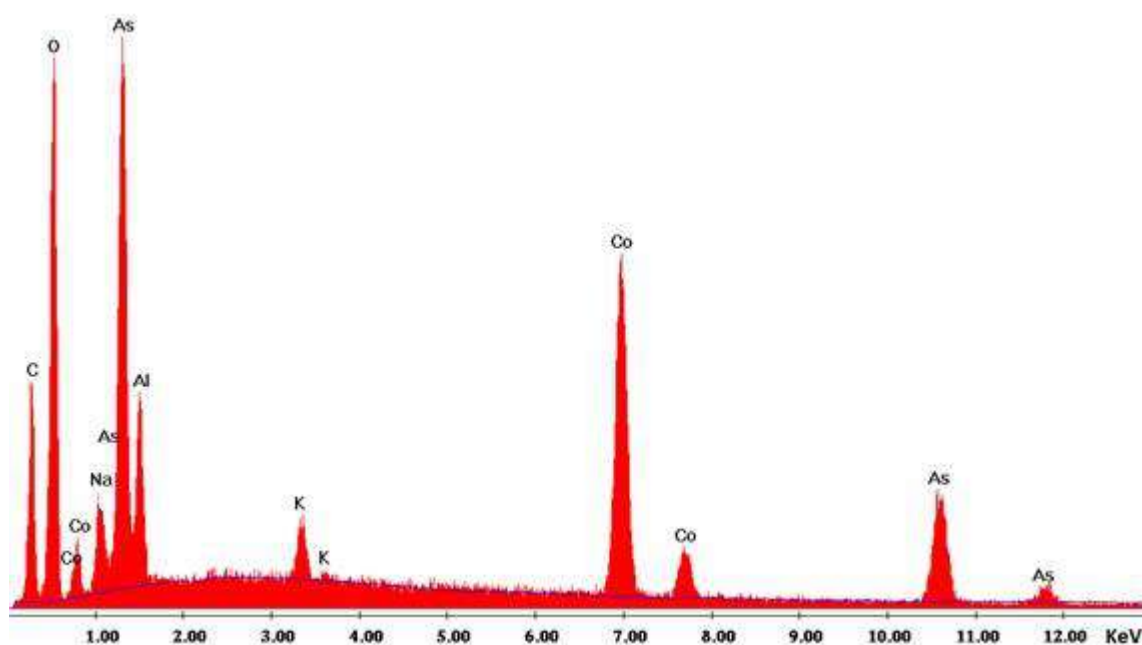
Figure 1. EDX spectrum of $Na_2K_2Co_{5.5}Al(AsO_4)_6$.

3.1. Crystal structure description

The $Na_2K_2Co_{5.5}Al(AsO_4)_6$ material is a new member of the $Ag_4Co_7(AsO_4)_6$ [27], $Na_4Co_7(AsO_4)_6$ [28], and $Na_4Co_{5.63}Al_{0.91}(AsO_4)_6$ [29] isostructural phases. Two tetrahedra AsO_4, two octahedra $Co3O_6$, and $M1O_6$ ($M1 = Co_{0.286}Al_{0.714}$) and $M2O_4$ ($M2= Co_{0.607}Al_{0.143}$) tetrahedra constitute the $Na_2K_2Co_{5.5}Al(AsO_4)_6$ structure. The polyhedra (Co, Al) are organized in the ab plan. The corners of the Co_2O_{10} octahedral units are joined by $M2O_4$ tetrahedra. Polyhedral chains propagate in the [100] direction as a result. The ribbons are connected by $M1O_6$ octahedra, while the windows in these plans are occupied by $As1O_4$ tetrahedra. $As2O_4$ tetrahedra share corners and edges with $M1O_6$ polyhedra, ensuring a connection between the plans. Hexagonal tunnels along a (Figure 4) connect with quadrilateral windows parallel to the [010] direction in the three-dimensional framework. The $(Na/K)^+$

cations spread on three distinct sites partially occupied at 50% are used to locate the tunnels. The agitation of the alkali cations is relatively high.
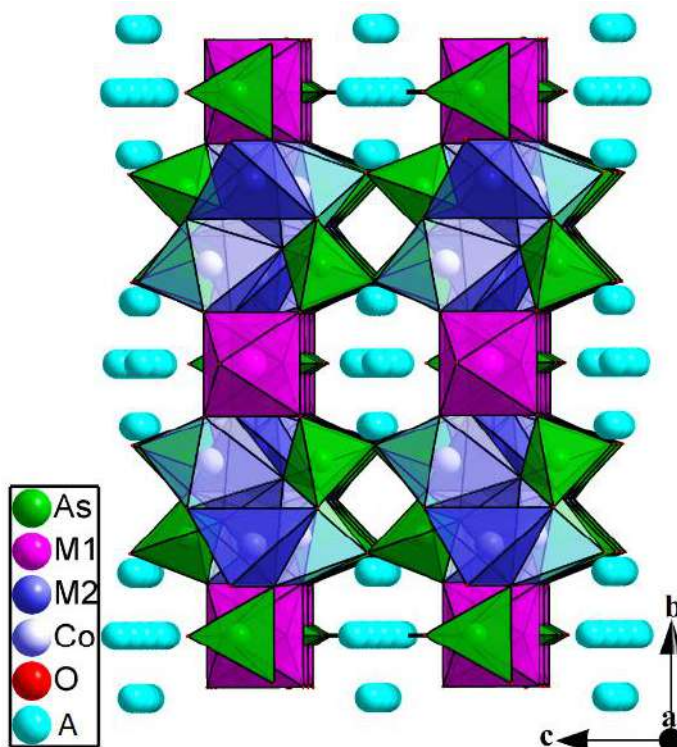
Figure 2. Projection of $Na_2K_2Co_{5.5}Al(AsO_4)_6$ structure along *a* direction
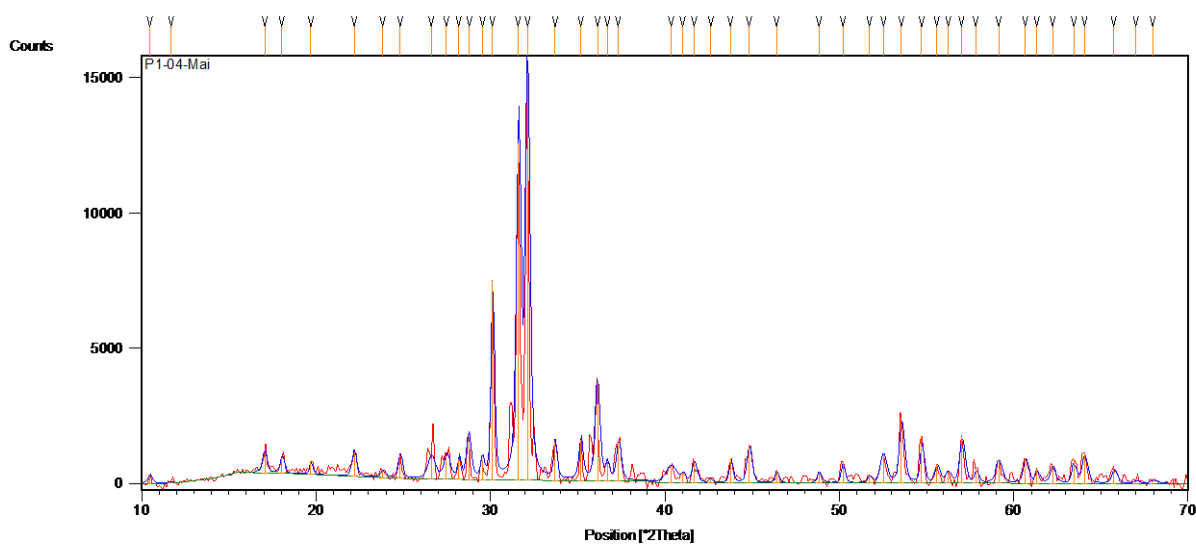
Figure 3. XRD pattern of the prepared powder of $Na_2K_2Co_{5.5}Al(AsO_4)_6$.

The anionic framework of the studied material is thus open, and alkali cation mobility through the tunnels appears to be possible, prompting us to investigate the ionic conduction of the studied material.

A Bruker D8 diffractometer was used to record an X-ray powder diffraction pattern using Cu anticathode K (=1.5406), in the from 10° to 70° with step of 0.02°, at room temperature. The XRD of the prepared powder and the XRD monocrystal determined from the crystallographic information file (CIF) of the single crystal are similar which confirm the purity of our material. The unit cell parameters of the prepared powder were determine using profile matching refinement via the X'Pert HighScore Software [30]: a = 10.736 (7) Å; b= 14.794 (8) c = 6.722 (7) Å and β = 105.36 ° (6) of the monoclinic system of the C2/m space group.

3.2. Infrared spectroscopy

Figure 5 shows the infrared spectrum measured in the region where the main vibrations occur.
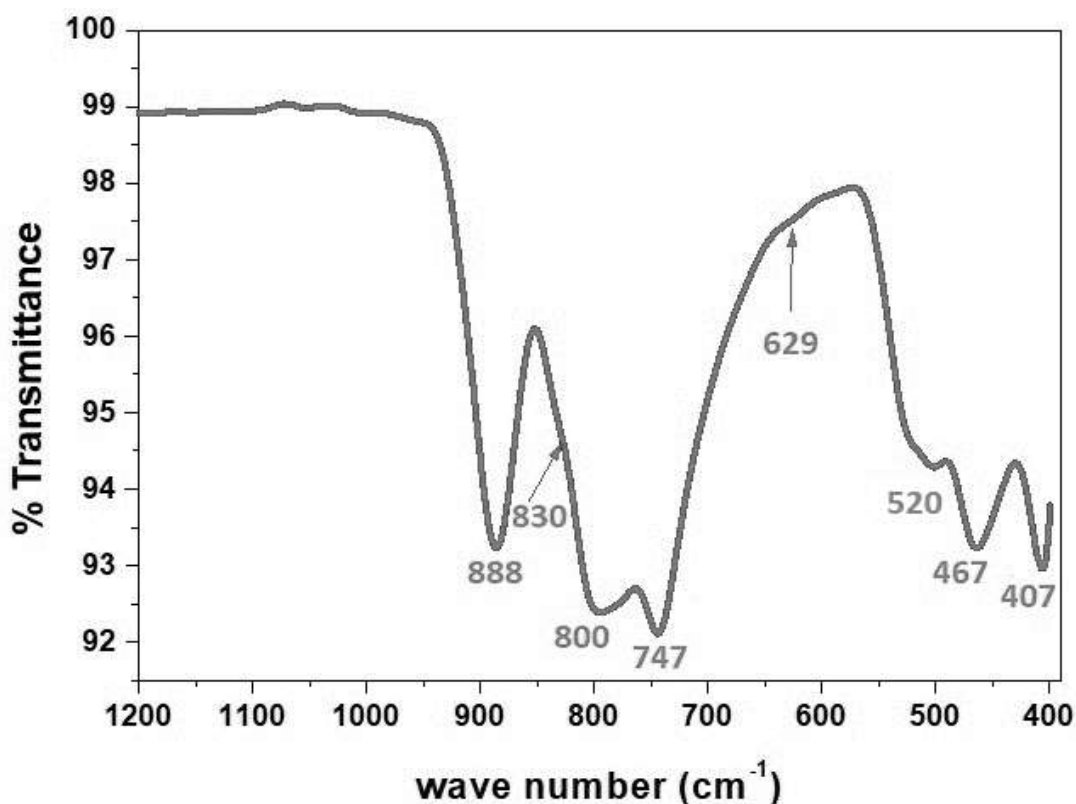
Figure 4. IR spectrum of $Na_2K_2Co_{5.5}Al(AsO_4)_6$ compound

Table 3 shows the vibrational bands assigned to the MO_4, AsO_4, and MO_6 groups, based on earlier work, particularly [11,29].

Table 3. Assignment of vibration frequencies in $Na_2K_2Co_{5.5}Al(AsO_4)_6$ compound $M=(Co,Al)$

Wave number (cm^{-1})	Assignment	Wave number (cm^{-1})	Assignment
407	$v_2(AsO_4)$	747	$v_1(MO_6)$
467	$v_4(AsO_4)$	800	$v_1(MO_4)$
520	$v_2(MO_6)$	830	$v_1(AsO_4)$
629	$v_3(MO_6)$	888	$v_3(AsO_4)$

3.3. Electrical properties

The measurements for the electrical analyses were preceded by a sample pretreatment to minimize the mean particle size of the acquired powder. Planatary grinding was carried out using FRISCH micromill pulverisette 7. Uniaxial pressing was followed by isostatic pressing at 2.5 kbar and sintering for 2 hours at 600 °C with 5 °C.min-1 heating and cooling rates. With a final diameter of 8 mm and a thickness of 2 mm, the sample obtained exactly 85% of the theoretical density after these treatments. To maintain good electric connections, platinum electrodes were glued to the two faces of the pellet with platinum paste. A Hewlett-Packard 4192a Impedance Analyzer was used to perform impedance spectroscopy studies. The impedance spectra were measured across a frequency range of 5 Hz to 13 MHz.
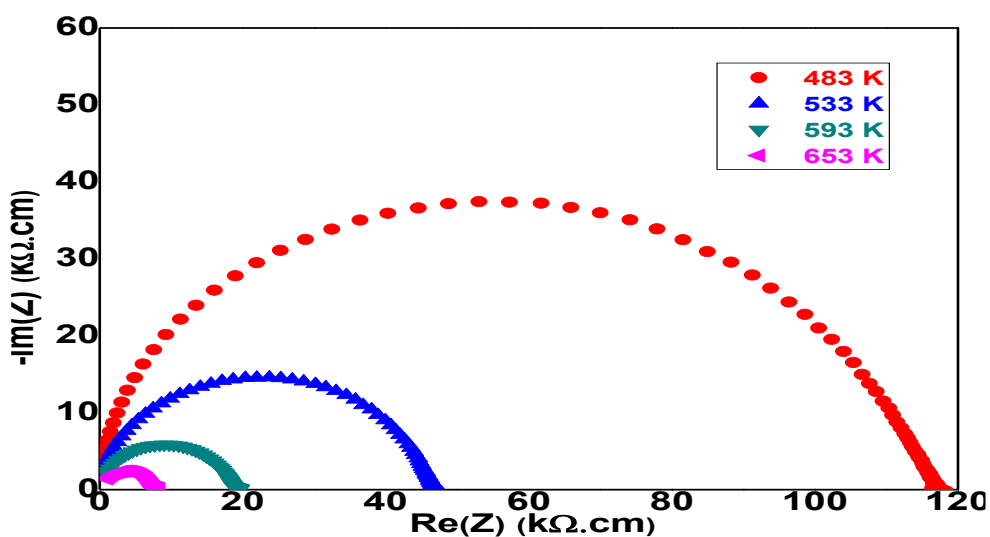
Figure 5. Impedance spectra of $Na_2K_2Co_{5.5}Al(AsO_4)_6$ recorded at 483-653K in air.

Complex impedance spectroscopy was used to determine the electrical characteristics of the title chemical. The electrical parameters were measured in air in the temperature range of 443–733 K after each phase of stabilization and in the frequency range of 5Hz–13MHz. The applied voltage was 0.5 V, which allowed aberrant points at low frequencies to be eliminated. The electrical parameters were determined using the Zview computer application [31] and a conventional electrical circuit as follows: CPE is a constant phase element in R/CPE-R/CPE:

$$Z_{CPE} = \frac{1}{A(j\omega)^p} \quad (4)$$

To account for instrumental contributions, especially at high temperatures, a supplemental inductance L was imposed. According to the following relationships, the true capacitance was determined from the pseudo-capacitance:

$$\omega_0 = (RA)^{-1/p} = (RC)^{-1} \quad (5)$$

where ω_0 = relaxation frequency, A = pseudo-capacitance calculated from the CPE, and C = the actual capacitance. Table 5 summarizes the electrical parameters.

Table 5. Electrical parameters of $Na_2K_2Co_{5.5}Al(AsO_4)_6$ determined by impedance spectroscopy

T (°C)	T (K)	1000/T (K^{-1})	Rt (10^4 Ω)	σ (10^{-5} S cm^{-1})	Ln(σ×T)
160	433	2.30946882	25.86	0.23	-7.66190007
210	483	2.07039337	7.06	0.86	-5.48901724
260	533	1.87617261	2.93	2.06	-4.51163079
320	593	1.68634064	1.18	5.10	-3.49778949
380	653	1.53139357	4.75	12.7	-2.48811313
445	718	1.39275766	1.90	31.9	-1.4753481
500	773	1.29366106	8.80	68.6	-0.63448641
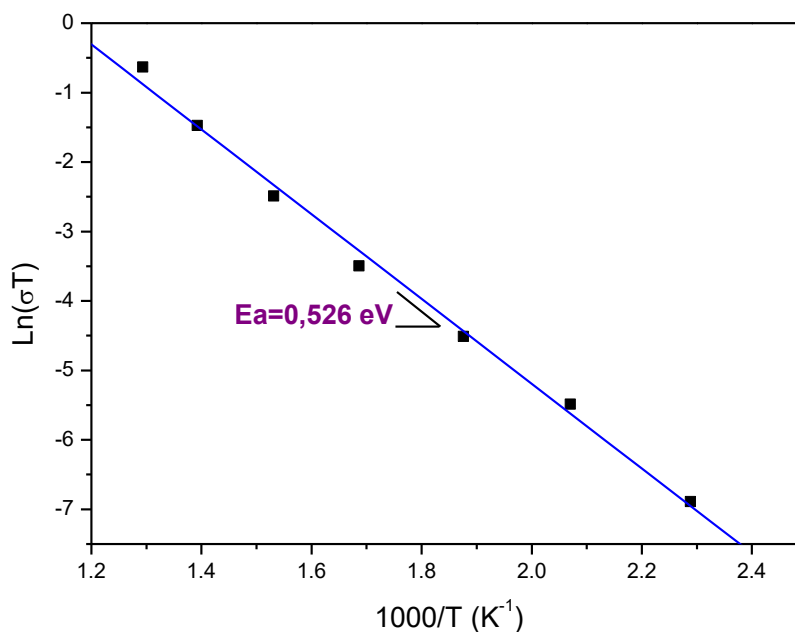
Figure 6. Arrhenius plot of conductivity of $Na_2K_2Co_{5.5}Al(AsO_4)_6$ sample.

The conductivity increases from 0.23×10^{-5} S cm^{-1} at 160°C to 68.6×10^{-5} S cm^{-1} at 500 °C (Table 5). Although, the conductivity value of the title material at 320 °C is higher than that of the parent material $Na_4Co_7(AsO_4)_6$ (2.51×10^{-5} S cm^{-1} at 360 °C [28]). The more critical parameter, the activation energy, decreases for $Na_4Co_7(AsO_4)_6$ compared to that of $Na_2K_2Co_{5.5}Al(AsO_4)_6$, i.e. 1.0 eV and 0.526 eV, respectively (Figure 6), in good agreement with the BVSE results discussed below.

3.4. Na$^+$ Transport pathways simulation

The BVSE simulation model was used to define the alkali-ion transport pathways in the anionic frameworks of the $Na_2K_2Co_{5.5}Al(AsO_4)_6$ via the 3DBVSMAPPER computer program.

Investigation of isosurfaces connecting sodium ion sites in the unit cells of isostructural materials show that the sodium can move along the *a* direction and form monodimensional infinite pathways (Fig. 7) while the calculated activation energy is 0.58 eV; suggest high ionic conductivity of the title material.
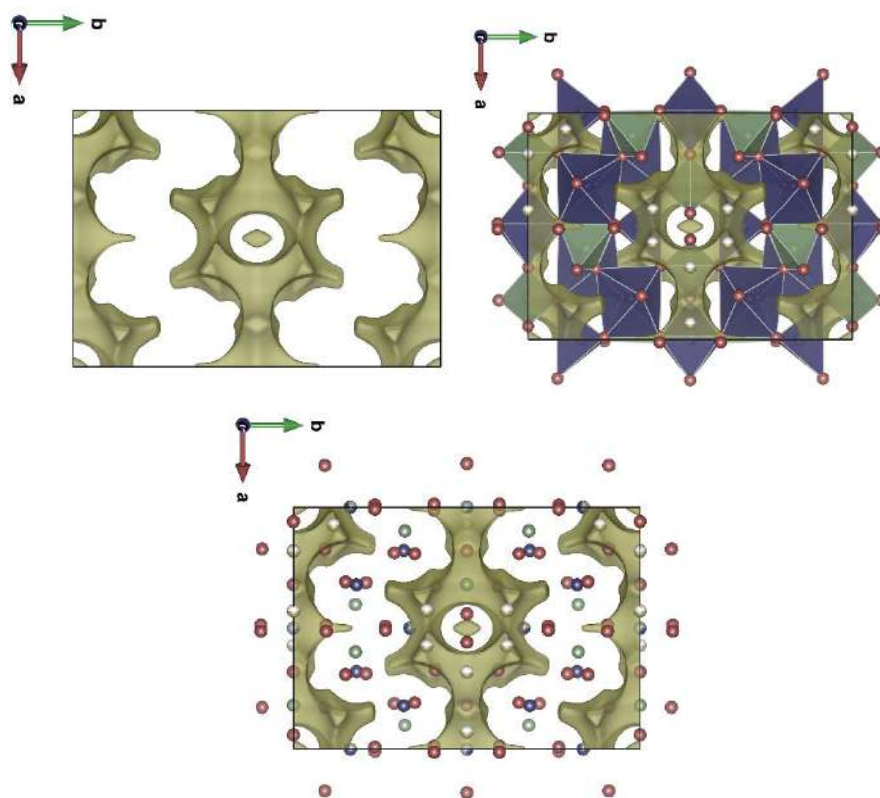
Figure 7. Projection along *c* direction of the $Na_2K_2Co_{5.5}Al(AsO_4)_6$ unit cell with coordination polyhera and without coordination polyhedra.

The BVS analyses support the structural studieswhich the most probable conduction pathways of the studied material are the tunnels of the *a* direction . Figure 8a shows the size of the hexagonal sections of tunnels . Two CoO_6 and two MO_6 octahedra, and two AsO_4 tetrahedra border these canals. These sections are the widest and therefore more conducive to sodium cation transport.

The [010] direction tends to be less favorable than the *a* direction. In fact, the square bases windows (Fig. 8b) produced along b direction have smaller section sized than those of the [100] direction, indicating that sodium ion migration is more advantageous in the *a* direction.

Crystallographic investigations, on the other hand, reveal that Co/Al substitution increase the tunnel section dimensions and also the unit cell parameters. In fact, the volume of the unit cell increase from V=1019.65(16) $Å^3$ in $Na_4Co_7(AsO_4)_6$ to V=1033.3(4) $Å^3$ in $Na_2K_2Co_{5.5}Al(AsO_4)_6$ which explain that the activation energy values of $Na_2K_2Co_{5.5}Al(AsO_4)_6$ are lower than that of $Na_4Co_7(AsO_4)_6$. In fact, sections tunnels along *a* direction in $Na_2K_2Co_{5.5}Al(AsO_4)_6$ are in the order: 4.467 - 4.823 Å. The tunnel sections along [100] direction $Na_4Co_7(AsO_4)_6$ are 4.636-4.730 Å.

Compared to activation energies of other phosphates such as $Na_{1.14}K_{0.86}CoP_2O_7$ (Ea = 1.34 eV) [32], $Na_{1.42}Ag_{0.58}CoP_2O_7$ (Ea = 1.37 eV) [33] and $Ag_{3.68}Co_2(P_2O_7)_2$ (Ea = 1.7 eV) [5] and other sodium compounds such as $Na_4Co_{5.63}Al_{0.91}(AsO_4)_6$ (Ea = 0.53 eV) [11] and sodium-cellulose (Ea = 0.49 eV and 0.68 eV) [34], $Na_2K_2Co_{5.5}Al(AsO_4)_6$ exhibit high electric conductivity with an activation energy value of 0.536 eV.

4. CONCLUSION

The studied compound, has been synthesized by solid-state reaction. Its structure has been determined by single-crystal XRD. FTIR spectroscopy show the existence of the vibrational group of the MO_6 and MO_4 (*M*=Co/Al) polyhedra. The Bond valence sum model (BVS) and charge distribution method (CHARDI) were used to approve the structural model. This structure, isostructural to $Na_2K_2Co_{5.5}Al(AsO_4)_6$, shows an open anionic framework facilitating monodimensional Na ionic conductivity. The modification of the crystallographic datadue to the Al/Co substitution reduces the activation energy of Na conductivity, as confirmed by impedance spectroscopy measurements and supported by BVSE simulation. Overall, our study suggests that the Al/Co substitution in the $Na_2K_2Co_{5.5}Al(AsO_4)_6$, can further improve Na ionic conductivity and thus rate capability of $Na_2K_2Co_{5.5}Al(AsO_4)_6$, based cathodes.

References

1. F. Erragh, A. Boukhari and E. M. Holt, *Acta Crystallogr. C Struct. Chem*., 52 (8) (1996) 1867
2. M. V. V. M. Satya Kishore and U. V. Varadaraju, *Mater. Res. Bull*., 41 (3) (2006), 601
3. P. B. Ranko and C. S. Slavi, *J. Mater. Chem*., 9 (1999) 2679
4. G. Muncaster, G. Sankar, C. R. A. Catlow, J. M. Thomas, R. G. Bell, P. A. Wright, S. Coles, S. J. Teat, W. Clegg and W. Reeve, *Chem. Mater*.,11 (1999)158
5. M. A. Ben Moussa, R. Marzouki, A. Brahmia, S. Georges, S. Obbade and M. F. Zid, *Int. J. Electrochem. Sci.*, 14 (2019) 1500

6.   P. Barpanda, M. Avdeev, C. D. Ling, J. Lu and A. Yamada, Physical Inorganic Chemistry, 44(12) (2013) https://doi.org/10.1002/chin.201312005
7.   F. Erragh, A. Boukhari, B. Elouadi and E. M. Holt, Journal of Crystallographic and Spectroscopic Research, 21(3) (1991)321
8.   P. Keller, H. Riffel, F. Zettler and H. Hess, Z. *Anorg. Allg. Chem*., 474(3) (1981)123
9.   K. Lii and P. Shih, *Inorg. Chem*. 33(14) (1994)3028
10. R. Marzouki, A. Guesmi and A. Driss, *Acta Crystallogr. C Struct. Chem*., 66 (2010)i95-98
11. R. Marzouki, A. Guesmi, M. F. Zid and A. Driss, Ann. *Chim. - Sci. Mat*., 38 (3-4) (2013) 117.
12. R. Marzouki, *Mater. Res. Express*, 7(1) (2020) 016313
13. A. J. M. Duisenberg, *J. Appl. Crystallogr*. 25 (1992) 92
14. J. Macíček and A. Yordanov, *J. Appl. Crystallogr*., 25 (1992) 73-80
15. A. C. T. North, D. C. Phillips and F. S. Mathews, *Acta Crystallogr*., A 24 (1968) 35116 G. M. Sheldrick, *Acta Cryst*., C71 (2015) 3
16. G. M. Sheldrick, *Acta Cryst*. C71 (2015**)** 3-8. Doi: 10.1107/S2053273314026370
17. L. J. Farrugia, *J. Appl. Crystallogr*., 32 (1999) 837
18. K. Brandenburg, M. Berndt, Diamond Version 3. Crystal Impact. Bonn, 2001.
19. J.-G. Eon and M. Nespolo, *Acta Cryst*., B71 (2015) 34
20. M. Nespolo and B. Guillot, *J. Appl. Cryst*., 49 (2016) 317
21. S. Adams, *Acta Cryst*., B57 (2001) 278
22. I. D. Brown, The Chemical Bond in Inorganic Chemistry – The Bond Valence Model. IUCr Monographs on Crystallography, No. 12. Oxford University Press, 2002.
23. S. Adams, softBV. University of Gottingen, Germany, 2003. http://www.softbv.net.
24. L. Pauling, *J. Am. Chem. Soc*., 51 (1929) 1010
25. I. D. Brown and D. Altermatt, *Acta Cryst*., B41 (1985) 244
26. D. Mazza, *J. Solid State Chem*., 156 (2001) 154
27. R. Marzouki, A. Guesmi, S. Georges, M. F. Zid and A. Driss, *J. Alloy. Compd*., 586 (2014) 74
28. Y. Ben Smida, R. Marzouki, S. Georges, R. Kutteh, M. Avdeev, A. Guesmi and M.F. Zid, *J. Solid State Chem.,* 239 (2016) 8
29. Kazuo Nakamoto, Infrared and Raman Spectra of Inorganic and Coordination Compounds: Part A: Theory and Applications in Inorganic Chemistry, Sixth Edition, 2008 https://doi.org/10.1002/9780470405840.ch2
30. X'Pert HighScore Plus, PaNalytical B.V. Amelo, The Netherlands 2003.
31. D. Johnson, Zview version3.1c, Scribner Associates, Inc.,1990–2007.
32. R. Marzouki, Y. Ben Smida, A. Guesmi, S. Georges, I. H. Ali, S. Adams and M. F. Zid, *Int. J. Electrochem. Sci.,* 13 (2018) 11648
33. R. Marzouki, A. Guesmi, M. F. Zid and A. Driss, Crystal Structure Theory and Applications, 1 (2013) 68
34. R. Marzouki, A. Brahmia, S. Bondock, S. M. A. S. Keshk, M. F. Zid, A. G. Al-Sehemi, A. Koschella and T. Heinze, *Carbohydr. Polym*. 221 (2019) 29

Article

Glucose Oxidase and Catalase Activities in Honey Samples from the Southwestern Region of Saudi Arabia

Rahaf Mohammed Hussein Alshareef [1,2,3], Badriah Saad Al-Farhan [4] and Mohammed Elimam Ahamed Mohammed [1,2,3,*]

1. Department of Chemistry, Faculty of Science, King Khalid University, Abha 61413, Saudi Arabia; 441813276@kku.edu.sa
2. Research Center for Material Science, King Khalid University, Abha 61413, Saudi Arabia
3. Unit of Honeybee Research and Honey Production, King Khalid University, Abha 61413, Saudi Arabia
4. Department of Chemistry, Faculty of Science for Girls, King Khalid University, Abha 61413, Saudi Arabia; bfrhan@kku.edu.sa
* Correspondence: meaahmad@kku.edu.sa

Abstract: The activity of honey enzymes are affected by floral and geographical origins, climate conditions, honeybee species, health and nutrition. This article investigated the effect of floral and geographical origins on the activity of glucose oxidase (GOx) and catalase (CAT) enzymes in honey samples from the southwestern region of Saudi Arabia. Moreover, the moisture, total sugars, pH and conductivity were measured as quality parameters. The floral origin of the honey samples was determined microscopically while the quality parameters were measured according to the methods of international honey commission. The activity of the honey enzyme was determined following the instructions of the Megazyme International kits. The obtained results were statistically analyzed by the statistical Package for Social Sciences (SPSS, v.20). The GOx activity of the *Acacia*, *Ziziphus* and polyfloral honey samples of the Asir region were $(5.19 \pm 2.33 \text{ U/g})$, $(4.01 \pm 1.17 \text{ U/g})$ and $(5.69 \pm 1.67 \text{ U/g})$, respectively. The *Acacia*, *Ziziphus* and polyfloral honey samples from the Jazan region had GOx activities of $(6.85 \pm 0.47 \text{ U/g})$, $(10.48 \pm 9.22 \text{ U/g})$ and $(5.31 \pm 2.7 \text{ U/g})$, respectively. The geographical origin significantly affected the GOx activity of *Ziziphus* honey (p-value = 0.005) and the GOx activity of the *Ziziphus* honey was significantly more than that of the polyfloral honey of the Jazan region (p-value = 0.009). With regard to the CAT activity in Asir region honey samples, the mean values of the *Acacia, Ziziphus and* polyfloral honeys were $(2.89 \pm 1.08 \text{ U/g})$, $(3.58 \pm 1.59 \text{ U/g})$ and $(2.84 \pm 1.24 \text{ U/g})$, respectively. The mean values of the CAT activity in the Jazan honey samples were *Acacia* $(4.35 \pm 1.01 \text{ U/g})$, *Ziziphus* $(3.94 \pm 0.04 \text{ U/g})$ and polyfloral $(3.43 \pm 0.67 \text{ U/g})$. The geographical origin significantly affected the CAT activity in *Acacia* honey (p-value = 0.014). The geographical and floral origins had significant effects on the activity of the honey GOx and CAT enzymes.

Keywords: enzymes; floral origin; geographical origin

1. Introduction

Honeybees (*Apis mellifera*) produce seven products; honey, royal jelly, propolis, bee venom, beeswax, bee bread and pollens. However, honey is the most famous and important among them as it is the only natural sweetener that humans consume without any processing [1–5]. Honey is a unique, sticky and aromatic substance that honeybees make from different sources such as the nectar of plants, from the secretions of the living parts of the plant or from the excretions of plant sucking insects [3,6]. Based on those sources, there are two types of honey named according to the source visited by the bee. The nectar honey comes from the nectar of the flowers and honeydew that is produced when the honeybees feed on the secretions of plants and excretions of plant-sucking insects [6].

The criteria for honey quality according to the international standards for honey are moisture, insoluble solids, sugars (glucose, fructose and sucrose), conductivity, pH, free

acidity and diastase [6]. The quality of honey depends on the botanical and geographical origin. It was proven that the oil composition of the plants depends on its geographical location even if they were from the same species [7]. Because of the effect of environmental conditions on the physiology of plants and chemical composition, there are no two similar types of honey [8,9]. Honey composition depends on several factors such as the type and flow of nectar, the vitality of the bee colony, climate and environmental conditions, seasons, treatment of beekeepers, extraction and storage [10,11].

Honey is well known by its biological and medical activities such as an antiseptic and a natural remedy, antibiotics (antibacterial, antiviral and antifungal) and antioxidants [12–15]. The activity of the honey varies according to the chemical composition of honey, its floral source and geographical location [10,11].

Enzymes are minor components in honey, and they are among the most important and interesting constituents. Being a mark of quality, it gives honey and contributes to its healing and nutritional properties [16–18]. Honey contains four main enzymes: diastase (amylase), invertase (sucrase), glucose oxidase, catalase and acid phosphatase [19]. Enzymes originate from different sources including the honeybees, nectar, pollen grains and microorganisms [20].

GOx is sensitive to light and storage conditions, and it is inactive in mature honey, while it is active in diluted honey due to the easy access of the enzyme to the substrate (glucose). Through the reaction of glucose oxidation, gluconic acid is produced, which is the most representative acid in honey. The hydrogen peroxide is the second product of the GOx. It is the primary and main factor behind the honey antimicrobial activity and has been called "inhibin" because it inhibits microbial growth in honey [16,21].

CAT degrades and hydrolyzes the hydrogen peroxide (H_2O_2) to water and oxygen. The origins of the catalase enzyme in honey are the plants and microbes. The activity of this enzyme varies according to its plant sources and storage conditions [22,23]. CAT detection methods vary, but all depend on the principle of H_2O_2 determination before and during the incubation period [24,25].

The aim of this article was to study and compare honey samples from the Asir and Jazan regions in the southwestern part of Saudi Arabia based on the effect of floral and geographical origins on GOx and CAT activity along with the values of moisture, total sugars, conductivity and pH.

2. Material and Methods

2.1. Honey Samples and Their Floral Origins

Thirty-seven and twenty-one honey samples were collected from the regions of Asir and Jazan, respectively (Figure 1). The Jazan area is approximately at sea level while the samples of the Asir region are from an altitude of 900 m above sea level. Jazan is characterized by the high temperature, high humidity and high barometric pressure compared to the Asir region.

Figure 1. Map of Asir and Jazan regions at the southwestern region of Saudi Arabia. Thirty-seven samples were collected from Asir region and twenty-one from Jazan region.

The floral origin of the honey samples was determined microscopically according to the method of Louveaux et al. [26]. In addition, 3 mL of each honey sample were diluted with 11 mL of distilled water in a 15 mL falcon tube. The content of the falcon tubes was centrifuged at 6000 rpm for 30 min, the pellet was mounted on a light microscope slide, and the pollens were identified and their percentage was determined. The honey sample is considered monofloral if the percentage of one pollen is ≥50%.

2.2. Moisture and Total Sugar Percentages (%)

The procedure of the harmonized methods of the international honey commission (2009) was used to determine the moisture percentage as follows: a small amount of honey was placed to cover the prism of a refractometer (ATC Refractometer for honey; Tiaoyeer, Xindacheng, China), the moisture percentage was read twice, and the mean value was taken as the final result [26].

The total sugar percentage was determined from the ATC refractometer reading screen.

2.3. Electrical Conductivity (mS/cm)

Two grams of each honey sample were dissolved in 10 mL distilled water (20%, W/V), and the conductivity was measured twice at a constant temperature of 20 ± 0.5 °C using conductivity meter (Hanna HI9811-5 Portable pH/EC/TDS/°C Meter, Phoenix, AZ, USA). The conductivity meter was calibrated with a ready-made KCl solution with a conductivity of 1413 μS/cm [26]. The average value of the two conductivities was considered as the final result of the conductivity.

2.4. pH

To the honey solution prepared to measure the conductivity, an extra 5 mL of distilled water were added to reach the dilution of 13.3% (*w/v*). The pH of the honey solution was measured twice using a pH meter at a constant temperature of 20 ± 0.5 °C (Hanna HI9811-5 Portable pH/EC/TDS/°C Meter, Phoenix, AZ, USA). The pH meter was calibrated using two ready-made buffer solutions of pH 4 and 7. The mean values of the two pH readings were taken as the sample result [26].

2.5. GOx Activity (U/g)

The GOx activity was determined according to the instructions of the megazyme international company kit (GOx kit number: 200221-8).

The GOx kit principle is the glucose oxidase reaction with the glucose in honey samples and with standard solution of glucose to produce (hydrogen peroxide). The product of the first reaction (hydrogen peroxide) reacts with peroxidase (POD) and p-hydroxybenzoic acid + 4-aminoantipyrine (chromogen) so as to produce a colored dye (quinoneimine). The dye density is measured spectrophotometrically at 500 nm. One gram of each honey sample was dissolved in 2 mL of distilled water (50%), and 0.5 mL of each sample solution was transferred to a test tube. In addition, 0.5 mL of standard glucose solution (90 mg/mL) was pippetted in a second tube and 2 mL of POD were blended with the glucose standard, and their absorbance was determined at 510 nm (A1) against a blank tube with 0.5 mL of water and 2 mL of POD. The contents of the sample tube were poured into the second tube contents, stirred, kept for 20 min at room temperature and their absorbance was measured at the same wavelength (A2). Standard GOx solutions were used to create a standard curve (0.0, 0.38, 0.75, 1.5, 3.0 and 6.0 U/mL). A straight line equation was created, and the GOx activity of the honey samples was determined using the Excel program and multiplied by 2 to obtain the activity in 1 g (U/g).

2.6. CAT Activity

CAT catalyzes the degradation of hydrogen peroxide to water and oxygen. CAT activity was evaluated following the decrease in hydrogen peroxide concentration after incubation of the honey sample with a standard solution of H_2O_2. The CAT activity was

measured following the instructions of the megazyme international company kit (CAT kit number: 200206-6). The kit contains two separate reactions: (1) The CAT of the honey sample is incubated with a standard solution of H_2O_2 for 5 min. Then, the enzyme is strongly inhibited by adding sodium azide solution. (2) The remaining H_2O_2 is degraded by POD in the presence of 3,5-dichloro-2-hydroxy-benzenesulfonic acid (DHBS) and 4-aminoantipyrine (AAP) to produce a complex dye (quinoneimine), which is measured at a wavelength of 520 nm.

One gram of each honey sample was diluted in 2 mL of distilled water (50%). In addition, 0.05 mL from each honey sample was added to 0.05 mL of a standard solution of H_2O_2 (130 mM) in a test tube and incubated for 5 min at 25 °C. After that, 0.9 mL of sodium azide solution (15 mM) was added to stop the reaction. Immediately after stopping the reaction, 0.04 mL of the mentioned tube was transferred to a spectrophotometer cuvette. To the cuvette, 3 mL of peroxidase solution (POD+ DHB+ AAP) were added and the contents were mixed and incubated for 15 min at 25 °C. Finally, the absorbance was read at 520 nm against a blank tube containing 0.05 mL of phosphate buffer (150 mM Potassium phosphate, pH 7.0) instead of the honey sample. For calculating the CAT activity in the different honey samples, a standard curve was created using CAT with different activities (0.0, 0.4, 0.8, 1.6, 3.2 and 6.4 U/mL) and following the same procedure as the honey and blank samples. A straight line equation was created using the Excel program, and the CAT activities were calculated following the line equation and multiplied by 2 (sample dilution factor) to obtain the activity of CAT in U/g of honey.

2.7. Statistical Analysis

The obtained results were statistically analyzed using the *t*-test and ANOVA of the Statistical Package of Social Sciences (SPSS). The difference between the compared results of the studied parameters was considered significant at the level of ≤ 0.05. Moreover, the agglomerative hierarchical clustering analysis for the results was carried out.

3. Results

3.1. Results of Floral Origin

The microscopic analysis of the honey pollens showed that the honey samples were *Acacia* (25), *Ziziphus* (6) and polyfloral (27) (Figure 2). The number of the *Acacia*, *Ziziphus* and polyfloral honey samples of Asir region were 21, 4 and 12, respectively. The numbers of the Jazan honey samples were *Acacia* (4), *Ziziphus* (2) and polyfloral (15).
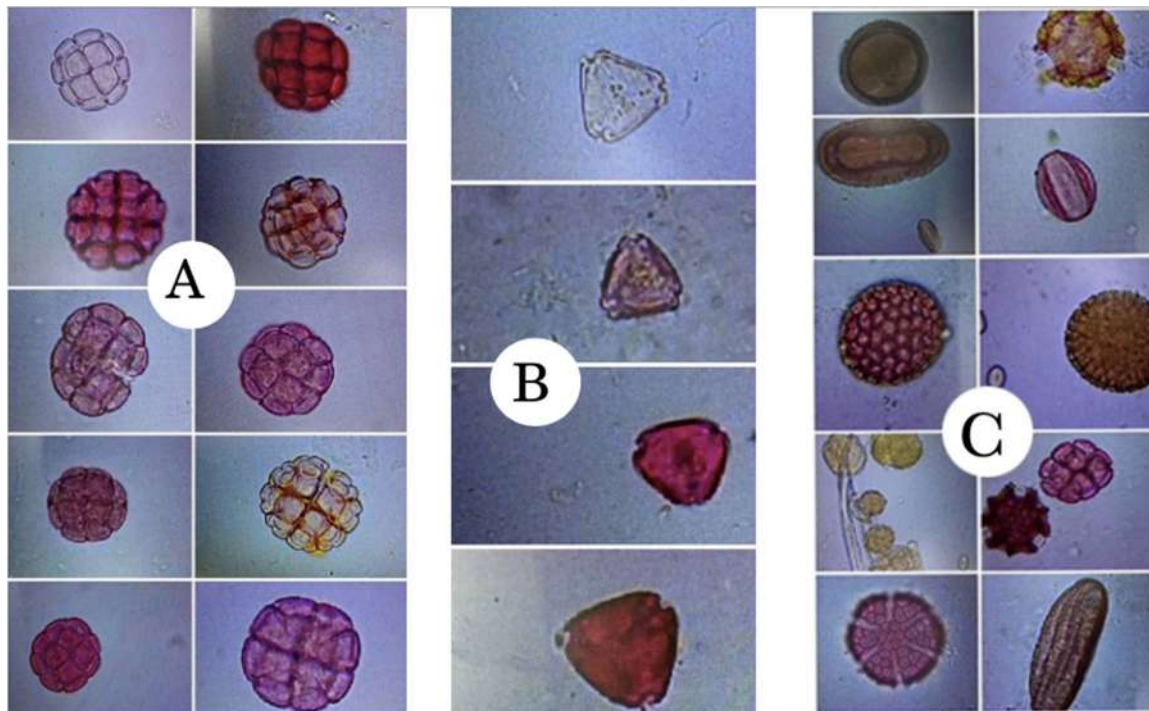
Figure 2. Representative pollens for the floral origins of the studied honey samples. The studied honey samples were of three floral origins: Acacia (**A**), Ziziphus (**B**) and polyfloral (**C**).

3.2. Results of the Studied Parameters

Table 1 presents the results of the studied parameters, and Table 2 summarizes the significant effects of the floral and geographical origins on the studied analytes.

Table 1. The results of the studied parameters.

		N	Mean	Std. Deviation	Minimum	Maximum
Moisture %	Ziziphus Asir	4	17.2500	1.84842	14.50	18.50
	Ziziphus Jazan	2	17.0500	0.07071	17.00	17.10
	Acacia Asir	21	16.5814	1.89471	13.95	20.25
	Acacia Jazan	4	14.7125	0.41105	14.25	15.15
	Polyfloral Asir	12	17.6750	1.50038	15.40	19.60
	polyfloral Jazan	15	17.2400	1.92977	14.20	19.50
	Total	58	16.9114	1.82670	13.95	20.25
Sugars %	Ziziphus Asir	4	80.4375	1.78390	79.00	83.00
	Ziziphus Jazan	2	81.3750	0.17678	81.25	81.50
	Acacia Asir	21	81.9643	2.25450	77.50	84.50
	Acacia Jazan	4	83.7125	0.40285	83.25	84.05
	Polyfloral Asir	12	80.8250	1.99437	78.50	84.00
	polyfloral Jazan	15	81.1633	1.96891	78.60	84.40
	Total	58	81.5164	2.07556	77.50	84.50
Conductivity μS/cm	Ziziphus Asir	4	651.2500	412.88366	35.00	910.00
	Ziziphus Jazan	2	595.0000	304.05592	380.00	810.00
	Acacia Asir	21	622.3810	324.79078	170.00	1390.00
	Acacia Jazan	4	475.0000	233.02360	130.00	630.00
	Polyfloral Asir	12	766.6667	423.52060	210.00	1420.00
	polyfloral Jazan	15	486.0000	136.84193	160.00	720.00
	Total	58	607.8448	316.78361	35.00	1420.00

Table 1. *Cont.*

		N	Mean	Std. Deviation	Minimum	Maximum
pH	Ziziphus Asir	4	4.7750	0.81803	3.80	5.50
	Ziziphus Jazan	2	5.4500	2.47487	3.70	7.20
	Acacia Asir	21	4.5667	0.55528	3.70	5.70
	Acacia Jazan	4	4.6000	0.27080	4.20	4.80
	Polyfloral Asir	12	4.5292	0.76410	3.70	6.00
	polyfloral Jazan	15	3.9400	0.47026	3.60	4.70
	Total	58	4.4440	0.73521	3.60	7.20
GOX U/g	Ziziphus Asir	4	4.0085	1.16655	3.02	5.70
	Ziziphus Jazan	2	10.4800	9.22067	3.96	17.00
	Acacia Asir	21	5.1934	2.33261	2.24	10.47
	Acacia Jazan	4	6.5800	0.46847	5.92	6.96
	Polyfloral Asir	12	5.6886	1.67169	3.44	9.02
	polyfloral Jazan	15	5.3100	2.70043	3.00	11.70
	Total	58	5.5222	2.64076	2.24	17.00
CAT U/g	Ziziphus Asir	4	3.5828	1.58816	1.22	4.68
	Ziziphus Jazan	2	3.9404	0.04295	3.91	3.97
	Acacia Asir	21	2.8909	1.07980	0.91	4.89
	Acacia Jazan	4	4.3531	1.01113	3.52	5.59
	Polyfloral Asir	12	2.8409	1.24159	1.44	5.47
	polyfloral Jazan	15	3.4265	0.67140	2.08	4.63
	Total	58	3.2038	1.09661	0.91	5.59

Table 2. The significant effects of the floral and geographical origins on the studied parameters.

Parameter	Honey Samples		*p*-Value
Moisture	Acacia Jazan	polyfloral Jazan	0.013
Sugars	Acacia Jazan	polyfloral Jazan	0.028
	Polyfloral Asir	polyfloral Jazan	0.025
pH	Ziziphus Jazan	polyfloral Jazan	0.005
	Polyfloral Asir	polyfloral Jazan	0.030
Glucose oxidase	Ziziphus Asir	Ziziphus Jazan	0.005
	Ziziphus Jazan	polyfloral Jazan	0.009
Catalase	Acacia Asir	Acacia Jazan	0.014

The floral origin in the Jazan region significantly affected the moisture, sugars, pH and the glucose oxidase while the geographical origin significantly affected the sugars, pH, GOx and CAT.

3.3. Hierarchical Clustering of the Honey Samples

The agglomerative hierarchical clustering was carried out to classify the honey samples according to the results of the studied parameters. Moreover, the classification according to the results of the studied parameters is compared to the classification of the floral and geographical origins (Figure 3).

The agglomerative clustering showed that there were two second level clusters. The first one clustered five samples containing two *Acacia* from the Asir region, one *Acacia* honey from Jazan, one polyfloral honey from Jazan and one *Ziziphus* honey from Asir region. The first cluster of level 2 grouped *Acacia* and ployfloral honey samples from the Asir and Jazan regions. However, one *zizphus* honey sample from the Asir region was classified with the *Acacia* honey samples, which may be due to the presence of *Acacia* pollens in the

honey. The second cluster of level one contained eleven honey samples containing four *Acacia* from Asir region, one *Acacia* from Jazan region, two polyfloral from Asir region and four polyfloral from Jazan region. The second cluster of level 2 classified some *Acacia* and polyfloral honey samples irrespective of their geographical origin. There is a presence of polyfloral honey samples with the *Acacia* honey samples because they contain *Acacia* pollens. The conclusion of level 2 classification is that the studied parameters can be used for the prediction of the floral origin (Figure 3).
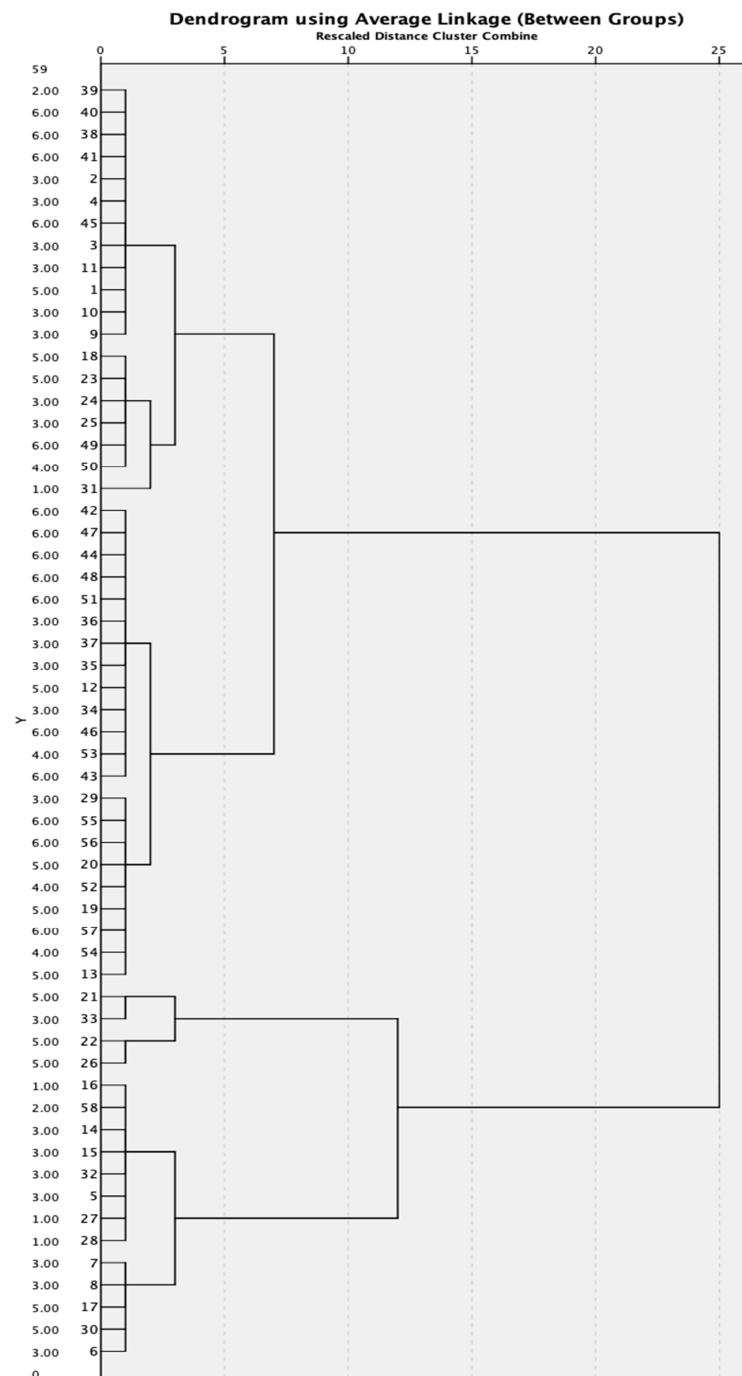
Figure 3. Agglomerative hierarchical clustering of the studied honey samples. The clustering was carried out to investigate the possibility of using the results of the studied parameters to predict the floral and geographical origins of the honey samples.

Level three contained three clusters with different numbers of honey samples. The first cluster was composed of 12 honey samples while the second cluster contained three honey samples. The third cluster was composed of seven honey samples. The samples of the first cluster were six *Acacia* samples from Asir region, one *Acacia* from Jazan region, three poly floral from Asir region, one polyfloral from Jazan and one *Ziziphus* from the Asir region. The first cluster classified the honey samples according to their floral origin except for one sample (*Ziziphus*). The second cluster of level three contained three samples, two ployfloral and one *Acacia* honey from the Asir region. The second cluster classified the honey samples according to their geographical origin. The third cluster of level 3 classified the honey samples according to their geographical origin since it was composed of seven honey samples from the Asir region. However, the seven honey samples were five *Acacia* honey and two *Ziziphus* honey samples (Figure 3).

Level four was composed of one group containing group one and two of level two, and group one of level three besides some other honey samples. The level four cluster contained 29 honey samples. The 29 honey samples were 12 *Acacia* honey from Asir region, five polyfloral from Asir, one *Ziziphus* from Asir, two *Acacia* from Jazan and nine polyfloral from Jazan. Level 4 classified the honey samples according to their floral and geographical origin (Figure 3).

Level five was composed of one cluster containing 14 honey samples. The honey samples were seven *Acacia* from Asir, three *Ziziphus* from Asir region, three polyfloral from the Asir region and one *Ziziphus* from the Jazan region. Level 5 clustered 13 honey samples according to their geographical origin (Asir region (Figure 3)).

Level six involved the clusters of level 4, level 5 and five samples (48 honey samples). Level six classified the honey samples according to their floral and geographical origins (Figure 3).

Ten samples were not involved in the different clusters: three *Acacia* Asir, two polyfloral Asir, four polyfloral Jazan and one *Ziziphus* Jazan (Figure 3).

4. Discussion

The studied quality parameters (moisture, pH and conductivity) were within the ranges of the Codex standards [6]. The moisture was significantly affected by the floral origin (*Acacia* vs. polyfloral) in the honey samples of the Jazan region. The total sugars are affected by the floral origin in the Jazan region (*Acacia* vs. polyfloral) and the geographical origin (polyfloral Jazan versus polyfloral Asir) [27]. The floral origin significantly affected the pH of the honey samples from the Jazan region (*Ziziphus* vs. polyfloral), whereas the geographical origin had a significant effect on the pH of the polyfrloal honey (Jazan vs. Asir). The geographical origin significantly affected the GOx activity of the *Ziziphus* honey samples and CAT activity of the *Acacia* honey samples. The GOX activity of the polyfloral honey samples was significantly different compared to its activity in the *Ziziphus* honey samples of the Jazan region.

The range of the moisture percentage in the honey samples of this study was (13.95–20.25%). The results were within the moisture range of honey according to the Codex standards [6] and according to the guide to the production, trading and import of honey and bee products issued by the Saudi Food and Drug Authority [28]. The previously published articles showed that the moisture percentage of the Saudi honey was ranging from 8.8–18.5% [29–31]. This study found that the floral origin in the Jazan region had a significant effect on the percentage of moisture similar to the findings of Corbella and Cozzolino [32] and Khan et al. [33].

The range of the pH of the honey samples was (3.6–7.2). The upper limit of the pH range was slightly higher than the previously reported pH values in Saudi Arabia (5.7) [31,33]. The US National Honey Board adopted a pH range for honey samples from 3.4 to 6.1 [34]. With regard to the effect of floral and geographical origin on the pH of honey, this study reported that the *Ziziphus* honey of the Jazan region had significantly increased pH value compared to the polyfloral honey of Jazan. The polyfloral honey of Asir region had significantly increased pH value compared to the pH of the polyfloral honey from the

Jazan region. Similar to our findings, Khan et al. [33] and Mohammed et al. [31] reported significant effects of the floral and geographical origins on the value of the honey pH.

Concerning the concentration of total sugars in honey, the range of the total sugars in the study samples was (77.5–84.5%). Similar to our findings, Buba et al. found that the range of the total sugars in Nigerian honey samples was (77.60–86.20) [35]. Other studies reported different total sugar ranges such as (62.85–77.39), (62.24–77.26), (64.99–72.54) and (69.76–79.92) [36]. Baloš et al. [36] concluded that the sugar concentration in honey samples from Serbia can be used to differentiate between honey samples of different plant origins. The total sugars of honey are affected by the geographical origin of the honey samples [37]. However, this study reported significant effects of the floral and geographical origins on the concentration of total sugars in honey.

The conductivity range of the honey samples of this study was (35–1420 μS/cm) and the floral and geographical origins had insignificant effects on the conductivity values. According to the Codex Alimentarius [6], the conductivity of honey depends on the floral origin; some honey samples have conductivity of not more than 800 μS/cm, while others have conductivity of not less than 800 μS/cm. One previous study reported very high conductivity values for honey samples from Egypt and Yemen ranging from 0.53 ± 0.03 to 4.18 ± 0.05 mS/cm [1].

The range of the GOx activity in the studied honey samples was (2.24–17.00 U/g). The unit of enzyme activity (U) is defined as the amount of the enzyme that converts micromoles of substrate to a product per minute (μmol/min) [38]. We were not able to compare our results to the previous findings of the published articles due to the difference in the measurement units. Strelec et al. [16] and Sahin et al. [39] measured the activity of GOx in micrograms of the hydrogen peroxide produced in one hour per gram of honey, while Bucekova et al. [19] measured the amount of the GOx enzyme in micrograms per gram of honey. The GOx activity of the *Ziziphus* honey samples from the Asir and Jazan regions was significantly different and the *Ziziphus* honey of the Jazan region was significantly increased compared to the polyfloral honey of Jazan. The conclusion of this study is that the floral and geographical origin had significant effects on the GOx activity. Similarly, Bucekova et al. [13], Strelec et al. [16], and Belay et al. [18] reported that the floral origin had significant effects on the activity of honey enzymes including the GOx.

This study found that the range of the CAT enzyme activity in the studied honey samples was (0.91–5.59 U/g). Schepartz and Subers [40] studied the CAT activity in different honey samples and found that the enzyme activity depends on the floral origin and ranges from 0–17 g/min [40]. Fourteen Brazilian honey samples from different floral origins were studied and their CAT activity was ranging from 9.97 to 99.07 U/mg [41].

The significant effect of the floral origin on the studied parameters in the Jazan region may be due to its climate conditions such as the high temperature, high humidity and barometric pressure.

The agglomerative hierarchical clustering showed the possibility of using the studied parameters' results to predict the floral and geographical origins of the honey samples. Many previous studies proved that the results of honey analysis are useful for the prediction of the floral and geographical origins of honey samples [42–44].

This study suffers from the small number of samples in the subgroups, but it opens windows to conduct future studies on the activities of the GOx and CAT enzymes. Moreover, measurement of the hydrogen peroxide is highly recommended.

5. Conclusions

Concerning the effect of the geographical origin on the studied parameters, it significantly affected the total sugars, pH and the activity GOx and CAT in the honey samples. Specifically, the polyfloral honey of Asir region was characterized by significantly high pH and low total sugars while its *Ziziphus* honey had significantly low GOx activity. Furthermore, the *Acacia* honey from the Asir region was with significantly low CAT activity compared to the *Acacia* honey from the Jazan region. The effect of the geographical origin

may be due to the fact that the Asir and Jazan regions are characterized by different climate conditions due to the different altitude levels.

The floral origin had significant effects on the studied parameters of the Jazan region while the floral origin in Asir region had no significant effect on the studied parameters. The *Acacia* honey of Jazan was characterized by significantly low moisture and high total sugars compared to the polyfloral honey. The *Ziziphus* honey compared to the polyfloral honey of Jazan was characterized by significantly high pH and GOx activity.

As the floral origin had significant effects on the studied parameters of Jazan honey only, it can be concluded that the effect of the floral origin of honey on the studied parameters is regulated by the geographical origin and its climate conditions.

References

1. El Sohaimy, S.A.; Masry, S.H.D.; Shehata, M.G. Physicochemical characteristics of honey from different origins. *Ann. Agric. Sci.* **2015**, *60*, 279–287. [CrossRef]
2. De Sousa, J.M.B.; de Souza, E.L.; Marques, G.; de Toledo Benassi, M.; Gullón, B.; Pintado, M.M.; Magnani, M. Sugar profile, physicochemical and sensory aspects of monofloral honeys produced by different stingless bee species in Brazilian semi-arid region. *LWT Food Sci. Technol.* **2016**, *65*, 645–651. [CrossRef]
3. de Almeida-Muradian, B.; Barth, O.M.; Dietemann, V.; Eyer, M.; Freitas, A.D.S.D.; Martel, A.-C.; Marcazzan, G.L.; Marchese, C.M.; Mucignat-Caretta, C.; Pascual-Maté, A.; et al. Standard methods for Apis mellifera honey research. *J. Apic. Res.* **2020**, *59*, 1–62. [CrossRef]
4. Desissa, Y. Detection of the electrical conductivity and acidity of honey from different areas of Tepi. *Food Sci. Technol.* **2014**, *2*, 59–63.
5. Martinello, M.; Mutinelli, F. Antioxidant Activity in Bee Products: A Review. *Antioxidants* **2021**, *10*, 71. [CrossRef] [PubMed]
6. Codex Alimentarius. Standard for Honey CXS 12-1981. Adopted in 1981. Revised in 1987, 2001. Amended in 2019. Available online: https://www.fao.org/fao-who-codexalimentarius/sh-proxy/en/?lnk=1&url=https%253A%252F%252Fworkspace.fao.org%252Fsites%252Fcodex%252FStandards%252FCXS%2B12-1981%252Fcxs_012e.pdf (accessed on 26 July 2022).
7. Monika, T.; Tarapatskyy, M.; Dżugan, M. The influence of geographical origin on honey composition studied by Polish and Slovak honeys. *Czech J. Food Sci.* **2019**, *37*, 232–238.
8. Irish, J.; Blair, S.; Carter, D.A. The antibacterial activity of honey derived from Australian flora. *PLoS ONE* **2011**, *6*, e18229. [CrossRef] [PubMed]
9. Bilandžić, N.; Sedak, M.; Đokić, M.; Bošković, A.G.; Florijančić, T.; Bošković, I.; Kovačić, M.; Puškadija, Z.; Hruškar, M. Element content in ten Croatian honey types from different geographical regions during three seasons. *J. Food Compost. Anal.* **2019**, *84*, 103305. [CrossRef]
10. El Sohaimy, S.A.; Masry, S.H.D.; Mohamed, G.; Rashad, H. Evaluation of functional properties of local and imported honey in Egypt. *Am.-Eurasian J. Agric. Environ. Sci.* **2015**, *15*, 1147–1154.
11. Mohammed, M.E.A. Factors Affecting the Physicochemical Properties and Chemical Composition of Bee's Honey. *Food Rev. Int.* **2022**, *38*, 1330–1341. [CrossRef]
12. Meo, S.A.; Al-Asiri, S.A.; Mahesar, A.L.; Ansari, M.J. Role of honey in modern medicine. *Saudi J. Biol. Sci.* **2017**, *24*, 975–978. [CrossRef]
13. Bucekova, M.; Jardekova, L.; Juricova, V.; Bugarova, V.; Marco, G.D.; Gismondi, A.; Leonardi, D.; Farkasovska, J.; Godocikova, J.; Laho, M.; et al. Antibacterial Activity of Different Blossom Honeys: New Findings. *Molecules* **2019**, *24*, 1573. [CrossRef] [PubMed]

14. Adgaba, N.; Al-Ghamdi, A.; Sharma, D.; Tadess, Y.; Alghanem, S.M.; Khan, A.K.; Mohammed, J.A.; Mohamed, G.K.A. Physico-chemical, antioxidant and anti-microbial properties of some Ethiopian mono-floral honeys. *Saudi J. Biol. Sci.* **2020**, *27*, 2366–2372. [CrossRef] [PubMed]

15. Tafere, D.A. Chemical composition and uses of Honey: A Review. *J. Food Nutr. Res.* **2021**, *4*, 194–201.

16. Strelec, I.; Crevar, B.; Kovač, T.; Rajs, B.B.; Primorac, L.; Flanjak, I. Glucose oxidase activity and hydrogen peroxide accumulation in Croatian honeys. *CJFST* **2018**, *10*, 33–41. [CrossRef]

17. Rossano, R.; Larocca, M.; Polito, T.; Perna, A.M.; Padula, M.C.; Martelli, G.; Riccio, P. What Are the Proteolytic Enzymes of Honey and What They Do Tell Us? A Fingerprint Analysis by 2-D Zymography of Unifloral Honeys. *PLoS ONE* **2012**, *7*, e49164. [CrossRef]

18. Belay, A.; Haki, G.D.; Birringer, M.; Borck, H.; Lee, Y.-C.; Kim, K.-T.; Baye, K.; Melaku, S. Enzyme activity, amino acid profiles and hydroxymethylfurfural content in Ethiopian monofloral honey. *J. Food Sci. Technol.* **2017**, *54*, 2769–2778. [CrossRef] [PubMed]

19. Samarghandian, S.; Farkhondeh, T.; Samini, F. Honey and Health: A Review of Recent Clinical Research. *Pharmacogn. Res.* **2017**, *9*, 121–127.

20. Weston, R.J. The contribution of catalase and other natural products to the antibacterial activity of honey: A review. *Food Chem.* **2000**, *71*, 235–239. [CrossRef]

21. Albaridi, N.A. Antibacterial Potency of Honey. *Int. J. Microbiol.* **2019**, *2019*, 2464507. [CrossRef]

22. Gillette, C.C. Honey catalase. *J. Econ. Entomol.* **1931**, *24*, 605–606. [CrossRef]

23. Brudzynski, K. A current perspective on hydrogen peroxide production in honey. A review. *Food Chem.* **2020**, *332*, 127229. [CrossRef]

24. Huidobro, J.F.; Sánchez, M.P.; Lorenzo, S.M.; Sancho, M.T. Precise method for the measurement of catalase activity in honey. *J. AOAC Int.* **2005**, *88*, 800–804. [CrossRef] [PubMed]

25. Kadhum, M.A.; Hadwan, M.H. A precise and simple method for measuring catalase activity in biological samples. *Chem. Pap.* **2021**, *75*, 1669–1678. [CrossRef]

26. Louveaux, J.; Maurizio, A.; Vorwohl, G. Methods of melissopalynology. *Bee World* **1978**, *59*, 139–157. [CrossRef]

27. International Honey Commission. *Harmonized Methods of the International Honey Commission*; 2009; pp. 1–63. Available online: https://ihc-platform.net/ihcmethods2009.pdf (accessed on 26 July 2022).

28. Saudi Food and Drug Authority. *Guide to the Production, Trading and Import of Honey and Bee Products*; Saudi Food and Drug Authority Publications: Riyadh, Saudi Arabia, 2021; pp. 14–18. Available online: https://sfda.gov.sa/sites/default/files/2021-03/%D8%AF%D9%84%D9%8A%D9%84%20%D8%A7%D9%84%D8%B9%D8%B3%D9%84%202021.pdf (accessed on 26 July 2022).

29. Mesallam, A.S.; EI-Shaarawy, M.I. Quality Attributes of Honey in Saudi Arabia. *Food Chem.* **1987**, *25*, 1–11. [CrossRef]

30. Al-Ghamdi, A.; Mohammed, S.E.A.; Ansari, M.J.; Adgaba, N. Comparison of physicochemical properties and effects of heating regimes on stored Apis mellifera and Apis florea honey. *Saudi J. Biol. Sci.* **2019**, *26*, 845–848. [CrossRef] [PubMed]

31. Mohammed, M.E.A.; Almadawi, A.; Alfifi, A.; Alfaifi, M.Y.; Elbehairi, S.E.I.; Al-bushnaq, H.A. Some physiochemical properties of Acacia honey from different altitudes of the Asir Region in Southern Saudi Arabia. *Czech J. Food Sci.* **2017**, *35*, 321–327. [CrossRef]

32. Corbella, E.; Cozzolino, D. Classification of the floral origin of Uruguayan honeys by chemical and physical characteristics combined with chemometrics. *LWT Food Sci. Technol.* **2006**, *39*, 534–539. [CrossRef]

33. Khan, K.A.; Ghramh, H.A.; Babiker, M.; Ahmad, Z.; El-Niweiri, M.A.A.; Ibrahim, E.H.; Brima, E.I.; Mohammed, M.E.A. Tolerance of Ziziphus and Acacia honeys to one year storage conditions and altitude. *J. King Saud Univ. Sci.* **2021**, *33*, 101577. [CrossRef]

34. National Honey Board. Honey: A Reference Quide to Nature's Sweetener. Firestone. 2005. Available online: https://honey.com/files/general/refguide.pdf (accessed on 26 July 2022).

35. Buba, F.; Gidado, A.; Shugaba, A. Analysis of Biochemical Composition of Honey Samples from North-East Nigeria. *Biochem. Anal. Biochem.* **2013**, *2*, 139.

36. Baloš, M.M.Ž.; Popov, N.S.; Radulović, J.Z.P.; Stojanov, I.M.; Jakšić, S.M. Sugar profile of different floral origin honeys from Serbia. *J. Apic. Res.* **2020**, *59*, 398–405. [CrossRef]

37. Agus, A.; Umami, N. The sugar content profile of honey produced by the Indonesian Stingless bee, Tetragonula laeviceps, from different regions. *Livest. Res. Rural Dev.* **2019**, *31*, 91.

38. Labuda, J.; Bowater, R.P.; Fojta, M.; Gauglitz, G.; Glatz, Z.; Hapala, I.; Havliš, J.; Kilar, F.; Kilar, A.; Malinovská, L.; et al. Terminology of bioanalytical methods (IUPAC Recommendations 2018). *Chem. Int.* **2018**, *40*, 34. [CrossRef]

39. Sahin, H.; Kolayli, S.; Beykaya, M. Investigation of Variations of Invertase and Glucose Oxidase Degrees against Heating and Timing Options in Raw Honeys. *J. Chem.* **2020**, *2020*, 5398062.

40. Schepartz, A.I.; Subers, M.H. Catalase in Honey. *J. Apic. Res.* **1966**, *5*, 37–43.

41. de Abreu Franchini, R.A.; Costa Matos, M.A.; Matos, R.C. Amperometric Determination of Catalase in Brazilian Commercial Honeys. *Anal. Lett.* **2011**, *44*, 232–240. [CrossRef]

42. Maione, C.; Barbosa, F.; Barbosa, R.M. Predicting the botanical and geographical origin of honey with multivariate data analysis and machine learning techniques: A review. *Comput. Electron. Agric.* **2019**, *157*, 436–446.

43. She, S.; Chen, L.; Song, H.; Lin, G.; Li, Y.; Zhou, J.; Liu, C. Discrimination of geographical origins of Chinese acacia honey using complex 13C/12C, oligosaccharides and polyphenols. *Food Chem.* **2019**, *272*, 580–585. [CrossRef] [PubMed]

44. Drivelos, S.A.; Danezis, G.P.; Halagarda, M.; Popek, S.; Georgiou, C.A. Geographical origin and botanical type honey authentication through elemental metabolomics via chemometrics. *Food Chem.* **2012**, *338*, 127936. [CrossRef]

Unsupported and silica-supported nickel nanoparticles: synthesis and application in catalysis

Mohamed Abboud (iD) · **Reem Alnefaie** · **Abdullah Alhanash**

Abstract In recent years, nickel nanoparticles (Ni NPs) have attracted a growing attention from the scientific research community, because they are inexpensive, eco-friendly, facile to prepare, and they could be used in a panoply of applications, ranging from catalysis to sensors and from fuel cells to photoelectrochemical devices. This review article recapitulates different synthesis methods which have been used to prepare unsupported and silica-supported Ni NPs and their utilisation as nanocatalysts in heterogeneous catalysis and photocatalysis. Firstly, various widely used techniques to synthesize unsupported Ni NPs have been briefly discussed. This includes ball milling, mechanochemical synthesis, laser ablation, and ion sputtering as top–down methods, and physical vapour deposition, chemical vapour deposition, sol–gel method, chemical precipitation, chemical reduction, hydrothermal method, solvothermal, spray pyrolysis, and biological techniques as bottom–up methods. Subsequently, the widely applied methods to incorporate Ni NPs in different types of silica (e.g. SBA-15, MCM-41, MCM-48, TUD-1) are briefly reviewed including impregnation, precipitation, and colloid methods. Finally, recent applications of both unsupported and supported Ni NPs in heterogeneous catalysis and photocatalysis have been discussed, with brief investigation of the effect of Ni NP size and aggregation on their catalytic activity and reusability.

M. Abboud (✉) · R. Alnefaie · A. Alhanash
Catalysis Research Group, Chemistry Department, College of Science, King Khalid University, P.O. Box 9004, Abha 61413, Saudi Arabia
e-mail: Abboud_med@yahoo.fr

Introduction

Catalysis is a fundamental process for many chemical protocols. A catalyst is mostly required to increase the rate of a chemical reaction in modern organic synthesis and to produce chemicals and materials at milder conditions (Sheldon and Dakka 1994; Sachdeva et al. 2013; Clark and Macquarrie 1998). In the last 10 years, research has become more intense on developing new and effective catalytic systems.

Catalysis has been applied in different areas including bio-, electro-, heterogeneous-, and homogeneous catalysis. Catalysts applied in electrochemical reactions are labelled electrocatalysts (e.g. fuel cells). Natural catalysts, involving cells or enzymes, are themed biocatalysts.

The terms heterogeneous and homogeneous catalyses are used if the catalyst and reactant (s) are in different phases (e.g. solid/liquid, solid/gas) or same (e.g. liquid/ liquid), respectively. When performing heterogeneous catalysis, two reaction set-ups can be employed: continuous flow or batch methods. The present review focuses on heterogeneous catalysis, in which the catalyst is present in the solid phase, and the reactants are in the liquid or gas phase.

Fig. 1 The fraction of atoms located on surface, corner or edge sites as a function of particle diameter (Lin et al. 2004)

The heterogeneous catalysis contributes to a sustainable future because it has many economic and environmental benefits. It enables large-scale and faster production compared to homogeneous catalysis, and usually, the catalyst is easily separable and recyclable (Sachdeva et al. 2013; Liu and Corma 2018).

The development in the area of heterogeneous catalysis over the last 30 years has mainly focused on engineering catalysts in nanoscale, as well as developing new effective and practical preparation methods. A particular interest has been devoted to metal nanoparticles (NPs) due to their favourable properties, including (i) high available surface area per mass unit, (ii) different fraction of the types of available active sites, (iii) the surface energy can be altered by the ultra-fine NPs, and (iv) reduction of metal NP load is required.

The important characteristics governing the catalytic activity of the metal NPs include particles size, structure, and shape. To disperse and stabilize the metal NPs, and to avoid their aggregation and deactivation, they are often incorporated into a solid matrix, and so the interaction between metal NPs and support is an additional factor to consider.

Transition metal oxides are a large class of materials that has been widely investigated due to their important electronic, magnetic, and catalytic properties (Kung 1989; Henrich and Cox 1996; Noguera 1996; Salem 2003). In recent years, transition metal nanoparticles

Fig. 2 Atomic arrangements of low index with highly coordinated atoms (e.g. (100), (110), (111)) and high index with lowly coordinated atoms (e.g. (557), (730)) (Demello 2006)

Bulk particles
Particles size: few mm-to few nm

Top down methods

Nanoparticles
Particles size: 1-100 nm

Bottom up methods

Atoms and Molecules
Size: 0.1-1 nm
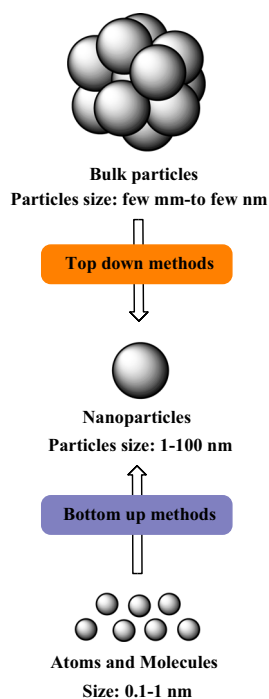
Fig. 3 An overview of top–down and bottom–up methods to prepare nickel nanoparticles

(TMNs) have attracted much attention in many technological and scientific fields, including heterogeneous catalysis (Ornelas et al. 2005; Astruc 2007). Many publications reported the utilisation of TMNs as catalysts for different important reactions (Zhong et al. 2007; Moreno-Manas and Pleixats 2003; Li et al. 2002). They have exhibited a high performance in terms of conversion, selectivity, and yields of products. In fact, the high surface/volume ratio of NPs affords a greater number of active sites per unit area compared to their bulky counterparts. In addition, TMNs have attracted a considerable interest in catalysis because usually, they are efficient catalysts, inexpensive, eco-friendly, and easy to prepare (Astruc (Ed.) (2008); Djakovitch et al. 2007; Durand et al. 2008). To extend the application of TMNs as nanocatalysts, many efforts have been devoted to tailor their nanostructure and minimize their size to ultrafine NPs and hence their surface chemistry (Yang et al. 2017; Astruc 2020).

One of the most promising TMNs is nickel. Due to its relative abundance, Ni is more cost-effective than most of the metals in use as a catalyst (Bian et al. 2017). Numerous research efforts have been recently devoted

Table 1 Top–down methods used to prepare nickel nanoparticles

Method	Advantages	Disadvantages
Ball milling (Balamurugan et al. 2015; Ahmadisoltansaraei and Moghaddam 2014)	- Useful for large production - Preparation of NPs with high purity	- Requires high energy and long time - Contamination is possible by steel balls
Mechanochemical synthesis (Fiss et al. 2020; Tang et al. 2014)	- Simple and efficient technique	- The formed microstructures are highly sensitive to grinding conditions - Contamination by milling media and atmosphere - Long time is required to synthesis very small NPs (size less than 20 nm)
Laser ablation (Gondal et al. 2012; Khashan et al. 2017; Mahdi et al. 2020; Safa et al. 2019)	-Simple and useful for large production of small nickel NPs in the form of suspension - Properties of NPs can be changed by changing laser parameters and liquid nature accordingly - No surfactant is needed in liquid media	-Prolonged time can lead to the blockage of the laser path by the formed NPs and reduction of ablation rate
Ion sputtering (Karpinski et al. 2012; Li et al. 2017; Salunkhe and AV, M. A., & Kekuda, D. 2020; Peng et al. 2010)	- Economical technique - No change in the composition of sputtered material compared to the targeted NPs - Suitable method for intermetallic compounds and refractory metals - Generates less impurity - Composition of alloy NPs can be easily controlled compared to other chemical methods - Appropriate for the preparation of ionic NPs with a large range of size and compositions	- The nature of sputtering gas (Ar, He, Ne, Xe, and Kr) can affect the morphology, texture, and composition of the obtained nanocrystalline nickel oxide films

Table 2 Bottom–up methods used to prepare nickel nanoparticles

Method		Advantages	Disadvantages
Solid-state methods	Physical vapour deposition (Lin et al. 2017)	- Simple technique for the synthesis of thin films	- Expensive technique - Produces a low quantity of material - For the implementation of this method at industrial level, high throughput with lower cost is necessary
	Chemical vapour deposition (Moravec et al. 2011; Napari et al. 2020)	- NP properties can be controlled, such as crystal structure and surface morphology - High film durability can be obtained - Easy to scale-up	- Corrosive, toxic, and explosive gases - Deposition of multicomponent material is difficult
Liquid-state synthesis methods	Sol–gel method (Pooyandeh et al. 2020; Shamim et al. 2019; Zorkipli et al. 2016)	- Simple technique - NP size and morphology can be controlled by monitoring reaction parameters	-
	Chemical precipitation (Abboud et al. 2020; Ebin 2018; Mahaleh and Y., Sadrnezhaad, S. K., & Hosseini, D. 2008)	- Simple and efficient approach to prepare metal NPs - Abundant bases can be used as precipitation agents (e.g. NaOH, NH$_4$OH) - Hydrothermal treatment can be used to accelerate the precipitation - High purity NPs can be obtained - Particle shape and size can be controlled using different complexation and protection agents, respectively	-
	Chemical reduction (Ebin 2018; El-Kemary et al. 2013)	- Simple technique - Abundant reducing agents can be used such as NaBH$_4$, ethylene glycol, glucose, ethanol, urea, hydrazine hydrate, citrate of sodium	- Reducing agents are usually toxic and contain impurities
	Hydrothermal method (Cao et al. 2020; Zhou et al. 2018; Ahire et al. 2012)	- Produces NPs with suitable size and shape, and high crystallinity	- Limitation of reproducibility and reliability
	Solvothermal (Gu et al. 2019; Beach et al. 2009)	- Produces monodispersed NPs with high crystallinity - Appropriate technique to prepare NPs with narrow size distribution using simple heating apparatus	-
Gas-phase methods	Spray pyrolysis (Ukoba et al. 2018; Desai 2016)	- Relatively simple technique - Inexpensive method - Reproducible - NP size is controllable	-
	Flame pyrolysis (Dillon et al. 2013; Seo et al. 2003)	- Promising method for the production of Ni NPs - Efficient for less volatile nickel precursors	-
Biological methods	Using fungi proteins (Salvadori et al. 2015; Yang et al. 2014)	- Easy to scale up - Economical flexibility - Large surface area	- Safety problem - NPs formed are of different sizes
	Using plant and plant products (Habtemariam and Oumer 2020; Sabouri et al. 2019; Helan et al. 2016; Ramalingam et al. 2019)	- No pathogenicity risk as that of bacteria and fungi methods - Formation of homogenous NPs	- Heating is required which increases the NP production cost
Other methods	Electrochemical deposition (Zhang et al. 2013; Moghaddam et al. 2008)	- Fast, simple and low-cost method - Produces NPs of controlled size and morphology - NPs attach directly to the substrate	
	Microwave-assisted method (Azhagu Raj et al. 2017; Jena and Shivashankar 2008; Nadagouda et al. 2011)	- Simple, rapid, and highly effective technique - Homogeneous heating	- Short crystallisation time
	Ultrasound technique (Vargas et al. 2016)	- Eco-friendly, easy, and fast method - Useful for less volatile materials - Different forms of NPs can be synthesized by changing reaction conditions	- The sonochemical reduction rate completely depends on the ultrasound frequency

Fig. 4 Principal steps involved in this the synthesis of flower-like NiO NPs

$$2NH_4OH \; (aq) \longrightarrow 2NH_4^+ \; (aq) + 2OH^- \; (aq)$$

$$Ni(CH_3CO_2)_2.4H_2O \; (s) \longrightarrow Ni^{2+} \; (aq) \; + 2CH_3CO_2^- \; (aq)$$

$$Ni^{2+} \; (aq) \; + 2OH^- \; (aq) + xH_2O \longrightarrow Ni(OH)_2. \; xH_2O \; (s)$$

$$Ni(OH)_2. \; xH_2O \; (s) \xrightarrow{\text{stir}} Ni(OH)_2. \; xH_2O \; Sol$$

$$Ni(OH)_2. \; xH_2O \; Sol \xrightarrow[\text{autoclave}]{100\,°C, \; 16h} Ni(OH)_2 \; \text{green powder} + xH_2O$$

$$Ni(OH)_2 \; \text{green powder} \xrightarrow[-H_2O]{500, \; 5h} \text{NiO black powder} \qquad (1)$$
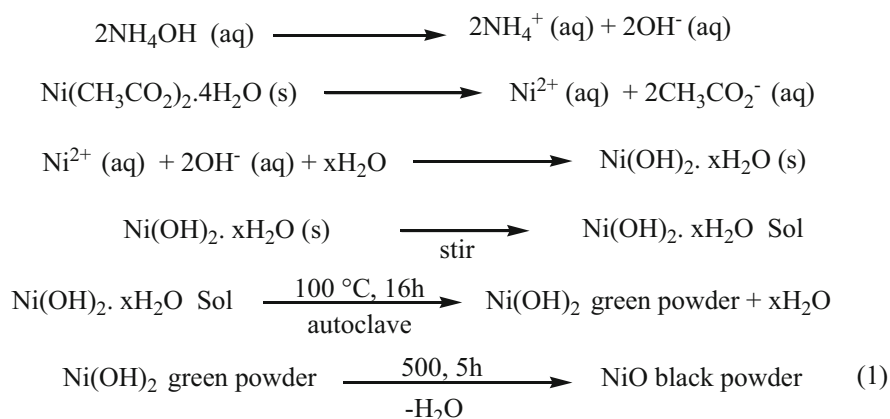
to the preparation of nickel nanoparticles (Ni NPs) with tailored features, because of their unique electronic, optical, and mechanical properties and their widespread potential applications in many fields including catalysis, nanoelectronics, optoelectronics, adsorption of dyes from industrial water, development of supercapacitors, fabrication of dye-sensitized solar cells, and sensors and biomedical applications (Jaji et al. 2020; Vollath and Szabó 2009; Schubert and Hüsing 2019; Ozin et al. 2009a; Lai et al. 2006, 2008; Christoskova and Stoyanova 2001; Ashik et al. 2017; Guo et al. 2011; Solsona et al. 2016; Vikraman and Park 2016; Sasaki et al. 2018; Gao et al. 2012; El-Safty et al. 2008; Adil et al. 2017; Arora et al. 2017; Pike et al. 2017; Chand and Sandhu 2015; Sun et al. 2016). Due to their unique magnetic, chemical, and physical properties, we believe that Ni NPs will gain more attention in future in various technological fields such as nanocatalysis, battery

Fig. 5 SEM images of the flower-like NiO microspheres
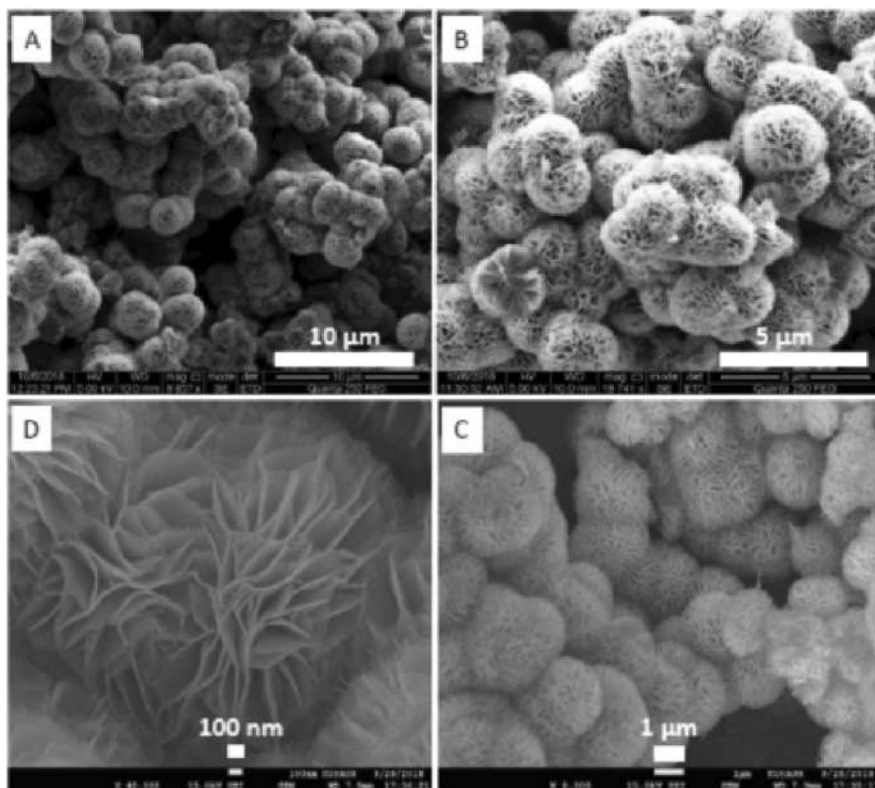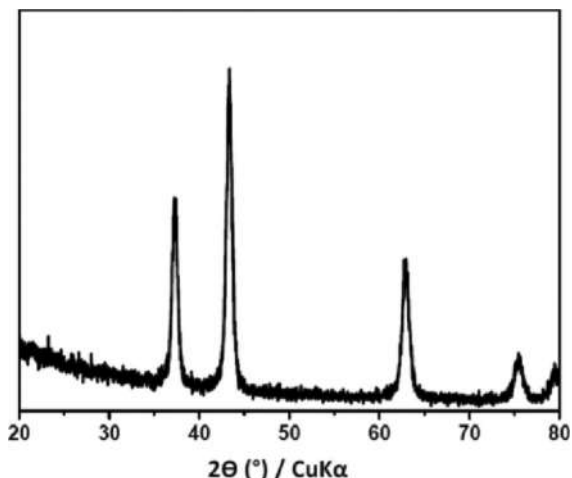
Fig. 6 XRD pattern of the NiO NPs obtained with CTAB

manufacture, dye-sensitized solar cells, enhanced pseudo-capacitance, and drug delivery.

Recently, Ni NP–based heterogeneous nanocatalysts have been employed for various organic transformations such as hydrogenation reaction of aromatics (Grosso et al. 2004), production of synthesis gas (Zou et al. 2005), steam reforming (Ying et al. 1999), methanation (Jia et al. 2003), isomerisation of hydrocarbons (Basha et al. 2006), and hydrocracking (Moreno-Tost et al. 2002) (Polshettiwar et al. 2009; Kalbasi and Mosaddegh 2011; Alonso et al. 2011). Ni NPs are considered as promising nanocatalysts because they are eco-friendly, nonexpansive, easy to prepare, and easily recoverable and recyclable.

Ni NPs have been also employed in photocatalysis. Nickel oxide is one of the promising intrinsic p-type transparent electrically conducting oxides (TCOs) that exhibit several interesting features such as wide band gap (3.5 to 4 eV), excellent durability, chemical stability, and large span optical density (Sriram et al. 2016).

Despite the importance of Ni NPs as efficient economic and eco-friendly nanocatalysts, characteristics such as optical and catalytic activity may be lost if the dispersion of these particles is not adequately modulated. Several efforts have been deployed to overcome their aggregation problem, low durability, low dispersibility, and electrons and holes recombination by incorporating them into a solid matrix, like mesoporous silica, zeolites, carbon, metal oxides, or polymers (Kumar et al. 2016; Wang et al. 2017; Jin et al. 2009; Martín-Jimeno et al. 2021).

Throughout this review, we will discuss the most common techniques used to prepare unsupported and silica-supported Ni NPs and their recent applications in heterogeneous catalysis, including photocatalysis. The effect of Ni NP size and aggregation on the catalytic activity of the reported catalysts will be briefly studied.

Designing metal nanoparticles

Effect of nanoparticle size and shape

Increasing the number of active sites in a surface unit of a metal by increasing the surface area per gram of the catalyst, by reducing the metal particles size, not only minimizes the cost of catalyst preparation but also reduces the associated side effects on the environment and public health of the catalytic process. It has been found that the reduced particle size has also a higher fraction of corner and edge sites as shown in Fig. 1 (Martín-Jimeno et al. 2021), which can affect the binding properties of reactants on the catalyst. Some reports mentioned that the catalysis occurs especially on isolated active sites, and thus, decreasing the NP size is recommended. This behaviour was observed for the oxidation reaction of

Fig. 7 TEM images of the obtained NiO nanoflakes. Red cycles in panel A show uniform and highly ordered channels
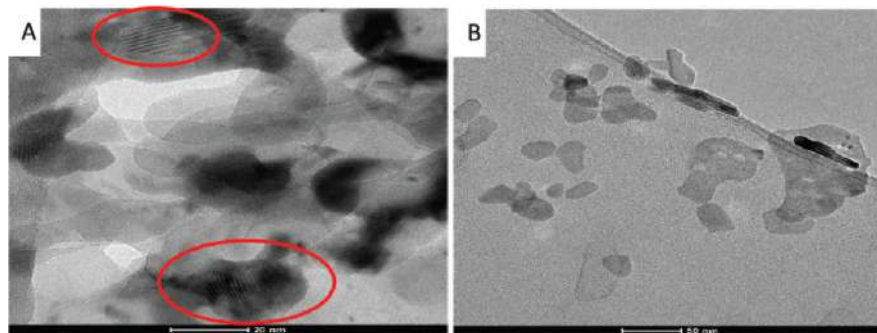
Fig. 8 Transformation of cyclohexene to cyclohexene oxide over flower-like NiO NPs (Abboud 2020)

Flower-Like mesoporous NiO NPs

+ m-CPBA

22 °C
1 atm

Immediately

Conversion: 91 %
Selectivity: 53 %
TOF: 0.88 s^{-1}
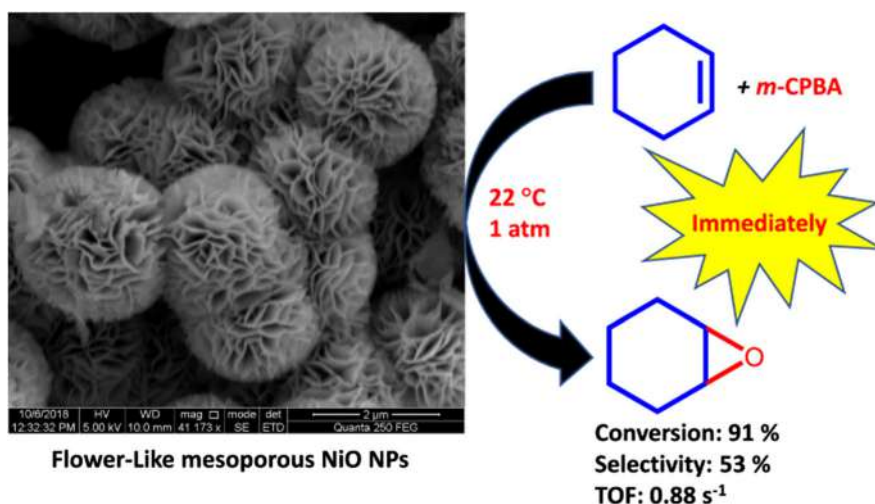
CO over Au NPs, in which the catalysis occurred in the isolated active sites located in corners and edges, where the Au atoms were lowly coordinated, and were able to bind both CO and oxygen (Lin et al. 2004). Conversely, Giordano et al. (Tsunoyama et al. 2008) reported that the oxygen reduction reaction (ORR) catalysed by Pt NPs preferably occurred in the active sites located in the planes, where each O_2 molecule was bound on two adjacent Pt atoms. This could lead to a mass normalized catalytic activity. The smallest NPs contain a low and isolated number of active sites, and the larger NPs have small surface area. Therefore, a compromised size
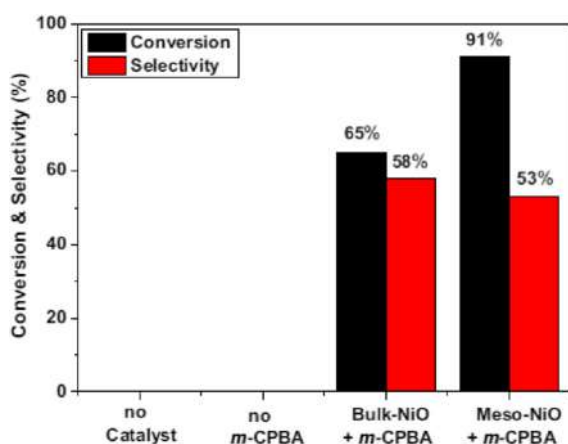
Fig. 9 The calculated conversion of the cyclohexene oxidation reaction at different blank reactions. 10 mg of NiO catalyst, 0.06 mL of cyclohexene, 156 mg of m-CPBA (1.5 equivalent), 3 mL of solvent: CH_3CN/CH_2Cl_2 (1:1 v/v), $T = 22$ °C, 1 atm

distribution could afford the highest mass normalized catalytic activity.

Particles shape is another important parameter which can affect the active sites distribution in the catalyst NPs. Controlling the metal NP shape is an ongoing challenge. However, using colloidal methods, this aim has been relatively achieved (Glasnov 2013; Rogers 2017). The obtained metal NP shapes are a result of the arrangement of different crystal planes (facets). NP shape could have a direct effect on reactants adsorption/desorption properties, reactant binding, and metal/support interactions. During the catalyst synthesis, different possible facet arrangements could be formed. But, typically, low index facets, such as (100), (110), and (111), are predominant, because these facet arrangements are characterized by low energy and high atomic coordination (Fig. 2). However, if the active species are located in corners and edges, it is preferable to prepare facet arrangements with high indexes (e.g. (557), (730), Fig. 2) (Baumgard et al. 2013).

The metal/support contact surface area and the number of active sites in the periphery depend on the shape of metal NPs. As mentioned above, the CO oxidation reaction over Au NPs preferentially occurred in the periphery active sites, and the catalytic performance was shape dependent (Woehl et al. 2012).

Support effect

The physical and chemical stability, good reusability, and high turnover numbers are important factors

Fig. 10 Epoxidation reaction of styrene oxide over flower-like NiO NPs

Flower-Like NiO NPs "Catalyst"

+ *m*-CPBA

Selectivity: 65 %
TOF: 243 s^{-1}
Time: < 1 min

Solvent: CH$_2$Cl$_2$/CH$_3$CN
22 °C, 1 atm
Conversion: 87 %
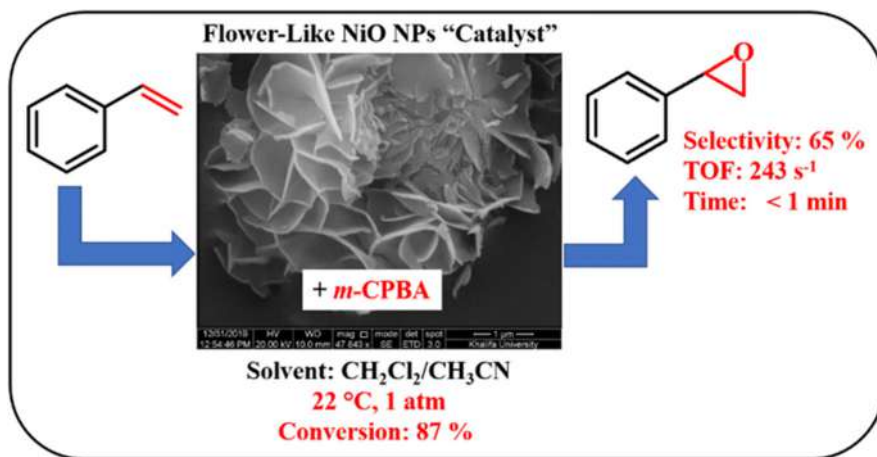
defining an efficient catalyst. To overcome metal NP deactivation due to the aggregation, low durability and dispersibility, electron–hole recombination, and degradation, metal NPs have been incorporated and immobilized into a support. However, the support can also affect the catalyst activity and performance either by (1) changing the shape and structure of NPs, (2) redox transforming the metal ions which have two or more redox states (e.g. MnO$_2$, Fe$_2$O$_3$, and CeO$_2$), and (3) support-metal NP charge transferring (Bönnemann and Richards 2001).

The choice of the type of support is usually governed by the application. Carbon is often used as a support for fuel cell owing to its high conductivity (Polte et al.

Fig. 11 The obtained conversion and selectivity of epoxidation of styrene catalysed by FL-NiO compared to BulkNiO and blank reactions. Conditions: catalyst: 10 mg, styrene: 0.06 mL, *m*-CPBA (1.5 eq): 156 mg, solvent: 3 mL of CH$_3$CN/CH$_2$Cl$_2$ (1:1 v/v), time: < 1 min, T = 22 °C, 1 atm

2010a), and titanium dioxide (TiO$_2$) has been widely used as a support in photocatalysis as it is a semiconductor characterized by an appropriate band gap (McKenzie et al. 2010), whereas silica (Polshettiwar et al. 2010), alumina, and other transition metal oxides (Gniewek et al. 2008) have demonstrated to be very appropriate supports for various applications, even for nanocatalysts, due to their high thermal and chemical stabilities and high surface areas (Polte et al. 2010b, 2010c). Mesoporous silica materials have attracted considerable interest as suitable catalyst matrices due to their unique features. These characteristics include high surface area; tunable pore size; uniform pore distribution; high adsorption capacity; high thermal, chemical, and mechanical stabilities; and highly ordered pore network which facilitate the diffusion of reagents and products.

Synthesis methods of nickel nanoparticles

Unsupported nickel nanoparticles

Several methods have been used to prepare nickel NPs which can be classified into two principal categories: top–down methods and bottom–up methods (Pacioni et al. 2015; Swathy 2014; Horikoshi et al. 2013; Ahmed et al. 2016; Jamkhande et al. 2019). The top–down methods reduce the size of bulk material particles to NPs, whereas the bottom–up methods prepare NPs from atoms or molecules, using different mechanical, physical, and chemical techniques (Fig. 3) (Pacioni et al. 2015; Jamkhande et al. 2019).

Fig. 12 Synthesis of 2,2′-di(indolyl)oxindole (a) and 3,3′-di(indolyl)oxindole (b) derivatives. Reaction conditions: isatin compounds (1 mmol), indole compounds (2 mmol), nano-NiO (0.004 g) and water (2 mL) at 70 °C. The yield refers to pure isolated product

R_1 = H, PhCH$_2$ or Me; R_2 = H, Br, or; NO$_2$
Yield = 80-98 %

R_1 = H or Me; R_2 = H; R_3 = H, Br, NO$_2$ or OMe
Yield = 60-98 %
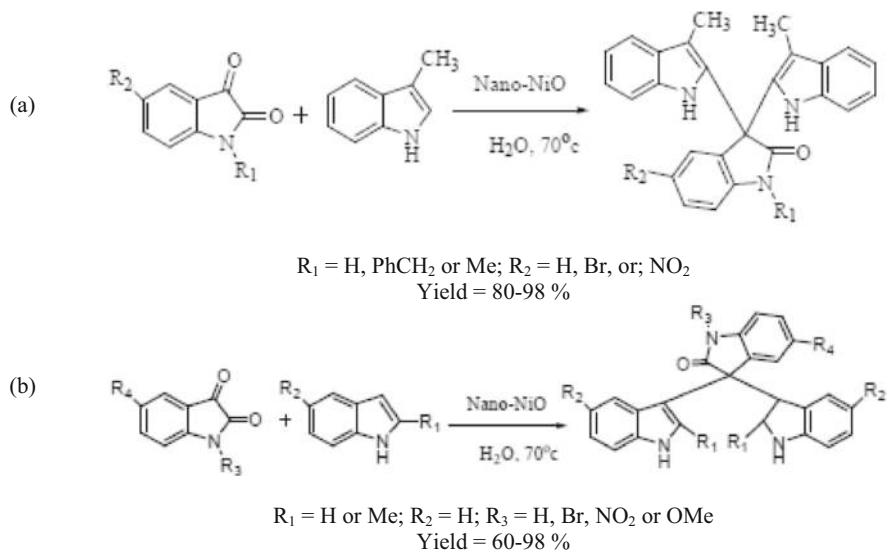
Top–down methods

Using these methods, bulk particles are reduced to NPs using different physical and chemical techniques such as mechanical milling, laser ablation, and thermal method (Meyers et al. 2006). Even though these methods are relatively easy to curry out, they are not suitable for synthesising NPs with determined shape and very small size. In addition, the top–down techniques can affect the physicochemical and surface of the obtained NPs (Ahmed et al. 2016). Table 1 recapitulates the most used techniques in top–down methods with their advantages and disadvantages.

Bottom–up methods

The synthesis of Ni NPs using these methods is based on joining of atoms or small molecules. Table 2 recapitulates the most used techniques in this category with their advantages and disadvantages.

Fig. 13 Preparation of oxindole (a) and indoline (b) derivatives. Reaction conditions: dicarbonyl compounds (1 mmol), isatins (1 mmol), malononitrile (1 mmol), catalyst (0.0007 g), and H$_2$O (2 mL); reactions conducted at r.t. for 5 min

R1 = H or Me; R2 = H, Et, or PhCH$_2$; R$_3$ = H, Cl, Br, Me, OMe or NO$_2$
Yield = 70-98 %

R1 = H, Me, Et, PhCH$_2$; R2 = H, Cl, Br, Me, OMe, NO$_2$
Yield = 75-98 %
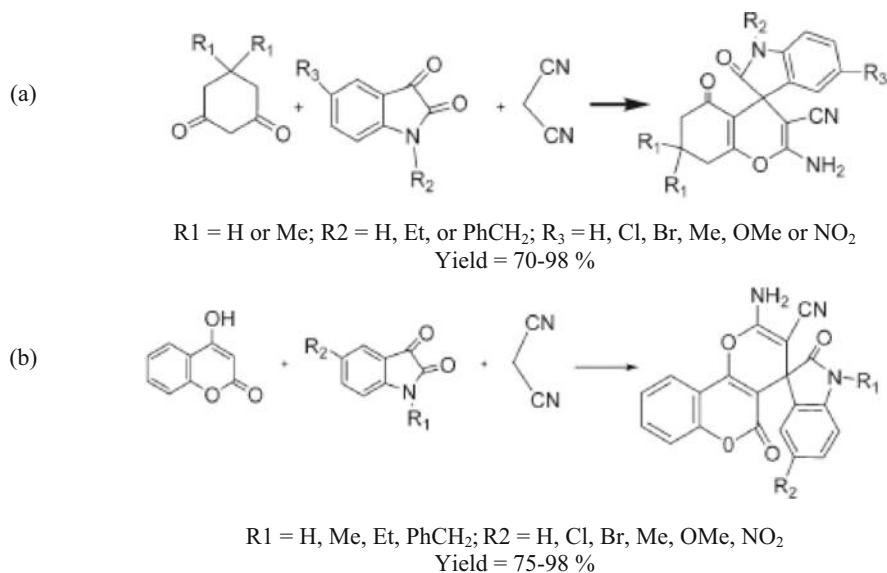
Fig. 14 XRD pattern of NiO nanoparticle
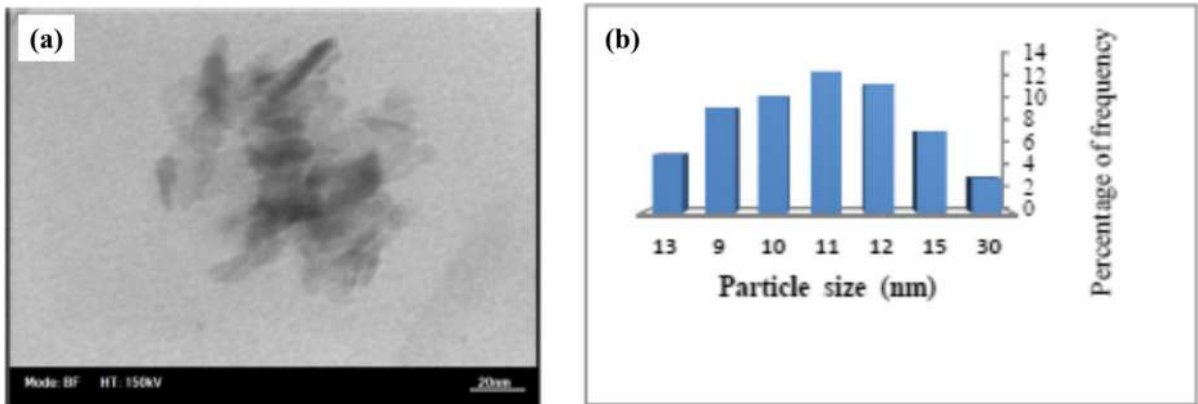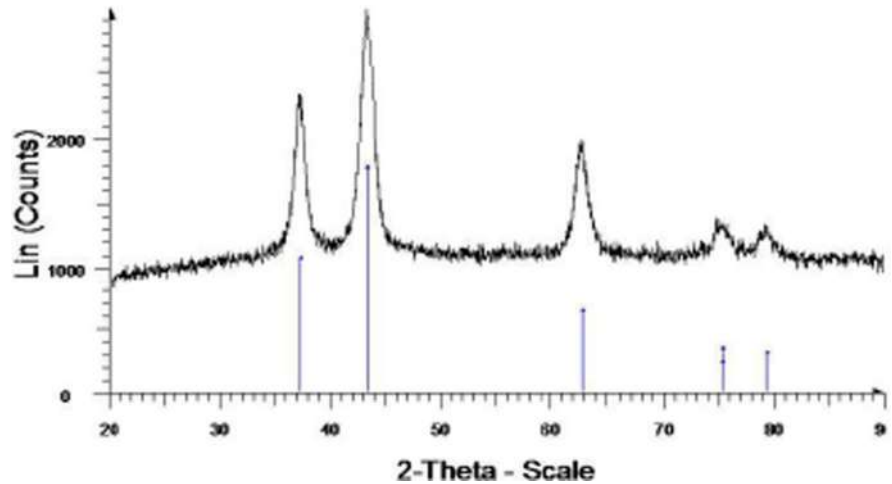
Fig. 15 (a) TEM pattern of NiO nanoparticle and (b) particle size distribution of NiO nanoparticle

Preparation of silica-supported nickel nanoparticles

Usually, silica-supported Ni NP-based catalysts are synthesized by introducing nickel precursors into the silica followed by calcination. The dispersion degree of nickel precursor in the silica before calcination will affect the particle size, degree of dispersion, and aggregation of the obtained Ni NPs and will then affect the catalytic activity of the final nanocatalyst (Ashik et al. 2017). Generally, metal NP species would exhibit higher catalytic activity and stability if the active sites are considerable, quantized, confined, and accessible (Alshammari and Kalevaru 2016).

In the past decade, several techniques have been developed for the preparation of silica materials
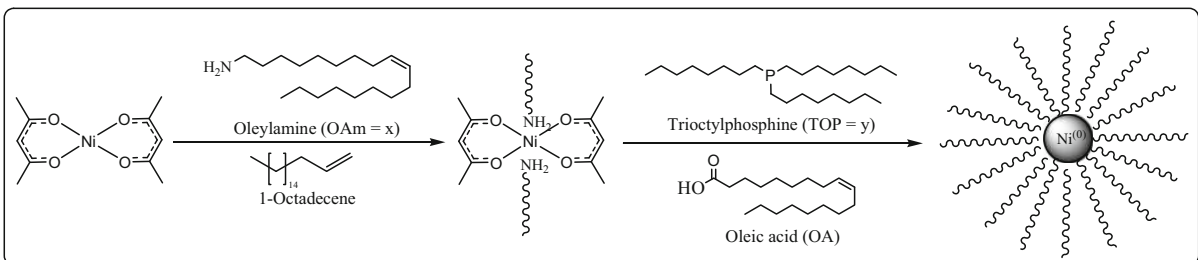
Fig. 16 Hot injection synthesis of monodispersed NPs

Table 3 Synthetic conditions and resulting size of Ni NPs

Samples	OAm[a] (x) [eq.]	TOP[b] (y) [eq.]	Size[c,d] [nm]
Ni_2.5×1.5y	2.5	1.5	1.3/8.0±1.4
Ni_5×1.5y	5	1.5	4.0/7.0±1.3
Ni_10×1.5y	10	1.5	5.6/10.6±1.9

[a] Total number of equivalents of oleylamine (OAm) and 1-octadecene (21) kept constant by varying the amount of solvent

[b] Trioctylphosphine

[c] Determined by XRD

[d] Determined by HAADF-STEM

supported Ni NPs. Among these techniques, the impregnation, ion exchange, sol–gel technique, microemulsion, co-precipitation, direct incorporation, and deposition of nickel precursors into the silica materials are the most commonly used methods (Solsona et al. 2016; Sasaki et al. 2018; Barhoum et al. 2017; Badari et al. 2015; Rudko et al. 2015; Ashik and Daud 2015). However, the use of these approaches is still limited by the NP size and aggregation, low dispersion, level of the incorporated Ni NPs into porous silica matrices, and the complicated, expensive, and time-consuming techniques.

The synthesis of Ni NPs with quantized size and high dispersion tended to be difficult. The study of the

Fig. 17 XRD pattern of Ni nanoparticles

catalytic activity of Ni NPs with quantized size was relatively scarce compared with other transition metal NPs.

In recent years, some traditional impregnation techniques and approaches have been developed to prepare highly active and well-dispersed supported nickel catalysts, such as using organic nickel precursor (Corma 1997), direct dispersion (Vadia et al. 2013), aqueous metal complexes (Ashik et al. 2017; Look and Claflin 2004), and surface modification (Ashik et al. 2017; Look and Claflin 2004). Despite this, the application of these techniques is still limited by the aggregation of Ni NPs, low dispersion, complicated preparation, and expensive metal precursors.

In addition, the carrier of the catalyst is another key factor for obtaining high catalytic activities. Mesoporous silica, as an important carrier, is well-known for its high surface area, high porosity, and oriented channels, which are ideal characteristics to enhance the catalyst activity (Kumar et al. 2016; Look and Claflin 2004; Rioux 2010; Rodríguez and Garcia 2007). Furthermore, due to the narrow size distribution of mesoporous silica channels, the growth of the metal particles would be well confined in these channels, and thus, quantized active sites would be produced (Wang et al. 2017; Penner 2014; Finiels et al. 2014). However, practical methods are still necessary to control the migration of Ni NPs from silica pores and channels and their aggregation, hence their deactivation. In addition, more efforts are still needed to control the dimension, geometry, and regularity of the silica channels and pores in a systematic and efficient methodology during the incorporation of these NPs into nanostructured mesoporous silica. Because if the interaction between metal particles and support is weak, metal species will migrate out of the silica pores and aggregate into bulk particles during the calcination step or during the catalysis process (Schubert and Hüsing 2005). Therefore, the force of the interaction between nickel and silica or the confinement of Ni NPs is necessary to stabilize the nickel species and to prevent their migration and aggregation during the calcining process (Lai et al. 2008; Ozin et al. 2009b).

Classical routes commonly used to date to prepare silica-supported Ni NPs with tailored properties are based on precipitation and impregnation techniques. Many efforts have been made to develop the colloidal methods to be able to tune the nickel-based catalyst properties, especially using sol immobilisation. The
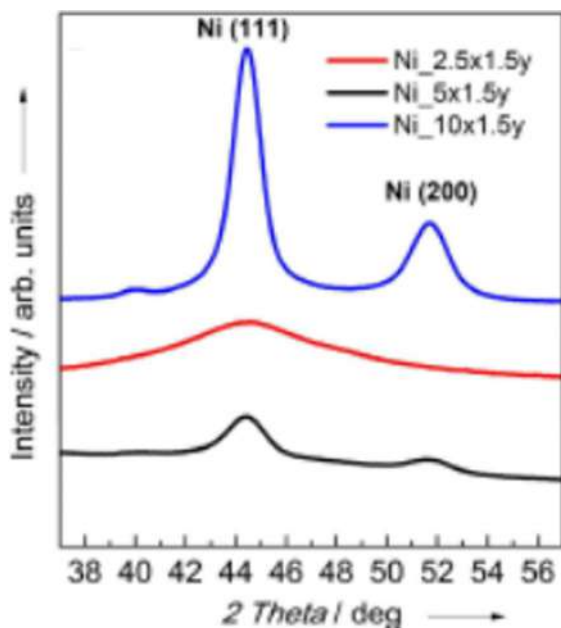
Fig. 18 (a) and (b) are HR-HAADF-STEM images of Ni_5 × 1.5y. The arrow indicates the twinned lamellae of the NPs in (a) and smaller Ni NPs embedded in the organic shell in (b); (c) and (d) are HR-HAADF-STEM images of Ni_10 × 1.5y. In (c), the arrow indicates the fivefold axis of a multiply twinned decahedron. In (d), the arrow indicates the Ni atoms of smaller NPs embedded in the organic shell
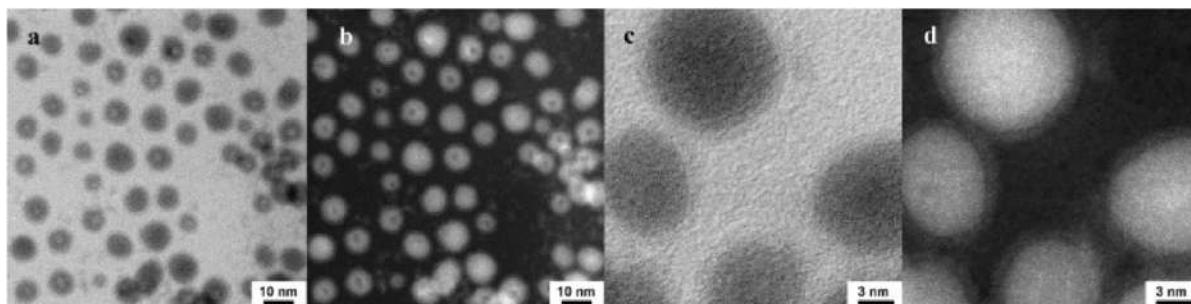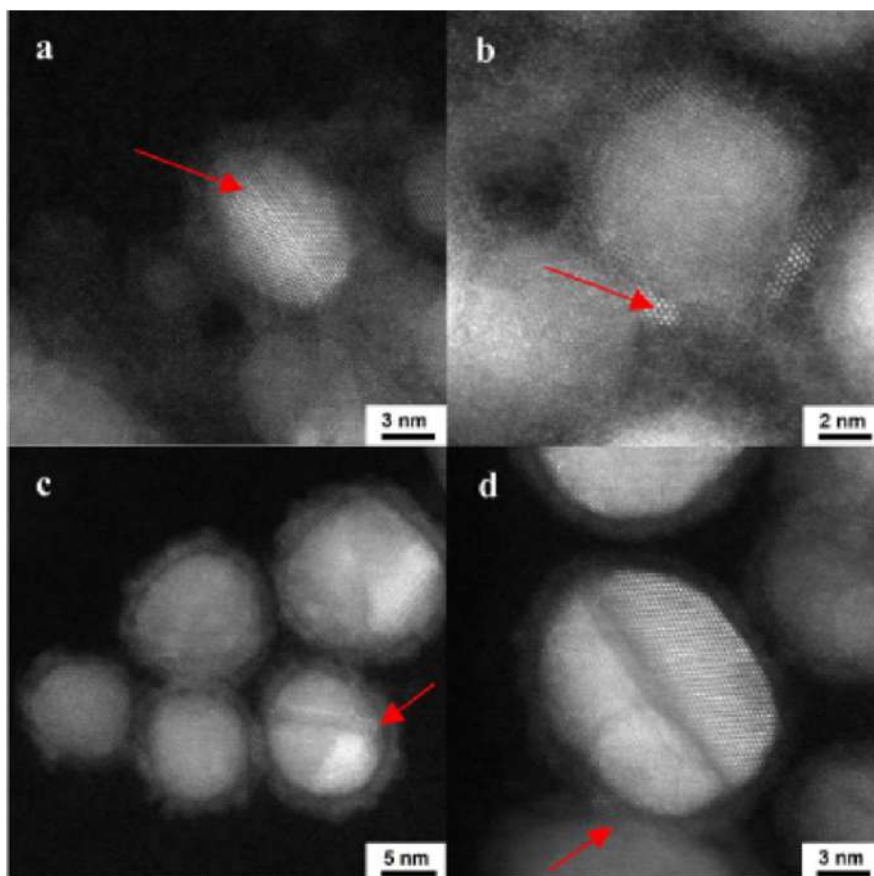
Fig. 19 (a) STEM images of Ni_2.5 × 1.5y. LM BF-STEM (LM, low magnification; BF, bright field), (b) corresponding HAADF-STEM, (c) HR BF-STEM of a Ni NPs, (d) corresponding HAADF-STEM
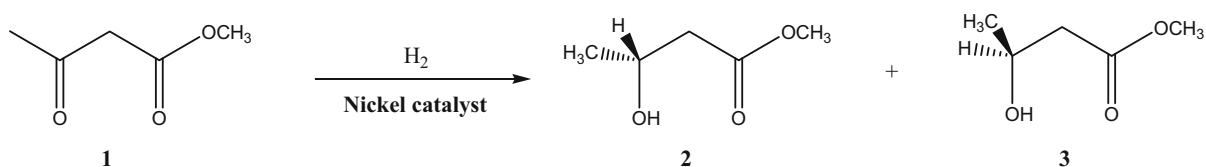
Fig. 20 Hydrogenation of methyl acetoacetate (1) and formation of two enantiomers, (R)- and (S)-methyl-3-hydroxybutyrate (2 and 3, respectively)

Table 4 Catalytic performance of Ni NPs in hydrogenation of methyl acetoacetate

Samples	Tot. MAA[a] conv. [%][c]	Inst. (R)-MHB[b] selec. [%][d]	Final ee [%][e]
Ni_5×1.5y	69	48	−3
Ni_2.5×1.5y	36	48	−3
Ni_10×1.5y	74	46	−4

[a] Methyl acetoacetate

[b] Methyl-3-hydroxybutyrate

[c] Conversion after 22 h of reaction

[d] Unless otherwise stated, selectivity at the same value (50%) of total MAA conversion

[e] Positive values indicate (R)-selectivity, negative (S)-selectivity

general procedures and advantages, as well as some drawbacks of these three principal methods, will be now discussed.

Impregnation method

Impregnation is a very commonly used procedure to synthesize nickel NPs with different sizes. This method involves 'wetting' the catalyst support (here silica) with a solution of the nickel precursor, which is commonly a nickel salt. If the nickel precursor is dissolved into a volume of solvent equal to the silica total pore volume, a thick-paste like material is obtained; this point is called 'incipient wetness point'. This technique is named as incipient wetness impregnation (IWI) (Frey and Hinrichsen 2012; He et al. 2015; Nakagawa et al. 2012). Then, the final material is obtained after the evaporation of the solvent followed by a calcination process, to transform the nickel precursor to nickel oxide NPs (NiO). The final material can be transformed to reduced form (Ni NPs), if required.

However, controlling the size and dispersion of NiO NPs using this method is still challenging. The size of the obtained NiO NPs can be affected by four principal factors: the silica surface area, nickel loading, solvent nature, and annealing conditions. A high surface area of the silica and low nickel loading promote the formation of smaller NiO NPs with high dispersion (Yao et al. 2010). In addition, high thermal treatment is required to remove chlorine residues, (Zhao et al. 2020) which thereafter could lead to particles agglomeration, in

Fig. 21 SEM pictures of NiO microspheres prepared without CTAB
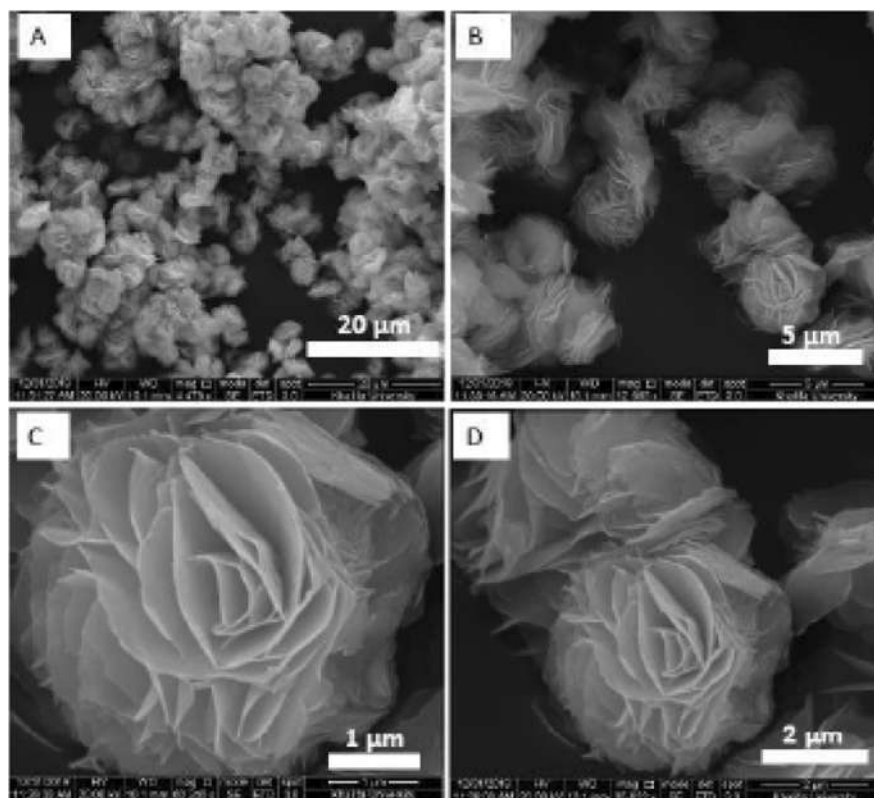
Fig. 22 SEM pictures of NiO microspheres prepared with CTAB
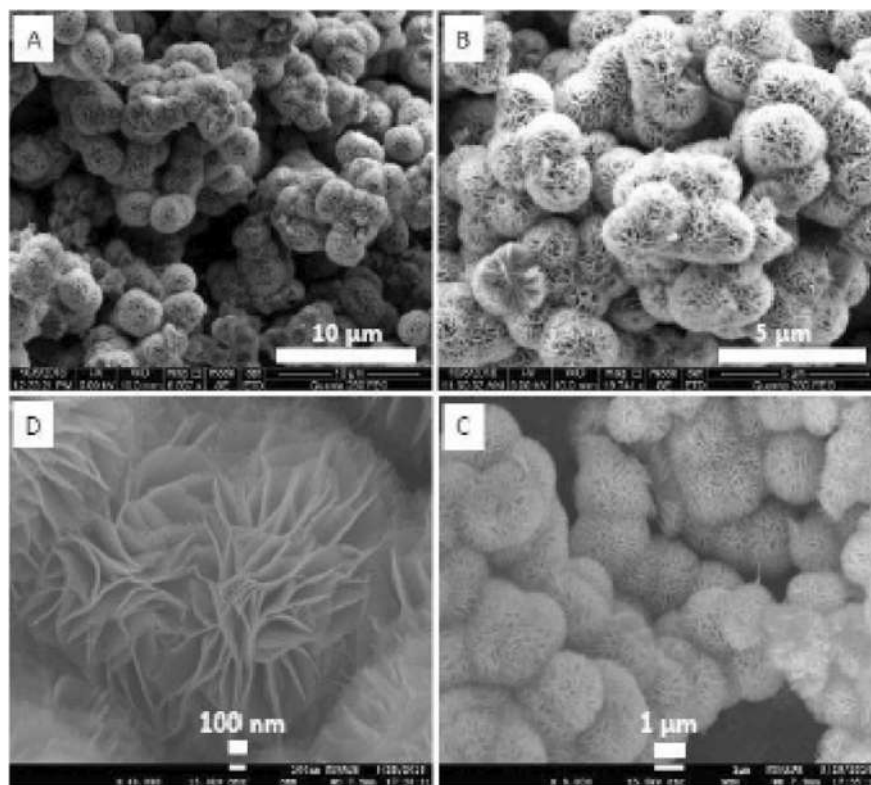
particular in case of high nickel loading (Spagnolo et al. 2016).

Precipitation methods

The co-precipitation is the most commonly used method for the preparation of mixed metal oxides NPs. This method is based on a simultaneous precipitation of both metal and support precursors, in an alkaline media, such as aqueous solutions of $NaCO_3$ or K_2CO_3. Generally, the co-precipitation process provides strong metal/support interactions.

The deposition–precipitation (DP) method is similar to co-precipitation. However, DP technique involves a controlled precipitation of highly soluble metal precursor (e.g. nickel nitrate or acetate) inside the silica. The precipitation of the metal precursor can be achieved either by changing the solution pH or the concentration of a complexation agent or by adding a precipitation or reducing agent (Bianchi et al. 2005). Two main factors have to be ensured to avoid a spontaneous precipitation of the metal precursor in solution, namely strong metal–support interaction and appropriate metal precursor concentration. In general, the silica surface acts as a

nucleation agent for the precipitation of the metal precursor. The desired catalyst is obtained after subsequent calcination steps (Patil et al. 2012).

Colloidal methods

Colloidal methods are three-dimensional syntheses which use stabilising agents (protective agent) to prevent the metal NP aggregation via electrostatic repulsion or steric inhibition. Different molecules can play the role of stabilising agent, including surfactants, polymers, and donor ligands.

These methods involve many steps: (i) preparation of a colloidal metal by dissolving the required metal precursor (commonly a salt) in a suitable solvent using a surfactant as protective agent (e.g. cetyltrimethylammonium bromide (CTAB)), (ii) deposition of the metal colloids into the selected support, and (iii) chemical reduction of the metal salt to zero valent mixture metal (Mehrabadi et al. 2017). Metal colloids can be carried out either in organic or aqueous medium, depending on the nature of the surfactant used.
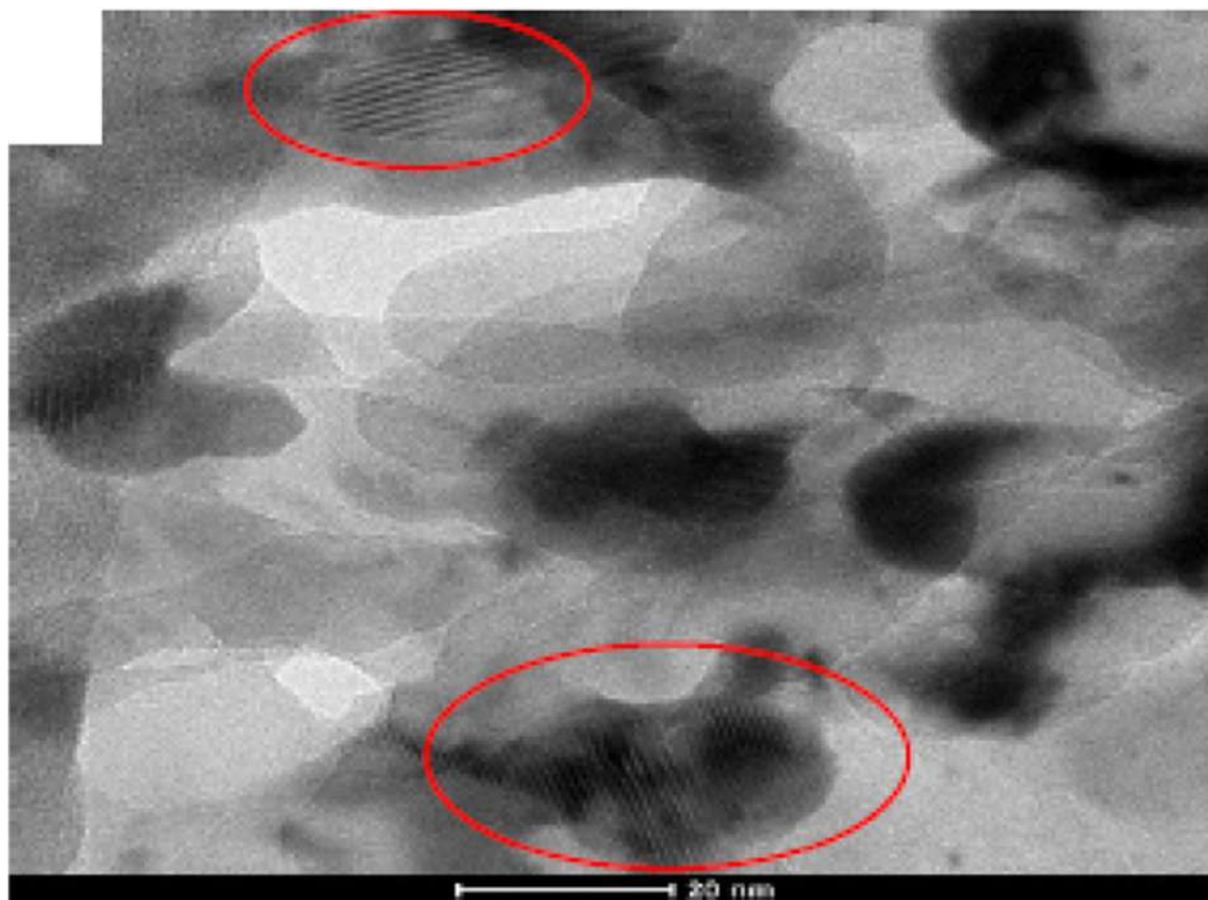
Fig. 23 TEM pictures of the obtained NiO nanoflakes

This method can produce very small nickel NP sizes. The surfactant can be removed either by solvent extraction in diluted acidic conditions (e.g. HCl, 2 M in ethanol) or by using high-temperature treatment (e.g. calcination). It is suitable to develop an alternative route to synthesize highly dispersed fine metal NPs without using surfactant or any protection agents, hence decreasing the level of complexity, avoiding final catalyst contamination and protecting the environment.

The sol immobilisation process is an extension of the colloidal methods and involves immobilizing the colloidal metal into a support material by changing the pH. The metal–support interaction can be enabled by reducing the pH under the isoelectric point of the support. Actually, the properties of the metal NPs can be tuned before their immobilisation by changing different reaction conditions such as reducing agent, metal concentration, and metal/stabilizer ratio (Kennedy et al. 2015).

The nature of the reducing agent can affect the metal NP properties. A panoply of reducing agents has been used for the preparation of metal NP catalysts, such as hydrogen, hydrazine, boron hydrides, and alcohols (Jia and Schüth 2011).

The utilisation of polymers as protecting agents is preferable as they are able to tailor the metal NP properties and also enhance their long-term stability during catalysis process (Yoshida et al. 2005). Polymers can bind selectively to specific crystal planes, leading to NPs with controlled shape and surface site (Chen et al. 2015; Zhou et al. 2002).

Recent applications of unsupported nickel nanoparticles in catalysis

Unsupported catalysts occupy the large section of industrial catalysis. This includes metals, metals alloys,

Fig. 24 The proposed photocatalytic mechanism of MG dye decolourisation over the flower-like NiO NPs
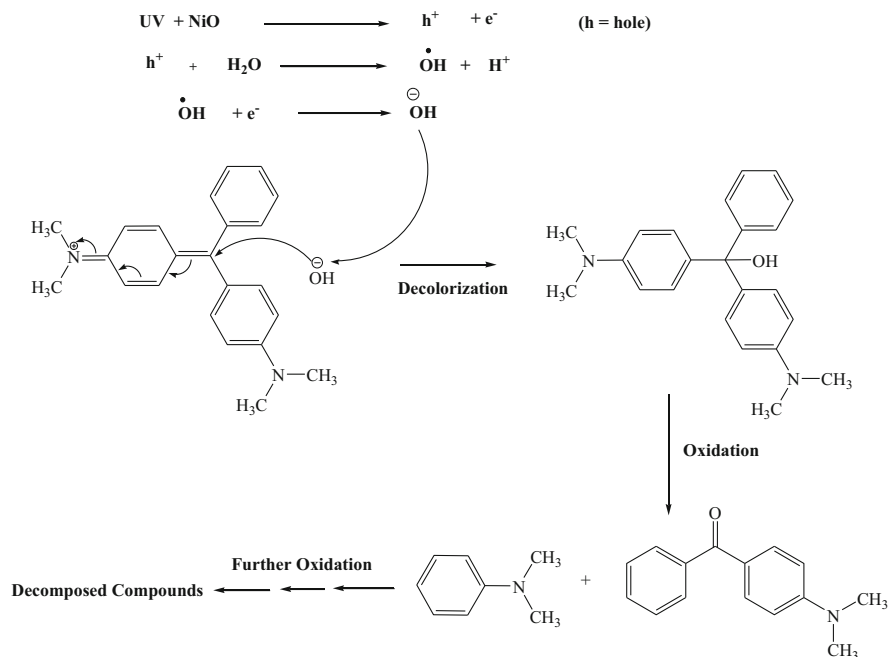
metal oxides, metal sulphides, zeolites, etc. Unsupported catalysts have much lower surface areas, typically in the range of 1 to 100 m²/g. Among the most important metal oxides, NiO NPs have been prepared by different methods and techniques and employed as a catalyst for many chemical transformations.

Different approaches are intensively investigated, and important progress has been made in the synthesis of NiO NPs with different morphologies, sizes, shapes, and crystalline structures. The most employed methods

for the synthesis of unsupported NiO NPs are discussed above. The common aim of all these methods and techniques is to obtain well-defined and reproducible nanoparticles by employing a simple, scalable, and low-cost process. Therefore, NiO NPs have been prepared in different morphological structures, such as nanoflakes, nanoflowers, nanorods, nanosheets, nanospheres, nanoballs, nanotubes, and nanowires (Paulose et al. 2017).

Heterogeneous catalysis

Only a few articles in the literature reported the investigation of Ni NPs in heterogeneous catalysis. Abboud et al. (Abboud 2020) reported recently the synthesis of highly ordered mesoporous flower-like NiO NPs and their utilisation as catalyst for the epoxidation reaction of cyclohexene to produce cyclohexene oxide. NiO NPs were prepared by hydrothermal-assisted chemical precipitation method, using nickel acetate tetrahydrate as a metal source, ammonium hydroxide (NH_4OH) as a base, diethanolamine (DEA) as complexing agent, and CTAB as a structure directing agent. The principal steps involved in this synthesis are described in Fig. 4 below.

The obtained material was characterized by SEM TEM and EDX. The SEM images (Fig. 5) clearly showed that the prepared NiO consists of fairly flower-

Fig. 25 XRD patterns obtained for NiO NPs prepared with a biosynthesis method using the extract from *Persea americana* seeds
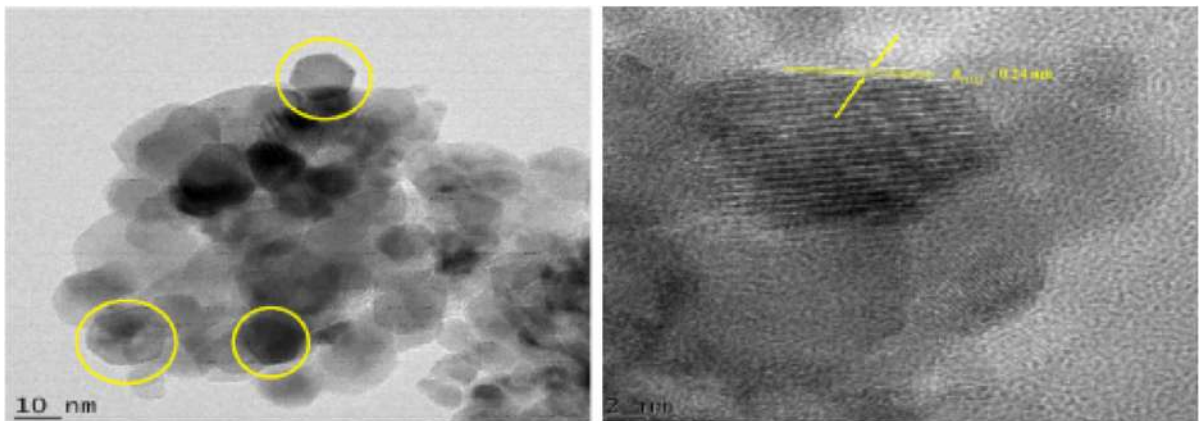
Fig. 26 High-resolution TEM images of the biosynthesized NiO NPs annealed at 500 °C

like microspheres, similar to peony flowers, with a uniform porous structure and size distribution, and ripple-like pores.

Powder X-ray diffraction (XRD) was used to identify the structure of NiO NPs (Fig. 6). The XRD pattern shows the principal peaks observed at 2θ = 37.311, 43.411, 62.871, 75.531, and 79.461, assigned to the (111), (200), (220), (311), and (110) planes, respectively, confirming the

formation of highly pure NiO NPs (Behnajady and Bimeghdar 2014).

The surface structure of the nanoflakes was investigated by TEM. The obtained images are presented in Fig. 7, which show very thin and aggregated nanoflakes in random directions (Fig. 7A), with different shapes, and with diameters ranging from 10 to 100 nm (Fig. 7B). The TEM images clearly illustrate the
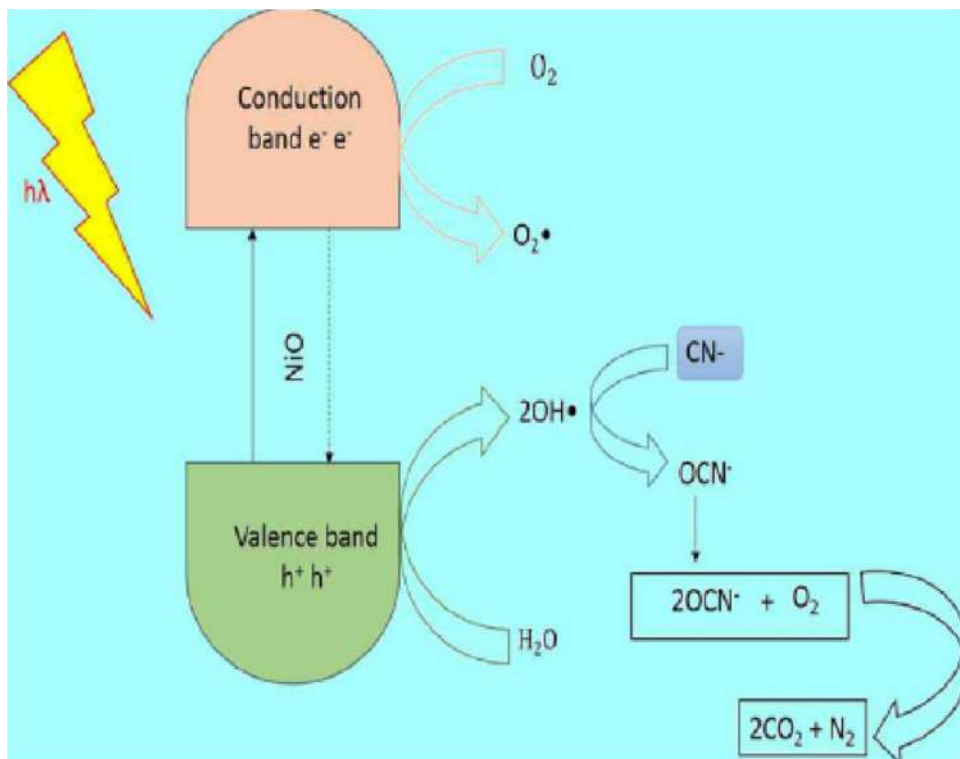
Fig. 27 Degradation mechanism proposed for photo-oxidation of FCN on the surfaces of NiO NPs
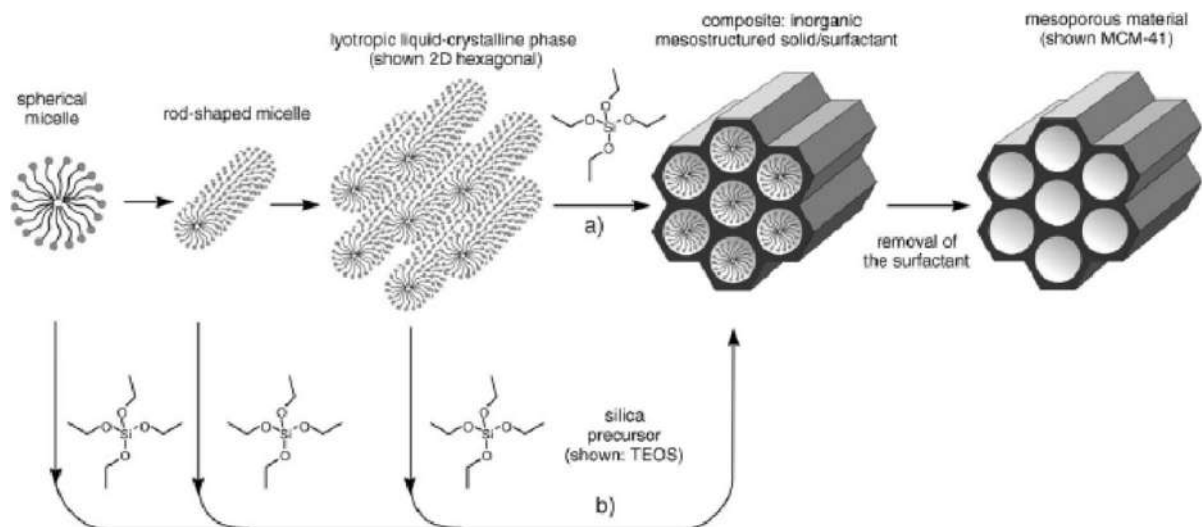
Fig. 28 Formation of mesoporous materials by structure-directing agents: (a) true liquid–crystal template mechanism, (b) cooperative liquid crystal template mechanism (Jadhav et al. 2015)

nanostructure inside of the nanoflakes in the form of uniform and highly ordered channels (see the red circles in Fig. 7A).

The prepared flower-like NiO NPs were used as a catalyst for the epoxidation reaction of cyclohexene to produce cyclohexene oxide. The *meta*-chloro peroxybenzoic acid (*m*-CPBA) was used as an oxidant and CH_2Cl_2/CH_3CN as a solvent at ambient conditions (Fig. 8). The obtained results shown an instant reaction with high conversion of cyclohexene of 91%, and cyclohexene oxide selectivity of 53%, compared to 65

and 58% for bulk NiO particles (prepared by calcination of Ni $(NO_3)_2$ $4H_2O$ at 500 °C for 4 h), respectively (Fig. 9). The reusability of mesoporous flower-like NiO NPs was also studied. After four successive runs, the conversion of cyclohexene was decreased to 63% with almost the same selectivity (53%). This decrease in the catalytic activity of NiO NPs was attributed to the aggregation and partial dissolution of NiO NPs in reaction mixture.

The flower-like NiO NP prepared with CTAB was also used by Abboud et al. as catalyst in the epoxidation

Table 5 SBA-15 supported NiO NPs reported in the literature

Catalyst	Nickel precursor	Synthesis method	Particle size (nm)	Application	Ref
NiO/Al-SBA-15	Ni$(NO_3)_2$.6H$_2$O	Wet impregnation	9–10	Solvent-free deoxygenation of palm fatty acid distillate	Baharudin et al. 2019)
NiO/SBA-15	Ni$(NO_3)_2$.6H$_2$O	Wet impregnation	8–20	Carbon dioxide reforming of methane	Yang et al. 2017)
NiO/Al-SBA-15	Molecular Ni$_4$O$_4$ clusters	Incipient wetness impregnation	<20	Dry reforming of methane	Baktash et al. 2015)
NiO/SBA-15	Ni$(NO_3)_2$.6H$_2$O	Direct wet impregnation[a] Post synthesis impregnation[b]	-	Conversion of producer gas	Lu et al. 2014)
NiO/SBA-15	Ni$(NO_3)_2$.6H$_2$O	Sol–gel coating	5–15	Dry reforming of methane	Ahmed et al. 2012)
NiO/SBA-15	Ni(OCOCH$_3$)$_2$.4H$_2$O	Post-synthesis grafting method	9±4	Carbon dioxide reforming of methane	Liu et al. 2009)

[a] Nickel precursor was added during the synthesis of SBA-15

[b] Nickel precursor was added to pre-prepared SBA-15
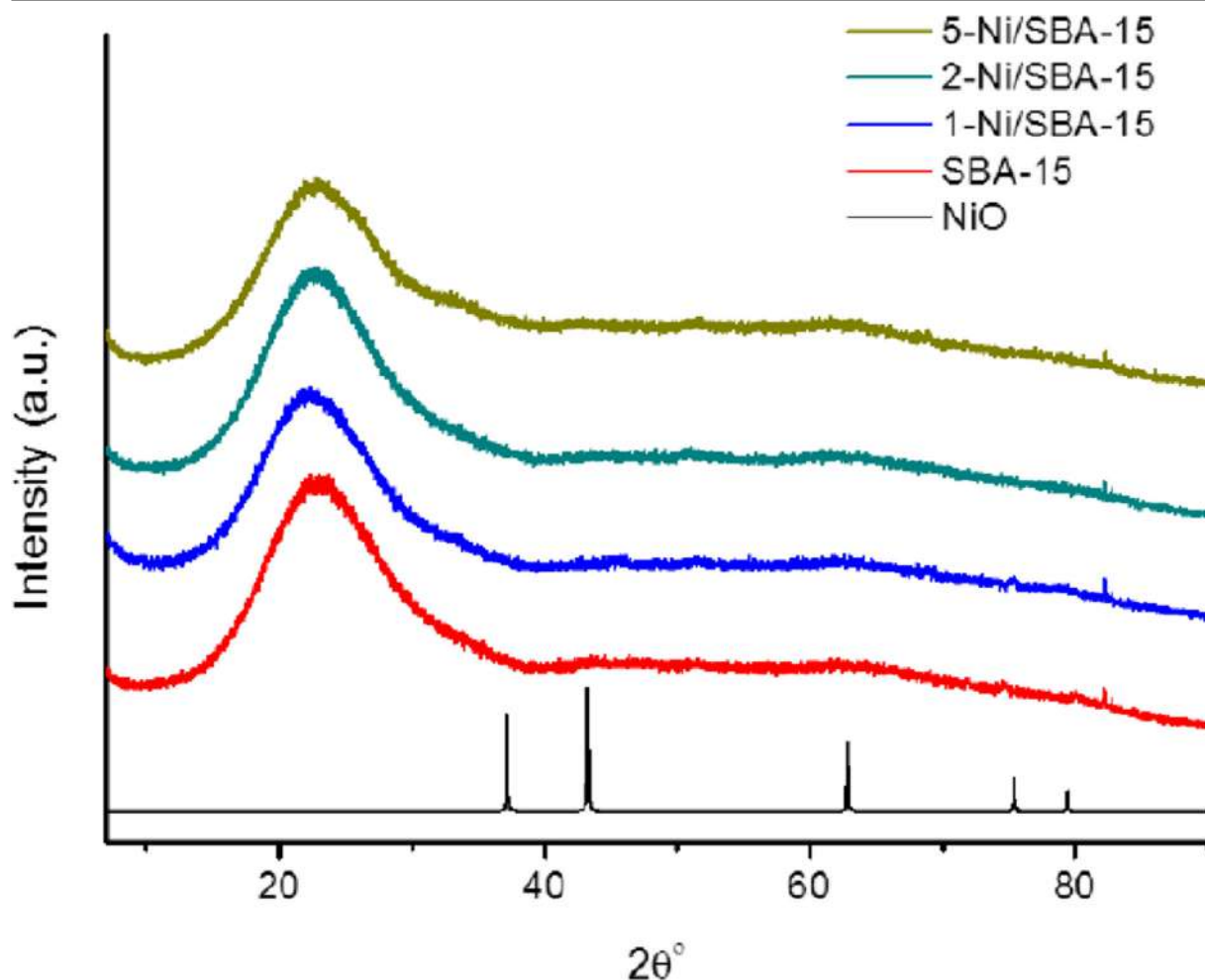
Fig. 29 Wide-angle XRD of Ni/SBA-15

Table 6 Characterisation and test results of the Ni4/SBA-15 and Ni/SBA-15 catalysts

Samples	Ni[a]	Activity[b] [mol$_{CH4}$/mol$_{Ni}$/min]		
	[wt%]	500 °C	550 °C	600 °C
1-Ni4/SBA-15	0.52	3.2	6.0	13.9
2-Ni4/SBA-15	0.81	3.5	5.5	9.7
5-Ni4/SBA-15	1.67	3.1	3.8	5.3
1-Ni/SBA-15	0.51	3.9	3.9	-
2-Ni/SBA-15	0.97	3.0	5.0	8.3
5-Ni/SBA-15	2.53	1.4	2.6	3.4

[a] Metal content from ICP measurement

[b] Reaction rate based on mole CH_4 converted per mole Ni per time on stream

reaction of styrene in ambient conditions, using *m*-CPBA (1.5 eq) as an oxidant and in the similar conditions used for the epoxidation of cyclohexene (Fig. 10) (Sahlabji et al. 2020). NiO NP catalyst also showed an immediate (less 1 min) reaction with high conversion of 87% and selectivity of 65% (Fig. 11), with high turnover frequency (TOF) of 243/s. Moreover, this catalyst is easily separable and recyclable up to four runs with slight decrease in the catalytic activity.

Unsupported NiO NPs were prepared and used by Nasseri and co-workers as green, inexpensive, and efficient heterogeneous nanocatalyst for the synthesized of diindolyloxindole (Fig. 12) and spirooxindoles (Fig. 13) derivatives in water, which are an important class of potentially bioactive compounds (Nasseri et al. 2015a, 2015b). The desired products were obtained with high yields in
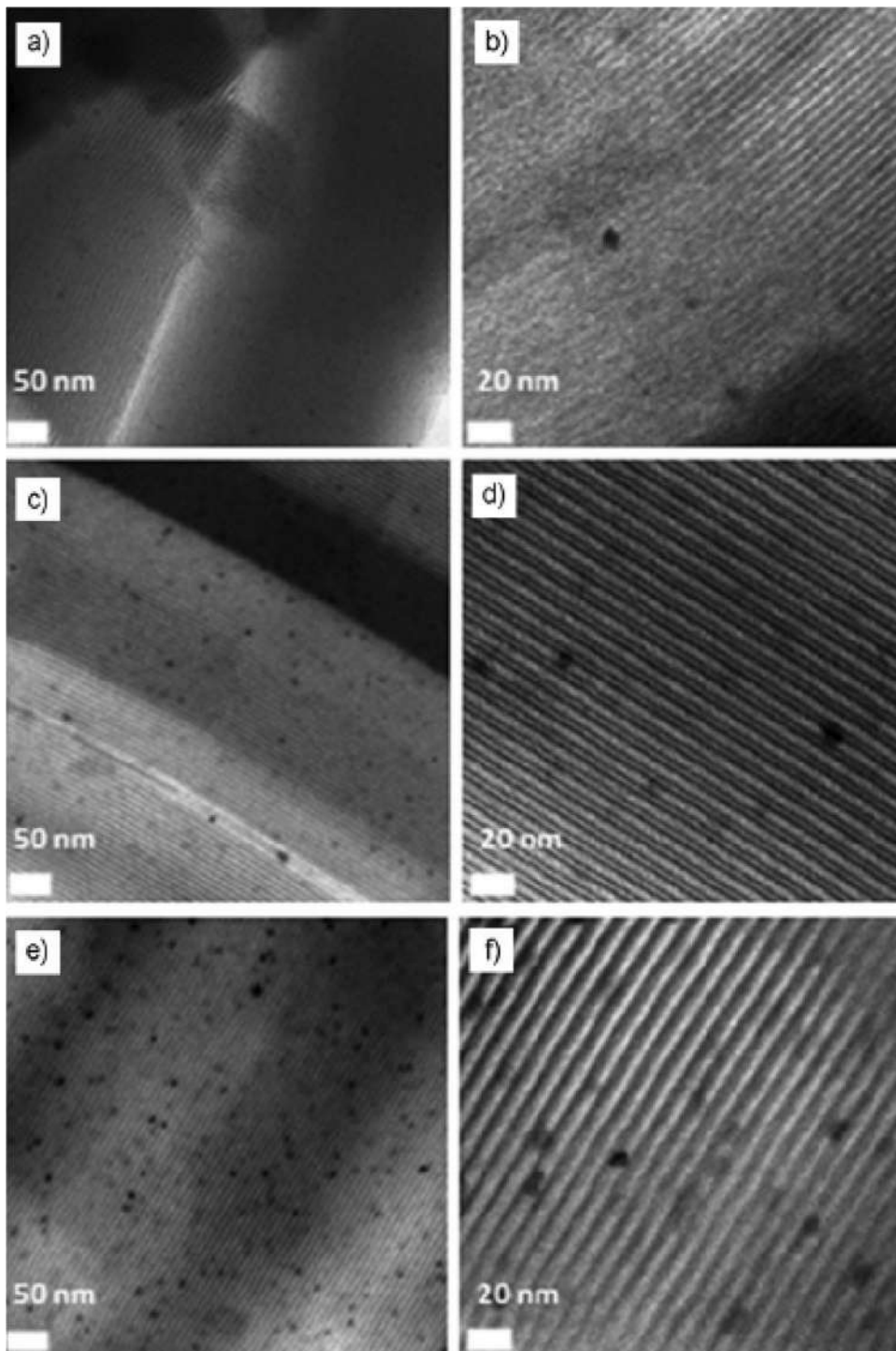
Fig. 30 TEM images of Ni/SBA-15. a, b) 1-Ni4/SBA-15, c, d) 2-Ni4/SBA-15, and e, f) 5-Ni4/ SBA-15 (Baktash et al. 2015)

mild conditions compared to other catalysts such as other transition metal oxides including bulk NiO particles.

The obtained NiO NPs in this work were prepared by chemical reduction method in water, using urea as a reducing agent. The structure of the prepared material
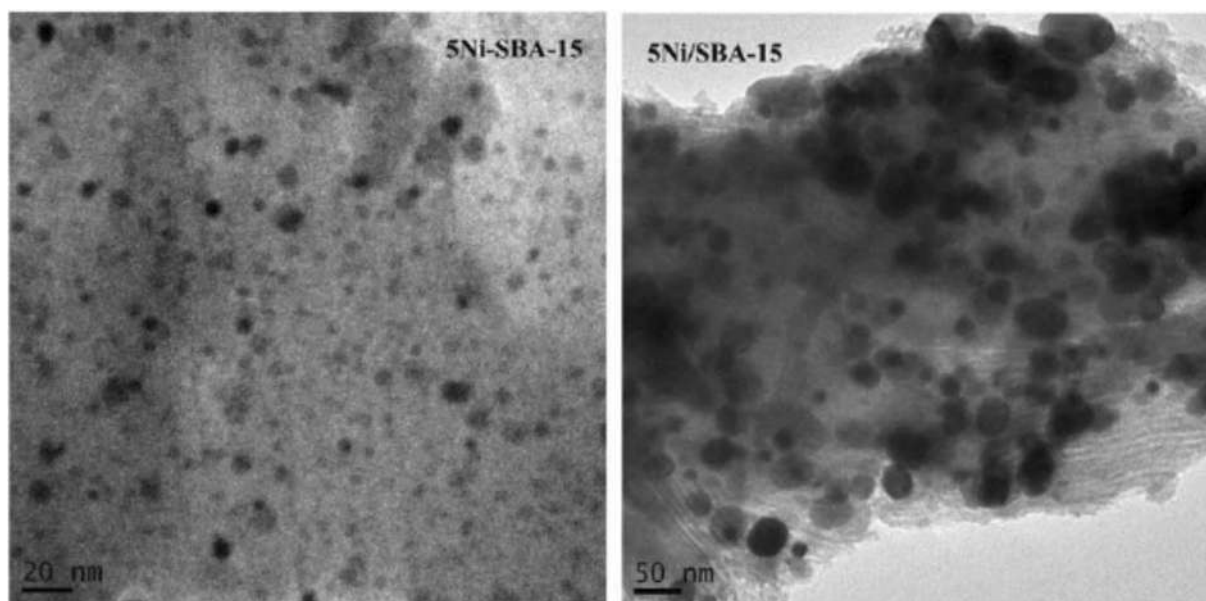
Fig. 31 TEM images of the spent catalysts. 5Ni-SBA-15 prepared by post-synthesis grafting, 5Ni/SBA-15 prepared by impregnation (Liu et al. 2009)

was confirmed by XRD (Fig. 14). XRD patterns of the products were obtained after the calcination of the precursor at 400 °C.

The obtained material was investigated by TEM. The average size of the obtained particles was around 11 nm (Fig. 15).
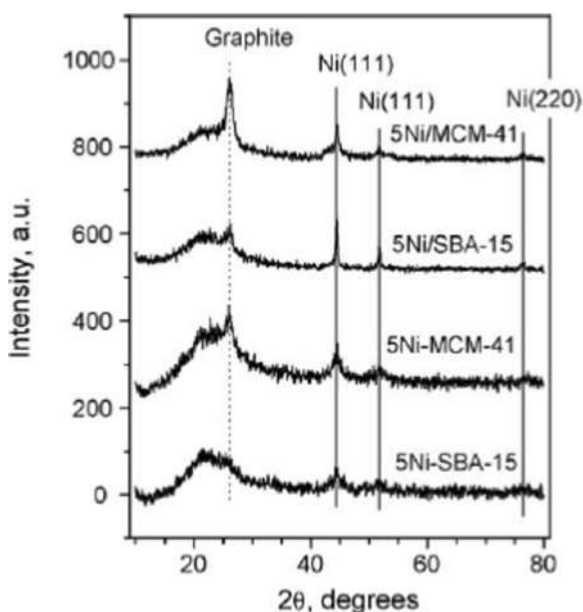
Fig. 32 XRD patterns of spent catalysts

Recently, Arrigo et al. (Arrigo et al. 2020) have investigated the influence of the preparation condition on the structure of Ni NPs, using hot injection colloidal method, with different amounts of oleylamine (OAm) and trioctylphosphine (TOP), which were used as reducing and protective agents, respectively (Fig. 16). It was found that changing the amount of OAm and TOP affected both the size of the NPs and the Ni electronic structure (Table 3).

The successful formation of metallic Ni NPs was confirmed by XRD (Fig. 17).

The obtained Ni_5 × 1.5y NPs were characterized by high-resolution high angle annular dark field scanning transmission electron microscopy (HA-HAADF-STEM) (Fig. 18a and b). This figure shows oval NPs with a twinned cuboctahedron (Fig. 18a) formed by many parallel twin lamellae. Ni NPs are embedded in an organic shell (Fig. 18b). Figure 19 shows the core–shell form of Ni_2.5 × 1.5y.

The catalytic activity of the obtained material was evaluated in selective asymmetric hydrogenation of methyl acetoacetate (MAA) to chiral methyl-3-hydroxy butyrate (Fig. 20). It was found that (R)-selectivity was higher on the oxidized surface of Ni NPs and at low conversion, without any impact of unsupported NP size on the selectivity (Table 4).
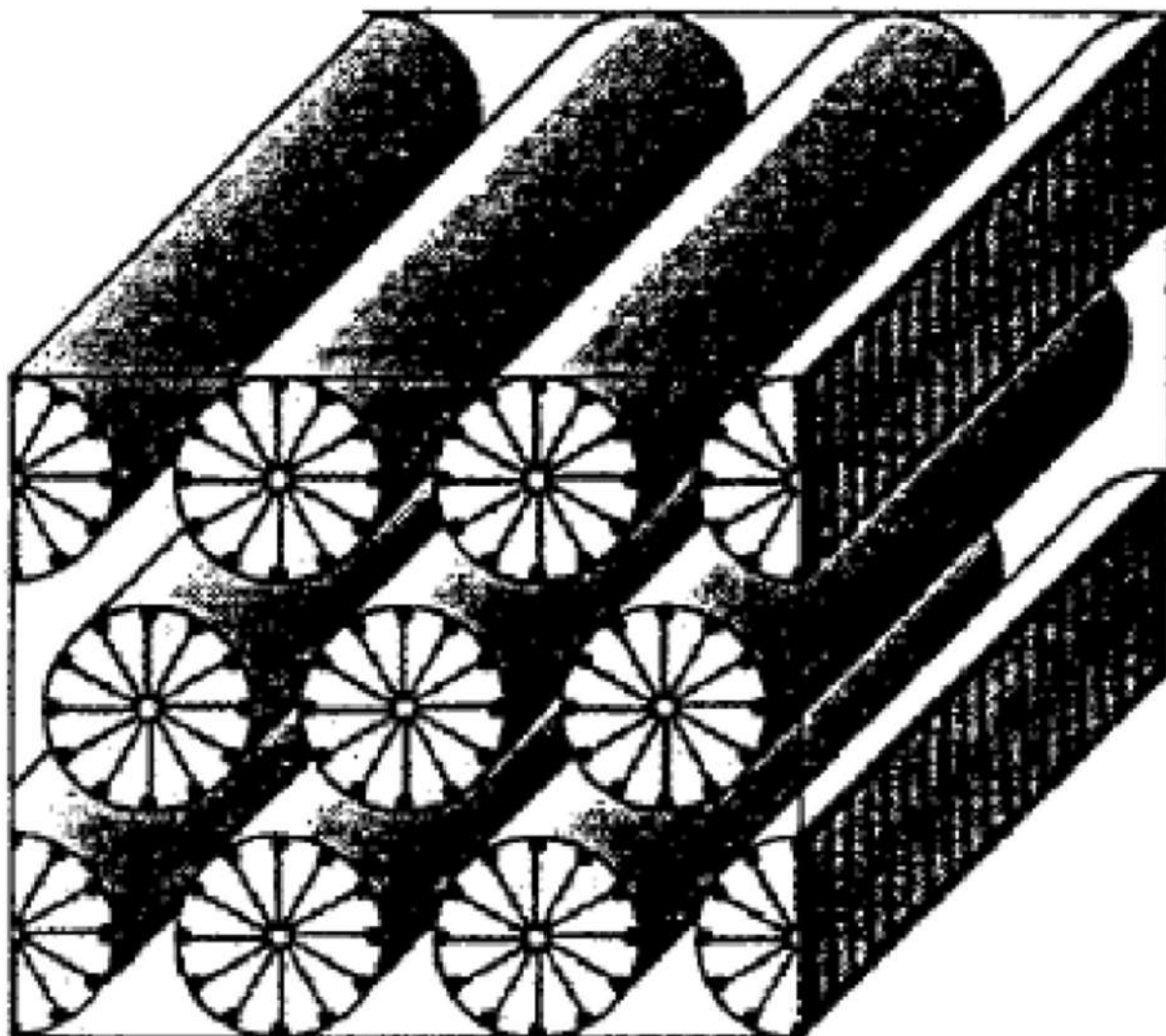
Fig. 33 Structure of MCM-41 (Schumacher et al. 2000)

Heterogeneous photocatalysis

Abboud et al. (Abboud et al. 2020) reported recently the synthesis of highly ordered mesoporous flower-like NiO NPs and their utilisation as a heterogeneous photocatalyst for the decolourisation of methyl green (MG) dye, under UV light in aqueous solution. NiO NPs were prepared by hydrothermal-assisted chemical precipitation method, using nickel acetate tetrahydrate as a metal source, ammonium hydroxide (NH_4OH) as a base, diethanolamine (DEA) as complexing agent, and cetyltrimethylammonium bromide (CTAB) as a structure directing agent. $Ni(OH)_2$ precursor was synthesized

with and without CTAB to investigate its effect on Ni NPs shape and size.

Figures 21 and 22 show the SEM micrographs of flower-like NiO NPs obtained with and without CTAB, respectively. The characterisation results revealed that both CTAB and DEA were involved in the synthesis process. The flower size of the obtained NiO microspheres with CTAB was ~ 2 μm with nanoflakes size ~ 10–100 nm. The size of flower-like NiO microspheres prepared without CTAB was increased to ~ 5 μm without any significant change in nanoflakes size.

The structure and the high purity of NiO NPs were confirmed by powder X-ray diffraction (see Fig. 6
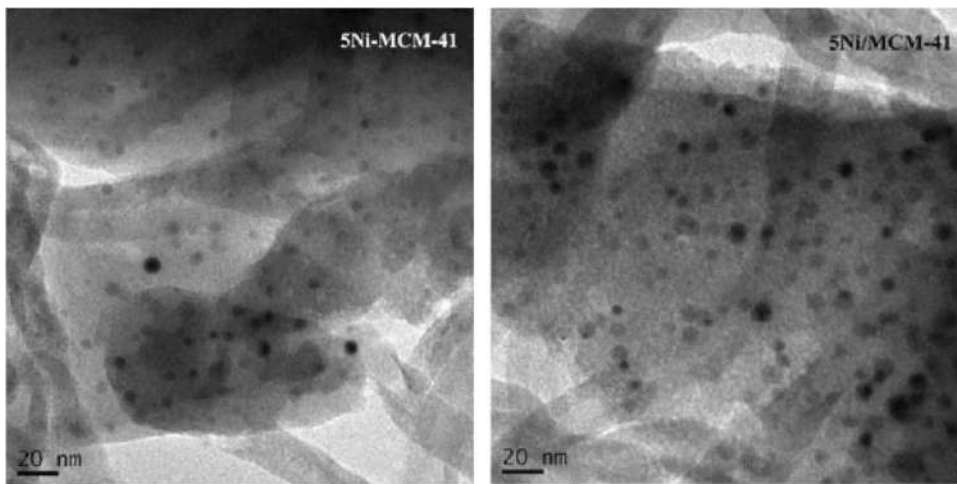
Fig. 34 TEM images of the spent catalysts. 5Ni-MCM-41 prepared by post-synthesis grafting, 5Ni/MCM-41 prepared by impregnation (Liu et al. 2009)

above). The investigation of these flower-like NiO NPs in nanoscale using TEM revealed the high order and uniform 2D nanostructure of the NiO nanoflakes (Fig. 23). In addition, BET results indicated the mesoporosity of the obtained material with a surface area of 21 m^2/g and pore diameter of ~ 6 nm.

The photocatalytic activity of the prepared mesoporous flower-like NiO NPs was evaluated in the decolourisation of methyl green (MG) dye in water under UV light illumination (Fig. 24). This nanocatalyst exhibited an excellent dispersion in the dye's solution, and a good photocatalytic degradation of MG, with a rate constant about 10 times higher than that of the bulk NiO counterpart.

Bashir et al. recently prepared NiO NPs with cubic-type structure, using nickel nitrate hexahydrate, as a nickel precursor, dissolved in an extract of *Persea americana* seeds as an ecofriendly biosynthesis method
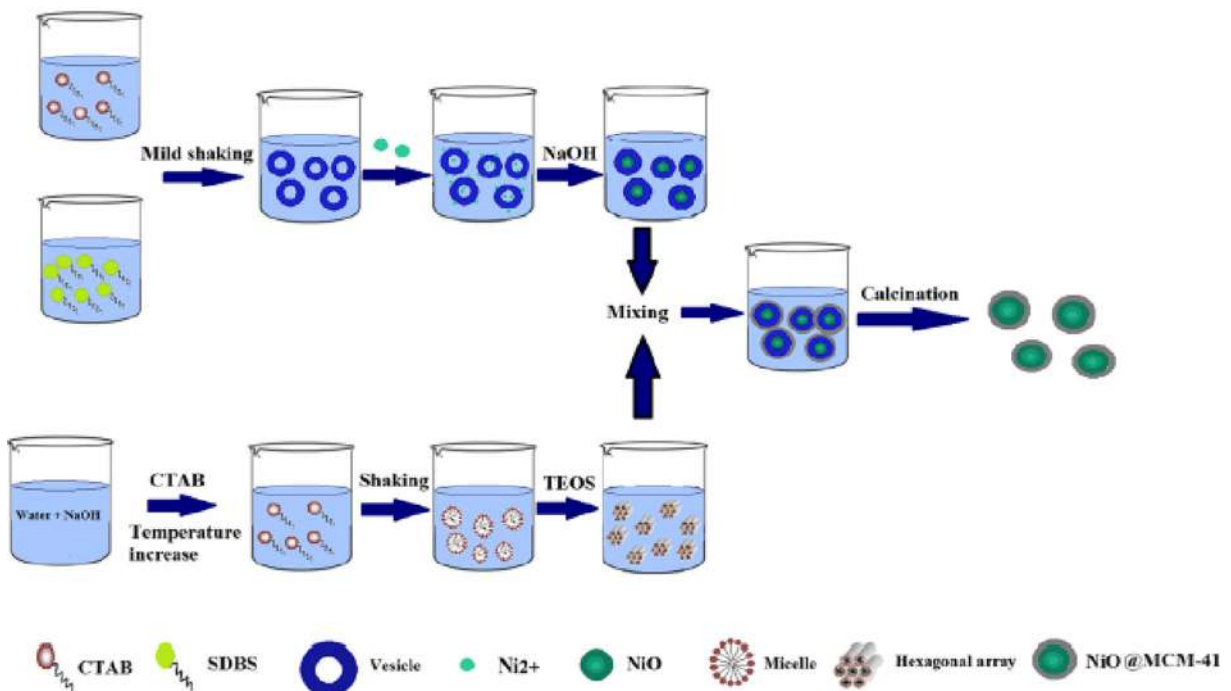
Fig. 35 Schematic diagram of the formation mechanism of the NiO@MCM-41 nanocomposite (Roosta et al. 2018)
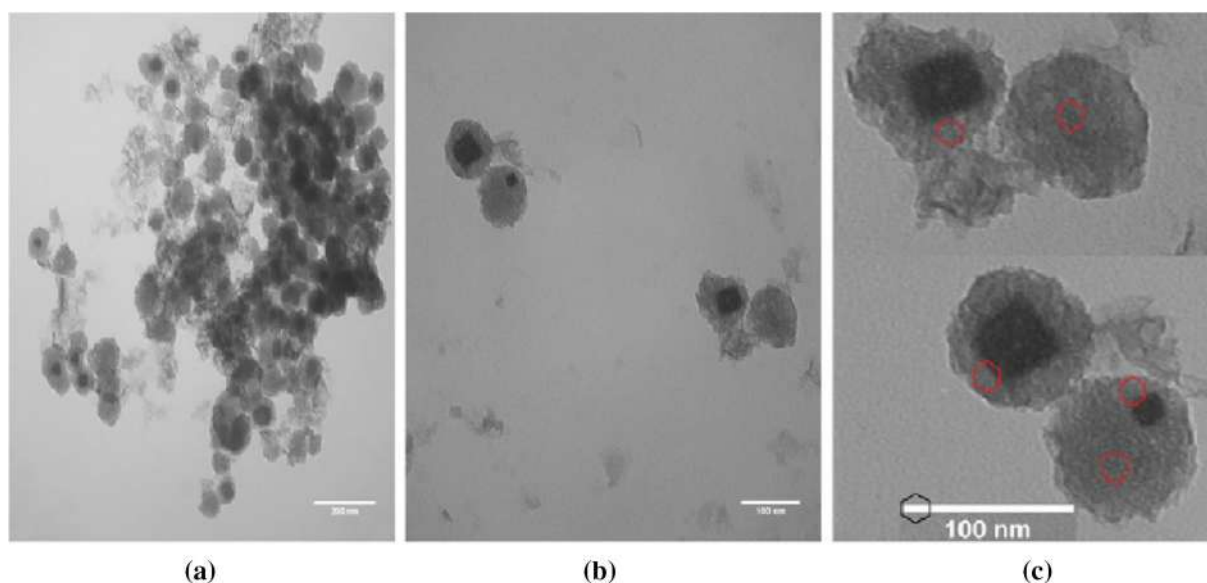
Fig. 36 TEM images of NiO@MCM-41 nanocrystals, (a) zoomed out, (b) zoomed in; (c) image (b) was enlarged, cropped, and recombined, and the hexagonal order of pores was made distinguishable via red polygons. (Colour figure online) (Roosta et al. 2018)

(Bashir et al. 2019). The NiO NP type structure was confirmed by XRD (Fig. 25).

TEM images showed rhombohedral and spherical shapes of NiO NPs with low agglomeration, and particle size around 11 nm (Fig. 26). The obtained NiO NPs were used as a catalyst for the photodegradation of free cyanide (Fig. 27). The obtained material exhibited a good photocatalytic activity with a maximum photocatalytic oxidation efficiency of 84% after 30 min.

However, unsupported Ni NPs still suffer from different drawbacks such as deactivation by aggregation, low durability, low dispersibility, and electron and hole recombination. Characteristics such as optical and catalytic activity may be lost if the dispersion of unsupported Ni NPs is not adequately modulated.

Mesoporous silica–supported nickel nanoparticles

Introduction

Several efforts have been deployed to overcome the unwanted effects of unsupported Ni NPs by either in situ synthesis or incorporating them into a solid matrix, like silica, carbon, or polymers. Among the different solid supports that have been used to encapsulate, these NP catalysts are the porous silica materials. They have been considered as excellent transparent solid supports,

because of their high surface area, thermal stability, chemical inertia, transmittance to radiation, high absorption capacity, and facilitating the interface reaction with organic compounds for photocatalytic degradation (Barhoum et al. 2017). Therefore, a porous silica framework facilitates the use of Ni NPs for the desired purposes while avoiding the drawbacks mentioned above.

Since Mobil Oil Corporation scientists discovered the Mobil Crystalline Materials (MCMs), such as MCM-41 and SBA-15 in 1992 and 1998, respectively, these mesoporous silica materials (MSMs) have attracted much attention in a wide variety of applications including catalysis, adsorption, separation, drug delivery, and sensing (Amin 2020). The importance of these materials is due to their important intrinsic properties such as tunable porosity and morphology, large internal surface area, narrow and highly uniform pore size distribution, and three-dimensional space required to realize the doping and confinement of different functional components, in addition to their high thermal and chemical stability. MSM also shows a high adsorption capacity and an ordered porous 3-D network that make them have a high diffusion of substrates and reaction products. All these properties open up a high application potential of those materials in the field of catalysis (Amin 2020; Weiping and Lide 1997; Lai 2013; Dixit et al. 2013; Luque et al. 2012).
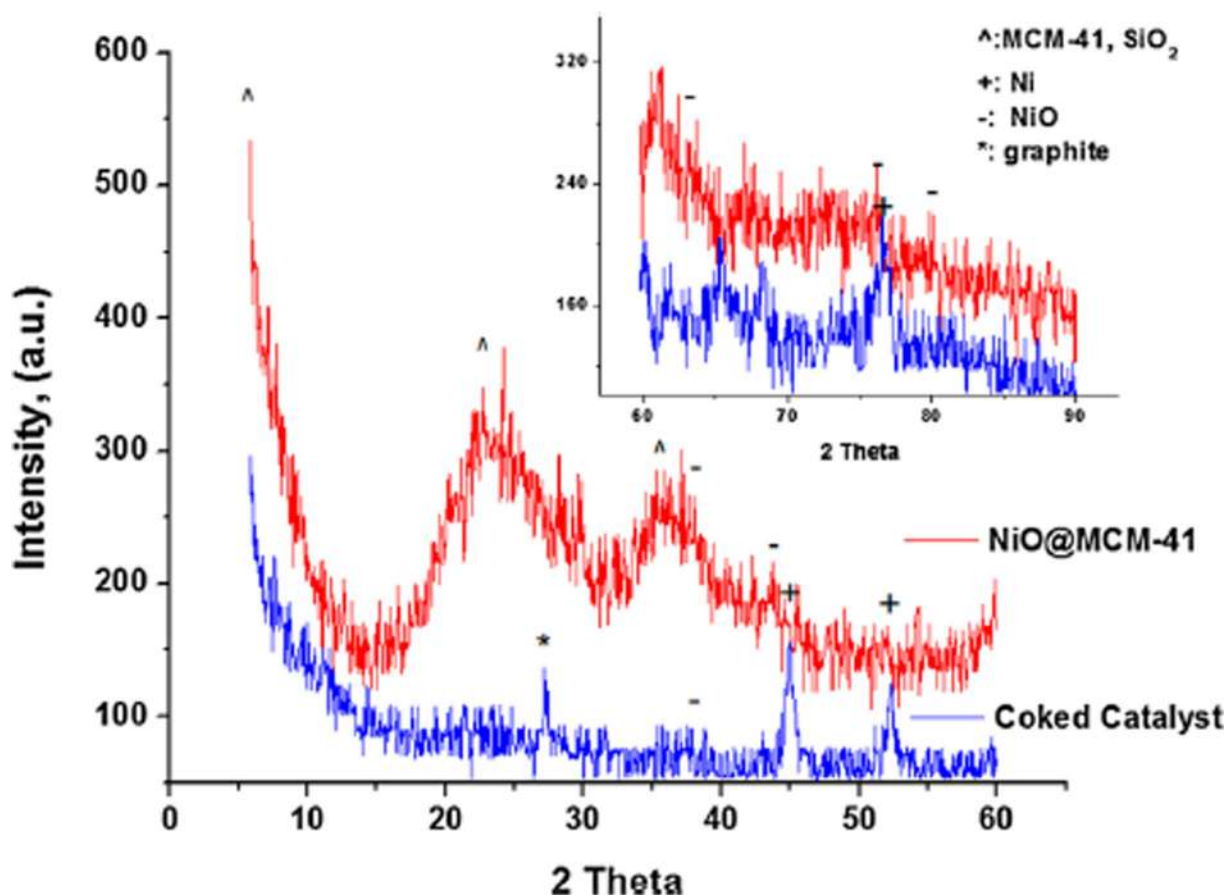
Fig. 37 Wide-angle X-ray diffraction pattern of the nanocomposite and the used catalyst. Diffraction data of inset figure were recorded in a different analysis

The successful incorporation of Ni NPs in mesoporous silica with stable and quantified NP size will increase the surface area to volume ratio and consequently increase the number of active sites of Ni NPs per area unit, inhibit the particles aggregation, improve the reusability of the obtained nanocatalyst, and consequently improve its catalytic performance.

Here we are going to discuss some recent applications in heterogeneous catalysis of Ni NPs supported on different types of MSMs, such as SBA-15, MCM-41, MCM-48, TUD-1, and other MSMs.

Nickel NPs supported into SBA-15

SAB-15 is one of the most used MSMs as a support in heterogeneous catalysis. SAB-15 is characterized by high specific surface area (400–900 m^2/g), tunable uniform hexagonal pore-network that have high hydrothermal and mechanical stability, with narrow pore size distribution, pore diameter ranges from 5 to 15 nm, pore volume up to 1.1 cm^3/g, and relatively thick walls that range between 3.1 and 6.4 nm, with a circular pore shape.

SAB-15 has been prepared in acidic medium, using the triblock copolymer (EO$_{20}$PO$_{70}$EO$_{20}$) Pluronic 123 (P123) as a structure directing agent, and tetraethyl orthosilicate (TEOS) as a silica source, following the mechanism described in Fig. 28 below (Jadhav et al. 2015).

Ni NPs have been incorporated in SBA-15 using different methods and applied as catalysts for various chemical transformations. The most techniques used to incorporate Ni NPs into SBA-15 are wet impregnation using nickel nitrate hexahydrate as nickel precursor (Table 5). The nickel particle size of the obtained materials was between 5 and 20 nm. The most Ni@SBA-15 catalysts prepared are used for reforming of methane.
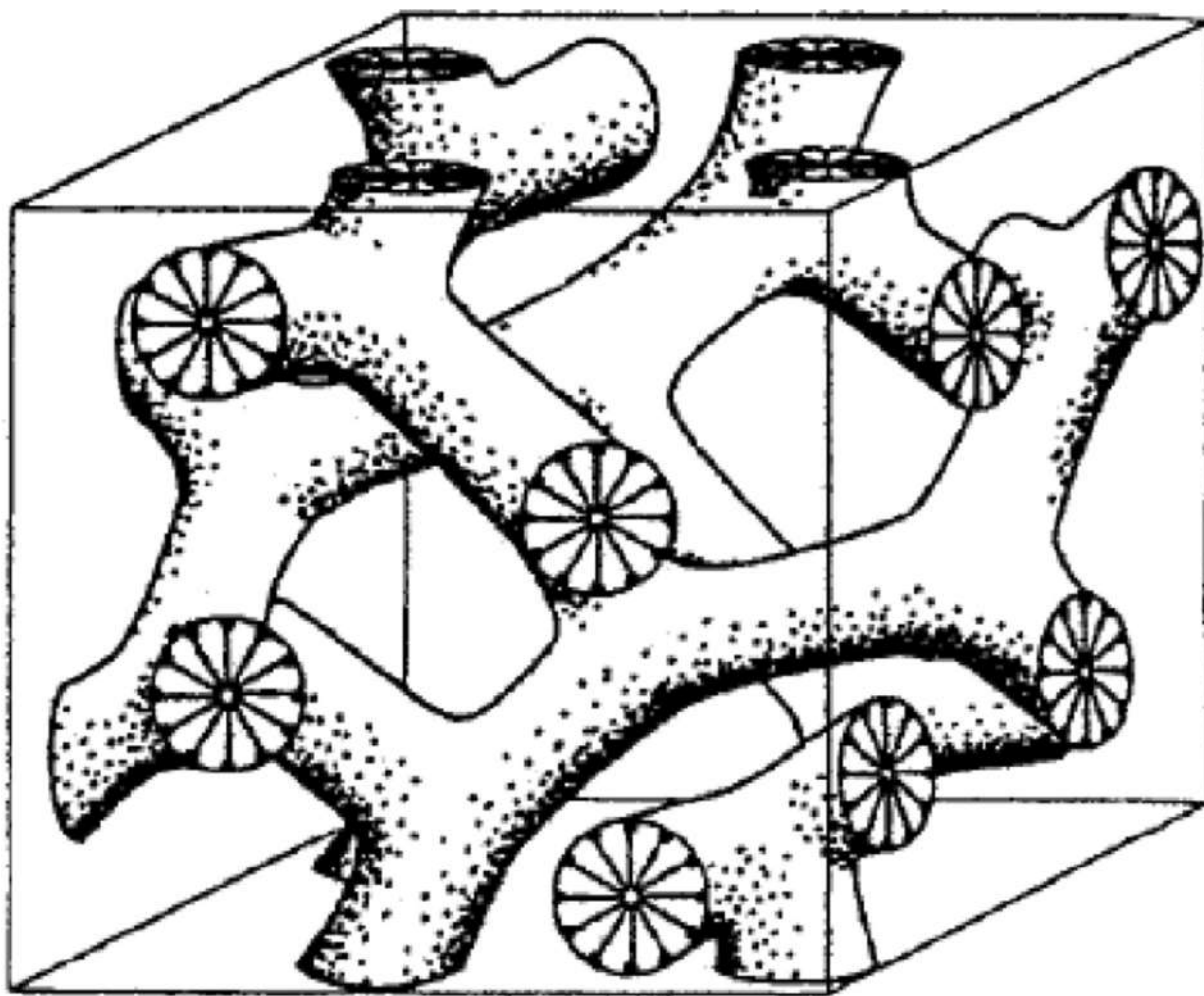
Fig. 38 Structure of MCM-48 (Schumacher et al. 2000)

Thomas et al. (Baktash et al. 2015) used incipient wetness impregnation method to prepare NiO NPs supported on SBA-15 using molecular Ni_4O_4 clusters as nickel precursor.

The XRD patterns of Ni/SBA-15 samples after calcination (before reduction) are presented in Fig. 29. The characteristic reflexes for NiO at 2θ = 37.2, 43.1, and 62.88, corresponding to the (111), (200), and (220) planes of cubic NiO, respectively, were not observed for all Ni/SBA-15 samples. The observed reflexes are very weak and broad, which points to the formation of very small and highly dispersed Ni species.

The presence of nickel and the actual metal contents of the samples were determined after the calcination step by inductively coupled plasma (ICP), and the obtained results are presented in Table 6.

The TEM images revealed the formation of NiO NPs with particle size < 20 nm (Fig. 30). Authors claimed that the utilisation of these clusters may have a significant effect on the dispersion of NiO NPs through the SBA-15 framework compared to other traditional precursors such as nickel nitrate. The obtained nanocatalyst was reduced to Ni(0) and used for dry reforming of methane.

Liu and co-workers (Liu et al. 2009) reported the synthesis of SBA-15 supported Ni catalysts using a post-synthesis grafting method and nickel acetylacetonate as nickel precursor. In this method, the appropriate amount of nickel acetylacetonate complex was added dropwise to a suspension of SBA-15 in toluene. After refluxing the mixture overnight, filtration, and washing, the obtained SBA-15 grafted nickel acetylacetonate
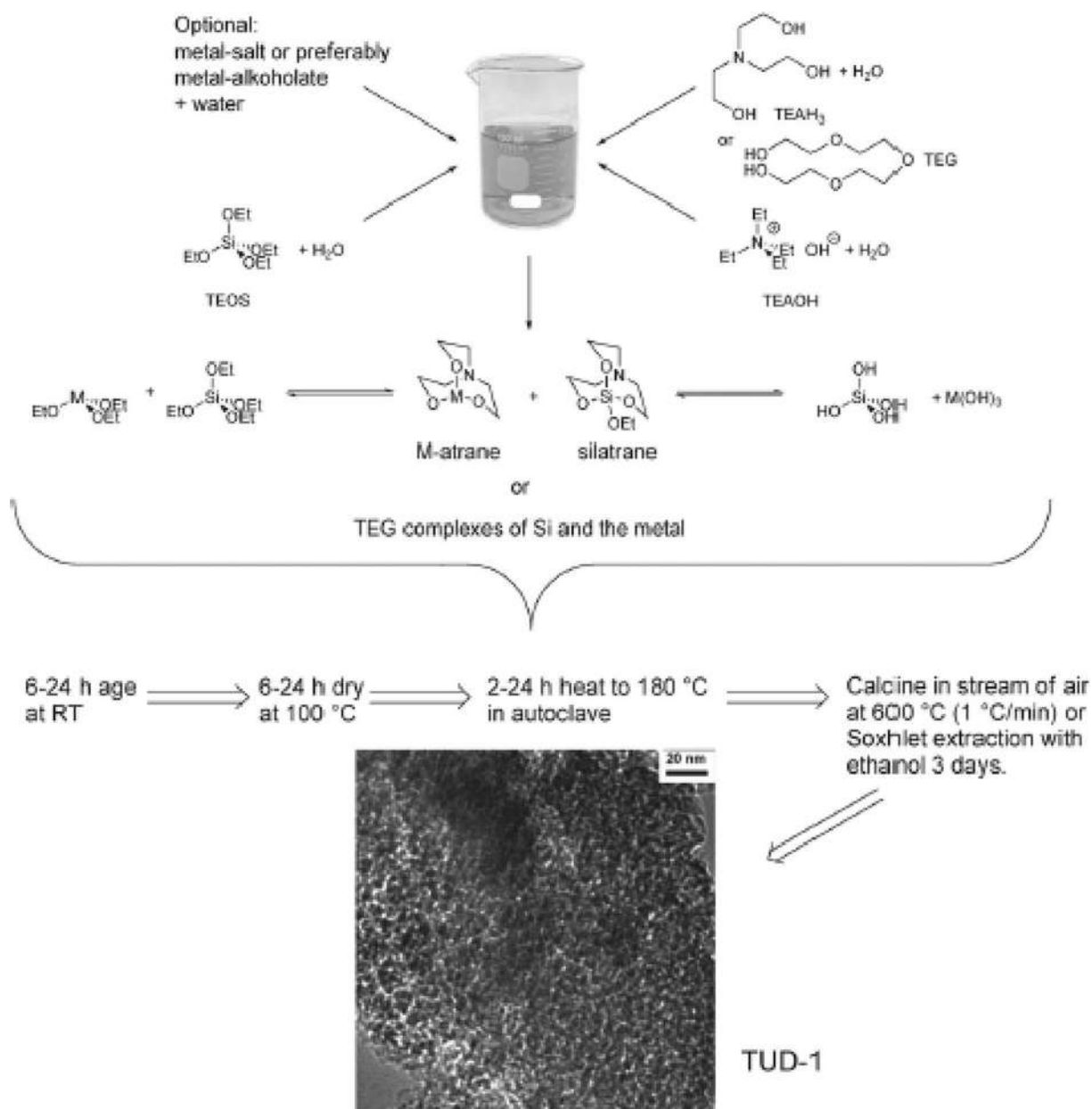
Fig. 39 The synthesis of mesoporous TUD-1 and M-TUD-1 is straightforward (Telalović et al. 2010)

powder was calcined at 540 °C to obtain the desired catalyst. The Ni particle size of the material obtained by post-synthesis grafting method was 9 ± 4 nm compared to 31 ± 12 nm for the material prepared by conventional impregnation method (Fig. 31). The existence of nickel particles with large size, especially for the catalysts prepared via impregnation, could be attributed to a remarkable sintering of Ni particles occurring during the stability test.

The catalytic activity of the obtained catalysts was evaluated in CO_2 reforming of methane. The highest catalytic performance and stability and high Ni NP dispersion through silica matrix were observed over a 5-wt% Ni loading prepared by post-synthesis grafting method.

The structure of fresh Ni NPs in these materials was not confirmed by XRD or EDX. Only low-angle XRD was performed to demonstrate that the structural
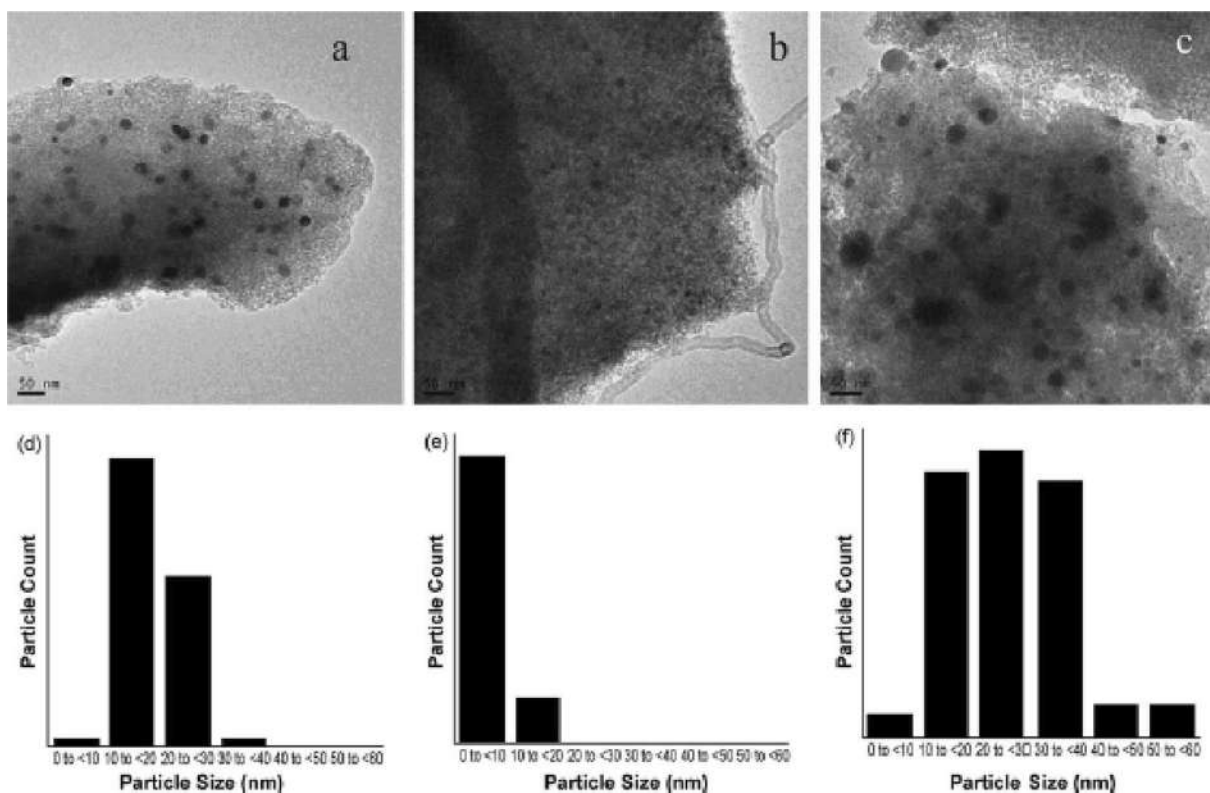
Fig. 40 TEM results for spent catalysts: (1) TEM images for (a) spent Ni-DHT, (b) spent Ni-GRF, and (c) spent Ni-IMP, respectively; (2) nickel particle size distributions for (d) spent Ni-DHT, (e) spent Ni-GRF, and (f) spent Ni-IMP, respectively (Quek et al. 2010)

integrity was retained after the incorporation of Ni and the calcination process. However, XRD was performed to the spent catalysts to determine its crystalline phases after reaction. As shown in Fig. 32, the diffraction peaks of Ni particles can be seen over all the spent catalysts.

Nickel NPs supported in MCM-41

MCM-41 is one of the most widely investigated ordered mesoporous silica materials due to its valuable physical properties. MCM-41 is characterized by highly ordered hexagonal one-dimensional and unidirectional pores system (Fig. 33) (Schumacher et al. 2000) and narrow pore size distribution, with pore size that ranges from 3 to 7 nm, pore volume nearly 1.0 cm^3/g, and high surface area up to 1000 m^2/g, with wall thickness up to 1.8 nm. In addition, MCM-41 presents good thermal and chemical stability, uniform channels 2–10 nm in diameter, and no toxicity of both template and silicon source.

MCM-14 materials have been synthesized in an alkaline condition using cetyltrimethylammonium bromide (CTAB) as structure directing agent, and TEOS as silica source, following the same mechanism described for the synthesis of SBA-15 (Fig. 28). The main differences between the structure of MCM-41 and SBA-15 are primarily in pore geometry, pore shape, and the wall thicknesses.

However, only few publications reported the incorporation of Ni NPs in MCM-41 and the obtained nanocatalysts mainly applied for CO_2 reforming of methane.

Liu et al. (Liu et al. 2009) also reported the preparation of Ni-MCM-41 catalyst and its evaluation in CO_2 reforming of methane. This material was prepared using the same method described for Ni-SBA-15 which is the post-synthesis grafting method, using nickel acetylacetonate as nickel precursor. The Ni NP size of Ni-MCM-41 was 7.6 ± 1.8 nm, compared to 12.1 ± 3.2 nm for Ni/MCM-41 which was prepared using conventional impregnation technique. The Ni NP size obtained with MCM-41 was smaller than that observed in SBA-15 (Fig. 34). However, Ni-SBA-15 obtained by grafting
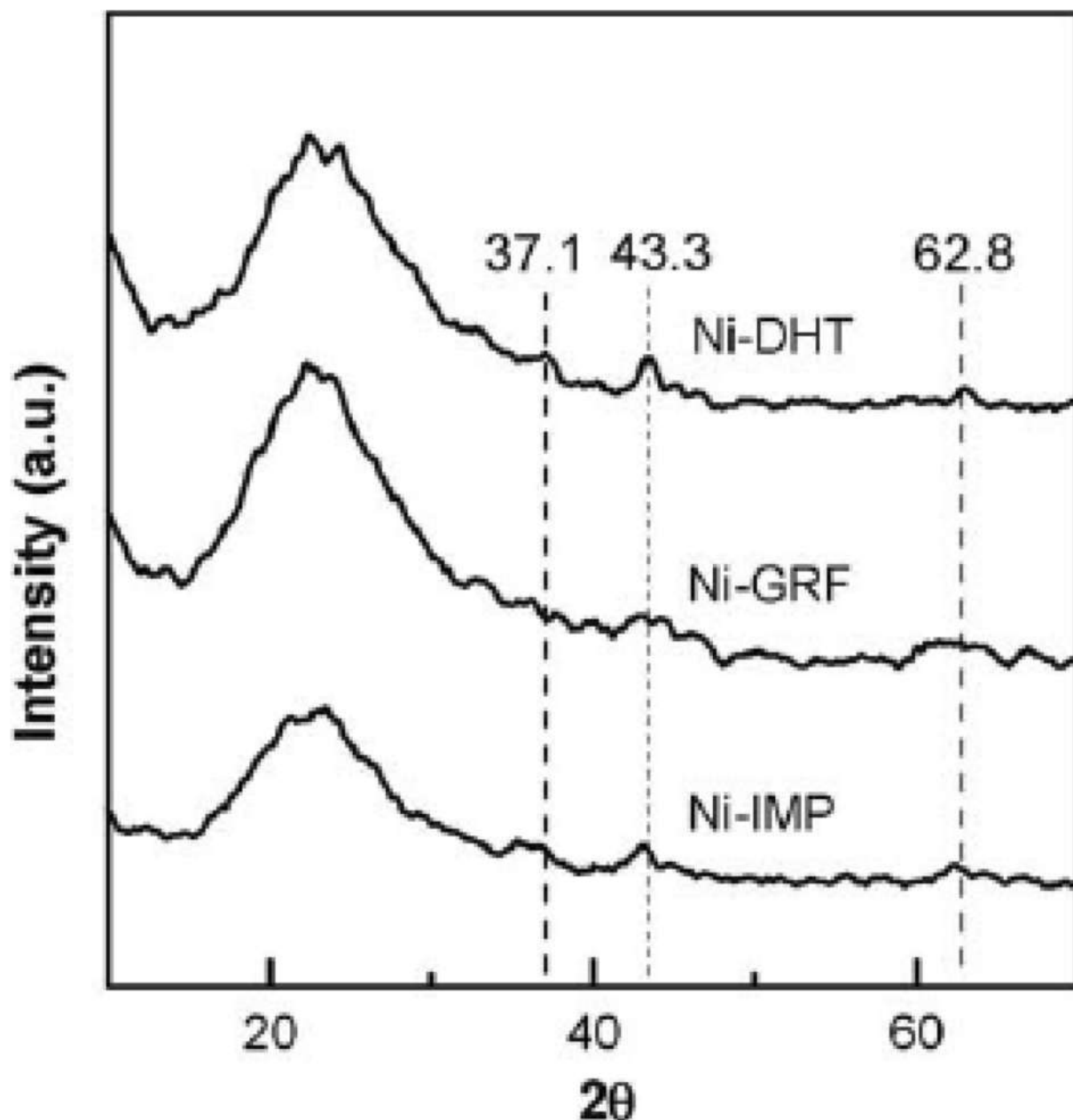
Fig. 41 High-angle XRD patterns of Ni-containing TUD-1 catalysts

method exhibited an excellent catalytic activity and high stability over Ni-MCM-41, due to its high inhibition on nickel sintering and carbon formation.

As mentioned above for SBA-15, only low-angle XRD was performed to demonstrate the preservation of the mesoporosity of the material after the incorporation of Ni and the calcination process. Wide-angle XRD was performed only to the spent catalysts to determine its crystalline phases. The average sizes of Ni particles

calculated by Scherrer equation revealed the following sequence: 5Ni-MCM-41 (7.3 nm) < 5Ni-SBA-15 (8.4 nm) < 5Ni/ MCM-41 (14.0 nm) < 5Ni/SBA-15 (19.4 nm).

In another work, Roosta et al. reported the synthesis of NiO@MCM-41 catalyst in the form of core–shell nanocomposite and its catalytic evaluation in CO_2 reforming of methane (Roosta et al. 2018). NiO@MCM-41 nanocomposite was prepared by two-
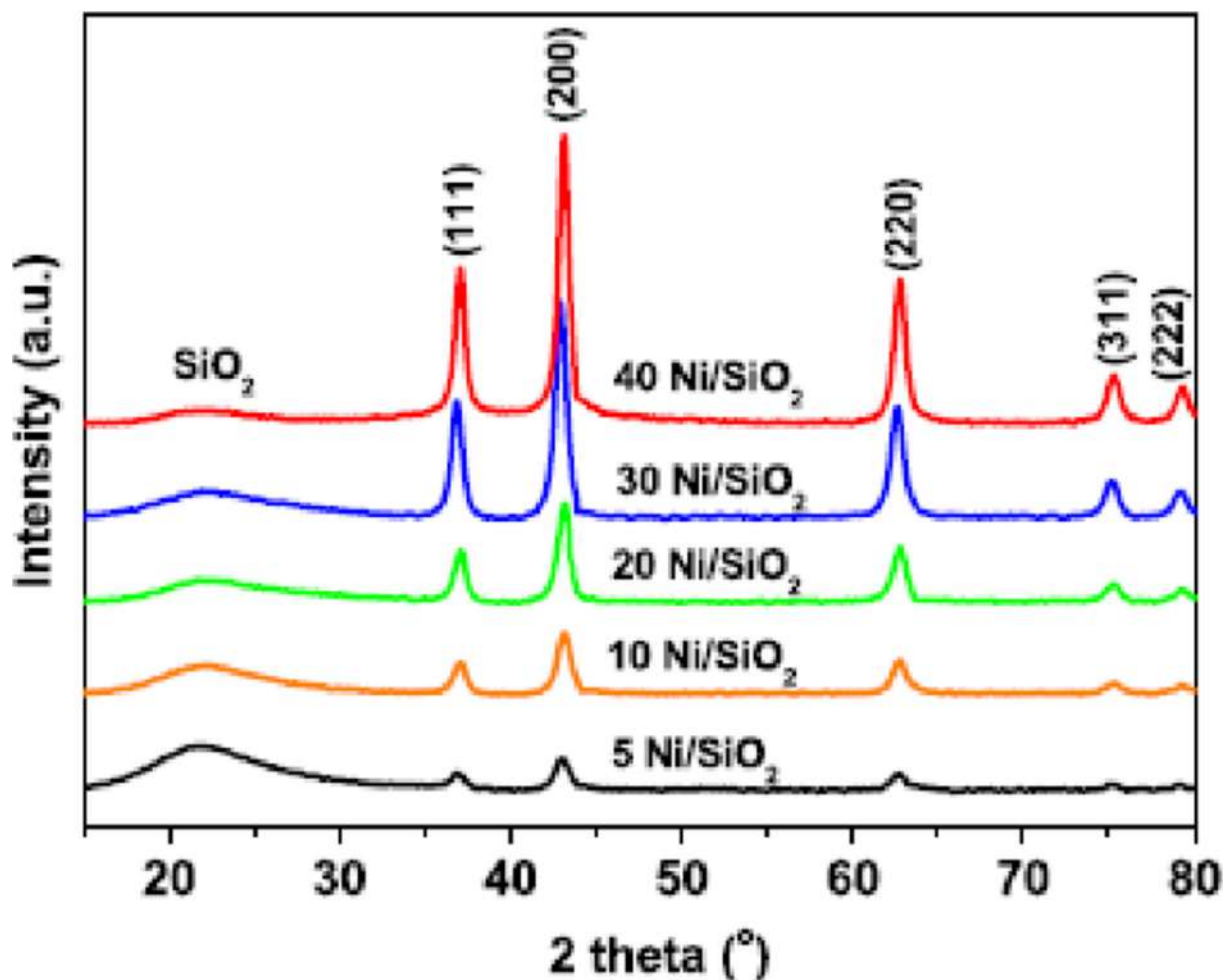
Fig. 42 Powder XRD patterns of Ni/SiO$_2$ catalysts

step soft templated nanocasting method, using vesicles as soft template (Fig. 35). First, stable vesicles were formed by a mixture of two surfactants, CTAB and SDBS, with a ratio of CTAB/SDBS 1:2. Then, nickel nitrate was inserted inside the vesicles. The obtained Ni@vesicles were covered by MCM-41 gel. After the calcination step, the NiO@MCM-41 core–shell nanocomposite was obtained.

The TEM images (Fig. 36) of the obtained core–shell nanocomposite showed a particle's average diameter of 70–80 nm, with a spherical shape. CO$_2$ reforming of methane conversion over the prepared core–shell nanocatalyst led to CO$_2$ and H$_2$ conversion of 48% and 42%, respectively.

XRD analyses were performed before and after the reaction to evaluate the present crystalline phases in the catalyst (Fig. 37). NiO lattice reflection appeared at 2θ = 38, 43.8, 63.2, 76.2, and 79.8 (Zhang et al. 2017), and FCC Ni lattice reflection appeared at 2θ = 45, 52.2, and 76.7 (Zhang and Li 2015). The absence and presence of reflection attributed to the metallic nickel (Ni) in the spent catalyst confirmed the reduction of NiO to Ni in the core of NPs. The presence of distinct reflections of Ni lattice of spent catalyst indicated the stable condition of the metallic phase of the core region of NPs after the reaction.

Nickel supported in MCM-48

MCM-48 is an important member of the M41S family (e.g. MCM-41, MCM-48, MCM-50). (Kresge et al. 1992). It is characterized by 3-D cubic structure, with two non-intersecting gyroidal pores (Fig. 38) (Schumacher et al. 2000). MCM-48 is characterized by
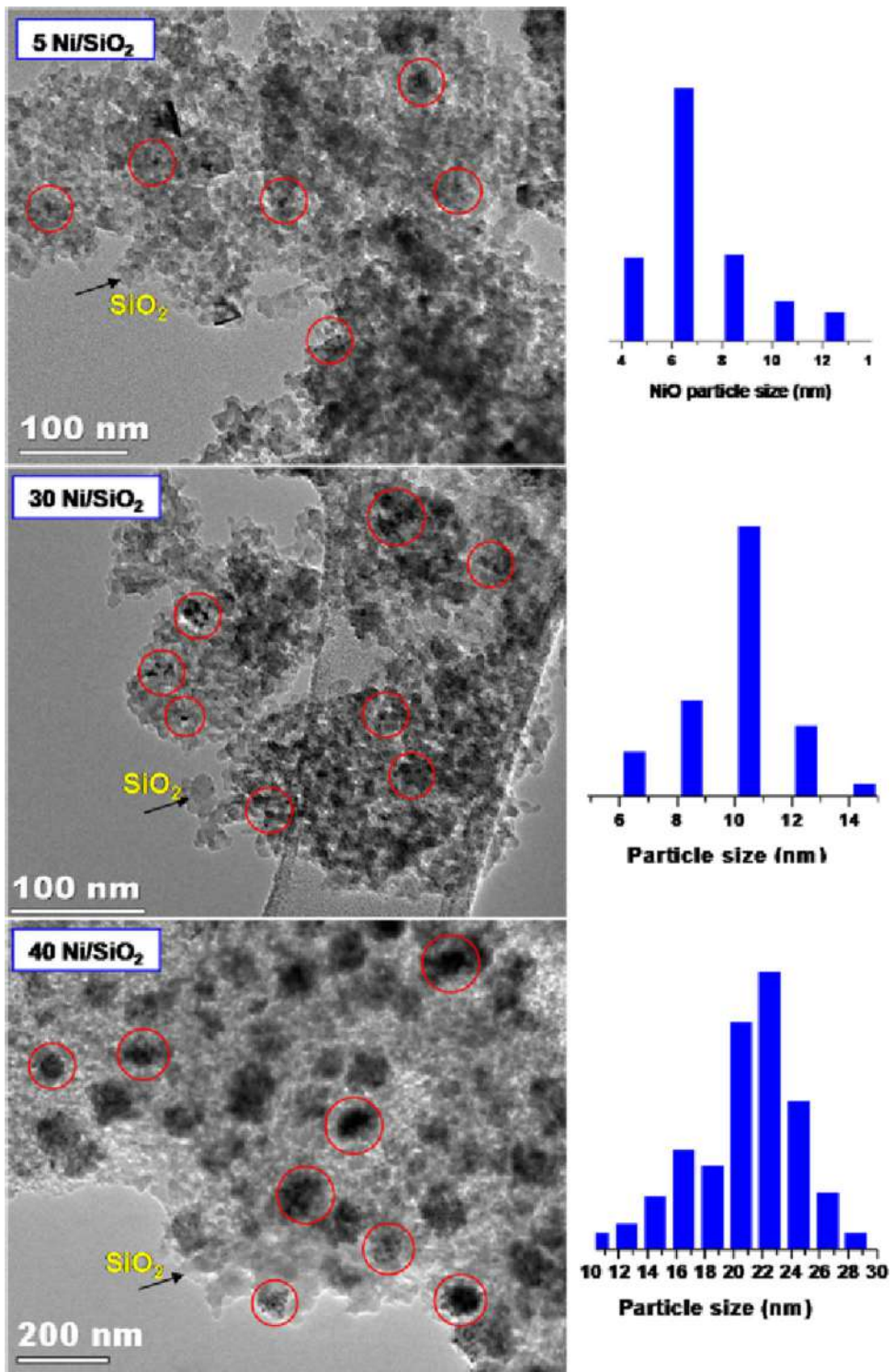
Fig. 43 TEM images and the corresponding particle size distribution of 5% Ni/SiO₂, 30% Ni/SiO₂, and 40% Ni/SiO₂ catalysts (Mallesham et al. 2018)
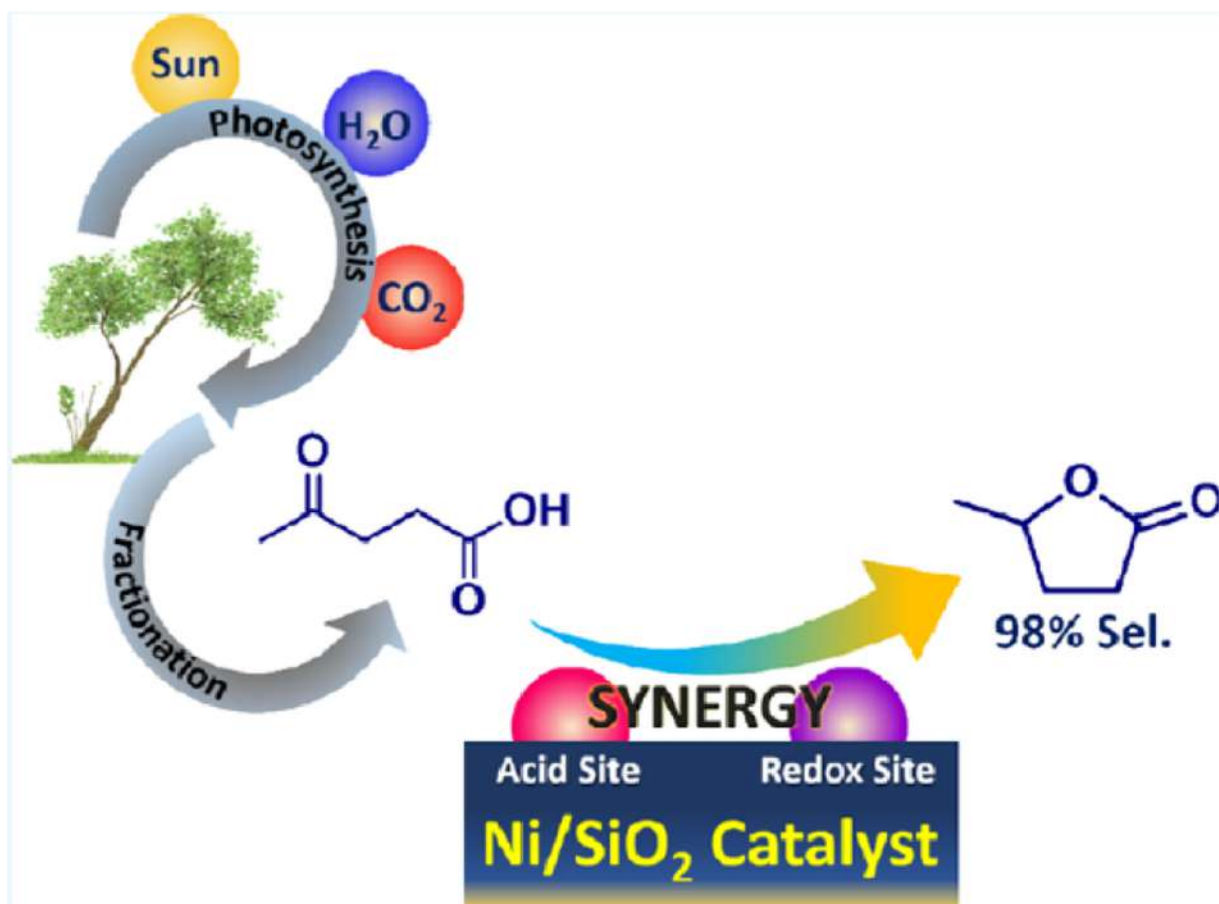
Fig. 44 Conversion of levulinic acid to γ-valerolactone over Ni/SiO$_2$ (Mallesham et al. 2018)

a high surface area up to 1000 m^2/g, pore size ranges from 2 to 4 nm, and pore volume up to 0.8, with wall thickness around 1.5 nm. Compared to MCM-41, MCM-48 is more resistant to pore blocking because it provides fast diffusion of molecules through its 3-D pore network, which is very suitable in catalysis. Although MCM-48 has, doubtlessly, a high potential as a catalytic support and selective adsorbent, it has not received enough attention compared to MCM-41. This is probably due to the difficulty of synthesising it.

Indeed, the classic structure directing agents (SDAs) that have been used in the preparation of the M41S family are the alkyltrimethylammonium halides. These surfactants form preferentially a hexagonal or lamellar structure in solution, which makes the preparation of MCM-48 (cubic structure) with high quality is very sensitive to a narrow margin of error, with very poor reproducibility. The synthesis of MCM-41 can be

affected by different synthesis parameters, such as the type of surfactant, temperature, solution composition, even stirring speed, and type of washing solvent (Mokri et al. 2019).

Only a few publications reported the incorporation of nickel particles into MCM-48 for utilisation in catalysis. Shaban et al. reported recently the preparation of MCM-48 supported NiO NPs by wet impregnation method, using nickel chloride hexahydrate as metal precursor in water, with MCM-48/nickel precursor ratio of 1:1 (w/w) (Shaban et al. 2020). Unfortunately, the NiO particle size and their dispersion in the MCM-48 framework were not investigated in this work, using neither TEM nor XRD. Authors claim that the incorporation of NiO in MCM-48 led to a considerable reduction in NiO band gap energy to 2.4 eV. The obtained material was used as a catalyst for the photodegradation of Congo red dye. It has been reported that the adsorption capacity and the
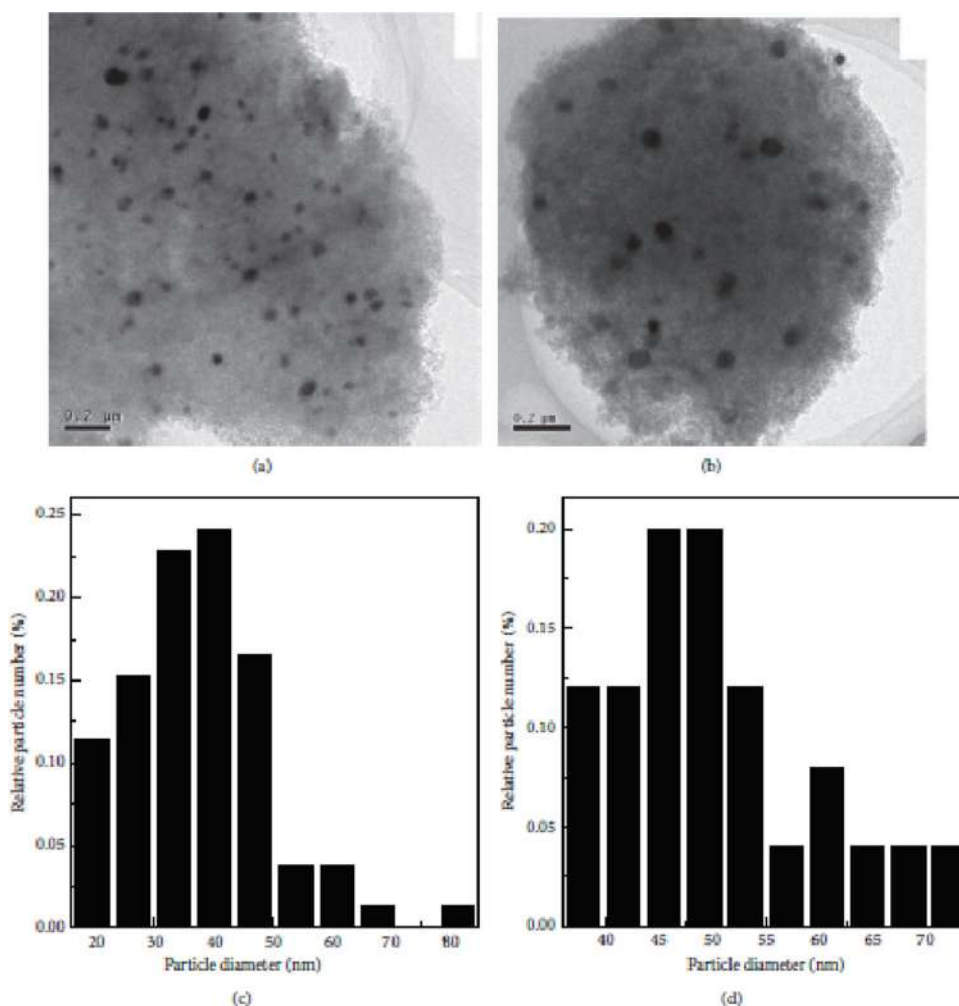
Fig. 45 TEM images of (a) reduced 3NiSN and (b) deactivated 3NiSN, and histogram of the particle size distribution obtained from sampling of nanoparticles from TEM data (c) for reduced 3NiSN and (d) for deactivated 3NiSN (He et al. 2015)

photocatalytic activity were enhanced in the composite NiO/MCM-48 compared to that in both NiO and MCM-48.

In another work, Hinrichsen and co-workers reported the synthesis of MCM-48 and its functionalisation with nickel and aluminium, using two different methods, which are incipient wetness impregnation (IWI) and template ion exchange (TIE) (Frey and Hinrichsen 2012). The characterisation results showed that the structure of MCM-48 was preserved after the functionalisation step using the IWI method, whereas the MCM-48 was partly affected by the TIE method. Here, also, the NiO particle size and their dispersion in MCM-48 were not studied using TEM and/or XRD.

The obtained materials were used to catalyse the conversion of ethene to propene. The highest

conversion and selectivity obtained with the optimal nickel and aluminium loadings, prepared by both methods, were 40% and 56%, respectively.

Ni nickel supported in TUD-1

TUD-1 is a mesoporous silicate material, first prepared by Jansen et al. in 2001 at Technische Universiteit Delft (TUD) (Jansen et al. 2001). Unlike most other mesoporous silica materials, TUD-1 is relatively simple to synthesize (Telalović et al. 2010). It has three-dimensional and irregular sponge-like porous structure, with high surface area (> 1200 m^2/g), pores of varying diameter (2.5–20 nm), and wall thickness ranges from 2.5 to 4 nm. These properties allow fast diffusion through
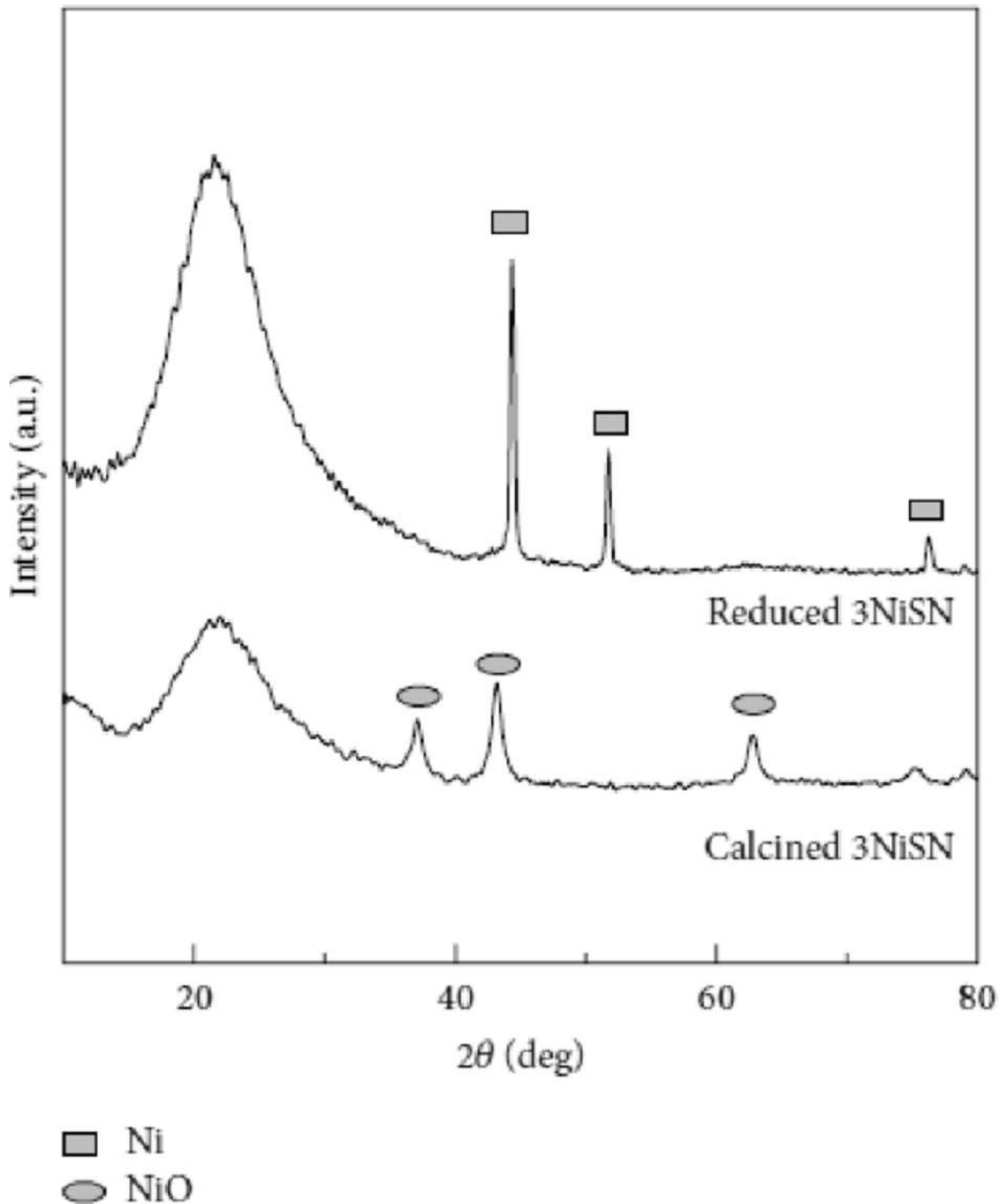
Fig. 46 XRD patterns of 3NiSN before and after reduction in H_2 for 4 h

TUD-1 pore network, making it an efficient and promising catalyst support in heterogeneous catalysis.

The synthesis of TUD-1 is based on the sol–gel process, using TEOS as silicon source. Unlike the

$$Ni(NO_3)_2 + H_2 \rightarrow NiO + 2\,NO_2 + H_2O \qquad (1)$$
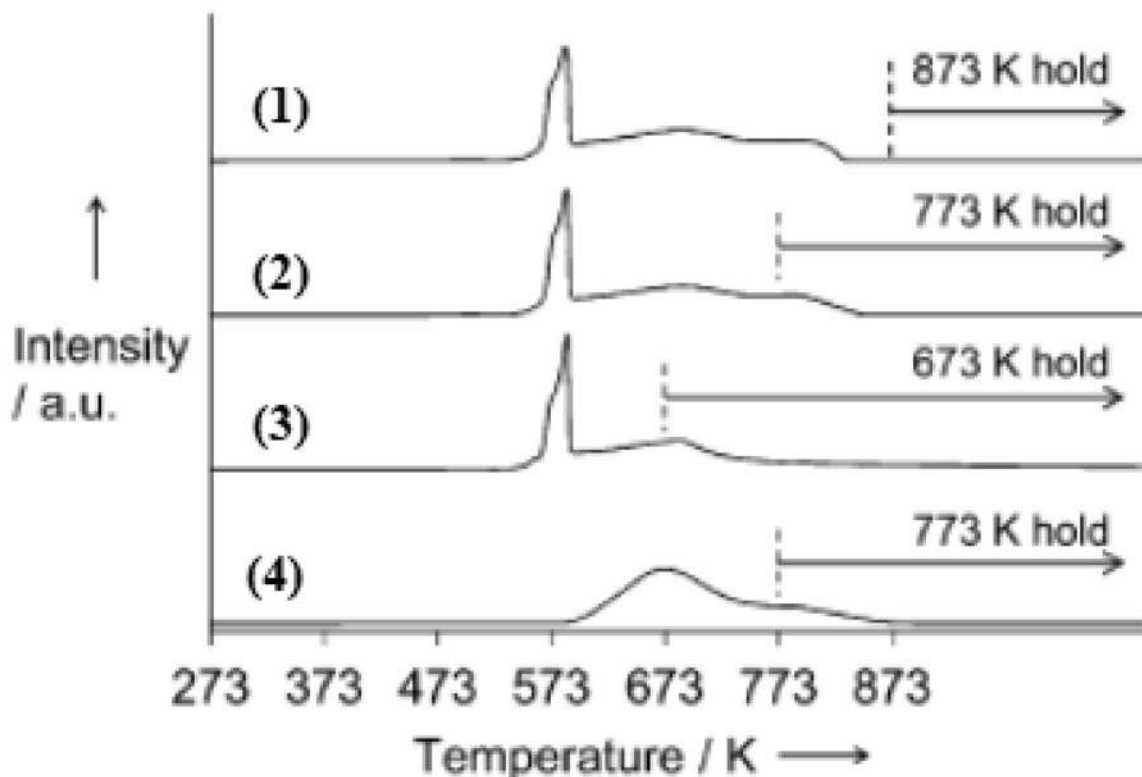
Fig. 47 TPR profiles of $Ni(NO_3)_2/SiO_2$. (1–3): without calcination and (4) after calcination at 773 K. Conditions: heating rate $= 10$ K/min, 5% H_2/Ar atmosphere

synthesis of many other mesoporous silica materials, no surfactant is needed to build the TUD-1 regular pore system. Instead, either tetraethylene glycol (TEG) or triethanolamine (TEAH$_3$) is used to chelate the silica and to obtain a porous structure. This synthesis method can be modified to introduce another metal (M) to the TUD-1 framework, to obtain a modified material (M-TUD-1) with different catalytic activities. Figure 39 illustrates the synthesis of TUD-1 and M-TUD-1 (M: metal).

Combination of two different metals into TUD-1 can induce a synergy between Brønsted and Lewis in the obtained catalyst. In addition to efficient applications in

acid, photocatalysis, and redox, TUD-1 demonstrated to be an outstanding carrier for many catalysts (Telalović et al. 2010; Gorsd et al. 2018; Tanglumlert et al. 2011).

However, only fewer publications reported the synthesis and catalytic activity evaluation of TUD-1 supported nickel NPs.

Yang et al. reported the synthesis of nickel containing TUD-1 nanocatalyst using three different methods, direct synthesis (Ni-DHT), grafting (Ni-GRF), and impregnation (Ni-IMP) method, and the obtained materials were used to catalyse CO_2 reforming of methane. (Quek et al. 2010).
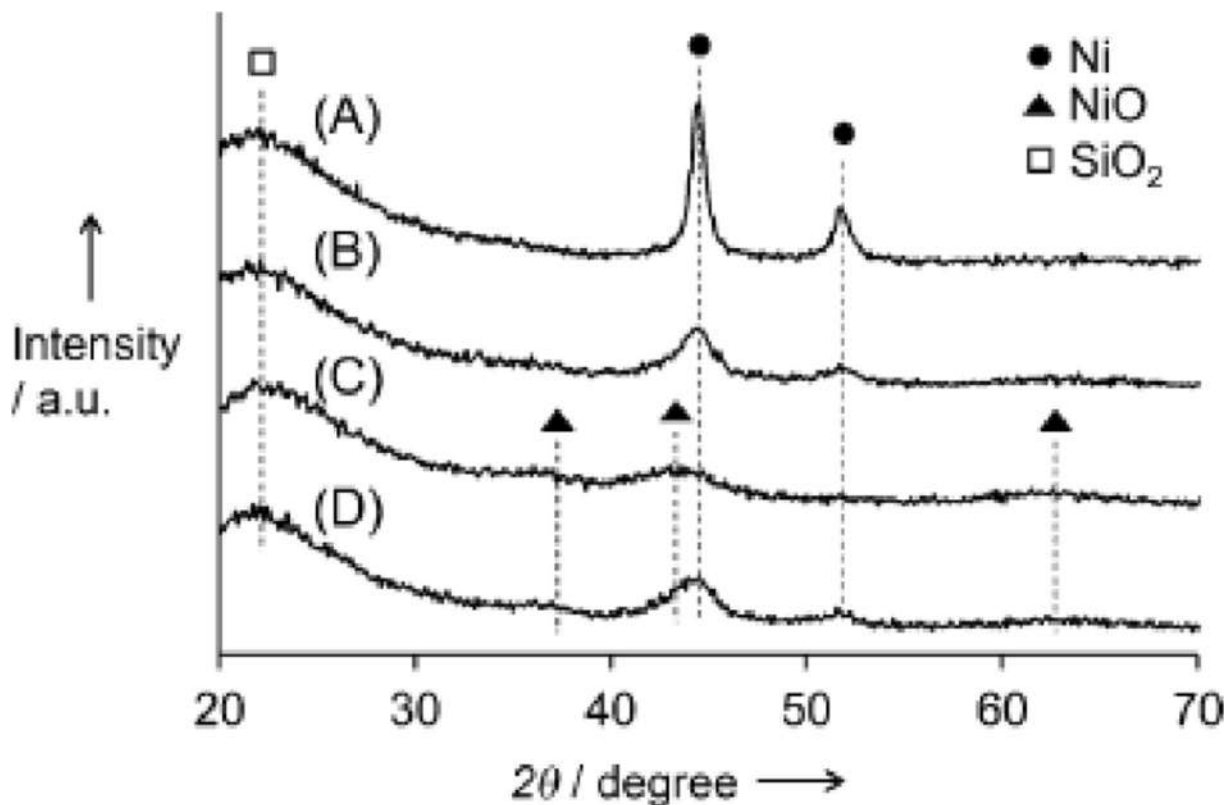
Fig. 48 XRD patterns of the catalysts under air. (A) Ni/SiO$_2$-cal-773, (B) Ni/ SiO$_2$-873, (C) Ni/SiO$_2$-773, and (D) Ni/SiO$_2$-673

Results showed that a small amount of aggregates was formed in the materials prepared by Ni-DHT and Ni-GRF, with high dispersion, compared to that prepared by Ni-IMP (Fig. 40). The smallest particle size was obtained by Ni-DHT. Although the catalyst prepared by the later method exhibited the highest catalytic activity. However, the grafted catalyst showed high stability and long-term activity. This is probably due to more easily accessible Ni-active sites in the grafted catalyst. Hence, the Ni-TUD-1 catalyst prepared by grafting method can be nominated as a better candidate for CO$_2$ reforming of methane.

The formation of crystalline NiO after calcination was confirmed by normal angle XRD (Fig. 41). Weak peak intensity was attributed to the high dispersion of NiO particles through the TUD-1 framework. The nickel content in all samples was measured by ICP test.

Nickel nanoparticles supported in other types of silica

Several works reported the incorporation of nickel NPs in other silica materials and their application in catalysis.

Reddy et al. (Mallesham et al. 2018) reported the preparation of silica-supported Ni NPs with different Ni loadings (5, 10, 20, 30, and 40%), using impregnation method. This catalyst was prepared by dispersing a colloidal SiO$_2$ in water followed by the addition of an aqueous solution of Ni(NO$_3$)$_2$·6H$_2$O. The obtained materials were calcined under air at 500 °C for 5 h.

The structure of NiO particles in all Ni/SiO$_2$ catalysts (with different Ni loading, from 5 to 40%) was confirmed by XRD (Fig. 42).

TEM images revealed the formation of uniformly dispersed NiO NPs on SiO$_2$ matrix (Fig. 43). The average particle size was around 9 nm for all samples with loadings up to 30%. However, the particle size was drastically increased to more than 21 nm at 40% Ni loading.

The high dispersion of NiO NPs has improved a synergistic metal–silica interaction, in particular for the 30% Ni loading sample, leading to enhanced acidic and redox properties. The prepared 30% Ni/SiO$_2$ material exhibited the best catalytic performance, with 98% selectivity to γ-valerolactone at total conversion of levulinic acid for 2 h (Fig. 44).

(A) Ni/SiO$_2$-cal-773
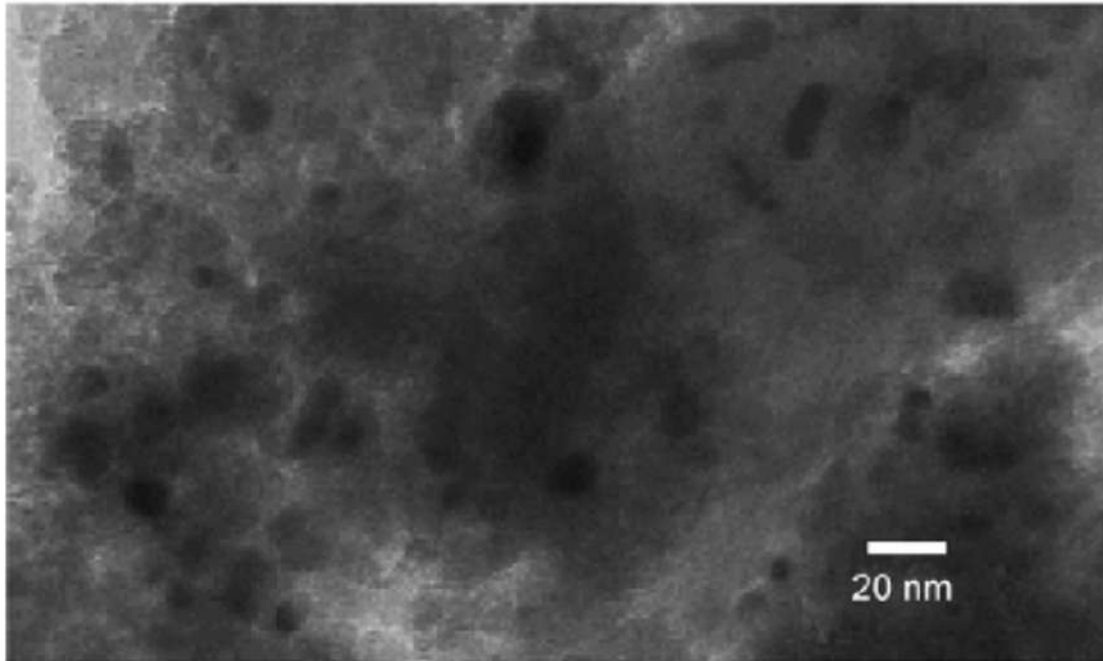
(B) Ni/SiO$_2$-873
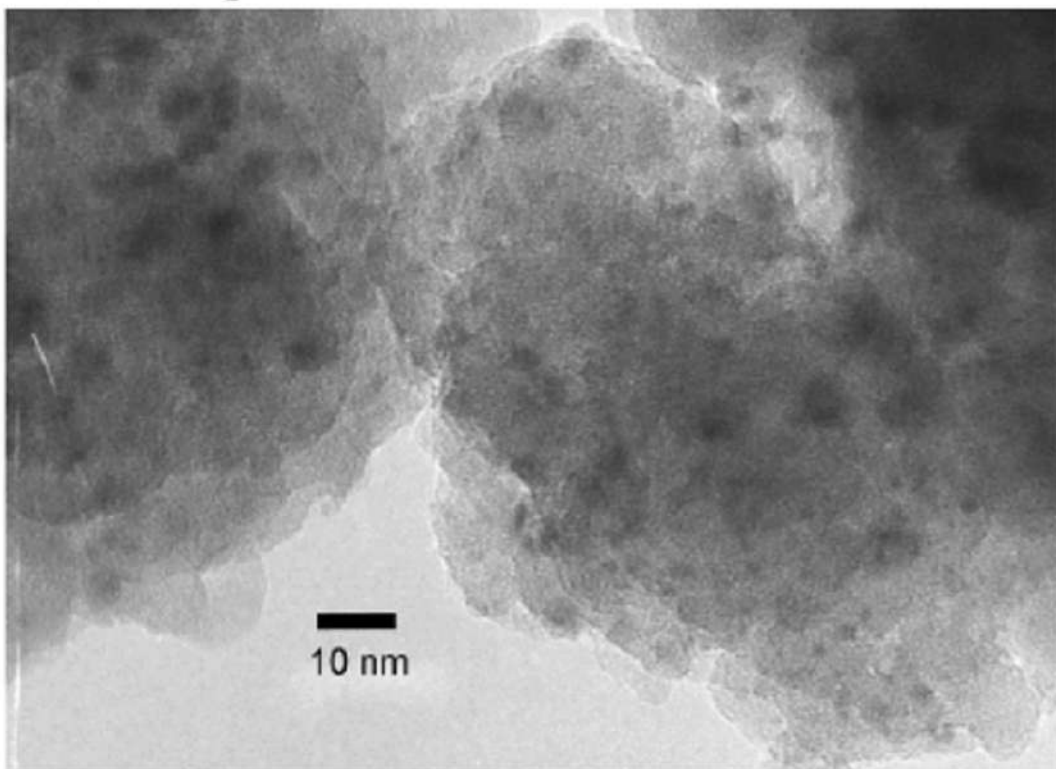
Fig. 49 TEM images of the reduced catalysts at (A) 773 K and (B) 873 K (Nakagawa et al. 2012)
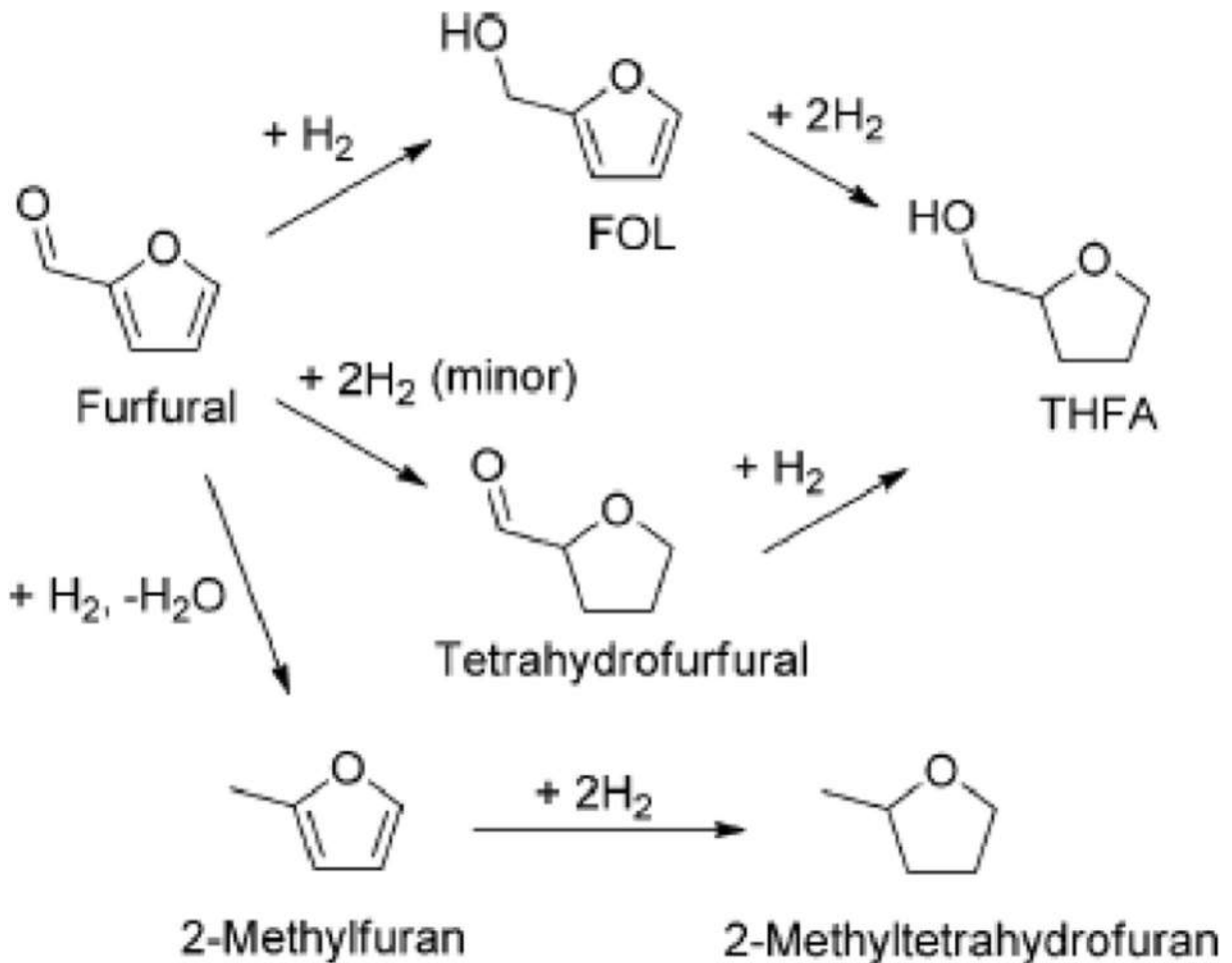
Fig. 50 Reaction pathways for the hydrogenation or hydrogenolysis of furfural (Nakagawa et al. 2012)

Luo et al. (He et al. 2015) reported the preparation of silica-supported NiO NPs using incipient wetness impregnation (IWI) method, with a commercial silica (S_{BET} = 498.8 m^2/g, Nanjing Tianyi Inorganic Chemical Factory) and nickel nitrate as a precursor. The as-made material was calcined at 380 °C then NiO reduced to Ni after treatment by H$_2$ at 700 °C. The Ni/SiO$_2$ catalyst was designated as 3NiSN. Ni NPs were highly dispersed in the silica framework, with particle size around 38 nm (Fig. 45). However, Ni NPs were weakly interacted with the support, with obvious particles sintering problems. Consequently, a rapid deactivation of the catalyst was observed during the combination process of CO$_2$ reforming and partial oxidation of methane (CRPOM) to produce syngas.

XRD analyses were carried out to understand the crystalline structure of 3NiSN catalysts, and the results

are presented in Fig. 46. The results showed only the FCC NiO phase, with typical reflections of the (111), (200), and (220) planes at 2θ = 37°, 43°, and 63°, respectively. After reduction under H$_2$ for 4 h, the peaks attributed to NiO disappeared, and three other peaks around 2θ = 44°, 52°, and 76° for Ni (111), Ni (200), and Ni (220) planes, respectively, were observed, indicating the successful transformation of NiO to metallic Ni.

Tomishige et al. (Nakagawa et al. 2012) reported the synthesis of silica-supported Ni NPs by reduction of nickel nitrate using H$_2$ (Eq. 1). The nickel nitrate in water was first impregnated in a commercial silica (Fuji Silysia G-6; BET surface area 523 m^2/g) using incipient wetness impregnation (IWI) method; then, the obtained as-made material was reduced to Ni NPs after treatment
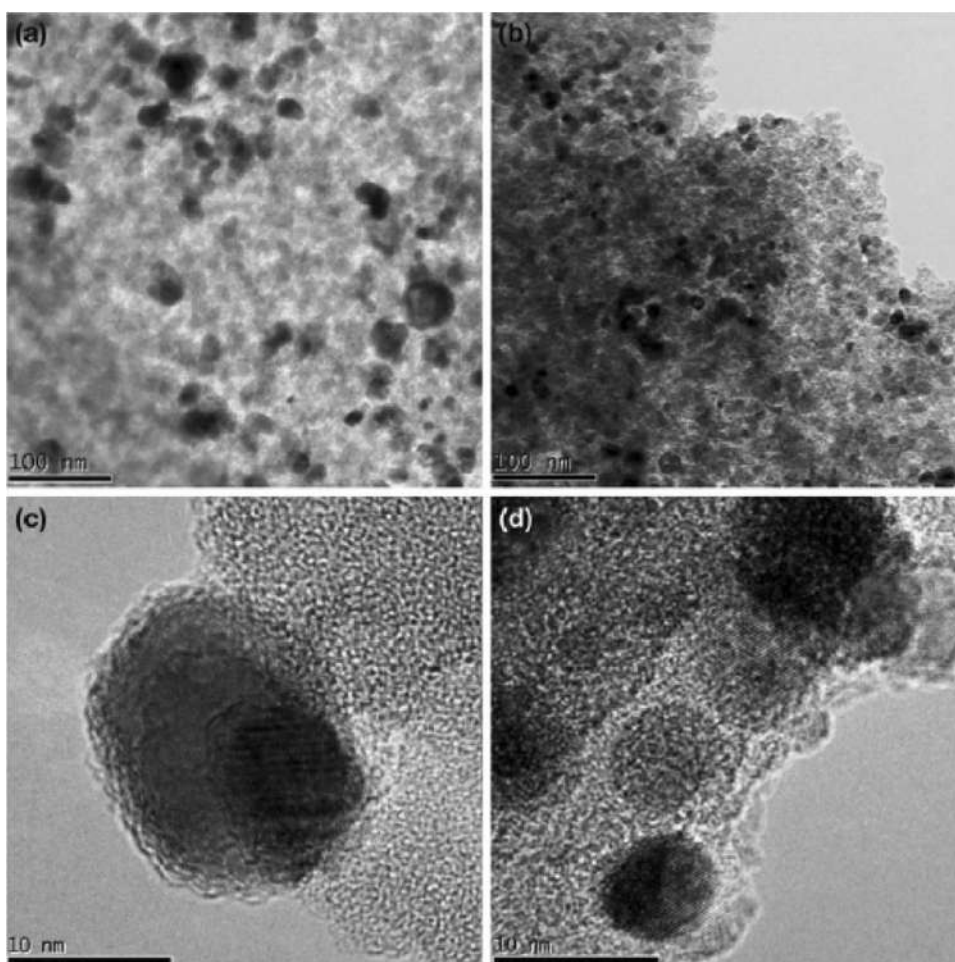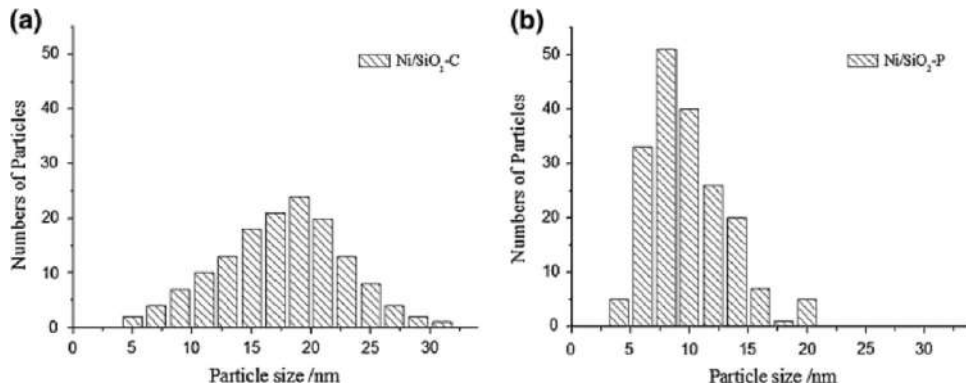
Fig. 51 TEM images of samples after reduction at 500 °C for 2 h. (a, c) Ni/SiO$_2$-C without treatment with plasma; (b, d) Ni/SiO$_2$-P treated with plasma (Shi and Liu 2009)

by flowing H$_2$ at different temperatures (670–870 K) (Fig. 47) in glass tube reactor.

$$Ni(NO_3)_2 + H_2 \rightarrow NiO + 2NO_2 + H_2O \qquad (1)$$
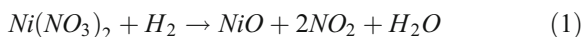
The structure of Ni species in the reduced catalysts was identified by powder XRD, and the obtained results are shown in Fig. 48.

For the samples reduced at high temperature, Ni/SiO$_2$-873 (Fig. 47—curve 1 and Fig. 48B) and Ni/SiO$_2$-cal-773 (Fig. 47—curve 4 and Fig. 48A), only peaks attributed to Ni metal were present. However, in the case of Ni/SiO$_2$-773 (Fig. 47—curve 2 and Fig. 48C) and Ni/SiO$_2$-673 (Fig. 47—curve 3 and Fig. 48D), both Ni metal and NiO particles were present.

The obtained Ni NP size was less than 4 nm with low dispersion as shown in TEM images (Fig. 49). The catalytic activity of the prepared catalyst was evaluated in the hydrogenation of furfural to 2-methyltetrahydrofuran (Fig. 50). The product was obtained with a maximum yield of 94%. It was found that low turnover frequency (TOF) was obtained with large Ni particle size.

In another work, Shi and Liu (Shi and Liu 2009) reported the synthesis of 10 wt% NiO NPs supported on silica, by conventional incipient impregnation method, using commercial SiO$_2$ powder, and nickel nitrate hexahydrate as precursor in water at room temperature. After stirring (12 h) and drying (100 °C/12 h), the obtained material was treated with a glow discharge plasma for 1 h and denoted by Ni/SiO$_2$-P. Another part of the sample was calcined at 500 °C without plasma

Fig. 52 Size distributions after reduction at 500 °C for 2 h. (a) Ni/SiO$_2$-C without treatment with plasma; (b) Ni/SiO$_2$-P treated with plasma (Shi and Liu 2009)

treatment. This thermal treated sample was denoted by Ni/SiO$_2$-C.

After calcination (500 °C/4 h) and reduction process (H$_2$, 500 C°/2 h), the obtained silica-supported Ni NPs
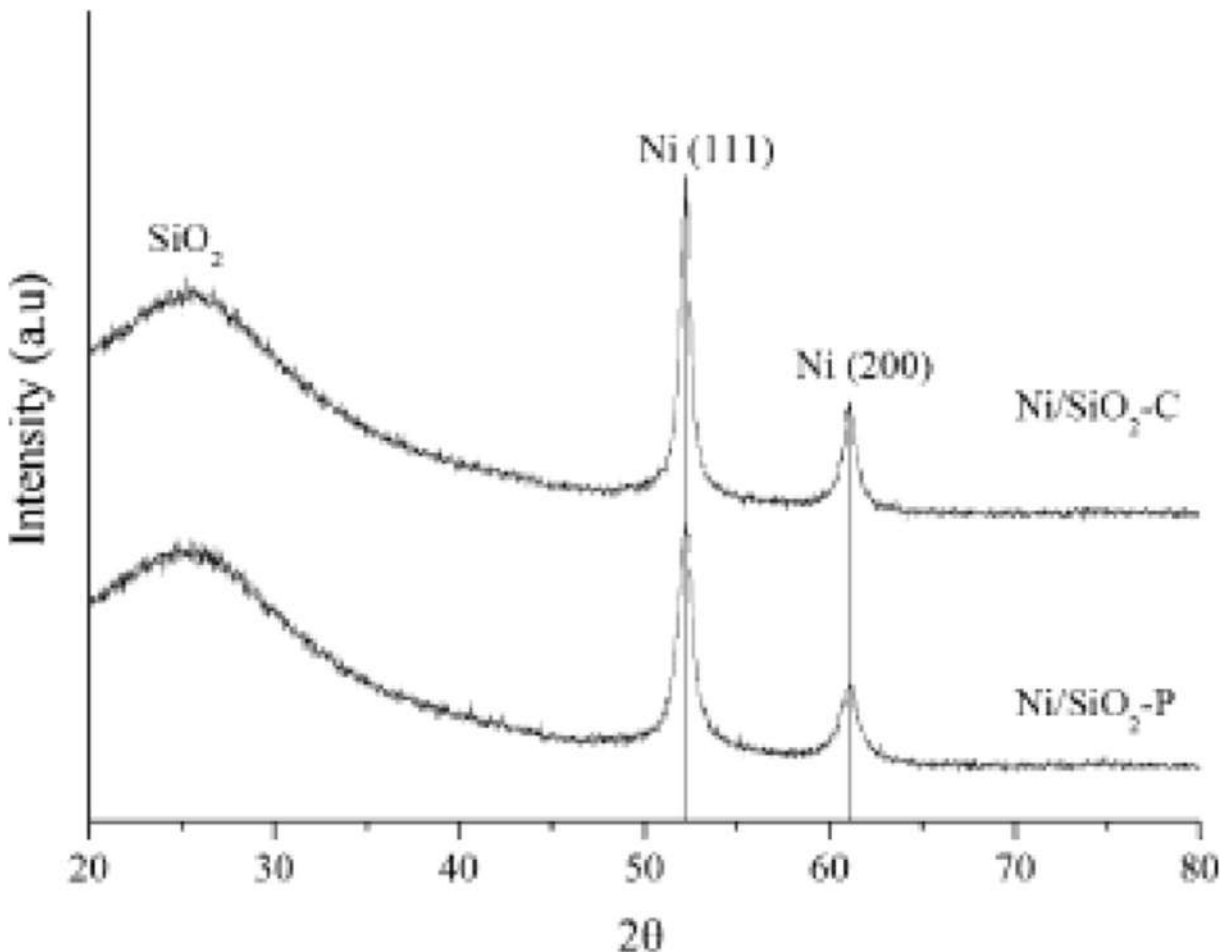
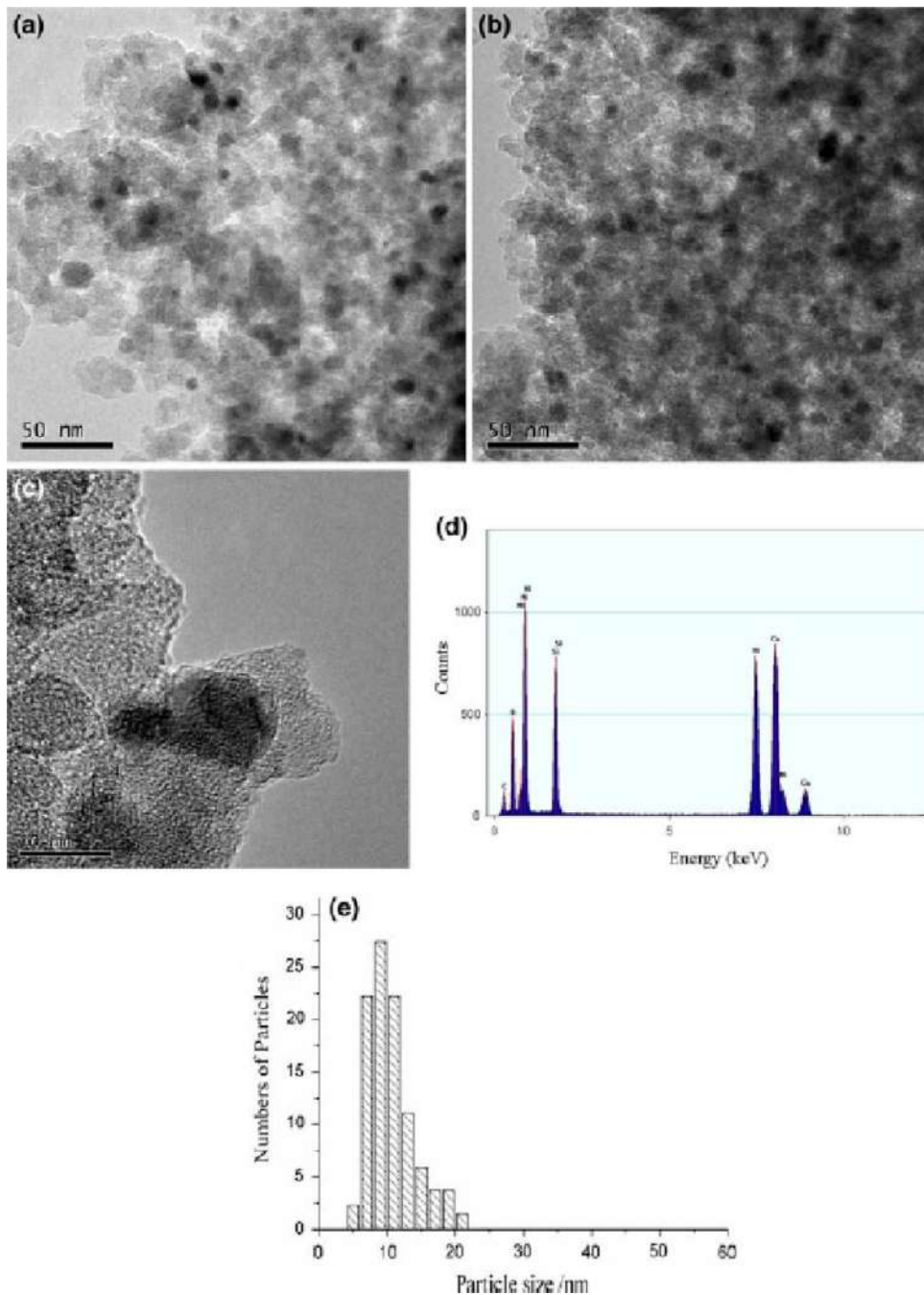**Fig. 53** XRD patterns of fresh samples after reduction at 500 °C for 2 h. Ni/SiO$_2$-P: plasma treated sample. Ni/SiO$_2$-C: thermal treated sample

Fig. 54 TEM images of nickel particles of Ni/SiO₂-P after reaction at 350 °C for 4 h (a, b, c) with EDX of image c (d) and size distribution (e)

were highly dispersed with smaller particle size and narrow size distribution at around 9.7 nm, compared to 17.5 nm for the material prepared without plasma treatment, with wide particle size distribution (Figs. 51 and 52).

The prepared material was analysed by XRD to identify the chemical structure of the nickel particles, and to calculate their size. XRD patterns of fresh samples are presented in Fig. 53. Two peaks assigned to Ni (111) at 52.2° and Ni (200) at 61.1°, respectively, appeared on the XRD patterns confirming the metallic nature of nickel particles. The average particle size calculated from Scherrer formula was about 14 nm for
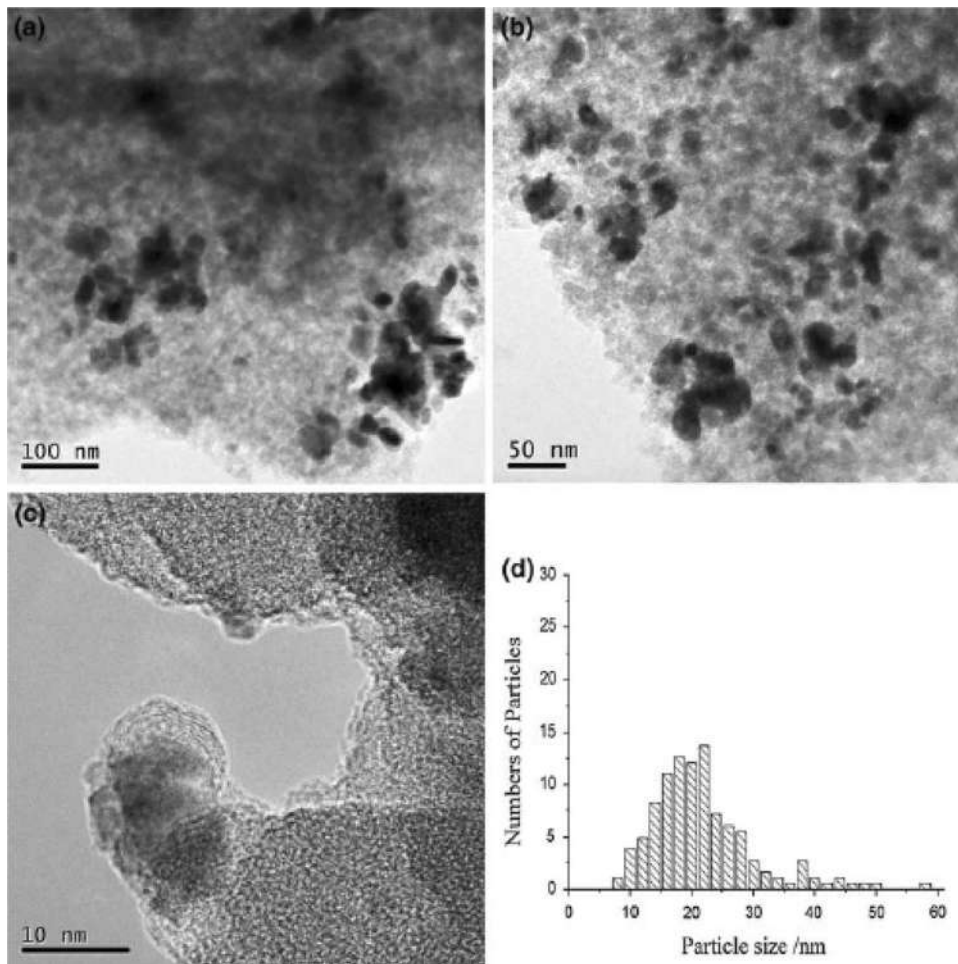
Fig. 55 TEM images of nickel particles of Ni/SiO$_2$-C after reaction at 350 °C for 4 h (a, b, c) and size distribution (d)

Ni/SiO$_2$-C and around 10 nm for Ni/SiO$_2$-P, which is in agreement with the results observed in TEM. The XRD and TEM analyses confirmed that smaller metal particles were obtained in the plasma treated sample.

The obtained catalysts were evaluated in the methanation reaction of carbon monoxide. The catalyst exhibited high conversion of carbon monoxide and hydrogen with less carbon deposition.

As shown in TEM images of Ni/SiO$_2$-P and Ni/SiO$_2$-C samples (Figs. 54 and 55, respectively), the plasma treated catalyst showed enhanced nickel–silica interaction with good dispersion after reaction. While aggregation of nickel was observed on Ni/SiO$_2$-C after reaction, with broad partition distribution of nickel particles (from 7.7 to 57.4 nm, with an average of 21.8 nm). In addition, nickel particles on Ni/SiO$_2$-C were covered by carbon species, with no visible carbon species found on Ni/SiO$_2$-P.

A new method to prepare ultra fine nickel NPs in mesoporous silica, called templating assemble method, was reported by Yang et al. (Yang et al. 2017). This process is based on the complexation of the nickel sources (precursor) by the amine groups attached to the surfactant followed by addition of TEOS then calcination (Fig. 56). In this process, dodecyl amine was used as a neutral structure directing agent for silica and as a complexing agent to capture the nickel ions which were added with different loadings (1, 2, 3 and 4 mmol for 10.73 mL of TEOS). The samples corresponding to different nickel amounts were labeled as H-xNi (x = 1, 2, 3, and 4), in which x stands for the nickel amount (number of moles of Ni(NO$_3$)$_2$·6H$_2$O mmol) of different samples.

After the calcination step, highly dispersed and fine NiO NPs were observed in TEM images (Fig. 57).
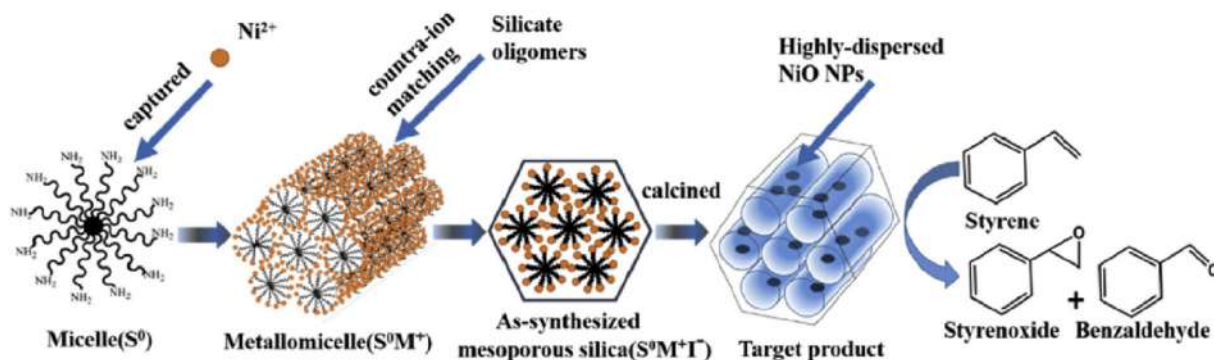
Fig. 56 Preparation of mesoporous silica–supported NiO NPs using a templating assembly route (Yang et al. 2017)

TEM images showed a sponge-like framework mesoporous structure with wormhole pore for the prepared samples. In addition, these images demonstrated the presence of fine Ni NPs (2–5 nm) with high dispersion in mesoporous silica. However, some Ni aggregates have been observed in high Ni loading material. As expected, the surface area, pore size, and pore volume were decreased by increasing the Ni loading.

Because nickel oxide nanoparticles prepared by the templating route (H-xNi series) were mono-dispersed in the silica framework, only broad peaks were observed in XRD patterns (Fig. 58). In this work, the loadings of

nickel in catalysts were measured using the inductively coupled plasma spectrometer (ICP).

The obtained nanocatalyst exhibited a good catalytic activity for the epoxidation reaction of styrene. The maximum conversion of styrene (67%) and high styrene oxide selectivity (94%) were obtained using the catalyst with high Ni loading (4 mmol of nickel nitrate) which was named H-4Ni.

However, using functionalized surfactant to interact with the metal sources can affect the silica structure and its porosity. In addition, this method is limited by the use of some specific and expensive surfactants which carry
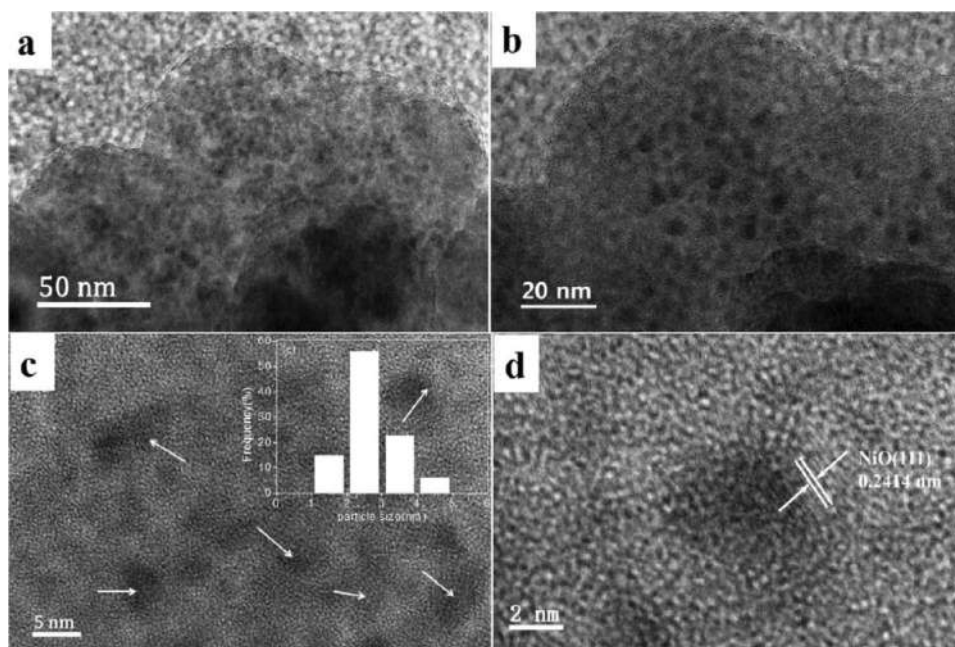
Fig. 57 TEM images of sample of H-4Ni and size distribution of NiO NPs (inset) (Yang et al. 2017)
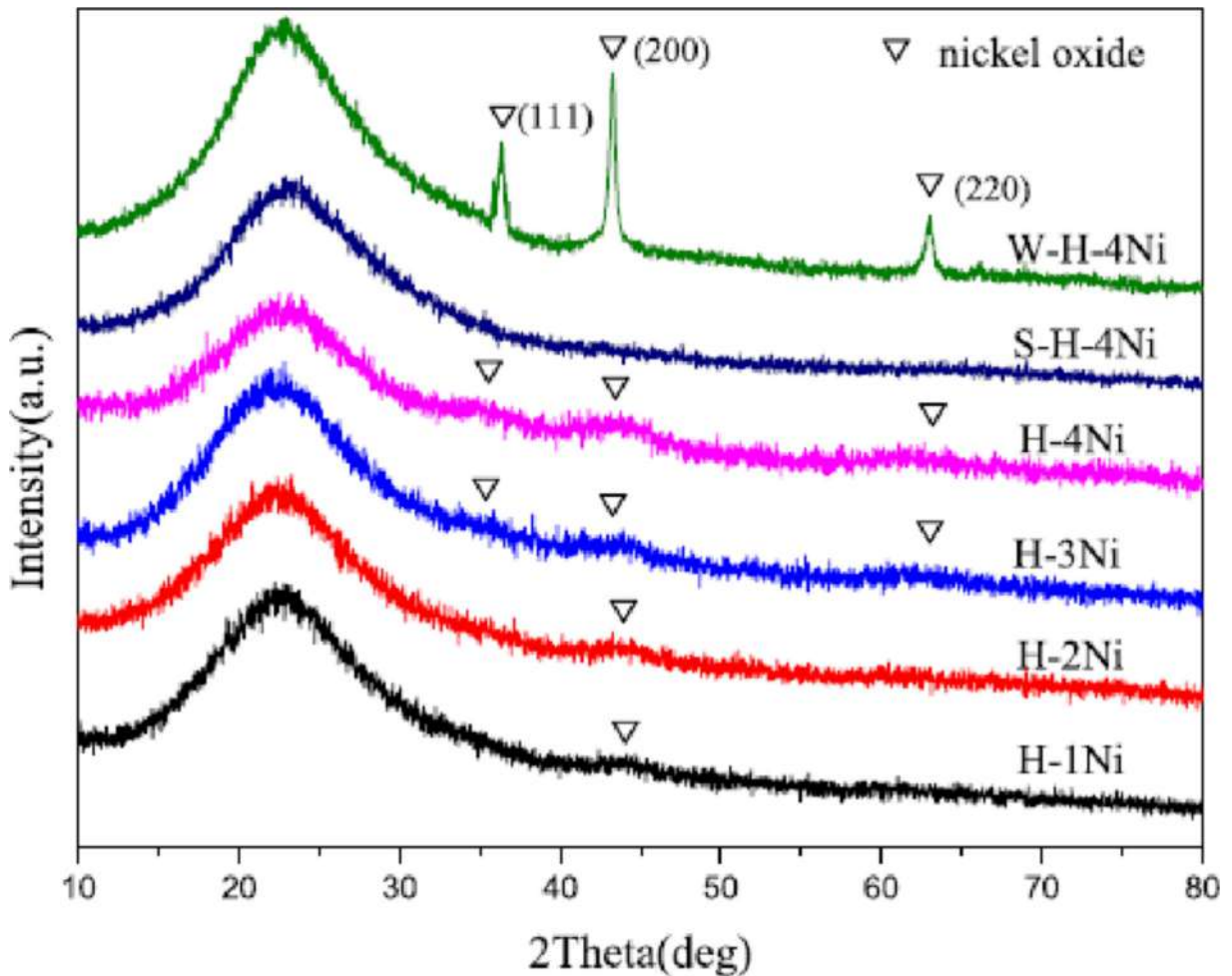
Fig. 58 High-angle patterns of the series samples of H-xNi (samples prepared by templating route), S–H-4Ni (sample prepared via a single-step procedure), and W–H-4Ni (sample prepared by wetness impregnation)

amine groups; thus, the access to commercial mesoporous silica such as SBA-15 and MCM-41 is not possible.

Nickel-based bimetallic NPs incorporated in mesoporous silica material have been also prepared and used in catalysis. Recently, Pandey et al. (Pandey et al. 2021) reported the synthesis of Pd–Ni bimetallic NPs incorporated in mesoporous silica and the utilisation of the obtained material as an efficient and cheaper photocatalyst for the degradation of anionic and cationic dyes.

Mesoporous silica nanoparticles (MSNPs) supported Pd–Ni NPs were prepared in situ using an organo trialkoxysilane as a template and stabilizer for efficient reduction. Briefly, in the first step, silica-supported palladium NPs were prepared by impregnation of tetrachloropalladate in MSNPs using ethylene glycol.

The obtained palladium cations dispersed MSNPs were suspended in a solution of 3-aminopropyltrimethoxysilane (template) in ethylene glycol. After addition of formaldehyde and microwave treatment, PdNP-inserted MSNPs was obtained. A similar method was used to prepare mesoporous silica-supported PdNPs. In the second step, PdNP-inserted MSNPs was suspended in an aqueous solution of nickel sulphate containing 1% PVP under stirring followed by the addition of $NaBH_4$ aqueous solution under stirring resulting the formation of Pd–Ni NP–inserted MSNPs and collected by centrifugation.

In this method, 3-aminopropyltrimethoxysilane had an active role in efficient reduction of palladium cations along with in situ providing a template for efficient reduction and stabilisation of Pd–Ni nanocrystallite. In addition, this

organotrialkoxysilane enabled controlled insertion of bi-

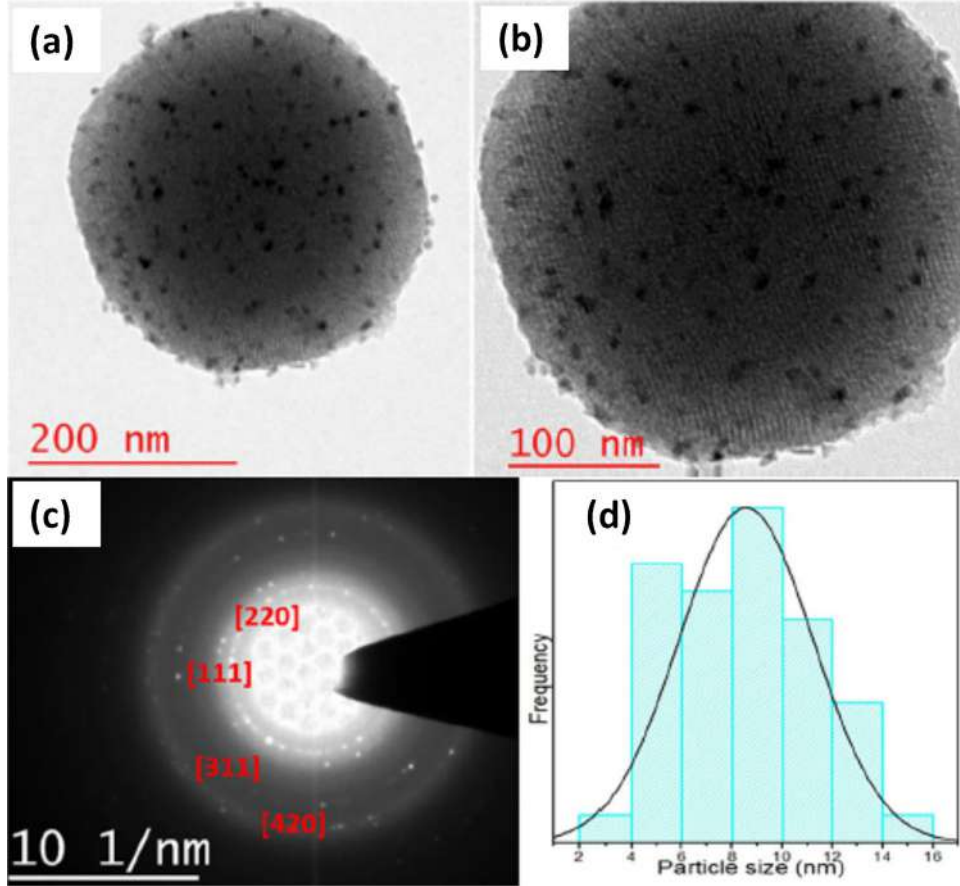Pd–Ni particle size and structure of the prepared

Fig. 59 (a, b) TEM images of Pd–Ni NP–inserted MSNPs; (c) selected area diffraction pattern; (d) particle size distribution curve

metallic Pd–Ni nanocrystallite within mesoporous silica support.

material were investigated by TEM and selected area electron diffraction pattern (SAED) (Fig. 59). The TEM
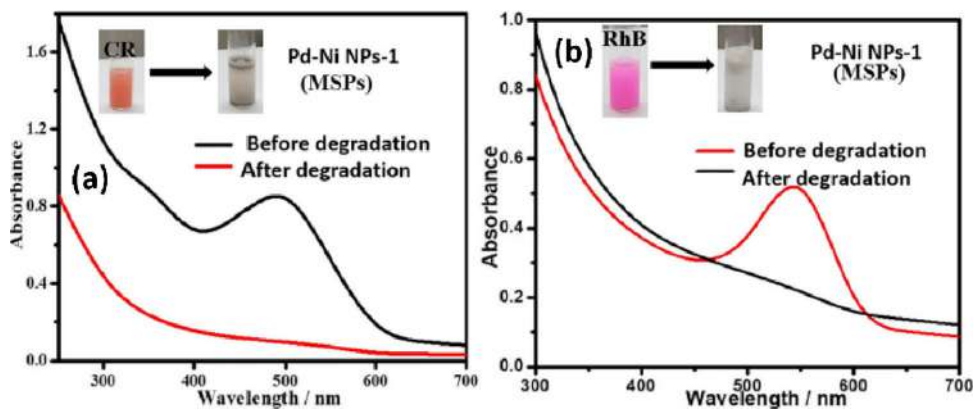

Fig. 60 UV–Vis absorption spectra of the real textile sample in the absence and the presence of Pd–Ni NPs-1 inserted MSPs, (a) for Congo red and (b) for Rh B. The samples were collected from the washout of stencil used in fabric printing using dye embedded with binder and thinner

images of Pd–Ni NP inserted MSNPs are shown in Fig. 59a and b. SAED as shown in Fig. 59c confirms the presence of 111, 311 planes assigned to nickel, whereas 220, 420 planes are assigned the presence of palladium nanocatalyst. Figure 59d shows the average size of Pd–Ni NPs nanocrystallite to the order of 8 nm.

Compared to Pd–Ni bimetallic nanocatalyst (made at Pd:Ni ratio of 1:1), the use of Pd–Ni NP–inserted MSNPs yielded faster degradation of both Rh B and Congo red dyes to the order of 50 s and 150 s, respectively (Fig. 60), justifying potent catalytic behaviour for real-time degradation of toxic industrial dye. In addition, this nanocatalytic system showed high stability and excellent reusability.

Conclusion

Throughout this review, the most commonly used techniques to prepare unsupported Ni NPs and their recent applications in heterogeneous catalysis, including photocatalysis, have been discussed.

Despite the importance of Ni NPs as efficient economic and eco-friendly nanocatalysts, characteristics such as optical and catalytic activity may be lost if the dispersion of these particles is not adequately modulated. Several efforts have been deployed to overcome their aggregation problem, low durability, low dispersibility, and electrons and holes recombination by incorporating them into solid matrices such as porous silica materials.

In this review, we have discussed the most commonly used methods to incorporate Ni NPs into different types of porous silica materials (e.g. SBA-15, MCM-41, MCM-48, TUD-1, and other silica) and their applications in heterogeneous catalysis. The most used technique to prepare Ni NPs@silica is the impregnation, with nickel nitrate as nickel precursor, and reforming of methane as the most used application.

However, the use of different approaches to prepare Ni NPs@silica is still limited by the Ni NP size and aggregation, particles sintering, low dispersion, Ni loading, and the complicated, expensive, and time-consuming techniques.

The synthesis of stable Ni NPs@silica with quantized size and high dispersion tended to be difficult. This explains why the investigation of Ni NP catalytic activity is relatively scarce compared with other transition metal NPs. Hence, the development of more efficient approaches remains a fecund area of research.

Declarations

Conflict of interest   The authors declare no competing interests.

References

Sheldon RA, Dakka J (1994) Heterogeneous catalytic oxidations in the manufacture of fine chemicals. Catal Today 19(2):215–245. https://doi.org/10.1016/0920-5861(94)80186-X

Sachdeva, H., Dwivedi, D., Bhattacharjee, R. R., Khaturia, S., & Saroj, R. (2013). NiO nanoparticles: an efficient catalyst for the multicomponent one-pot synthesis of novel spiro and condensed indole derivatives. Journal of Chemistry, 2013. https://doi.org/10.1155/2013/606259

Clark J, Macquarrie D (1998) Catalysis of liquid phase organic reactions using chemically modified mesoporous inorganic solids. Chem Commun 8:853–860. https://doi.org/10.1039/A709143E

Liu L, Corma A (2018) Metal catalysts for heterogeneous catalysis: from single atoms to nanoclusters and nanoparticles. Chem Rev 118(10):4981–5079. https://doi.org/10.1021/acs.chemrev.7b00776

Kung, H. H. (1989). Transition metal oxides: surface chemistry and catalysis. Elsevier

Henrich, V. E., & Cox, P. A. (1996). The surface science of metal oxides. Cambridge university press

Noguera, C. (1996). Physics and chemistry at oxide surfaces. Cambridge University Press

Salem I (2003) Recent studies on the catalytic activity of titanium, zirconium, and hafnium oxides. Catalysis Reviews 45(2):205–296. https://doi.org/10.1081/CR-120015740

Ornelas C, Méry D, Blais JC, Cloutet E, Ruiz Aranzaes J, Astruc D (2005) Efficient mono- and bifunctionalization of polyolefin dendrimers by olefin metathesis. Angew Chem Int Ed 44(45):7399–7404. https://doi.org/10.1002/anie.200502848

Astruc D (2007) Palladium nanoparticles as efficient green homogeneous and heterogeneous carbon–carbon coupling precatalysts: a unifying view. Inorg Chem 46(6):1884–1894. https://doi.org/10.1021/ic062183h

Zhong LS, Hu JS, Cui ZM, Wan LJ, Song WG (2007) In-situ loading of noble metal nanoparticles on hydroxyl-group-rich titania precursor and their catalytic applications. Chem Mater 19(18):4557–4562. https://doi.org/10.1021/cm0714032

Moreno-Manas M, Pleixats R (2003) Formation of carbon–carbon bonds under catalysis by transition-metal nanoparticles. Acc Chem Res 36(8):638–643. https://doi.org/10.1021/ar020267y

Li Y, Boone E, El-Sayed MA (2002) Size effects of PVP–Pd nanoparticles on the catalytic Suzuki reactions in aqueous solution. Langmuir 18(12):4921–4925. https://doi.org/10.1021/la011469q

Astruc, D. (Ed.). (2008). Nanoparticles and catalysis. John Wiley & Sons.

Djakovitch, L., Köhler, K., & Vries, J. G. D. (2007). The role of palladium nanoparticles as catalysts for carbon–carbon coupling reactions. Nanoparticles and Catalysis, 303-348. https://doi.org/10.1002/9783527621323.ch10

Durand J, Teuma E, Gómez M (2008) An overview of palladium nanocatalysts: surface and molecular reactivity. Eur J Inorg Chem 2008(23):3577–3586. https://doi.org/10.1002/ejic.200800569

Yang F, Zhou S, Gao S, Liu X, Long S, Kong Y (2017) In situ embedding of ultra-fine nickel oxide nanoparticles in HMS with enhanced catalytic activities of styrene epoxidation. Microporous Mesoporous Mater 238:69–77. https://doi.org/10.1016/j.micromeso.2016.03.007

Astruc D (2020) Introduction: nanoparticles in catalysis. Chem Rev 120(2):461–463. https://doi.org/10.1021/acs.chemrev.8b00696

Bian Z, Das S, Wai MH, Hongmanorom P, Kawi S (2017) A review on bimetallic nickel-based catalysts for CO2 reforming of methane. ChemPhysChem 18(22):3117–3134. https://doi.org/10.1002/cphc.201700529

Jaji N-D, Lee HL, Hussin MH, Akil HM, Zakaria MR, Othman MBH (2020) Advanced nickel nanoparticles technology: from synthesis to applications. Nanotechnol Rev 9:1456–1480. https://doi.org/10.1515/ntrev-2020-0109

Vollath, D., & Szabó, D. V. (2009). Nonmetallic bulk nanomaterials. Bulk nanostructured materials', (eds MJ Zehetbauer and YT Zhu), 49–85.

Schubert, U., & Hüsing, N. (2019). Synthesis of inorganic materials. John Wiley & Sons

Ozin, G. A., Arsenault, A. C., & Cademartiri, L. (2009). Nanorod, nanotube, nanowire self-assembly. Nanochemistry: A Chemical Approach to Nanomaterials, 215.

Lai TL, Lee CC, Wu KS, Shu YY, Wang CB (2006) Microwave-enhanced catalytic degradation of phenol over nickel oxide. Appl Catal B 68(3–4):147–153. https://doi.org/10.1016/j.apcatb.2006.07.023

Lai TL, Lee CC, Huang GL, Shu YY, Wang CB (2008) Microwave-enhanced catalytic degradation of 4-chlorophenol over nickel oxides. Appl Catal B 78(1–2):151–157. https://doi.org/10.1016/j.apcatb.2007.09.015

Christoskova ST, Stoyanova M (2001) Degradation of phenolic waste waters over Ni-oxide. Water Res 35(8):2073–2077. https://doi.org/10.1016/S0043-1354(00)00469-3

Ashik UPM, Daud WW, Hayashi JI (2017) Governance of the porosity and of the methane decomposition activity sustainability of NiO/SiO2 nanocatalysts by changing the synthesis parameters in the modified Stöber method. C R Chim 20(9–10):896–909. https://doi.org/10.1016/j.crci.2017.06.007

Guo XF, Kim YS, Kim GJ (2011) Synthesis of mesoporous metal oxides and their efficient property for super capacitor application. J Nanosci Nanotechnol 11(2):1672–1675. https://doi.org/10.1166/jnn.2011.3321

Solsona B, Concepción P, Nieto JL, Dejoz A, Cecilia JA, Agouram S, Castellón ER (2016) Nickel oxide supported on porous clay heterostructures as selective catalysts for the oxidative dehydrogenation of ethane. Catal Sci Technol 6(10):3419–3429. https://doi.org/10.1039/C5CY01811K

Vikraman D, Park HJ (2016) Shape-selective synthesis of NiO nanostructures for hydrazine oxidation as a nonenzymatic amperometric sensor. RSC Adv 6(89):86101–86107. https://doi.org/10.1039/C6RA12805J

Sasaki T, Ichikuni N, Hara T, Shimazu S (2018) Study on the promoting effect of nickel silicate for 1-phenylethanol oxidation on supported NiO nanocluster catalysts. Catal Today 307:29–34. https://doi.org/10.1016/j.cattod.2017.05.076

Gao X, Mao H, Lu M, Yang J, Li B (2012) Facile synthesis route to NiO–SiO2 intercalated clay with ordered porous structure: intragallery interfacially controlled functionalization using nickel–ammonia complex for deep desulfurization. Microporous Mesoporous Mater 148(1):25–33. https://doi.org/10.1016/j.micromeso.2011.07.022

El-Safty SA, Kiyozumi Y, Hanaoka T, Mizukami F (2008) Heterogeneous catalytic activity of NiO-silica composites designated with cubic Pm3n cage nanostructures. Appl Catal B 82(3–4):169–179. https://doi.org/10.1016/j.apcatb.2008.01.027

Adil SF, Assal ME, Kuniyil M, Khan M, Shaik MR, Alwarthan A, Siddiqui MRH (2017) Synthesis and comparative catalytic study of zinc oxide (ZnO x) nanoparticles promoted MnCO3, MnO2 and Mn2O3 for selective oxidation of benzylic alcohols using molecular oxygen. Mater Express 7(2):79–92. https://doi.org/10.1166/mex.2017.1357

Arora AK, Kumar P, Kumar S (2017) Synthesis of ZnO nanoparticle and its application in catalytic hydrolysis of p-acetoxynitrobenzene. Int J Nanosci 16(04):1750005. https://doi.org/10.1142/S0219581X17500053

Pike SD, García-Trenco A, White ER, Leung AH, Weiner J, Shaffer MS, Williams CK (2017) Colloidal Cu/ZnO catalysts for the hydrogenation of carbon dioxide to methanol: investigating catalyst preparation and ligand effects. Catal Sci Technol 7(17):3842–3850. https://doi.org/10.1039/C7CY01191A

Chand, S., & Sandhu, J. S. (2015). ZnO Nanoparticles: an efficient green reusable catalyst for the synthesis of 3-formyl benzopyranones chalcones by Claisen-Schmidt reaction under solvent-free condition. https://hdl.handle.net/123456789/33037

Sun X, Zhang X, Cao X, Zhao X (2016) Optimization of reaction conditions for cyclohexane to cyclohexanone with t-butylhydroperoxide over CuCl2 loaded with activated carbon. J Braz Chem Soc 27(1):202–208. https://doi.org/10.5935/0103-5053.20150271

Grosso C, Boissiere BS, Brezesinski T, Pierre N, Albouy P, Amenitsch H, Antonietti M, Sanchez C (2004) Periodically ordered nanoscale islands and mesoporous films composed of nanocrystalline multimetallic oxides. Nat Mater 3(11):787–92. https://doi.org/10.1038/nmat1206

Zou X, Conradsson T, Klingstedt M, Dadachov MS, O'Keeffe M (2005) A mesoporous germanium oxide with crystalline pore walls and its chiral derivative. Nature 437(7059):716–719. https://doi.org/10.1038/nature04097

Ying JY, Mehnert CP, Wong MS (1999) Synthesis and applications of supramolecular-templated mesoporous materials. Angew Chem Int Ed 38(1–2):56–77. https://doi.org/10.1002/(SICI)1521-3773(19990115)38:1/2%3C56::AID-ANIE56%3E3.0.CO;2-E

Jia J, Wang Y, Tanabe E, Shishido T, Takehira K (2003) Carbon fibers prepared by pyrolysis of methane over Ni/MCM-41 catalyst. Microporous Mesoporous Mater 57(3):283–289. https://doi.org/10.1016/S1387-1811(02)00598-X

Basha SS, Sasirekha NR, Maheswari R, Shanthi K (2006) Mesoporous H-AlMCM-41 supported NiO-MoO3 catalysts for hydrodenitrogenation of o-toluidine: I. Effect of MoO3 loading. Appl Catal A 308:91–98. https://doi.org/10.1016/j.apcata.2006.04.013

Moreno-Tost R, Santamaría-González J, Maireles-Torres P, Rodríguez-Castellón E, Jiménez-López A (2002) Nickel oxide supported on zirconium-doped mesoporous silica for selective catalytic reduction of NO with NH 3. J Mater Chem 12(11):3331–3336. https://doi.org/10.1039/B204041G

Polshettiwar V, Baruwati B, Varma RS (2009) Nanoparticle-supported and magnetically recoverable nickel catalyst: a robust and economic hydrogenation and transfer hydrogenation protocol. Green Chem 11(1):127–131. https://doi.org/10.1039/B815058C

Kalbasi RJ, Mosaddegh N (2011) Suzuki-Miyaura cross-coupling reaction catalyzed by nickel nanoparticles supported on poly(N-vinyl-2-pyrrolidone)/TiO2-ZrO2 composite. Bull Korean Chem Soc 32:2584–2592

Alonso F, Riente P, Yus M (2011) Nickel nanoparticles in hydrogen transfer reactions. Acc Chem Res 44(5):379–391. https://doi.org/10.1021/ar1001582

Sriram S, Thayumanavan A, Ravichandran K (2016) Influence of nitrogen doping on properties of NiO films. Surf Eng 32(3):207–211. https://doi.org/10.1179/1743294414Y.0000000380

Kumar R, Singh RK, Singh DP, Savu R, Moshkalev SA (2016) Microwave heating time dependent synthesis of various dimensional graphene oxide supported hierarchical ZnO nanostructures and its photoluminescence studies. Mater Des 111:291–300. https://doi.org/10.1016/j.matdes.2016.09.018

Wang Y, Ma J, Xu Q, Zhang J (2017) Fabrication of antibacterial casein-based ZnO nanocomposite for flexible coatings. Mater Des 113:240–245. https://doi.org/10.1016/j.matdes.2016.09.082

Jin Y, Li A, Hazelton SG, Liang S, John CL, Selid PD, Zhao JX (2009) Amorphous silica nanohybrids: synthesis, properties and applications. Coord Chem Rev 253(23–24):2998–3014. https://doi.org/10.1016/j.ccr.2009.06.005

Martín-Jimeno FJ, Suarez-García F, Paredes JI, Martínez-Alonso A, Tascon JMD (2021) Nickel nanoparticle/carbon catalysts derived from a novel aqueous-synthesized metal-organic framework for nitroarene reduction. J Alloys Compd 853:157348. https://doi.org/10.1016/j.jallcom.2020.157348

Lin XZ, Terepka AD, Yang H (2004) Synthesis of silver nanoparticles in a continuous flow tubular microreactor. Nano Lett 4(11):2227–2232. https://doi.org/10.1021/nl0485859

Tsunoyama H, Ichikuni N, Tsukuda T (2008) Microfluidic synthesis and catalytic application of PVP-stabilized, ~ 1 nm gold clusters. Langmuir 24(20):11327–11330. https://doi.org/10.1021/la801372j

Glasnov TN (2013) Highlights from the flow chemistry literature 2013 (part 3). J Flow Chem 3(4):132–140. https://doi.org/10.1556/JFC-D-13-00026

Rogers, S. M. (2017). Designing metal nanoparticles for catalysis (Doctoral dissertation, UCL (University College London). https://core.ac.uk/download/pdf/111015385.pdf

Baumgard J, Vogt AM, Kragl U, Jähnisch K, Steinfeldt N (2013) Application of microstructured devices for continuous synthesis of tailored platinum nanoparticles. Chem Eng J 227:137–144. https://doi.org/10.1016/j.cej.2012.08.066

Woehl TJ, Evans JE, Arslan I, Ristenpart WD, Browning ND (2012) Direct in situ determination of the mechanisms controlling nanoparticle nucleation and growth. ACS Nano 6(10):8599–8610. https://doi.org/10.1021/nn303371y

Demello AJ (2006) Control and detection of chemical reactions in microfluidic systems. Nature 442(7101):394–402. https://doi.org/10.1038/nature05062

Bönnemann H, Richards RM (2001) Nanoscopic metal particles – synthetic methods and potential applications. Eur J Inorg Chem 2001(10):2455–2480. https://doi.org/10.1002/1099-0682(200109)2001:10%3C2455::AID-EJIC2455%3E3.0.CO;2-Z

Polte J, Erler R, Thunemann AF, Sokolov S, Ahner TT, Rademann K, Kraehnert R (2010a) Nucleation and growth of gold nanoparticles studied via in situ small angle X-ray scattering at millisecond time resolution. ACS Nano 4(2):1076–1082. https://doi.org/10.1021/nn901499c

McKenzie LC, Haben PM, Kevan SD, Hutchison JE (2010) Determining nanoparticle size in real time by small-angle X-ray scattering in a microscale flow system. J Phys Chem C 114(50):22055–22063. https://doi.org/10.1021/jp1077533

Polshettiwar V, Cha D, Zhang X, Basset JM (2010) High-surface-area silica nanospheres (KCC-1) with a fibrous morphology. Angew Chem Int Ed 49(50):9652–9656. https://doi.org/10.1002/anie.201003451

Gniewek A, Ziółkowski JJ, Trzeciak AM, Zawadzki M, Grabowska H, Wrzyszcz J (2008) Palladium nanoparticles supported on alumina-based oxides as heterogeneous catalysts of the Suzuki-Miyaura reaction. J Catal 254(1):121–130. https://doi.org/10.1016/j.jcat.2007.12.004

Polte, J., Kraehnert, R., Radtke, M., Reinholz, U., Riesemeier, H., Thünemann, A. F., & Emmerling, F. (2010). New insights of the nucleation and growth process of gold nanoparticles via in situ coupling of SAXS and XANES. In Journal of Physics: Conference Series (Vol. 247, No. 1, p. 012051). IOP Publishing. https://iopscience.iop.org/article/. https://doi.org/10.1088/1742-6596/247/1/012051/pdf

Polte J, Ahner TT, Delissen F, Sokolov S, Emmerling F, Thünemann AF, Kraehnert R (2010c) Mechanism of gold nanoparticle formation in the classical citrate synthesis method derived from coupled in situ XANES and SAXS evaluation. J Am Chem Soc 132(4):1296–1301. https://doi.org/10.1021/ja906506j

Pacioni, N. L., Borsarelli, C. D., Rey, V., & Veglia, A. V. (2015). Synthetic routes for the preparation of silver nanoparticles. In Silver nanoparticle applications (pp. 13–46). Springer, Cham. https://link.springer.com/book/. https://doi.org/10.1007/978-3-319-11262-6

Swathy, B. (2014). A review on metallic silver nanoparticles. IOSR J Pharm, 4(7), 2250–3013. https://iosrphr.org/papers/v4i07/F047038044.pdf

Horikoshi, S., & Serpone, N. (Eds.). (2013). Microwaves in nanoparticle synthesis: fundamentals and applications. John Wiley & Sons. https://books.google.com.sa/books?id=6D2ZC3qjYCoC&printsec=frontcover

Ahmed S, Ahmad M, Swami BL, Ikram S (2016) A review on plants extracts mediated synthesis of silver nanoparticles for antimicrobial applications: a green expertise. J Adv Res 7(1):17–28. https://doi.org/10.1016/j.jare.2015.02.007

Jamkhande PG, Ghule NW, Bamer AH, Kalaskar MG (2019) Metal nanoparticles synthesis: an overview on methods of preparation, advantages and disadvantages, and applications. J Drug Deliv Sci Technol 53:101174. https://doi.org/10.1016/j.jddst.2019.101174

Meyers MA, Mishra A, Benson DJ (2006) Mechanical properties of nanocrystalline materials. Prog Mater Sci 51(4):427–556. https://doi.org/10.1016/j.pmatsci.2005.08.003

Nadagouda MN, Speth TF, Varma RS (2011) Microwave-assisted green synthesis of silver nanostructures. Acc Chem Res 44(7):469–478. https://doi.org/10.1021/ar1001457

Balamurugan S, Philip AJ, Kiruba V, Veluraja K (2015) Simple and efficient way of synthesizing NiO nanoparticles by combustion followed by ball milling method. Nanosci Nanotechnol Lett 7(2):89–93. https://doi.org/10.1166/nnl.2015.1889

Ahmadisoltansaraei K, Moghaddam J (2014) Preparation of NiO nanoparticles from Ni(OH)2·NiCO3·4H2O precursor by mechanical activation. Int J Miner Metall Mater 21(7):726–735. https://doi.org/10.1007/s12613-014-0964-z

Fiss BG, Vu NN, Douglas G, Do TO, Friščić T, Moores A (2020) Solvent-free mechanochemical synthesis of ultrasmall nickel phosphide nanoparticles and their application as a catalyst for the hydrogen evolution reaction (HER). ACS Sustain Chem Eng 8(32):12014–12024. https://doi.org/10.1021/acssuschemeng.0c02762

Tang A, Li X, Zhou Z, Ouyang J, Yang H (2014) Mechanochemical synthesis of Ni (OH) 2 and the decomposition to NiO nanoparticles: thermodynamic and optical spectra. J Alloy Compd 600:204–209. https://doi.org/10.1016/j.jallcom.2014.02.120

Gondal MA, Saleh TA, Drmosh QA (2012) Synthesis of nickel oxide nanoparticles using pulsed laser ablation in liquids and their optical characterization. Appl Surf Sci 258(18):6982–6986. https://doi.org/10.1016/j.apsusc.2012.03.147

Khashan KS, Sulaiman GM, Hamad AH, Abdulameer FA, Hadi A (2017) Generation of NiO nanoparticles via pulsed laser ablation in deionised water and their antibacterial activity. Appl Phys A 123(3):190. https://doi.org/10.1007/s00339-017-0826-4

Mahdi, R. O., Hadi, A. A., Taha, J. M., & Khashan, K. S. (2020, March). Preparation of nickel oxide nanoparticles prepared by laser ablation in water. In AIP Conference Proceedings (Vol. 2213, No. 1, p. 020309). AIP Publishing LLC. https://doi.org/10.1063/5.0000116

Safa M, Dorranian D, Masoudi AA, Matin LF (2019) Characterizing nickel oxide nanostructures produced by laser ablation method: effects of laser fluence. Appl Phys A 125(10):1–9. https://doi.org/10.1007/s00339-019-2986-x

Karpinski A, Ferrec A, Richard-Plouet M, Cattin L, Djouadi MA, Brohan L, Jouan PY (2012) Deposition of nickel oxide by direct current reactive sputtering: effect of oxygen partial pressure. Thin Solid Films 520(9):3609–3613. https://doi.org/10.1016/j.tsf.2011.12.068

Li G, Jiang Y, Deng S, Tam A, Xu P, Wong M, Kwok HS (2017) Overcoming the limitations of sputtered nickel oxide for high-efficiency and large-area perovskite solar cells. Advanced Science 4(12):1700463. https://doi.org/10.1002/advs.201700463

Salunkhe P, Ali AVM, Kekuda D (2020) Investigation on tailoring physical properties of nickel oxide thin films grown by dc magnetron sputtering. Mater Res Express 7(1):016427. https://doi.org/10.1088/2053-1591/ab69c5

Peng, J., Xu, Z., Wang, S., Jie, Q., & Chen, C. (2010). Preparation and performance of nickel oxide films by ion beam sputtering deposition and oxidation annealing. Sensors and Materials, 22(8), 409–416. https://myukk.org/SM2017/sm_pdf/SM820.pdf

Lin CW, Chung WC, Zhang ZD, Hsu MC (2017) P-channel transparent thin-film transistor using physical-vapor-deposited NiO layer. Jpn J Appl Phys 57(1S):01AE01. https://doi.org/10.7567/JJAP.57.01AE01

Moravec, P., Keskinen, H., Jyrki, M. M., Bakardjieva, S., & Levdansky, V. V. (2011). NiO x nanoparticle synthesis by chemical vapor deposition from nickel acetylacetonate. Materials Sciences and Applications, 2(04), 258. https://www.scirp.org/html/4360.html

Napari M, Huq TN, Hoye RL, MacManus-Driscoll JL (2020) Nickel oxide thin films grown by chemical deposition techniques: potential and challenges in next-generation rigid and flexible device applications. InfoMat. https://doi.org/10.1002/inf2.12146

Pooyandeh, S., Shahidi, S., Khajehnezhad, A., & Ghoranneviss, Z. (2020) Synthesizing and deposition of nickel oxide nanoparticles on glass mat using sol–gel method (morphological and magnetic properties) J Text Inst 1–9. https://doi.org/10.1080/00405000.2020.1785606

Shamim, A., Ahmad, Z., Mahmood, S., Ali, U., Mahmood, T., & Ahmad, Z. (2019). Synthesis of nickel nanoparticles by sol-gel method and their characterization. Open J. Chem. 2(1), 16–20. https://pdfs.semanticscholar.org/0c75/3ea0c2700b6f6449f17873f8b713fbec9f7f.pdfhttps://

Zorkipli NNM, Kaus NHM, Mohamad AA (2016) Synthesis of NiO nanoparticles through sol-gel method. Procedia Chemistry 19:626–631. https://doi.org/10.1016/j.proche.2016.03.062

Abboud M, Haija MA, Bel-Hadj-Tahar R, Mubarak AT, Ismail I, Hamdy MS (2020) Highly ordered mesoporous flower-like NiO nanoparticles: synthesis, characterization and photocatalytic performance. New J Chem 44(8):3402–3411. https://doi.org/10.1039/C9NJ04955J

Ebin B (2018) Simple preparation of Ni and NiO nanoparticles using raffinate solution originated from spent NiMH battery recycling. J Inorg Organomet Polym Mater 28(6):2554–2563. https://doi.org/10.1007/s10904-018-0926-4

Bahari Molla Mahaleh, Y., Sadrnezhaad, S. K., & Hosseini, D. (2008). NiO nanoparticles synthesis by chemical precipitation and effect of applied surfactant on distribution of particle sizeJ Nanomater 2008https://doi.org/10.1155/2008/470595

El-Kemary M, Nagy N, El-Mehasseb I (2013) Nickel oxide nanoparticles: synthesis and spectral studies of interactions with glucose. Mater Sci Semicond Process 16(6):1747–1752. https://doi.org/10.1016/j.mssp.2013.05.018

Cao S, Peng L, Han T, Liu B, Zhu D, Zhao C, He S (2020) Hydrothermal synthesis of nanoparticles-assembled NiO microspheres and their sensing properties. Physica E 118: 113655. https://doi.org/10.1016/j.physe.2019.113655

Zhou Q, Lu Z, Wei Z, Xu L, Gui Y, Chen W (2018) Hydrothermal synthesis of hierarchical ultrathin NiO nanoflakes for high-performance CH4 sensing. Front Chem 6:194. https://doi.org/10.3389/fchem.2018.00194

Ahire, D. V., Patil, G. E., Jain, G. H., & Gaikwad, V. B. (2012, December). Synthesis of nanostructured NiO by hydrothermal route and its gas sensing properties. In 2012 Sixth International Conference on Sensing Technology (ICST) (pp. 136–141). IEEE. https://doi.org/10.1109/ICSensT.2012.6461656

Gu Y, Sun S, Liu Y, Dong M, Yang Q (2019) Solvent effect on the solvothermal synthesis of mesoporous NiO catalysts for activation of peroxymonosulfate to degrade organic dyes. ACS Omega 4(18):17672–17683. https://doi.org/10.1021/acsomega.9b01883

Beach ER, Shqau K, Brown SE, Rozeveld SJ, Morris PA (2009) Solvothermal synthesis of crystalline nickel oxide nanoparticles. Mater Chem Phys 115(1):371–377. https://doi.org/10.1016/j.matchemphys.2008.12.018

Ukoba KO, Eloka-Eboka AC, Inambao FL (2018) Review of nanostructured NiO thin film deposition using the spray pyrolysis technique. Renew Sustain Energy Rev 82:2900–2915. https://doi.org/10.1016/j.rser.2017.10.041

Desai JD (2016) Nickel oxide thin films by spray pyrolysis. J Mater Sci Mater Electron 27(12):12329–12334. https://doi.org/10.1007/s10854-016-5617-8

Dillon F, Copley M, Koós AA, Bishop P, Grobert N (2013) Flame spray pyrolysis generated transition metal oxide nanoparticles as catalysts for the growth of carbon nanotubes. RSC Adv 3(43):20040–20045. https://doi.org/10.1039/C3RA40773J

Seo DJ, Park SB, Kang YC, Choy KL (2003) Formation of ZnO, MgO and NiO nanoparticles from aqueous droplets in flame reactor. J Nanopart Res 5(3):199–210. https://doi.org/10.1023/A:1025563031595

Salvadori MR, Ando RA, Oller Nascimento CA, Corrêa B (2015) Extra and intracellular synthesis of nickel oxide nanoparticles mediated by dead fungal biomass. PLoS ONE 10(6): e0129799. https://doi.org/10.1371/journal.pone.0129799

Yang P, Gu H, Zhao Z, Wang W, Cao B, Lai C, Wang X (2014) Angiotensin-converting enzyme 2 (ACE2) mediates influenza H7N9 virus-induced acute lung injury. Sci Rep 4(1):1–6. https://doi.org/10.1038/srep07027

Habtemariam AB, Oumer M (2020) Plant extract mediated synthesis of nickel oxide nanoparticles. Mater Int 2:205–209. https://doi.org/10.33263/Materials22.205209

Z Sabouri N Fereydouni A Akbari HA Hosseini A Hashemzadeh MS Amiri M Darroudi 2019 Plant-based synthesis of NiO nanoparticles using salvia macrosiphon Boiss extract and examination of their water treatment Rare Met 1–11 https://doi.org/10.1007/s12598-019-01333-z

Helan V, Prince JJ, Al-Dhabi NA, Arasu MV, Ayeshamariam A, Madhumitha G, Jayachandran M (2016) Neem leaves mediated preparation of NiO nanoparticles and its magnetization, coercivity and antibacterial analysis. Results Phys 6:712–718. https://doi.org/10.1016/j.rinp.2016.10.005

Ramalingam R, Fazil MHUT, Verma NK, Arunachalam KD (2019) Green synthesis, characterization and antibacterial evaluation of electrospun nickel oxide nanofibers. Mater Lett 256:126616. https://doi.org/10.1016/j.matlet.2019.126616

Zhang Y, Xiao X, Sun Y, Shi Y, Dai H, Ni P, Wang L (2013) Electrochemical deposition of nickel nanoparticles on reduced graphene oxide film for nonenzymatic glucose sensing. Electroanalysis 25(4):959–966. https://doi.org/10.1002/elan.201200479

Moghaddam AB, Ganjali MR, Saboury AA, Moosavi-Movahedi AA, Norouzi P (2008) Electrodeposition of nickel oxide nanoparticles on glassy carbon surfaces: application to the direct electron transfer of tyrosinase. J Appl Electrochem 38(9):1233–1239. https://doi.org/10.1007/s10800-008-9541-3

Azhagu Raj R, AlSalhi MS, Devanesan S (2017) Microwave-assisted synthesis of nickel oxide nanoparticles using Coriandrum sativum leaf extract and their structural-magnetic catalytic properties. Materials 10(5):460. https://doi.org/10.3390/ma10050460

Jena, A., & Shivashankar, S. A. (2008, October). Microwave-assisted synthesis of NiO nanoparticles. In AIP Conference Proceedings (Vol. 1063, No. 1, pp. 211–216). American Institute of Physics. https://doi.org/10.1063/1.3027161

Vargas E, Romero-Sáez M, Denardin JC, Gracia F (2016) The ultrasound-assisted synthesis of effective monodisperse nickel nanoparticles: magnetic characterization and its catalytic activity in CO2 methanation. New J Chem 40(9):7307–7310. https://doi.org/10.1039/C6NJ01574C

A Alshammari VN Kalevaru 2016 Supported gold nanoparticles as promising catalysts Catalytic Application of Nano-Gold Catalysts 57–81

Barhoum A, Van Assche G, Rahier H, Fleisch M, Bals S, Delplancked MP, Bahnemann D (2017) Sol-gel hot injection synthesis of ZnO nanoparticles into a porous silica matrix and reaction mechanism. Mater Des 119:270–276. https://doi.org/10.1016/j.matdes.2017.01.059

Badari CA, Lónyi F, Drotár E, Kaszonyi A, Valyon J (2015) A study of the hydrodenitrogenation of propylamine over supported nickel phosphide catalysts using amorphous and nanostructured silica supports. Appl Catal B 164:48–60. https://doi.org/10.1016/j.apcatb.2014.09.001

Rudko, G. Y., Kovalenko, S. A., Gule, E. G., Bobyk, V. V., Solomakha, V. M., & Bogoslovskaya, A. B. (2015). Zinc oxide nanoparticles fabricated in the porous silica matrix by the sublimation method. Semiconductor physics quantum electronics & optoelectronics, (18, № 1), 20–25. https://dspace.nbuv.gov.ua/handle/123456789/119991

Ashik UPM, Daud WW (2015) Probing the differential methane decomposition behaviors of n-Ni/SiO2, n-Fe/SiO2 and n-Co/SiO2 catalysts prepared by co-precipitation cum modified Stöber method. RSC Adv 5(82):67227–67241. https://doi.org/10.1039/C5RA10997C

Corma A (1997) From microporous to mesoporous molecular sieve materials and their use in catalysis. Chem Rev 97(6): 2373–2420. https://doi.org/10.1021/cr960406n

Vadia, N., Desai, D., & Rajput, S. (2013). Hydrothermal treatment and mesoporosity of MCM-41 mesoporous nanocomposite. Journal of Applied Pharmaceutical Science, 3(3), 24. https://japsonline.com/admin/php/uploads/812_pdf.pdf

Look DC, Claflin B (2004) P-type doping and devices based on ZnO. Physica Status Solidi (b) 241(3):624–630. https://doi.org/10.1002/pssb.200304271

Rioux, R. (2010). Model Systems in Catalysis. Springer, Ed. 1, New York, NY. pp XIX, 526. https://doi.org/10.1007/978-0-387-98049-2

Rodríguez JA, Garcia MF (2007) The world of oxide nanomaterials. John Wiley & Sons Inc, Hoboken, NJ, p 15

Penner S (2014) Pure and mixed-oxide thin film model systems grown on sodium chloride templates for structural and catalytic studies. Thin Solid Films 562:1–15. https://doi.org/10.1016/j.tsf.2014.03.001

Finiels A, Fajula F, Hulea V (2014) Nickel-based solid catalysts for ethylene oligomerization–a review. Catal Sci Technol 4(8):2412–2426. https://doi.org/10.1039/C4CY00305E

Schubert, U., & Hüsing, N. (2005). Synthesis of inorganic materials, 2nd. Synthesis of Inorganic Materials, 429.

Ozin, G. A., Arsenault, A. C., & Cademartiri, L. (2009). Nanocrystal synthesis and self-assembly. Nanochemistry: A Chemical Approach to Nanomaterials, 335. https://books.google.com.sa/books?id=CdrUwo3HvPwC&printsec=frontcover

Frey AS, Hinrichsen O (2012) Comparison of differently synthesized Ni (Al) MCM-48 catalysts in the ethene to propene reaction. Microporous Mesoporous Mater 164:164–171. https://doi.org/10.1016/j.micromeso.2012.07.015

S He L Zhang S He L Mo X Zheng H Wang Y Luo 2015 Ni/SiO2 catalyst prepared with nickel nitrate precursor for combination of CO2 reforming and partial oxidation of methane: characterization and deactivation mechanism investigation J Nanomater 2015https://doi.org/10.1155/2015/659402

Nakagawa Y, Nakazawa H, Watanabe H, Tomishige K (2012) Total hydrogenation of furfural over a silica-supported nickel catalyst prepared by the reduction of a nickel nitrate precursor. ChemCatChem 4(11):1791–1797. https://doi.org/10.1002/cctc.201200218

Yao T, Sun Z, Li Y, Pan Z, Wei H, Xie Y, Wei S (2010) Insights into initial kinetic nucleation of gold nanocrystals. J Am Chem Soc 132(22):7696–7701. https://doi.org/10.1021/ja101101d

Zhao K, Hu Y, Tian Y, Chen D, Feng Y (2020) Chlorine removal from MSWI fly ash by thermal treatment: effects of iron/aluminum additives. J Environ Sci 88:112–121. https://doi.org/10.1016/j.jes.2019.08.006

Spagnolo S, Spolaore M, Dalla Palma M, Pasqualotto R, Sartori E, Serianni G, Veltri P (2016) Preliminary design of electrostatic sensors for MITICA beam line components. Rev Sci Instrum 87(2):02B931. https://doi.org/10.1063/1.4935612

Bianchi CL, Canton P, Dimitratos N, Porta F, Prati L (2005) Selective oxidation of glycerol with oxygen using mono and bimetallic catalysts based on Au, Pd and Pt metals. Catal Today 102:203–212. https://doi.org/10.1016/j.cattod.2005.02.003

Patil GA, Bari ML, Bhanvase BA, Ganvir V, Mishra S, Sonawane SH (2012) Continuous synthesis of functional silver nanoparticles using microreactor: effect of surfactant and process parameters. Chem Eng Process 62:69–77. https://doi.org/10.1016/j.cep.2012.09.007

Mehrabadi BA, Eskandari S, Khan U, White RD, Regalbuto JR (2017) A review of preparation methods for supported metal catalysts. Adv Catal 61:1–35. https://doi.org/10.1016/bs.acat.2017.10.001

Kennedy J, Jones W, Morgan DJ, Bowker M, Lu L, Kiely CJ, Dimitratos N (2015) Photocatalytic hydrogen production by reforming of methanol using Au/TiO2, Ag/TiO2 and Au-Ag/TiO2 catalysts. Catal Struct React 1(1):35–43. https://doi.org/10.1179/2055075814Y.0000000006

Jia CJ, Schüth F (2011) Colloidal metal nanoparticles as a component of designed catalyst. Phys Chem Chem Phys 13(7):2457–2487. https://doi.org/10.1039/C0CP02680H

Yoshida, H., Nonoyama, S., Yazawa, Y., & Hattori, T. (2005). Quantitative determination of platinum oxidation state by XANES analysis. Physica Scripta, 2005(T115), 813. https://iopscience.iop.org/article/. https://doi.org/10.1238/Physica.Topical.115a00813/meta

Chen S, Yang Q, Wang H, Zhang S, Li J, Wang Y, Song L (2015) Initial reaction mechanism of platinum nanoparticle in methanol–water system and the anomalous catalytic effect of water. Nano Lett 15(9):5961–5968. https://doi.org/10.1021/acs.nanolett.5b02098

Zhou QF, Bao JC, Xu Z (2002) Shape-controlled synthesis of nanostructured gold by a protection–reduction technique. J Mater Chem 12(2):384–387. https://doi.org/10.1039/B103767F

Paulose R, Mohan R, Parihar V (2017) Nanostructured nickel oxide and its electrochemical behaviour—a brief review. Nano-Struct Nano-Objects 11:102–111

Abboud M (2020) Immediate epoxidation of cyclohexene at room temperature using mesoporous flower-like NiO nanoparticles. RKM Cat 131:781–792. https://doi.org/10.1007/s11144-020-01864-y

Behnajady MA, Bimeghdar S (2014) Synthesis of mesoporous NiO nanoparticles and their application in the adsorption of Cr(VI). Chem Eng J 239:105–113. https://doi.org/10.1016/j.cej.2013.10.102

Sahlabji T, Abboud M, Bel-Hadj-Tahar R, Hamdy MS (2020) Spontaneous epoxidation of styrene catalyzed by flower-like NiO nanoparticles under ambient conditions. J Nanopart Res 22(12):1–10. https://doi.org/10.1007/s11051-020-05098-w

Nasseri MA, Ahrari F, Zakerinasab B (2015a) Nickel oxide nanoparticles: a green and recyclable catalytic system for the synthesis of diindolyloxindole derivatives in aqueous medium. RSC Adv 5(18):13901–13905. https://doi.org/10.1039/C4RA14551H

Nasseri MA, Kamali F, Zakerinasab B (2015b) Catalytic activity of reusable nickel oxide nanoparticles in the synthesis of spirooxindoles. RSC Adv 5(34):26517–26520. https://doi.org/10.1039/C5RA02825F

Arrigo R, Gallarati S, Schuster ME, Seymour J, Gianolio D, da Silva I, Held G (2020) Influence of synthesis conditions on the structure of nickel nanoparticles and their reactivity in selective asymmetric hydrogenation. ChemCatChem 12(5):1491–1503. https://doi.org/10.1002/cctc.201901955

Bashir AKH, Razanamahandry LC, Nwanya AC, Kaviyarasu K, Saban W, Mohamed HEA, Maaza M (2019) Biosynthesis of NiO nanoparticles for photodegradation of free cyanide solutions under ultraviolet light. J Phys Chem Solids 134:133–140. https://doi.org/10.1016/j.jpcs.2019.05.048

Amin MH (2020) Relationship between the pore structure of mesoporous silica supports and the activity of nickel

nanocatalysts in the CO2 reforming of methane. Catalysts 10(1):51. https://doi.org/10.3390/catal10010051

Weiping, C., & Lide, Z. (1997). Synthesis and structural and optical properties of mesoporous silica containing silver nanoparticles. Journal of Physics: Condensed Matter, 9(34), 7257. https://iopscience.iop.org/article/. https://doi.org/10.1088/0953-8984/9/34/015/meta

Lai, C. Y. (2013). Mesoporous silica nanomaterials applications in catalysis. J Thermodyn Catal, 5(1), 1000e124. https://www.longdom.org/open-access/mesoporous-silica-nanomaterials-applications-in-catalysis-2157-7544.1000e124.pdf

Dixit M, Mishra M, Joshi PA, Shah DO (2013) Study on the catalytic properties of silica supported copper catalysts. Procedia Engineering 51:467–472. https://doi.org/10.1016/j.proeng.2013.01.066

Luque R, Balu AM, Campelo JM, Gracia MD, Losada E, Pineda A, Serrano-Ruiz JC (2012) Catalytic applications of mesoporous silica-based materials. Catalysis 24:253–280. https://doi.org/10.1039/9781849734776-00253

Jadhav KS, Dumbare PS, Pande VV (2015) Mesoporous silica nanoparticles (MSN): a nanonetwork and hierarchical structure in drug delivery. J Nanomed Res 2(5):1–8. https://doi.org/10.15406/jnmr.2015.02.00043

Baharudin KB, Taufiq-Yap YH, Hunns J, Isaacs M, Wilson K, Derawi D (2019) Mesoporous NiO/Al-SBA-15 catalysts for solvent-free deoxygenation of palm fatty acid distillate. Microporous Mesoporous Mater 276:13–22. https://doi.org/10.1016/j.micromeso.2018.09.014

Baktash E, Littlewood P, Pfrommer J, Schomäcker R, Driess M, Thomas A (2015) Controlled formation of nickel oxide nanoparticles on mesoporous silica using molecular Ni4O4 clusters as precursors: enhanced catalytic performance for dry reforming of methane. ChemCatChem 7(8):1280–1284. https://doi.org/10.1002/cctc.201402983

Lu B, Ju Y, Kawamoto K (2014) Conversion of producer gas using NiO/SBA-15 obtained with different synthesis methods. Int J Coal Sci Technol 1(3):315–320. https://doi.org/10.1007/s40789-014-0037-y

Ahmed RA, Pang YX, Olea M, Hodgson SNB (2012) Preparation and structural characterisation of SBA-15 supported nickel catalysts via sol-gel nickel oxide coatings for dry reforming of methane. WIT Trans Eng Sci 81:71–82

Liu D, Quek XY, Wah HHA, Zeng G, Li Y, Yang Y (2009) Carbon dioxide reforming of methane over nickel-grafted SBA-15 and MCM-41 catalysts. Catal Today 148(3–4):243–250. https://doi.org/10.1016/j.cattod.2009.08.014

Schumacher K, Ravikovitch PI, Du Chesne A, Neimark AV, Unger KK (2000) Characterization of MCM-48 materials. Langmuir 16(10):4648–4654. https://doi.org/10.1021/la991595i

Roosta Z, Izadbakhsh A, Sanati AM, Osfouri S (2018) Synthesis and evaluation of NiO@ MCM-41 core–shell nanocomposite in the CO 2 reforming of methane. J Porous Mater 25(4):1135–1145. https://doi.org/10.1007/s10934-017-0525-8

Zhang Q, Zhang T, Shi Y, Zhao B, Wang M, Liu Q, Wang J, Long K, Duan Y, Ning P (2017) A sintering and carbon-resistant Ni-SBA-15 catalyst prepared by solid-state grinding method for dry reforming of methane. J CO2 Utilization 17:10–19. https://doi.org/10.1016/j.jcou.2016.11.002

Zhang J, Li F (2015) Coke-resistant Ni@ SiO_2 catalyst for dry reforming of methane. Appl Catal B 176:513–521. https://doi.org/10.1016/j.apcatb.2015.04.039

Kresge CT, Leonowicz ME, Roth WJ, Vartuli JC, Beck JS (1992) Ordered mesoporous molecular sieves synthesized by a liquid-crystal template mechanism. Nature 359(6397):710–712. https://doi.org/10.1038/359710a0

Mokri, N. A., Ching, O. P., Mukhtar, H., & Leng, C. T. (2019). Tailoring Particle Size and Agglomeration State of Mesoporous MCM-48 via Optimisation of Sol-gel Silica Process. Journal of Physical Science, 30(1). https://doi.org/10.21315/jps2019.30.1.11

M Shaban A Hamd RR Amin MR Abukhadra AA Khalek AAP Khan AM Asiri 2020 Preparation and characterization of MCM-48/nickel oxide composite as an efficient and reusable catalyst for the assessment of photocatalytic activity Environ Sci Pollut Res 1–13. https://doi.org/10.1007/s11356-020-09431-7

Jansen JC, Shan Z, Marchese L, Zhou W, Puil N v d, Maschmeyer T (2001) A new templating method for three-dimensional mesopore networks. Chem Comm 8:713–714. https://doi.org/10.1039/B101000J

Telalović S, Ramanathan A, Mul G, Hanefeld U (2010) TUD-1: synthesis and application of a versatile catalyst, carrier, material. J Mater Chem 20(4):642–658. https://doi.org/10.1039/B904193A

Gorsd MN, Sosa AA, Frenzel RA, Pizzio LR (2018) Synthesis and characterization of tungstophosphoric acid-modified mesoporous sponge-like TUD-1 materials. J Sol-Gel Sci Technol 87(1):204–215. https://doi.org/10.1007/s10971-018-4677-z

Tanglumlert W, Yang ST, Jeong KE, Jeong SY, Ahn WS (2011) Facile synthesis of Ti-TUD-1 for catalytic oxidative desulfurization of model sulfur compounds. Res Chem Intermed 37(9):1267–1273. https://doi.org/10.1007/s11164-011-0393-9

Quek XY, Liu D, Cheo WNE, Wang H, Chen Y, Yang Y (2010) Nickel-grafted TUD-1 mesoporous catalysts for carbon dioxide reforming of methane. Appl Catal B 95(3–4):374–382. https://doi.org/10.1016/j.apcatb.2010.01.016

Mallesham B, Sudarsanam P, Venkata Shiva Reddy B, Govinda Rao B, Reddy BM (2018) Nanostructured nickel/silica catalysts for continuous flow conversion of levulinic acid to γ-valerolactone. ACS omega 3(12):16839–16849. https://doi.org/10.1021/acsomega.8b02008

Shi P, Liu CJ (2009) Characterization of silica supported nickel catalyst for methanation with improved activity by room temperature plasma treatment. Catal Lett 133(1):112–118. https://doi.org/10.1007/s10562-009-0163-0

Pandey PC, Mitra MD, Tiwari AK, Singh S (2021) Synthetic incorporation of palladium-nickel bimetallic nanoparticles within mesoporous silica/silica nanoparticles as efficient and cheaper catalyst for both cationic and anionic dyes degradation. J Environ Sci Health A 56(4):460–472. https://doi.org/10.1080/10934529.2021.1886793

Article

Efficient Oxidation of Cyclohexane over Bulk Nickel Oxide under Mild Conditions

Reem S. Alnefaie, Mohamed Abboud * , **Abdullah Alhanash** and **Mohamed S. Hamdy**

Catalysis Research Group, Chemistry Department, College of Science, King Khalid University, Abha 61413, Saudi Arabia; 438800026@kku.edu.sa (R.S.A.); alhnsh@kku.edu.sa (A.A.); mhsaad@kku.edu.sa (M.S.H.)

* Correspondence: abboud_med@yahoo.fr or mabboud@kku.edu.sa; Tel.: +966-53-48-46-782

Abstract: Nickel oxide powder was prepared by simple calcination of nickel nitrate hexahydrate at 500 °C for 5 h and used as a catalyst for the oxidation of cyclohexane to produce the cyclohexanone and cyclohexanol—KA oil. Molecular oxygen (O_2), hydrogen peroxide (H_2O_2), t-butyl hydrogen peroxide (TBHP) and *meta*-chloroperoxybenzoic acid (*m*-CPBA) were evaluated as oxidizing agents under different conditions. *m*-CPBA exhibited higher catalytic activity compared to other oxidants. Using 1.5 equivalent of *m*-CPBA as an oxygen donor agent for 24 h at 70 °C, in acetonitrile as a solvent, NiO powder showed exceptional catalytic activity for the oxidation of cyclohexane to produce KA oil. Compared to different catalytic systems reported in the literature, for the first time, about 85% of cyclohexane was converted to products, with 99% KA oil selectivity, including around 87% and 13% selectivity toward cyclohexanone and cyclohexanol, respectively. The reusability of NiO catalyst was also investigated. During four successive cycles, the conversion of cyclohexane and the selectivity toward cyclohexanone were decreased progressively to 63% and 60%, respectively, while the selectivity toward cyclohexanol was increased gradually to 40%.

Keywords: bulk nickel oxide; cyclohexane oxidation; *m*-CPBA; KA oil; mild conditions

1. Introduction

The oxidation of cyclohexane is an important industrial chemical reaction. The oxidation of cyclohexane affords cyclohexanol and cyclohexanone, which are together known as ketone–alcohol (KA) oil, the main feedstock for the production of nylon 6,6 fibers (Figure 1). The further oxidation of KA oil by nitric acid led to the formation of adipic acid, which is a key monomer for the preparation of very important polymers such as nylon 6,6 [1]. In addition, adipic acid is an important synthetic intermediate in the chemical industry [2,3].
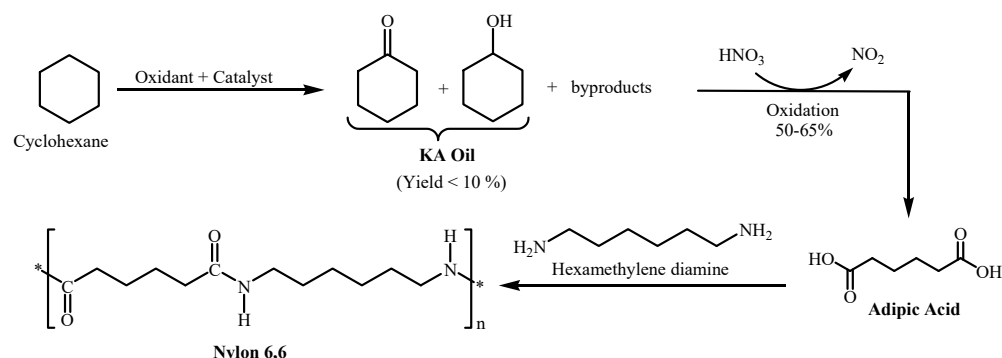

Figure 1. Synthesis pathway of nylon 6,6 from cyclohexane.

The current industrial process for the oxidation of cyclohexane to produce KA oil involves the utilization of cobalt or manganese salts as homogenous catalysts. The operating

conditions consist of high temperature (150–160 °C) and high pressure (10–20 atm) of air or molecular oxygen (O_2) due to the stable nature of the cyclohexane. However, since the desired products, cyclohexanol and cyclohexanone, are less stable than the starting material, cyclohexane, many by-products are formed during the oxidation of cyclohexane at high temperature and pressure. Thus, at high conversion of cyclohexane, the KA oil can be formed with low selectivity, which makes the purification of KA oil difficult with a high-cost process, in addition to the major issue of the regeneration and reutilization of the homogeneous catalysts. Therefore, the commercial processes usually operate at a low cyclohexane conversion of about 4–6% to maintain the high selectivity of KA oil at 70–85% [4].

To improve the process for the oxidation of cyclohexane, the heterogeneous catalysts have been considered as good alternatives to improve the cyclohexane conversion while maintaining high KA oil selectivity and minimizing the catalyst utilization and separation costs.

Therefore, many heterogeneous catalytic systems have been developed during the last two decades. Various supported metal catalysts were prepared, such as metal transition Au, Ti, Ag, Co, Mo, Fe, Mn, Cr, and V, and even lanthanides such as La, Ce, Sm, Dy, Y, and Gd, using different type of supports such as silica, alumina, zeolites, graphite, and aluminophosphates (AlPo) [5]. Air was the preferred oxidant due to its low cost, along with other oxidants such as molecular oxygen (O_2), hydrogen peroxide (H_2O_2), and t-butyl hydrogen peroxide (TBHP). However, the utilization of H_2O_2 and TBHP is not industrially viable due to their high cost compared to air and O_2. Thus, higher attention has been paid to the liquid phase process using O_2 as an oxidation agent.

The high dispersion of some transition metals in high surface-area supports, such as gold nanoparticles in mesoporous silica, exhibited relatively effective oxidation of cyclohexane. Xu et al. [4] reported the utilization of silica-supported gold catalyst doped with titania under air at high temperature (150 °C) and high pressure (1.5 MPa) to convert the cyclohexane to KA oil. However, the highest conversion was 9.2% with 82.6 selectivity. Similar results (10–13% conversion, 84–87% selectivity) were obtained by Xu and coworkers when gold was supported on alumina (Au/Al_2O_3) under similar conditions, using the molecular oxygen as an oxidant [6]. Better results (16.6% conversion, 92.4% selectivity) were obtained with highly dispersed gold nanoparticles on functionalized SBA-15 mesoporous silica, using molecular oxygen under similar conditions (150 °C, 1 MPa) [7]. Similar results (16.9% conversion, 93% selectivity) were obtained by Wang et al. [8] when bismuth-containing SBA-15 (Bi-SBA-15) was used as catalyst, with molecular oxygen as oxygen donor.

However, when supported gold was used in mild conditions, both conversion and selectivity decreased. For example, when Enache et al. used graphite-supported gold under mild conditions (70 °C, 1 atm) the conversion (2–7%) and selectivity (10–23%) were very low [9]. However, all of these catalytic systems still suffer from low cyclohexane conversion, expensive and complicated synthesis of the catalyst, and high-cost processes. Hence, the selective oxidation of cyclohexane with high conversion in mild conditions is still a challenge. Therefore, there is still great interest among industry and academia for the development of simple, low-cost, reusable and efficient heterogeneous catalytic systems.

One of the most promising transition metals is nickel. Due to its relative abundance, nickel is more cost-effective than most metals as a catalyst [10]. Numerous research efforts have been recently devoted to the preparation of nickel particles with tailored features, because of their unique electronic, optical, and mechanical properties and their widespread potential applications in many fields including catalysis, electronics, optoelectronics, adsorption of dyes from industrial water, development of supercapacitors, fabrication of dye-sensitized solar cells and sensors, and biomedical applications [11–32].

Due to their unique magnetic, chemical, and physical properties, we believe that Ni particles will gain more attention in future in various technological fields such as catalysis, battery manufacture, dye-sensitized solar cells, enhanced pseudo-capacitance, and drug delivery.

Recently, Ni-based heterogeneous catalysts have been employed for various organic transformations such as hydrogenation reactions of aromatics [33], oxidation of hydrocarbons [34–36], production of synthesis gas [37], steam reforming [38], methanation [39], isomerization of hydrocarbons [40], hydrocracking [41], etc. [42–44]. Ni is considered as a promising catalyst because it is eco-friendly, inexpensive, easy to prepare, and easily recoverable and recyclable.

In this work, we report a very simple and highly efficient nickel-based heterogeneous catalytic system for the oxidation of cyclohexane to KA oil. Surprisingly, the utilization of bulk nickel oxide as a catalyst with *meta*-chloroperoxybenzoic acid (*m*-CPBA) as oxidant in mild conditions allowed us to quantitively convert cyclohexane to KA oil with 99% selectivity.

2. Results

2.1. Characterization of Bulk NiO

The prepared bulk NiO was characterized by SEM, EDX, XRD and TGA.

SEM images (Figure 2) show aggregated microparticles of nickel oxide particles forming worm-like shapes. The particle size distribution was measured using ImageJ software, and the obtained results are presented in Figure 3. The average NiO particles size was found to be around 148 nm.
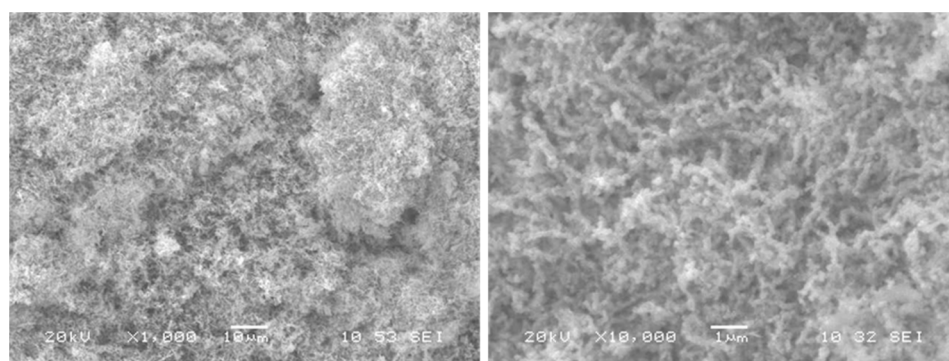
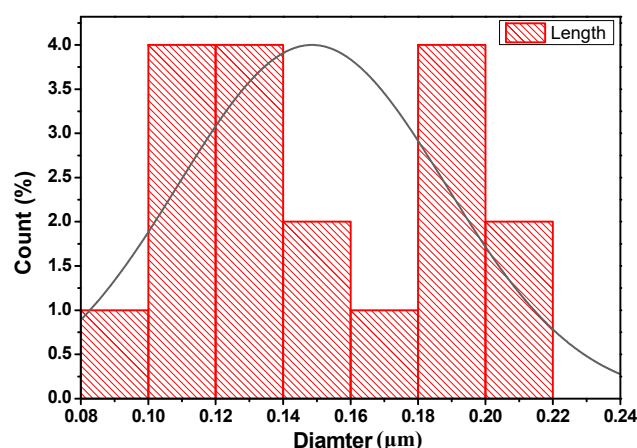**Figure 2.** SEM pictures of NiO powder.

Figure 3. Particle diameter distribution in NiO catalyst.

The prepared NiO was also studied by EDX. Figure 4 shows the EDX spectrum of NiO particles. Ni and O peaks were clearly observed, and the [Ni]/[O] ratio was 1.13, which is consistent with NiO molecular structure.
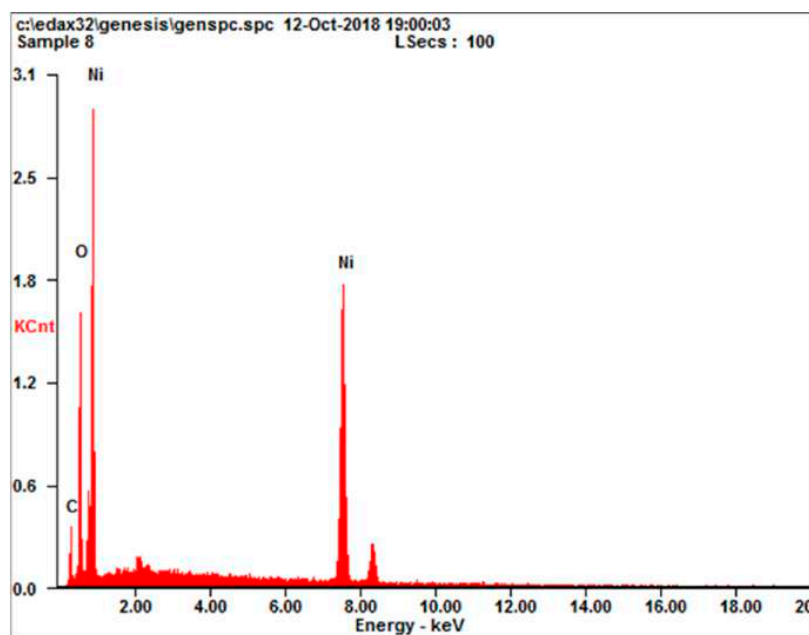
Figure 4. EDX spectra of NiO powder.

Powder XRD analysis was used to identify the synthesized NiO powder (Figure 5). The XRD pattern shows the principal peaks of NiO, which were observed at $2\theta = 37.31°$, $43.41°$, $62.87°$, $75.53°$, and $79.46°$ and assigned to the (111), (200), (220), (311), and (222) planes, respectively [45]. This confirmed the formation of pure NiO particles [46,47].
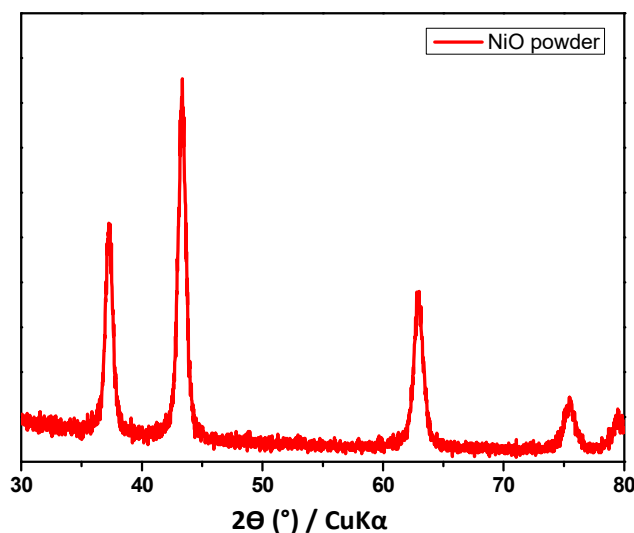

Figure 5. XRD pattern of NiO powder.

Figure 6 illustrates the thermal decomposition patterns of nickel nitrate hexahydrate precursors under air. The thermogram of $Ni(NO_3)_2 \cdot 6H_2O$ can be divided into three segments. The first region from 25 °C to 250 °C with low weight loss of about 2 wt.% corresponds to the elimination of residual solvents and physically absorbed water. The second segment from 250 °C to 440 °C, with rapid weight loss of about 28%, is related to water separation and decomposition of $Ni(NO_3)_2$ and formation of NiO.
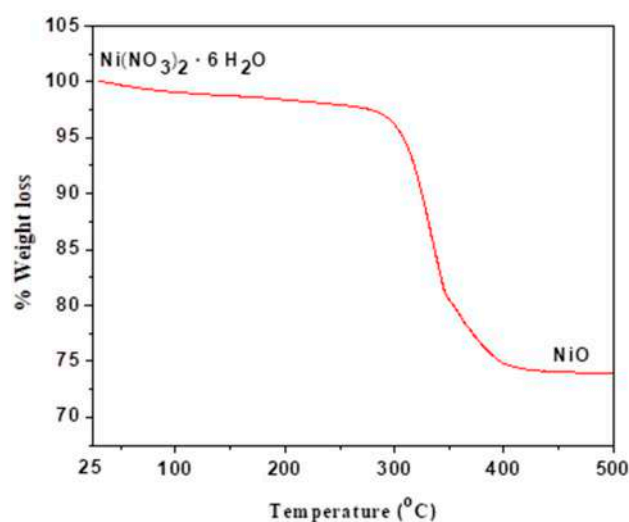
Figure 6. TGA thermogram of the decomposition of nickel nitrate hexahydrate under air.

2.2. The Oxidation of Cyclohexane over NiO Powder

2.2.1. Effect of Oxidant

The selective oxidation of cyclohexane in the presence of NiO as a catalyst was investigated together with the liquid-phase oxidation by using different oxidants at 70 °C for 24 h, and the obtained results are presented in Figure 7. When molecular oxygen was used as an oxidant, only 2.4% of cyclohexane was converted to the oxidized products: cyclohexanone (60%) and cyclohexanol (40%). The use of liquid-phase oxidation in the presence of H_2O_2 and TBHP did not improve the conversion of cyclohexane, and only 2.5% and 3.1% of KA oil was obtained, respectively. A dramatic increase in cyclohexane oxidation was obtained in the liquid-phase system when *m*-CBPA was applied as an oxidant; 84.8% of cyclohexane was oxidized to 99% KA oil, with 87.4% and 12.6% selectivity towards cyclohexanone and cyclohexanol, respectively. The obtained results clearly show that the catalytic activity of NiO can be severely improved by using a suitable oxidant such as *m*-CBPA.
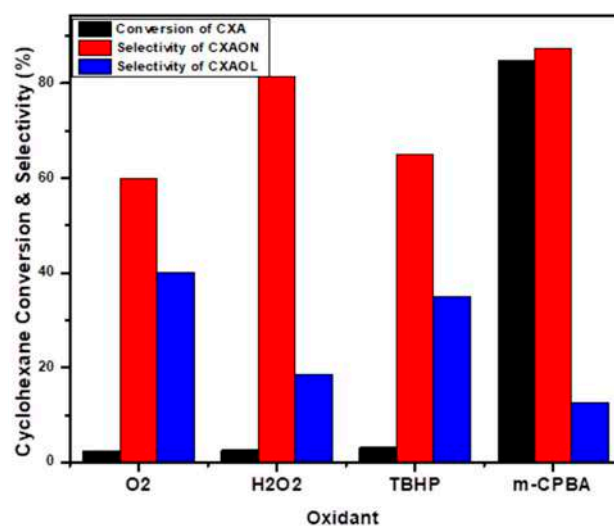

Figure 7. Oxidation of cyclohexane using different types of oxidants.

2.2.2. Effect of Reaction Temperature

The selective oxidation of cyclohexane by using NiO powder as a catalyst and *m*-CBPA as an oxidant was investigated under different applied temperatures: 25, 40, 60 and 70 °C. The obtained results are presented in Figure 8, which shows that an almost

negligible amount of cyclohexane was oxidized at room temperature, and less than 5% conversion was obtained at 40 °C or 60 °C. However, the best results were observed at 70 °C, with 84.8% cyclohexane conversion, with 99% KA selectivity and 87.4% selectivity towards cyclohexanone.
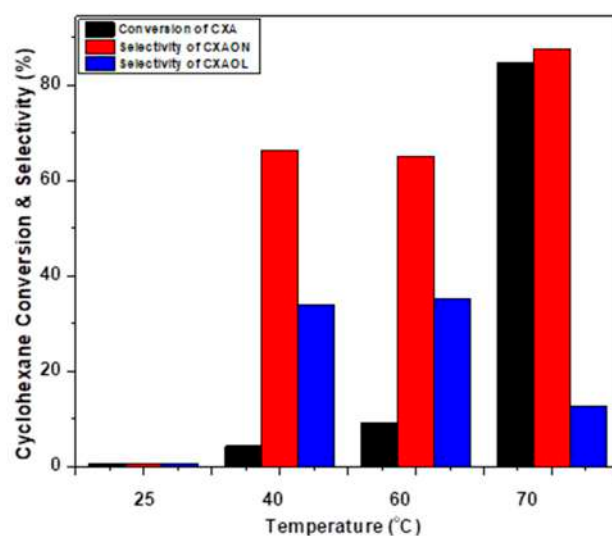

Figure 8. The oxidation of cyclohexane by *m*-CPBA for 24 h using different temperatures.

2.2.3. Effect of Reaction Time

The selective oxidation of cyclohexane using NiO as a catalyst and *m*-CPBA as an oxidant was studied at different reaction times at 70 °C. The obtained results are plotted in Figure 9. After 4 h of the reaction, less than 5% conversion of cyclohexane was obtained. More importantly, the selectivity of cyclohexanol was found to be decreased, while the selectivity of cyclohexanone increased, which means that *m*-CPBA could also oxidize cyclohexanol to cyclohexanone. The obtained results confirm the relatively long life of the oxidant with high ability to oxidize cyclohexane during the entire reaction time. Moreover, *m*-CPBA was not only active in the oxidation of cyclohexane, but also more selective towards cyclohexanone. The best results were obtained after 24 h with around 85% conversion, 99% KA oil selectivity, with 87% of cyclohexanone and 12% of cyclohexanol.
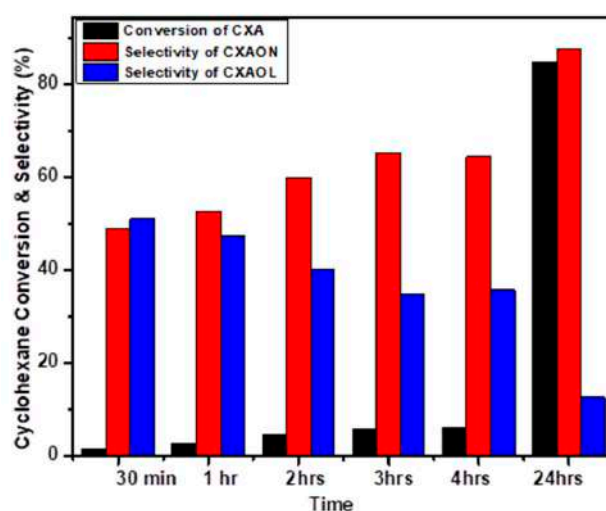

Figure 9. Effect of reaction time on the oxidation of cyclohexane over NiO powder, using *m*-CPBA, T = 70 °C, time: 30 min–24 h.

2.2.4. Effect of Catalyst Amount

The catalyst amount was optimized in order to achieve the best substrate/catalyst ratio. Several amounts of NiO were used in separate experiments to oxidize cyclohexane at 70 °C for 24 h in the presence of 1.5 eq of *m*-CPBA as an oxidant. The obtained results are presented in Figure 10. The conversion of cyclohexane was found to be increased by increasing the amount of NiO catalyst, while the amount of the produced cyclohexanol was found to be decreased. The best result was obtained when 50 mg of bulk NiO was applied, and no significant change was observed when the NiO dose was increased to 100 mg. It should be noted that the reaction proceeded without NiO catalyst and in the presence of *m*-CPBA. However, the conversion of cyclohexane to KA oil was very low, about 7.3%, which shows the importance of the catalyst.
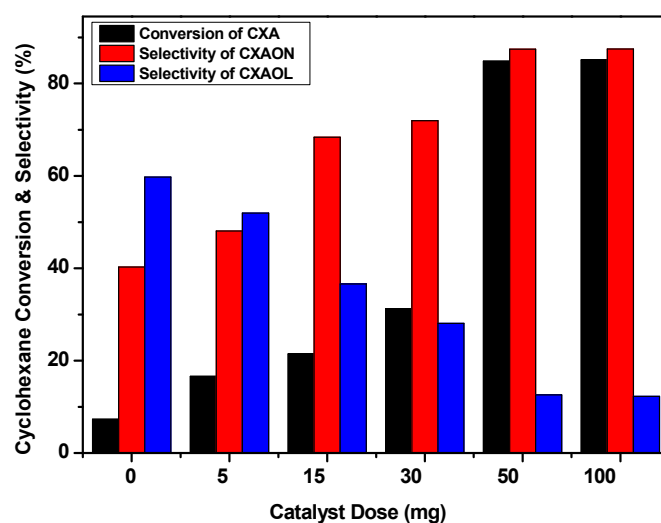

Figure 10. Catalyst dose effect. Reaction conditions: Catalyst is bulk NiO, *m*-CPBA, T = 70 °C, 24 h.

2.3. Catalyst Recycling

To investigate the stability and reusability of NiO catalyst for the oxidation of cyclohexane in the reaction conditions, NiO powder was recycled and reused under the same conditions mentioned above for four consecutive runs, and the obtained results are presented in Figure 11. After cycle one of the oxidation reaction of cyclohexane, the NiO catalyst was separated by filtration using a centrifuge. Then, the recycled NiO was washed three times with chloroform to remove the reactants, products, and the *meta*-chlorobenzoic acid (*m*-CBA) that were formed after the degradation of the *m*-CPBA. Then, the obtained NiO powder was dried in an oven at 100 °C for around 15 h. After this treatment, the NiO powder was ready to be reused in the following cycle. This treatment was repeated after each cycle, and the final products were detected by GC to calculate the CXE conversion and the product selectivity according to Equations (1)–(3) (above).

The obtained results show a slight decrease in the activity during four successive runs. The cyclohexane conversion was decreased from 85% to 63% with constant KA oil selectivity (99%), and the selectivity of cyclohexanone and cyclohexanol was decreased from 87% and 12% to 60% and 39%, respectively. This decrease in the conversion of cyclohexane was probably due to diminution of NiO amounts during the four cycles. The amount of NiO can be decreased by loss during the recycling and washing process, and also by the degradation (leaching) of NiO particles in the reaction acidic medium.
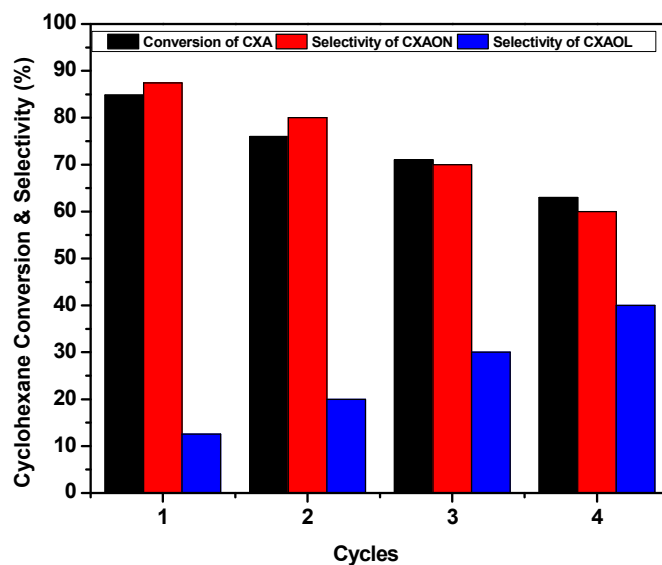
Figure 11. Reusability of NiO powder as a catalyst in the oxidation of cyclohexane with *m*-CPBA. Conditions: catalyst: 50 mg, *m*-CPBA (1.5 eq), time: 24 h, T = 70 °C, 1 atm.

3. Materials and Methods

3.1. Materials

Nickel (II) nitrate hexahydrate (≥98.5%), cyclohexane (ACS reagent, ≥99%), cyclohexanone (analytical standard), cyclohexanol (analytical standard), *meta*-chloroperoxybenzoic acid (*m*-CPBA) (≤77%), t-butyl hydrogen peroxide (TBHP) 5.0–6.0 M in decane, hydrogen peroxide (H_2O_2) 50 wt.% in H_2O, stabilized, molecular oxygen O_2 cylinder supplied by Southern Gases, acetonitrile (≥99.5%), n-hexane (≥98%), chloroform (≥99.5%), magnesium sulphate (anhydrous, reagent grade, ≥97%) were purchased from Sigma Aldrich. All reagents were of analytical grade and used without further purification.

3.2. Methods

3.2.1. Synthesis of NiO Powder

The bulk NiO particles were prepared via the thermal treatment of nickel (II) nitrate hexahydrate. In a typical synthesis reported previously [30], 5 g of nickel nitrate was heated under static conditions in a muffle furnace at 500 °C for 5 h with a heating ramp of 5 °C min^{-1}. The obtained material was a black-gray powder.

3.2.2. Characterization of NiO Powder

The prepared NiO powder was characterized by X-ray diffraction (XRD), scanning electron microscopy (SEM), energy dispersive X-ray (EDX), and thermogravimetric analysis (TGA).

The morphology of the obtained NiO powder was observed using SEM Philips EM 300 (Siemens Autoscan, Munchen, Germany). The X-ray diffraction pattern was measured on a Shimadzu Lab-XRD–6000 with CuKα radiation and a secondary monochromator. TGA was investigated under air conditions using a Shimadzu thermogravimetric analyzer operating at a rate of 50 mL min^{-1} of air. In this process, a 20.0 mg sample was submitted in a platinum crucible and heated at 15 K min^{-1} from 30 to 900 °C.

The epoxidation reaction was monitored by a Shimadzu GC-17A gas chromatograph (GC) equipped with flam ionization detector and RTX-5 column, 30 m × 0.25 mm, 1 µm film thickness. Helium was used as the carrier gas at a flow rate of 0.6 mL/min. Samples were withdrawn from the reaction mixture periodically. Injection volume was 1 µL, and total flow was 100 mL/min.

3.3. Oxidation of Cyclohexane over Bulk NiO

In order to determine the optimal conditions for the oxidation of cyclohexane over bulk NiO, such as the temperature, reaction time, catalyst dose and the best oxidant, the extreme conditions of the temperature (70 °C), reaction time (24 h) and catalyst amount as used in the literature [5] were used as the starting point in this study to determine the best oxidant. Different oxygen donors were used in this study, including H_2O_2, O_2, TBHP and *m*-CPBA.

The most promising results were obtained with *m*-CPBA. Therefore, other parameters were also investigated using *m*-CPBA as the oxidant, such as the effect of catalyst dose, temperature, and reaction time. The following are the experimental conditions used for each oxidant. Each reaction was run twice. The dodecane was used as internal reference. The oxidation reaction was monitored by GC, and the average conversion and selectivity are presented.

3.3.1. Molecular Oxygen (O_2)

The oxidation of cyclohexane over bulk NiO using molecular O_2 was performed in a high-pressure reactor vessel. A 100 mg amount of the bulk NiO, 20 mL of cyclohexane and 0.1 mL of dodecane (internal standard) were added in the reactor. Then, the reactor was closed and temperature of the mixture was increased to 140–150 °C under magnetic stirring. The pressure inside the reactor was stabilized at about 0.5 MPa. After 24 h, the temperature was cooled down to room temperature, and a sample (30 µL) was withdrawn from the reaction mixture, filtered through hydrophobic membrane, and injected into GC.

3.3.2. Using Hydrogen Peroxide (H_2O_2)

The oxidation of cyclohexane over bulk NiO using H_2O_2 was performed as follows. Briefly, in a 50 mL flask equipped with a condenser, 50 mg of bulk NiO was dispersed in 10 mL of acetic acid, then 2 mL of the substrate (cyclohexane) and 0.1 mL of dodecane (internal reference) were added. After stirring this mixture for 5 min at 70 °C, 2.7 mL of H_2O_2 was added, wherein the 0 time of the reaction was considered at this moment. After 24 h, the organic phase was extracted by n-hexane and dried over $MgSO_4$. Sample (30 µL) was withdrawn from the organic phase, filtered through hydrophobic membrane, and injected into GC.

3.3.3. Tert-Butyl Hydroperoxide (TBHP)

The oxidation of cyclohexane over bulk NiO using TBHP was performed as follows. Briefly, in a 50 mL flask equipped with a condenser, the appropriate amount of bulk NiO (50 mg) was dispersed in 10 mL of acetonitrile, then 0.12 mL of substrate (cyclohexane) and 0.1 mL of dodecane (internal reference) were added. After stirring this mixture for 5 min at 70 °C, 0.3 mL of TBHP was added, wherein the 0 time of the reaction was considered at this moment. After 24 h, a sample of about 30 µL was withdrawn from the reaction mixture, filtered through hydrophobic membrane to remove the solid catalyst, and then injected into GC.

3.3.4. *Meta*-Chloroperoxybenzoic Acid (*m*-CPBA)

The oxidation of cyclohexane over bulk NiO using *m*-CPBA was performed following a modified procedure reported by Abboud et al. [34]. Briefly, in a 50 mL flask equipped with a condenser, 50 mg of bulk NiO was dispersed in 10 mL of acetonitrile, then 0.12 mL of cyclohexane (substrate) and 0.1 mL of dodecane (internal reference) were added. After stirring this mixture for 5 min at 70 °C, 288 mg of *m*-CPBA was added, wherein the 0 time of the reaction was considered at this moment. After 24 h, a sample of about 30 µL was withdrawn from the reaction mixture, filtered through hydrophobic membrane to remove the solid catalyst, and then injected into GC.

3.3.5. The Optimization of the Oxidation of Cyclohexane over Bulk NiO Using *m*-CPBA

Following the same procedure described in Section 3.4 above, the catalyst dose, temperature, and reaction time were studied, as described in the following Table 1.

Table 1. Parameters investigated in the oxidation reaction of cyclohexane over bulk NiO using *m*-CPBA as oxygen donor.

Catalyst Dose (mg)	Temperature (°C)	Reaction Time (hours)
5, 10, 30, 50	25, 40, 60, 70	0.5, 1, 2, 4, 24

3.4. The Calculation of Conversion and Selectivity

The conversion and selectivity were calculated according to the following equations:

$$\text{Conversion (\%)} = 100 - \frac{Peak\ area\ of\ cyclohexane}{Peak\ areas\ of\ (cyclohexane + all\ products)} \times 100 \qquad (1)$$

Equation (1). Conversion calculation.

$$\text{Selectivity to CXAON (\%)} = \frac{Peak\ area\ of\ cyclohexanone}{Peak\ areas\ of\ all\ products} \times 100 \qquad (2)$$

Equation (2). Selectivity to CXAON calculation.

$$\text{Selectivity to CXAOL (\%)} = \frac{Peak\ area\ of\ cyclohexanol}{Peak\ areas\ of\ all\ products} \times 100 \qquad (3)$$

Equation (3). Selectivity to CXAOL calculation.

3.5. Catalyst Recycling

The bulk NiO was reused in five successive cycles following the same procedure described in Section 3.4. After 24 h of the first cycle, the mixture was filtered using a centrifuge to recover the catalyst. The catalyst was washed three times with chloroform to remove the remaining substrate, products, internal reference, *m*-CPBA, solvent, and the *meta*-chlorobenzoic acid (*m*-CBA) formed after the degradation of *m*-CPBA. Then, the recycled catalyst was dried in the oven at 100 °C for around 15 h to be ready for the following cycle. At the end of each cycle, a sample of about 30 μL was withdrawn from the reaction mixture, filtered through hydrophobic membrane to remove the solid catalyst, and then injected into GC.

3.6. Possible Mechanism

m-CPBA is among the most important organic peroxides (ROOH or ROOR′) that have been used as strong oxidants for various organic transformations. *m*-CPBA showed high activity even for the hydroxylation reaction of methane in the presence of iron porphyrin complex or its enzymatic model P450 [48,49]. *m*-CPBA also has been used to activate the C–H bonds of hydrocarbons, which is one of the most challenging chemical reactions in recent chemistry [50–52]. In contrast to O_2, H_2O_2 and TBHP, *m*-CPBA is a stable and selective oxidant, which are important features in organic synthesis. Moreover, *m*-CPBA can form selective and highly active intermediates in the presence of auxiliary reagents [53–55]. In addition, *m*-CPBA is an easy-to-handle and convenient terminal oxidant. However, *m*-CPBA may produce a broader mixture of radicals [56–58]. Therefore, the presence of a catalyst is necessary to activate the O–O bond in a suitable way, and to suppress the secondary reaction pathways.

According to some theoretical predictions and previous mechanistic investigations for the oxidation of hydrocarbons catalyzed by transition metals [38,59–64], and based on the obtained results in the current work, we believe that after homolysis of the O–O bond of

m-CPBA in the presence of NiO active sites, nickel-oxo (O=NiO) species and *m*-CBOO• can be formed (Figure 12, step 1). In the proposed mechanism, *m*-CBOO• are the cyclohexane-C-H bond attacking species. After H abstraction by *m*-CBOO• species, cyclohexane radical (CXA•) can be formed with the generation of *m*-CBA (Figure 12, step 2). CXA• reacts with another molecule of *m*-CPBA to form CXAOL with the regeneration of *m*-CBOO• species (Figure 12, step 3). Then, a portion of CXAOL will be converted to CXAON after further oxidation over NiO (Figure 12, step 4). The ratio CXAON/CXAOL is related to the catalyst dose. The low conversion of CXA to CXAON and CXAOL over *m*-CPBA in the absence of the catalyst (Figure 10) can be explained by slow conversion of *m*-CPBA to *m*-CBOO• species under heat (Figure 12, step 5). In addition, the formation of a small amount of CXAON compared to CXAOL in the absence of the catalyst (Figure 10) can be attributed to the slow conversion of CXAOL to CXAON over *m*-CPBA (Figure 12, step 6).
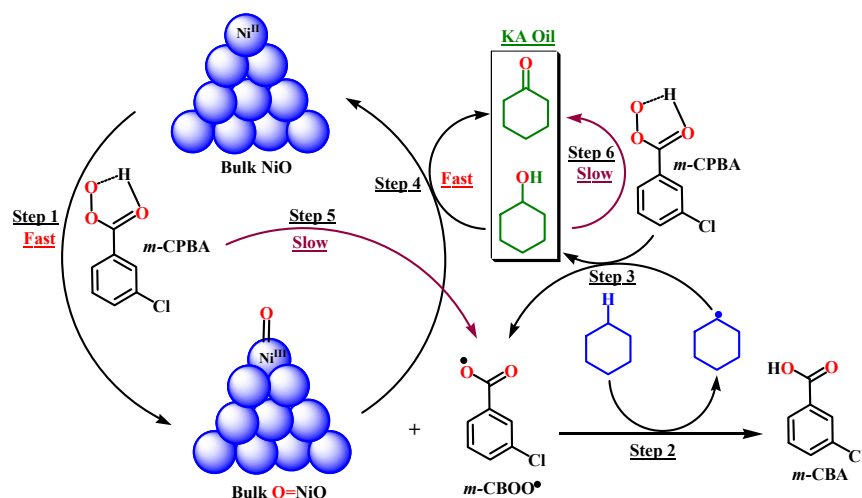

Figure 12. Possible mechanism for the oxidation of cyclohexane over bulk NiO.

4. Conclusions

This work reported an efficient process for the oxidation of cyclohexane to produce KA oil (cyclohexanone plus cyclohexanol) catalyzed by bulk NiO powder under mild conditions using *meta*-chloroperoxybenzoic acid (*m*-CPBA) as oxygen donor. NiO powder was prepared by simple calcination (500 °C, 5 h) of nickel (II) nitrate hexahydrate. For the first time, around 85% of cyclohexane was converted to products, with 99% KA oil selectivity, including about 87% of cyclohexanone (K) and 13% cyclohexanol (A), using 1.5 eq of *m*-CPBA as an oxidant, in acetonitrile as a solvent, and under 70 °C for 24 h. This reaction was monitored by gas chromatography (GC) using dodecane as internal standard. Furthermore, the reusability of NiO catalyst was also evaluated. This catalyst was easily separable and recyclable up to four cycles, with a slight decrease in the catalytic activity. After four cycles, the conversion of cyclohexane was decreased gradually to 63% with constant KA selectivity (99%), while the selectivity toward cyclohexanone was progressively decreased to 60%. Its features as a very efficient catalytic system under mild conditions, with low cost, easy synthesis, high cyclohexane conversion, high KA oil selectivity, and superiority to all reported catalysts available in the literature make this catalytic system very promising for the industrial production of adipic acid and nylon fibers.

Author Contributions: Conceptualization, M.A.; Funding acquisition, M.S.H.; Investigation, M.A. and R.S.A.; Methodology, M.A. and R.S.A.; Project administration, M.A.; Resources, M.S.H. and A.A.; Supervision, A.A.; Validation, M.S.H. and A.A.; Visualization, M.S.H. and A.A.; Writing—original draft, M.A. and R.S.A.; Writing—review and editing, M.A. and M.S.H. All authors have read and agreed to the published version of the manuscript.

References

1. Van de Vyver, S.; Román-Leshkov, Y. Emerging catalytic processes for the production of adipic acid. *Catal. Sci. Technol.* **2013**, *3*, 1465–1479. [CrossRef]
2. Sato, K.; Aoki, M.; Noyori, R. A Green Route to Adipic Acid: Direct Oxidation of Cyclohexenes with 30% Hydrogen Peroxide. *Science* **1998**, *281*, 1646–1647. [CrossRef]
3. Hwang, K.C.; Sagadevan, A. One-pot room-temperature conversion of cyclohexane to adipic acid by ozone and UV light. *Science* **2014**, *346*, 1495–1498. [CrossRef]
4. Yang, J.; Liu, J.; Neumann, H.; Franke, R.; Jackstell, R.; Beller, M. Direct synthesis of adipic acid esters via palladium-catalyzed carbonylation of 1,3-dienes. *Science* **2019**, *366*, 1514–1517. [CrossRef]
5. Deng, W.P.; Yan, L.F.; Wang, B.J.; Zhang, Q.H.; Song, H.Y.; Wang, S.S.; Zhang, Q.H.; Wang, Y. Efficient Catalysts for Green Synthesis of Adipic Acid from Biomass. *Angew. Chem. Int. Ed.* **2021**, *60*, 4712–4719. [CrossRef]
6. Xu, L.; He, C.H.; Zhu, M.Q.; Wu, K.; Lai, Y. Silica-Supported Gold Catalyst Modified by Doping with Titania for Cyclohexane Oxidation. *Catal. Lett.* **2007**, *118*, 248–253. [CrossRef]
7. Priyank, K.; Rajubhai, M. Review of a Cyclohexane Oxidation Reaction Using Heterogenous Catalyst. *Int. J. Eng. Dev. Res.* **2014**, *2*, 2321–9939.
8. Xu, L.X.; He, C.H.; Zhu, M.Q.; Fang, S. A highly active Au/Al_2O_3 catalyst for cyclohexane oxidation using molecular oxygen. *Catal. Lett.* **2007**, *114*, 202–205. [CrossRef]
9. Wu, P.; Bai, P.; Loh, K.P.; Zhao, X.S. Au nanoparticles dispersed on functionalized mesoporous silica for selective oxidation of cyclohexane. *Catal. Today* **2010**, *158*, 220–227. [CrossRef]
10. Wang, H.; Li, R.; Zheng, Y.; Chen, H.; Wang, F.; Ma, J. An Efficient and Reusable Catalyst of Bismuth-Containing SBA-15 Mesoporous Materials for Solvent-free Liquid Phase Oxidation of Cyclohexane by Oxygen. *Catal. Lett.* **2008**, *122*, 330–337. [CrossRef]
11. Enache, D.; Carley, A.F.; Roberts, M.W.; Hutchings, G.J. Selective conversion of cyclohexane to cyclohexanol and cyclohexanone using a gold catalyst under mild conditions. *Catal. Lett.* **2005**, *101*, 175–179. [CrossRef]
12. Abboud, M.; Alnefaie, R.; Alhanash, A. Unsupported and silica-supported nickel nanoparticles: Synthesis and application in catalysis. *J. Nanopart. Res.* **2022**, *24*, 21. [CrossRef]
13. Jaji, N.-D.; Lee, H.L.; Hussin, M.H.; Akil, H.M.; Zakaria, M.R.; Othman, M.B.H. Advanced nickel nanoparticles technology: From synthesis to applications. *Nanotechnol. Rev.* **2020**, *9*, 1456–1480. [CrossRef]
14. Vollath, D.; Szabó, D.V. Nonmetallic bulk nanomaterials. In *Bulk Nanostructured Materials*; Zehetbauer, M.J., Zhu, Y.T., Eds.; Wiley-VCH Verlag GmbH & Co.: Weinheim, Germany, 2009; pp. 49–85.
15. Schubert, U.; Hüsing, N. *Synthesis of Inorganic Materials*, 4th ed.; John Wiley & Sons: Hoboken, NJ, USA, 2019; pp. 1–424.
16. Ozin, G.A.; Arsenault, A.C.; Cademartiri, L. Chapter 5. Nanorod, Nanotube, Nanowire Self-Assembly. In *Nanochemistry: A Chemical Approach to Nanomaterials*; Royal Society of Chemistry: London, UK, 2009; pp. 215–330.
17. Lai, T.L.; Lee, C.C.; Wu, K.S.; Shu, Y.Y.; Wang, C.B. Microwave-enhanced catalytic degradation of phenol over nickel oxide. *Appl. Catal. B* **2006**, *68*, 147–153. [CrossRef]
18. Lai, T.L.; Lee, C.C.; Huang, G.L.; Shu, Y.Y.; Wang, C.B. Microwave-enhanced catalytic degradation of 4-chlorophenol over nickel oxides. *Appl. Catal. B* **2008**, *78*, 151–157. [CrossRef]
19. Christoskova, S.T.; Stoyanova, M. Degradation of phenolic waste waters over Ni-oxide. *Water Res.* **2001**, *35*, 2073–2077. [CrossRef]
20. Ashik, U.P.M.; Daud, W.W.; Hayashi, J.I. Governance of the porosity and of the methane decomposition activity sustainability of NiO/SiO_2 nanocatalysts by changing the synthesis parameters in the modified Stöber method. *C. R. Chim.* **2017**, *20*, 896–909. [CrossRef]
21. Guo, X.F.; Kim, Y.S.; Kim, G.J. Synthesis of Mesoporous Metal Oxides and Their Efficient Property for Super Capacitor Application. *J. Nanosci. Nanotechnol.* **2011**, *11*, 1672–1675. [CrossRef]
22. Solsona, B.; Concepción, P.; Nieto, J.L.; Dejoz, A.; Cecilia, J.A.; Agouram, S.; Soriano, M.D.; Torres, V.; Jiménez-Jiménez, J.; Castellón, E.R. Nickel oxide supported on porous clay heterostructures as selective catalysts for the oxidative dehydrogenation of ethane. *Catal. Sci. Technol.* **2016**, *6*, 3419–3429. [CrossRef]
23. Vikraman, D.; Park, H.J. Shape-selective synthesis of NiO nanostructures for hydrazine oxidation as a nonenzymatic amperometric sensor. *RSC Adv.* **2016**, *6*, 86101–86107. [CrossRef]

24. Sasaki, T.; Ichikuni, N.; Hara, T.; Shimazu, S. Study on the promoting effect of nickel silicate for 1-phenylethanol oxidation on supported NiO nanocluster catalysts. *Catal. Today* **2018**, *307*, 29–34. [CrossRef]

25. Gao, X.; Mao, H.; Lu, M.; Yang, J.; Li, B. Facile synthesis route to NiO–SiO₂ intercalated clay with ordered porous structure: Intragallery interfacially controlled functionalization using nickel–ammonia complex for deep desulfurization. *Microporous Mesoporous Mater.* **2012**, *148*, 25–33. [CrossRef]

26. El-Safty, S.A.; Kiyozumi, Y.; Hanaoka, T.; Mizukami, F. Heterogeneous catalytic activity of NiO-silica composites designated with cubic Pm3n cage nanostructures. *Appl. Catal. B* **2008**, *82*, 169–179. [CrossRef]

27. Adil, S.F.; Assal, M.E.; Kuniyil, M.; Khan, M.; Shaik, M.R.; Alwarthan, A.; Labis, J.P.; Siddiqui, M.R.H. Synthesis and comparative catalytic study of zinc oxide (ZnOx) nanoparticles promoted MnCO₃, MnO₂ and Mn₂O₃ for selective oxidation of benzylic alcohols using molecular oxygen. *Mater. Express* **2017**, *7*, 79–92. [CrossRef]

28. Arora, A.K.; Kumar, P.; Kumar, S. Synthesis of ZnO Nanoparticle and its Application in Catalytic Hydrolysis of p-Acetoxynitrobenzene. *Int. J. Nanosci.* **2017**, *16*, 1750005. [CrossRef]

29. Pike, S.D.; García-Trenco, A.; White, E.R.; Leung, A.H.; Weiner, J.; Shaffer, M.S.; Williams, C.K. Colloidal Cu/ZnO catalysts for the hydrogenation of carbon dioxide to methanol: Investigating catalyst preparation and ligand effects. *Catal. Sci. Technol.* **2017**, *7*, 3842–3850. [CrossRef]

30. Chand, S.; Sandhu, J.S. ZnO Nanoparticles: An efficient green reusable catalyst for the synthesis of 3-formyl benzopyranones chalcones by Claisen-Schmidt reaction under solvent-free condition. *Indian J. Chem. Sect. B* **2015**, *54*, 1350–1354. [CrossRef]

31. Sun, X.; Zhang, X.; Cao, X.; Zhao, X. Optimization of Reaction Conditions for Cyclohexane to Cyclohexanone with t-Butylhydroperoxide Over CuCl₂ Loaded with Activated Carbon. *J. Braz. Chem. Soc.* **2016**, *27*, 202–208.

32. Abboud, M.; Haija, M.A.; Bel-Hadj-Tahar, R.; Mubarak, A.T.; Ismail, I.; Hamdy, M.S. Highly ordered mesoporous flower-like NiO nanoparticles: Synthesis, characterization and photocatalytic performance. *New J. Chem.* **2020**, *44*, 3402–3411. [CrossRef]

33. Abboud, M. Immediate epoxidation of cyclohexene at room temperature using mesoporous flower-like NiO nanoparticles. *React. Kinet. Mech. Catal.* **2020**, *131*, 781–792. [CrossRef]

34. Sahlabji, T.; Abboud, M.; Bel-Hadj-Tahar, R.; Hamdy, M.S. Spontaneous epoxidation of styrene catalyzed by flower-like NiO nanoparticles under ambient conditions. *J. Nanopart. Res.* **2020**, *22*, 364. [CrossRef]

35. Grosso, C.; Boissiere, B.S.; Brezesinski, T.; Pinna, N.; Albouy, P.; Amenitsch, H.; Antonietti, M.; Sanchez, C. Periodically Ordered Nanoscale Islands and Mesoporous Films Composed of Nanocrystalline Multimetallic Oxides. *Nat. Mater.* **2004**, *3*, 787–792. [CrossRef] [PubMed]

36. Abboud, M.; Al-Zaqri, N.; Sahlabji, T.; Eissa, M.; Mubarak, A.T.; Bel-Hadj-Tahar, R.; Alsalme, A.; Alharthi, F.A.; Alsyahi, A.; Hamdy, M.S. Instant and quantitative epoxidation of styrene under ambient conditions over a nickel(ii)dibenzotetramethyltetraaza annulene complex immobilized on amino-functionalized SBA-15. *RSC Adv.* **2020**, *10*, 35407–35418. [CrossRef] [PubMed]

37. Abboud, M.; Sahlabji, T.; Eissa, M.; Bel-Hadj-Tahar, R.; Mubarak, A.T.; Al-Zaqri, N.; Hamdy, M.S. Nickel(II)dibenzotetramethyltetra aza[14]annulene complex immobilized on amino-functionalized TUD-1: An efficient catalyst for immediate and quantitative epoxidation of cyclohexene under ambient conditions. *New J. Chem.* **2020**, *44*, 20137–20147. [CrossRef]

38. Hamdy, M.S.; Al-Zaqri, N.; Sahlabji, T.; Eissa, M.; Abu Haija, M.; Alhanash, A.M.; Alsalme, A.; Alharthi, F.A.; Abboud, M. Instant Cyclohexene Epoxidation Over Ni-TUD-1 under Ambient Conditions. *Catal. Lett.* **2021**, *151*, 1612–1622. [CrossRef]

39. Zou, X.; Conradsson, T.; Klingstedt, M.; Dadachov, M.S.; O'Keeffe, M. A mesoporous germanium oxide with crystalline pore walls and its chiral derivative. *Nature* **2005**, *437*, 716–719. [CrossRef]

40. Ying, J.Y.; Mehnert, C.P.; Wong, M.S. Synthesis and applications of supramolecular-templated mesoporous materials. *Angew. Chem. Int. Ed.* **1999**, *38*, 56–77. [CrossRef]

41. Jia, J.; Wang, Y.; Tanabe, E.; Shishido, T.; Takehira, K. Carbon fibers prepared by pyrolysis of methane over Ni/MCM-41 catalyst. *Microporous Mesoporous Mater.* **2003**, *57*, 283–289. [CrossRef]

42. Basha, S.S.; Sasirekha, N.R.; Maheswari, R.; Shanthi, K. Mesoporous H-AlMCM-41 supported NiO-MoO₃ catalysts for hydrodeni-trogenation of o-toluidine: I. Effect of MoO₃ loading. *Appl. Catal. A-Gen.* **2006**, *308*, 91–98. [CrossRef]

43. Moreno-Tost, R.; Santamaría-González, J.; Maireles-Torres, P.; Rodríguez-Castellón, E.; Jiménez-López, A. Nickel oxide supported on zirconium-doped mesoporous silica for selective catalytic reduction of NO with NH₃. *J. Mater. Chem.* **2002**, *12*, 3331–3336. [CrossRef]

44. Polshettiwar, V.; Baruwati, B.; Varma, R.S. Nanoparticle-supported and magnetically recoverable nickel catalyst: A robust and economic hydrogenation and transfer hydrogenation protocol. *Green Chem.* **2009**, *11*, 127–131. [CrossRef]

45. Kalbasi, R.J.; Mosaddegh, N. Suzuki-Miyaura Cross-coupling Reaction Catalyzed by Nickel Nanoparticles Supported on Poly(N-vinyl-2-pyrrolidone)/TiO₂-ZrO₂ Composite. *Bull. Korean Chem. Soc.* **2011**, *32*, 2584–2592. [CrossRef]

46. Alonso, F.; Riente, P.; Yus, M. Nickel nanoparticles in hydrogen transfer reactions. *Acc. Chem. Res.* **2011**, *44*, 379–391. [CrossRef] [PubMed]

47. Meher, S.K.; Justin, P.; Ranga, R.G. Microwave-mediated synthesis for improved morphology and pseudocapacitance performance of nickel oxide. *ACS Appl. Mater. Interfaces* **2011**, *3*, 2063–2073. [CrossRef] [PubMed]

48. Li, J.F.; Xiao, B.; Du, L.J.; Yan, R.; Liang, T.D. Preparation of nano-NiO particles and evaluation of their catalytic activity in pyrolyzing cellulose. *J. Fuel Chem. Technol.* **2008**, *36*, 42–47. [CrossRef]

49. Behnajady, M.A.; Bimeghdar, S. Synthesis of mesoporous NiO nanoparticles and their application in the adsorption of Cr(VI). *Chem. Eng. J.* **2014**, *239*, 105–113. [CrossRef]

50. Chen, M.M.; Coelho, P.S.; Arnold, F.H. Utilizing Terminal Oxidants to Achieve P450-Catalyzed Oxidation of Methane. *Adv. Synth. Catal.* **2012**, *354*, 964–968. [CrossRef]

51. Kudrik, E.V.; Afanasiev, P.; Alvarez, L.X.; Dubourdeaux, P.; Clemancey, M.; Latour, J.M.; Blondin, G.; Bouchu, D.; Albrieux, F.; Nefedov, S.E.; et al. An N-bridged high-valent diiron-oxo species on a porphyrin platform that can oxidize methane. *Nat. Chem.* **2012**, *4*, 1024–1029. [CrossRef]

52. Lyakin, O.Y.; Bryliakov, K.P.; Talsi, E.P. Non-heme oxoiron(V) intermediates in chemo-, regio- and stereoselective oxidation of organic substrates. *Coord. Chem. Rev.* **2019**, *384*, 126–139. [CrossRef]

53. Singh, F.V.; Wirth, T. Hypervalent Iodine-Catalyzed Oxidative Functionalizations Including Stereoselective Reactions. *Chem. Asian J.* **2014**, *9*, 950–971. [CrossRef]

54. Clavier, H.; Pellissier, H. Recent Developments in Enantioselective Metal-Catalyzed Domino Reactions. *Adv. Synth. Catal.* **2012**, *354*, 3347–3403. [CrossRef]

55. Ghosh, P.; Ganguly, B.; Das, S. NaI/KI/NH4I and TBHP as powerful oxidation systems: Use in the formation of various chemical bonds. *Org. Biomol. Chem.* **2021**, *19*, 2146–2167. [CrossRef] [PubMed]

56. Wu, X.F.; Gong, J.L.; Qi, X.X. A powerful combination: Recent achievements on using TBAI and TBHP as oxidation system. *Org. Biomol. Chem.* **2014**, *12*, 5807–5817. [CrossRef] [PubMed]

57. Yoshimura, A.; Zhdankin, V.V. Advances in Synthetic Applications of Hypervalent Iodine Compounds. *Chem. Rev.* **2016**, *116*, 3328–3435. [CrossRef] [PubMed]

58. Fokin, A.A.; Schreiner, P.R. Selective alkane transformations via radicals and radical cations: Insights into the activation step from experiment and theory. *Chem. Rev.* **2002**, *102*, 1551–1593. [CrossRef] [PubMed]

59. Bravo, A.; Bjorsvik, H.R.; Fontana, F.; Minisci, F.; Serri, A. Radical versus "oxenoid" oxygen insertion mechanism in the oxidation of alkanes and alcohols by aromatic peracids. New synthetic developments. *J. Org. Chem.* **1996**, *61*, 9409–9416. [CrossRef]

60. Hussain, H.; Al-Harrasi, A.; Green, I.R.; Ahmed, I.; Abbas, G.; Rehman, N.U. Meta-Chloroperbenzoic acid (mCPBA): A versatile reagent in organic synthesis. *RSC Adv.* **2014**, *4*, 12882–12917. [CrossRef]

61. Smith, J.G. The Review of high pressure science and technology 7, 1250–1252, 1998. *Synth. Useful React. Epoxides* **1984**, *629*, 656. [CrossRef]

62. Parker, R.-E.; Isaacs, N.S. Mechanisms of Epoxide Reactions. *Chem. Rev.* **1959**, *198459*, 737–799. [CrossRef]

63. Kooti, M.; Afshari, M. Phosphotungstic acid supported on magnetic nanoparticles as an efficient reusable catalyst for epoxidation of alkenes. *Mater. Res. Bull.* **2012**, *47*, 3473–3478. [CrossRef]

64. Dmytro, S.N.; Oksana, V.N. Catalytic Oxidations with Meta-Chloroperoxybenzoic Acid (m-CPBA) and Mono- and Polynuclear Complexes of Nickel: A Mechanistic Outlook. *Catalysts* **2021**, *11*, 1148. [CrossRef]

Article

Effect of Different Zeolite Supports on the Catalytic Behavior of Platinum Nanoparticles in Cyclohexene Hydrogenation Reaction

Mohamed S. Hamdy [1,*], Fatimah A. Alqahtani [1], Mohd Shkir [2], Khaled F. Fawy [3], Mhamed Benaissa [4], Mohamed Bechir Ben Hamida [5] and Noureddine Elboughdiri [4]

[1] Catalysis Research Group (CRG), Department of Chemistry, Faculty of Science, King Khalid University, P.O. Box 9004, Abha 61413, Saudi Arabia
[2] Department of Physics, Faculty of Science, King Khalid University, P.O. Box 9004, Abha 61413, Saudi Arabia
[3] Department of Chemistry, Faculty of Science, King Khalid University, P.O. Box 9004, Abha 61413, Saudi Arabia
[4] Chemical Engineering Department, College of Engineering, University of Ha'il, P.O. Box 2440, Ha'il 81441, Saudi Arabia
[5] College of Engineering, Department of Mechanical Engineering, Imam Mohammad Ibn Saud Islamic University (IMSIU), Riyadh 11432, Saudi Arabia
[*] Correspondence: m.s.hamdy@gmail.com

Abstract: In this study, 1 wt% platinum (Pt) nanoparticles were incorporated into five types of zeolites (HY, Beta, mordenite, ZSM-5, and ferrierite) with an impregnation technique. The synthesis strategy included the use of water as a solvent for the applied Pt source. Moreover, the incorporation process was performed at ambient conditions followed by calcination at 450 °C. The five prepared materials were characterized by different physical and chemical characterization techniques and the obtained results confirmed the formation of Pt nanoparticles with an average size of 5–10 nm. The catalytic performance of the prepared materials was evaluated in the hydrogenation of cyclohexene under a solvent-free system at room temperature. Pt nanoparticles supported on ZSM-5 zeolite exhibited the best catalytic performance. Moreover, the optimization of operational conditions such as temperature, pressure, and catalyst amount was investigated and the obtained results showed the possibility to convert 100% of cyclohexene within 35 min over Pt-ZSM-5. Finally, the reusability of the Pt-ZSM-5 catalyst was investigated in four consecutive runs without treatment and the obtained results showed a negligible activity loss.

Keywords: hydrogenation; zeolite; Pt nanoparticles; cyclohexene; impregnation

1. Introduction

Hydrogenation reactions, which include the conversion of unsaturated double bonds into saturated bonds by using molecular hydrogen, play a crucial role in chemical industries [1,2]. Several daily-use commercial products are fabricated based on hydrogenation reactions, such as the variety of products which are based on margarine [3] and nylon [4,5]. One of the most interesting catalysts which has been deeply investigated in hydrogenation reactions is the Wilkinson catalyst [6]. However, due to the separation problem, which is associated with the use of homogeneous catalysts, scientists utilize heterogeneous catalysts in hydrogenation reactions. In addition to raney nickel [7], noble metals such as Pd [8], Pt [9], Rh [10] and Ru [11] were found to be superior in the heterogeneous activation of hydrogenation reactions. However, the high cost of noble metals motivated scientists to investigate several tactics to minimize the catalyst cost. One of these tactics is the use of well-distributed nanoparticles of the noble metal supported on porous material with high surface area [12–14]; the use of nanoparticles ensures the reaction activation with a minimum amount of noble metal [15].

Zeolites are naturally occurring crystalline porous materials with a large surface area [16]. Zeolites consist of tetrahedrally coordinated aluminosilicate with rigid anionic frameworks containing well-defined channels and cavities [17]. Natural zeolites have the general formula of $M_{2/n}:Al_2O_3:xSiO_2:yH_2O$, where M stands for the extra-framework cation [18]. It was found that tetrahedrally coordinated AlO_4 and SiO_4 can share one, two, or three oxygen atoms, which creates a wide variety of possible structures as the network is extended in three dimensions. Currently, 40 types of natural zeolite have been discovered and more than 150 types have been synthetized. Zeolites have a high potential in industry since they are used in water treatment, catalysis, agriculture, animal feed additives, and in biochemical applications [19]. Therefore, zeolites are considered a good candidate to support noble metal nanoparticles in hydrogenation reactions [20,21].

Kubicka used Beta zeolite to support the Pt nanoparticles as a catalyst in the hydrogenation of phenol and cresols [22]. In another study, zeolite Y was applied to support the Pt nanoparticles and the prepared catalyst was used in the hydrogenation of benzene [23]. Moreover, Wang et al. [24] investigated the use of Ru nanoparticles supported by ZSM-5 in the hydrogenation of phenol. Mordenite was also reported to support Pt in the hydrogenation of cyclohexene [25]. However, few studies have been conducted to systematically compare the effect of different zeolite supports in hydrogenation.

In the current study, Pt nanoparticles were incorporated into five different types of commercial zeolites (Y, Beta, ZSM-5, mordenite, and ferrierite) [26] with an impregnation technique. The prepared materials were characterized by various physical and chemical techniques to reveal their structure. Their catalytic activity was evaluated in the hydrogenation of cyclohexene under a solvent-free system at room temperature. The obtained results in terms of activity, stability and recycling were compared and the findings were discussed.

2. Experimental

2.1. Materials

In Table 1, a list of the applied materials that were used in the experimental work of the current study is presented. The listed chemical materials were used as received without any further purification and/or treatment.

Table 1. A list of materials which were used in this work.

Materials	Molecular Formula	Assay%	Source
Zeolite H-Beta	SiO_2	>97	ZEOLYST
Zeolite NH_4-ZSM-5	SiO_2, Al_2O_3 (Si/Al = 50)	>97	ZEOLYST
Zeolite NH_4-MOR	SiO_2, Al_2O_3 (Si/Al = 20)	>97	ZEOLYST
Zeolite NH_4-Ferrite	SiO_2, Al_2O_3, Fe_2O_3 (Si/Al = 20)	>97	ZEOLYST
Zeolite H-Y	SiO_2	>97	ZEOLYST
Platinum II Chloride	$PtCl_2$	98	ALDRICH
Cyclohexene	C_6H_{10}	99	MTEDIA
Cyclohexane	C_6H_{12}	99	ACROS

2.2. Catalysts Fabrication

First, 1 wt% of Pt was incorporated into five zeolite samples using an impregnation technique. In the real experiment, 1 g of the applied zeolite sample was suspended in 50 mL of distilled water. Then, a stoichiometric amount of $PtCl_2$ was dissolved in the above-mentioned suspension and the overall mixture was vigorously stirred for 48 h. After stirring, the mixture was dried at 100 °C for 24 h to remove the water and the solid powder was collected and finally calcined for 4 h at 450 °C. The obtained solid powder was carefully grinded and sieved through a 65-micron particle sieve.

2.3. Catalysts Characterization

The five prepared catalytic samples were characterized by several techniques to understand their structure. Powder X-ray diffraction patterns were used to assess the crystallinity of the manufactured samples. CuK radiation (λ = 0.1541 nm) was used to obtain XRD patterns on a Shimadzu 6000 DX instrument diffractometer with a graphite monochromator. The samples were scanned in steps of 0.02° over a range of 5–80° 2θ. ICP elemental analysis was used to determine the exact concentration of Pt in each sample. The samples were digested before being cooked in the microwave for 90 min. The digested samples were then filtered and washed numerous times. Finally, using inductively coupled plasma optical emission spectroscopy (Thermo scientific, ICAP 7000 series, component No: 1340910, Qtegra Softwear, Bremen, Germany), the concentration of Pt was determined. The textural parameters of the manufactured catalytic samples (i.e., total surface area, pore volume, and pore diameter) were determined using the N_2 sorption data. On a NOVA 2000e at 77 K, nitrogen adsorption/desorption isotherms were obtained. The Barret–Joyner–Halenda (BJH) model was used to derive the pore size distribution from the adsorption branch. The samples had previously been evacuated for 16 h at 623 K. The surface area (S_{BET}) of the samples was calculated using the BET method, while the pore volume (V_{pore}) was estimated using Lippens and Boer's t-plot approach. Using an Agilent Cary 630 FTIR Spectrometer, the produced catalytic samples were studied using Fourier transform infrared (FTIR) spectroscopy. At ambient conditions, the spectra were taken in the range 4000–400 cm^{-1} with a spectral resolution of 4 cm^{-1}. The morphological structure of the catalysts was investigated using SEM. The elementary decomposition and the purity of the samples were studied using EDX, and a semi-quantitative study of the elements that made up the catalysts was also performed. After coating them with gold, SEM micrographs were obtained using the Jeol Model (6360 LVSEM, Peabody, MA, USA). Furthermore, an EDX study was performed utilizing the Jeol Model (6360 LVSEM, Peabody, MA, USA). Using high-resolution transmission electron microscopy, the size and distribution of the Pt on the various supports were investigated (HR-TEM). The analysis was carried out using a JEOL-JEM-2100 with a 200 KV accelerating voltage. By sprinkling a few drops of ground sample suspension in ethanol on a carbon polymer grid with copper support and drying at room temperature, the samples were deposited and a LINK EDX system was employed.

2.4. Catalytic Activity Study

The hydrogenation of cyclohexene was performed in a 300 mL semi-batch Parr reactor at room temperature and 5 atm of H_2 gas for 1 h. In a typical experiment, 25 mL of cyclohexene and 0.25 g of catalyst were placed inside the reactor to form a suspension. The suspension was vigorously stirred at a constant rate of 1000 rpm to reduce the external mass transfer limitation, if present. After closing the reactor carefully, it was degassed with nitrogen gas and finally pressurized to 5 atm with hydrogen gas (99%). After elapsing the reaction time, the reactor was flushed with nitrogen gas and finally a sample of 0.5 mL was sent to GC for analysis. The applied GC was SHIMADZU GC-17, and the applied capillary column was RTX-5, 30 m × 0.25 mm × 0.25 μm. Finally, the applied detector was a flame ionization type (FID).

The conversion of cyclohexene (*CXE*) was calculated as follows:

$$\text{Conversion} = \frac{[CXE]_0 - [CXE]_t}{[CXE]_0} \times 100 \tag{1}$$

where *[CXE]*$_0$ is the concentration of cyclohexene at zero time and *[CXE]*$_t$ is the concentration of cyclohexene at (*t*) time.

Moreover, the turnover frequency (TOF) was calculated as follows:

$$\text{TOF} = \frac{[CXE]_0 - [CXE]_t}{[Pt] \times time(s)} \tag{2}$$

where [*Pt*] is the concentration of *Pt*, and the time of reaction was calculated in seconds.

3. Results

3.1. The Characterization Data

The exact amount of Pt was determined with ICP analysis. Table 2 shows a comparison between the intended Pt loading and the obtained loading in the final solid product.

Table 2. The ICP analysis of exact amount of Pt in each sample.

Sample	Technique	Intended Loading (%)	Obtained Loading (%)	Incorporation Efficiency (%)
Pt-ZSM-5	Impregnation	1	0.766	76.6
Pt-Beta	Impregnation	1	0.597	59.7
Pt-Y	Impregnation	1	0.562	56.2
Pt-MOR	Impregnation	1	0.588	58.8
Pt-FERR	Impregnation	1	0.673	67.3

The obtained result shows that a considerable amount of Pt was lost during the fabrication. This can be explained by the nature of the pore system of zeolite materials. The small pore volume partially allows Pt solution to access the entire zeolite channels. Moreover, the hydrophobic nature of silica in Y and Beta types hinders the accessibility of Pt solution to the zeolite channels. ZSM-5 exhibited the maximum impregnation efficiency, in which almost 76.6% of the Pt amount was obtained in the final solid product. While zeolite Y exhibited the lowest impregnation efficiency, only 56.2% was obtained in the final product.

The formation of Pt nanoparticles incorporated into the different applied supports was investigated using the XRD technique. Figure 1 shows the XRD analysis of the Pt-incorporated zeolite materials.
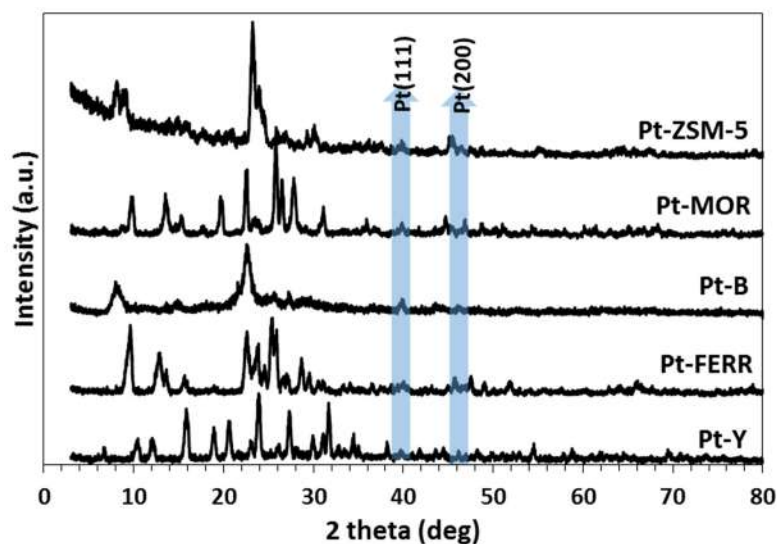

Figure 1. XRD patterns of the Pt-incorporated different zeolite materials.

The XRD patterns of the fabricated catalysts were dominated by the characteristic peaks of zeolite materials, as stated in the atlas of the zeolite framework [27]. Small peaks could be observed in the patterns at 2θ of 39.7° and 46.2°. As indicated in the reference (JCPDS card no 04-0802) of Pt nanoparticles, the positions and intensities of these peaks can be assigned to (111) and (200) of the metallic Pt nanoparticles [28]. The results showed that all the Pt was transformed directly into Pt^0 nanoparticles during the synthesis, which eliminated the need for a further hydrogenation step to generate the Pt^0 active sites.

N_2 sorption measurements were applied to determine the textural properties (total surface area, pore volume, and pore diameter) of the prepared materials. The obtained results are listed in Table 3.

Table 3. The texture properties of the prepared samples as determined using N_2 sorption analysis technique.

Sample	Surface Area (m²/g)	Pore Volume (cm³/g)	Pore Size (nm)
Pt-Y	436.9	0.07	8.6
Pt-Beta	491.9	0.14	5.5
Pt-MOR	414.4	0.13	1.2
Pt-FERR	309.9	0.10	1.5
Pt-ZSM-5	402.9	0.16	7.2

The surface area of the entire prepared samples ranged from 309 to 491 m^2/g. The maximum surface area of the Pt-incorporated mesoporous materials was obtained in the Pt-Beta sample, while Pt-FERR exhibited the smallest surface area between the Pt-incorporated zeolite samples. It was noticed that the total surface area was higher than the corresponding bare commercial samples. However, this can be related to the presence of Pt nanoparticles which increase the measurement of the surface area. On the other hand, the pore volume of the prepared samples ranged from 0.07 to 0.16 cm^3/g. Surprisingly, only two applied commercial zeolites were found to have pore sizes in the range of microporous materials: Pt-MOR and Pt-FERR. However, three zeolite materials were found to have pore sizes in the range of mesoporous materials: Pt-Y, Pt-Beta, and Pt-ZSM-5. To explain this finding, there is a possibility that the producer applied some additional tactics to improve the pore size of the commercial zeolites to be suitable in the different industrial applications notable in the reactions which deal with high organic molecules. The N_2 isotherms can give additional information about the porous systems of the prepared samples. Figure 2 presents the N_2 sorption isotherms for the Pt-incorporated zeolite samples. The N_2 sorption isotherms of Pt-incorporated zeolites are a mixture of type IV and type III as an indication of the dual nature of the pore system in the zeolite samples.
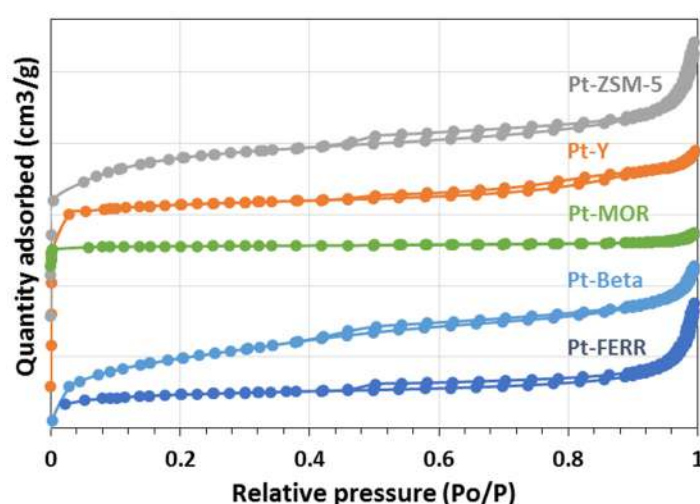

Figure 2. The nitrogen isotherms of the prepared Pt-incorporated zeolite materials (Y, Beta, MOR, FERR, and ZSM-5).

FTIR analysis was performed to investigate the changes which occurred in the zeolite framework as a result of Pt incorporation. The collected FTIR spectra for the samples are presented in Figure 3. The spectra of bare supporting zeolite samples are dominated

by two prominent bands at 1047 and 799 cm^{-1} which can be assigned to the stretching asymmetric and symmetric modes of the Si–O–Si lattice, respectively [28]. The addition of Pt^0 nanoparticles, which—most likely—increases the asymmetric vibration of the siliceous network, caused the intensity of the 1047 cm^{-1} band to be higher than that of the bare sample [29,30]. Finally, due to the presence of Pt^0 nanoparticles in the zeolite lattice, the shoulder around 1215 cm^{-1}, which also referred to the external asymmetric Si-O stretching mode in the bare support, was displaced to a smaller wavenumber. However, the obvious change in the entire spectra before and after Pt incorporation was the change in the two peaks of 2350 and 2880–2900 cm^{-1}, which can be attributed to the CO_2 and OH surface silanol groups, respectively. The reason for such a change is not clear and needs further investigation.
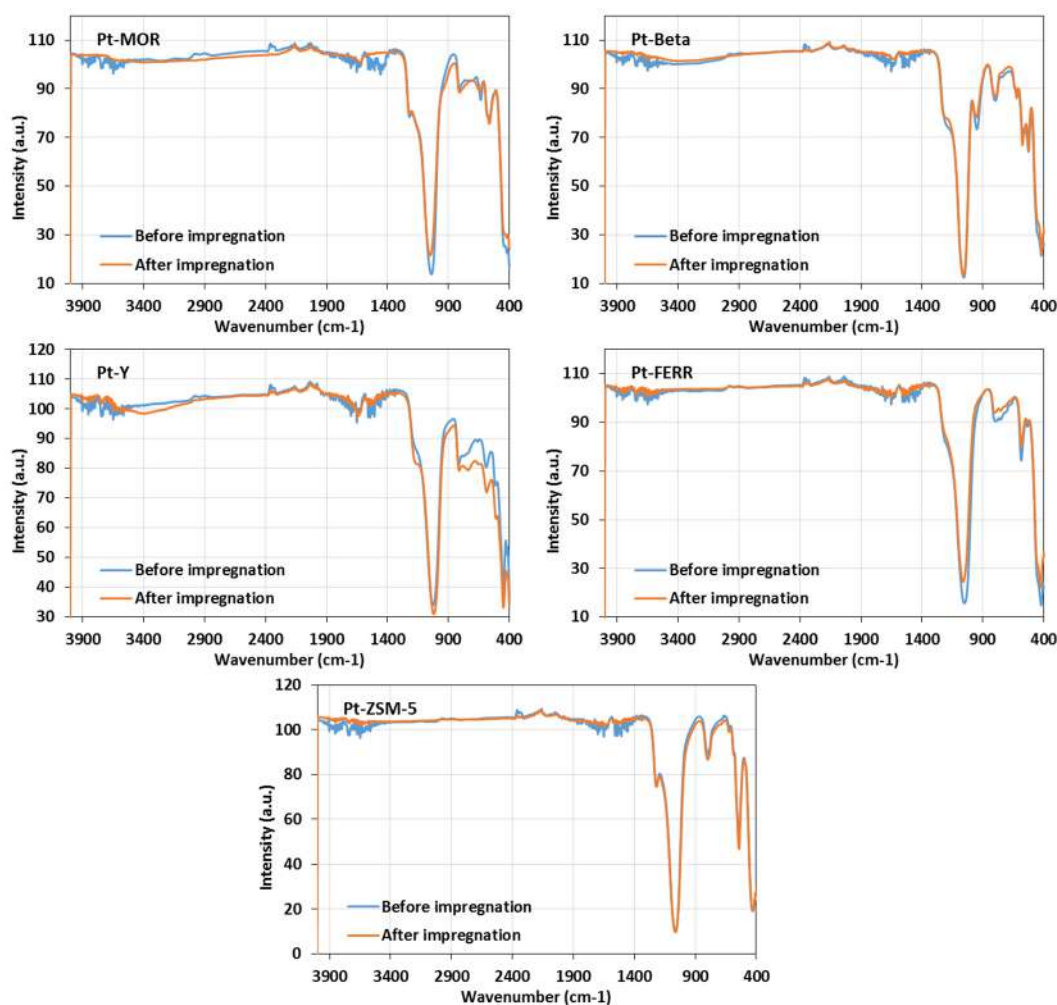
Figure 3. The FTIR spectra of the prepared Pt-incorporated zeolite materials (Y, Beta, MOR, FERR, and ZSM-5) before and after Pt incorporation.

The morphological structure of the prepared samples was investigated by SEM analysis. Figure 4 presents the SEM micrographs of the fabricated samples. Pt-Y exhibited a highly crystalline phase with partially replicated octahedral crystals (average size between 1 and 1.5 µm) with a few aggregates [30]. Pt-Beta showed a sphere-like morphology with a broad average size of 0.2–1 µm. Pt-MOR exhibited fused and aggregated prism-like crystals with an average crystal size of 1–1.5 µm [31]. Finally, Pt-ZSM-5 exhibited the aggregates' hexagonal crystal structure [32]. The average crystal size was hard to detect due to the high aggregation. More importantly, no Pt-separated phase could be detected in any micrograph, as an indication for the total incorporation of the Pt metal into the zeolite matrix. Moreover,

because water and Pt source were used only in the sample preparation, no carbon or carbonized species could be detected in the micrographs, which is an indication for the purity of the prepared samples.
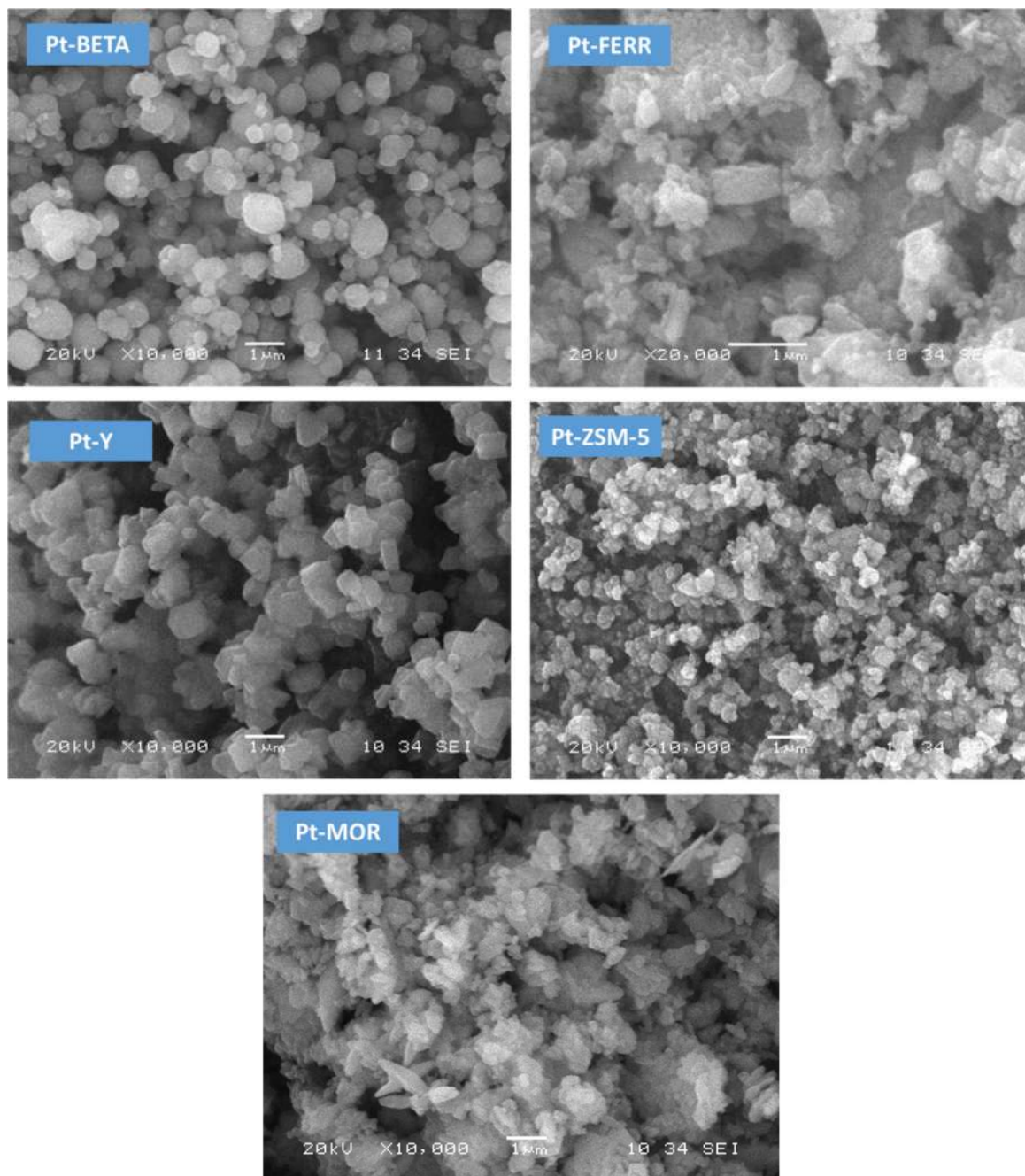

Figure 4. SEM micrographs with the same magnification for Pt-incorporated zeolite samples.

EDX analysis coupled with SEM analysis was carried out to reveal the chemical composition of the prepared catalytic samples. Figure 5 shows the obtained results of the EDX analysis for the Pt-incorporated zeolite materials.
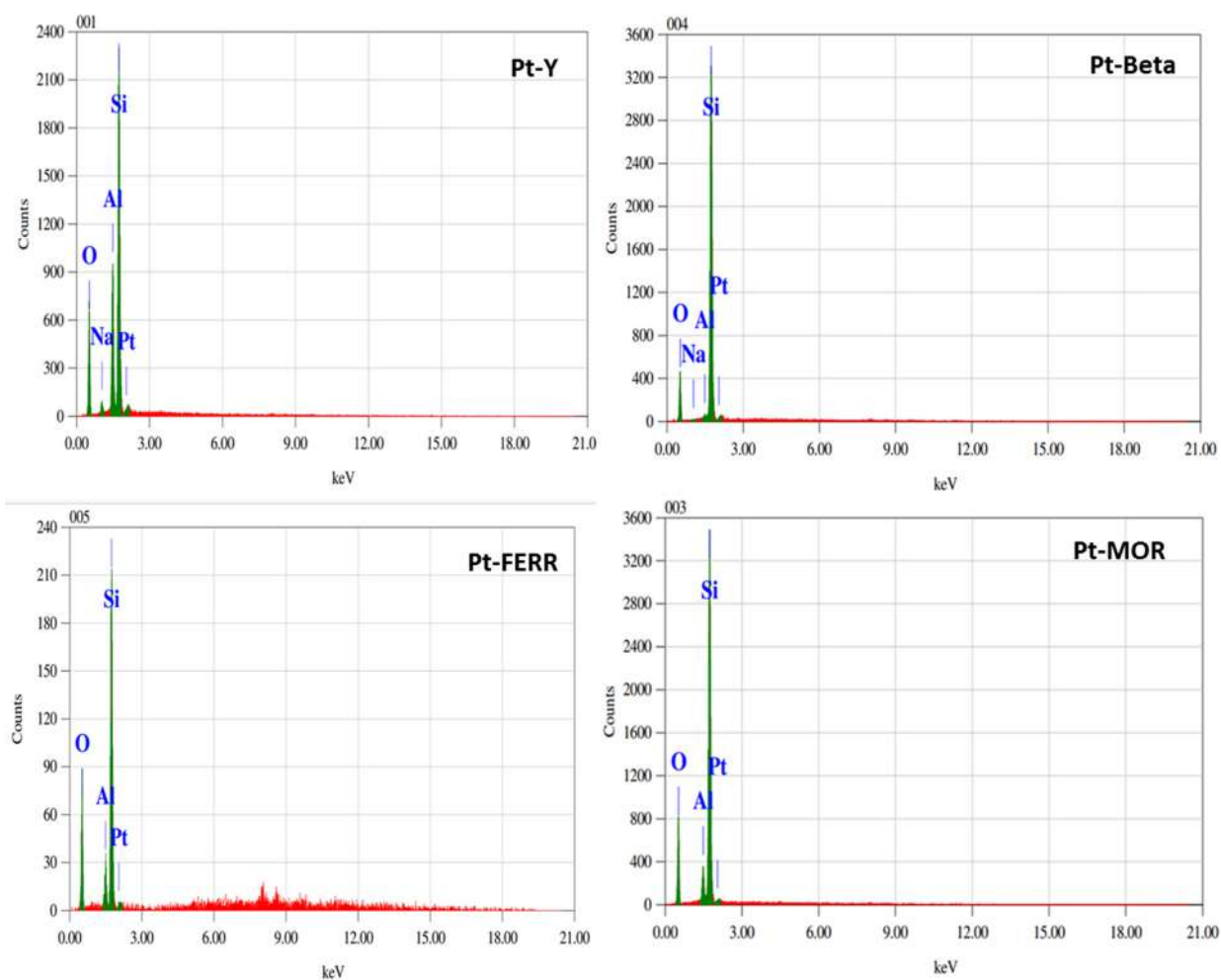
Figure 5. The EDX analysis of the prepared Pt-incorporated zeolite materials (Y, Beta, MOR, and FERR).

The Pt-incorporated zeolite materials showed peaks of Si, O, Al and Pt only. No other elements could be detected as an indication of the high purity of the prepared samples. Moreover, Na was detected in Pt-Y and Pt-Beta samples, which can be related to the chemicals which were used in the synthesis of the bare zeolite samples.

HR-TEM analysis was performed to investigate the incorporation and distribution of Pt nanoparticles into the different zeolite samples. Figure 6 presents the obtained micrographs with different magnification powers.
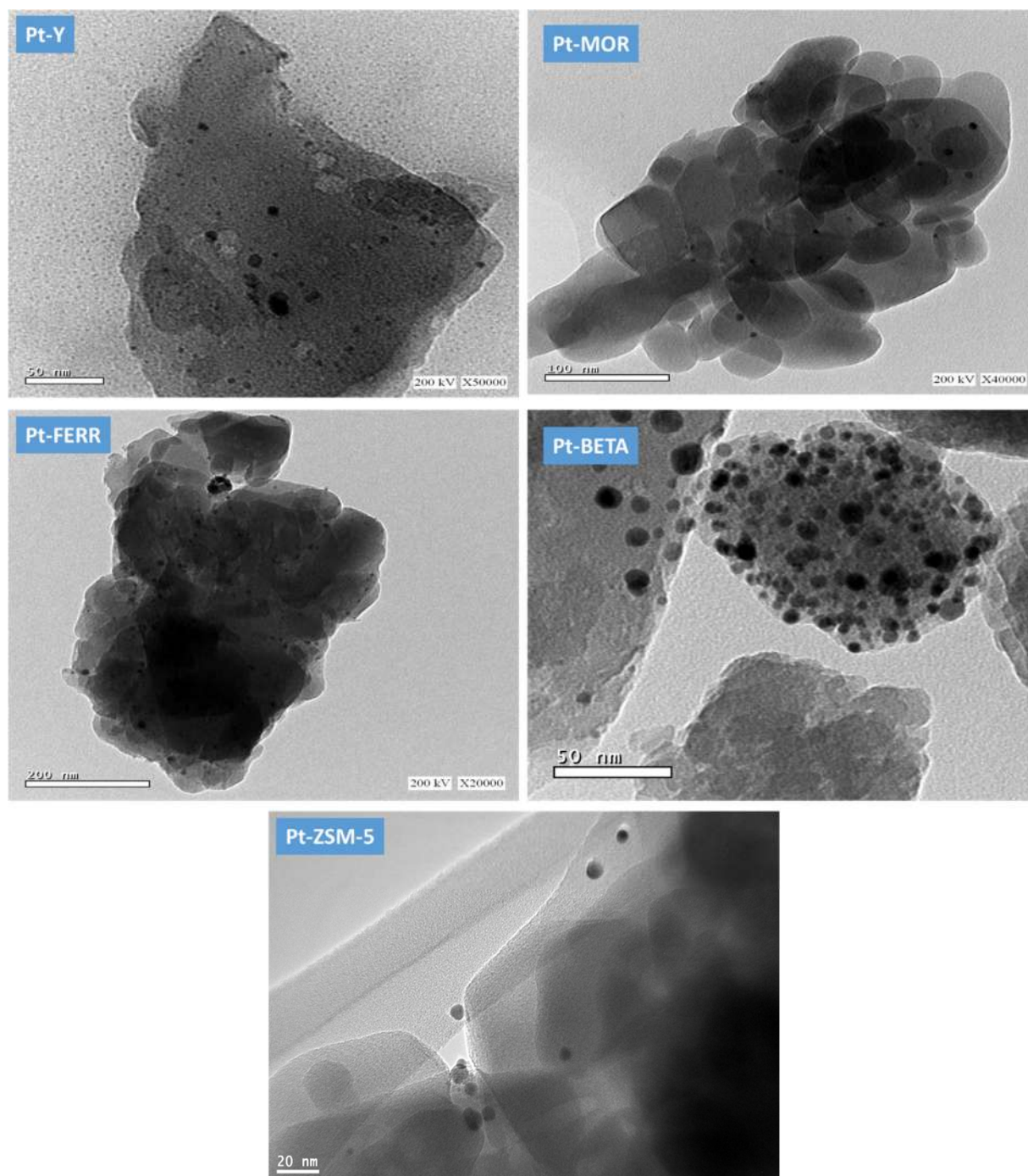
Figure 6. HR-TEM micrographs for Pt-incorporated different zeolite samples.

The micrographs of the entire samples show the Pt nanoparticles with an average size of 5–10 nm incorporated into the different supports with high distribution. Moreover, no bulky Pt particles could be observed, nor other bulky crystals, indicating the high efficiency of the synthesis method to incorporate Pt nanoparticles into the different zeolite samples.

3.2. The Hydrogenation of Cyclohexene

The catalytic performance study of the prepared catalysts was carried out in the reduction of cyclohexene by hydrogen gas to produce cyclohexane as a model reaction. The reactions were performed under solvent-free conditions and at room temperature by applying 5 atm of hydrogen pressure in a Parr reactor. The catalytic performance of each

catalyst was monitored by gas chromatography and the obtained results are reported in this section. In the beginning of the catalytic performance study, several blank experiments (normally called zero reactions) were performed. The aim of these experiments was to investigate the effect of different parameters such as self-catalysis, bare support, bulk catalyst, etc., on the chosen model reaction. The obtained results of the blank reactions are plotted in Figure 7.
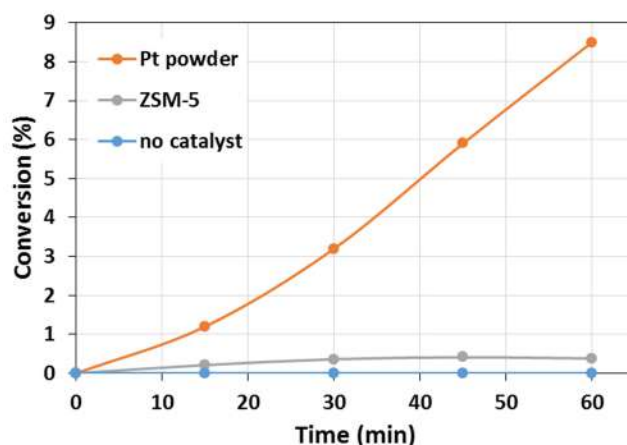

Figure 7. The conversion profiles of cyclohexene in the blank reactions as a function in the applied reaction time.

The model reaction proceeded without any catalyst to ensure that the reaction could not be catalyzed by the stainless steel of the Parr reactor or by the stirring rod. The obtaining conversion % was zero as an indication of the need for a catalyst to perform the reaction. In other experiments, the bare supports (without Pt active sites) were applied to catalyze the model reaction. The obtained results showed that a negligible % of conversions were obtained. Both supports could not convert more than 1% of cyclohexene. Moreover, bulk non-porous zero-valent Pt metal was applied to catalyze the reaction. The obtained results showed that only 8.5% of cyclohexene was converted into cyclohexane under the same reaction conditions. Finally, the reduction of cyclohexene into cyclohexane was performed at lower pressure, i.e., 1 and 3 atm, and catalyzed by bulk Pt particles. Almost no conversion could be detected. The results of the blank experiments clearly show that cyclohexene cannot be self-converted, there is no effect for the support, and the reaction can be proceeded only under 5 atm and at room temperature by using a metallic catalyst.

The catalytic performance of the Pt-incorporated zeolite samples is presented in Figure 8. Pt ZSM-5 exhibited the best catalytic performance, in which 22.4% conversion of cyclohexene was obtained with a total TOF of 0.63 s^{-1}. The Pt-Beta sample was able to convert 12.4% of cyclohexene with a total TOF of 0.44 s^{-1}. Similar catalytic behavior was observed with Pt-MOR and Pt-FERR samples, and almost the same TOF, 0.3 s^{-1}, was obtained. Finally, Pt-Y exhibited the lowest activity: only 6% of cyclohexene was converted with a total TOF of 0.23 s^{-1}.
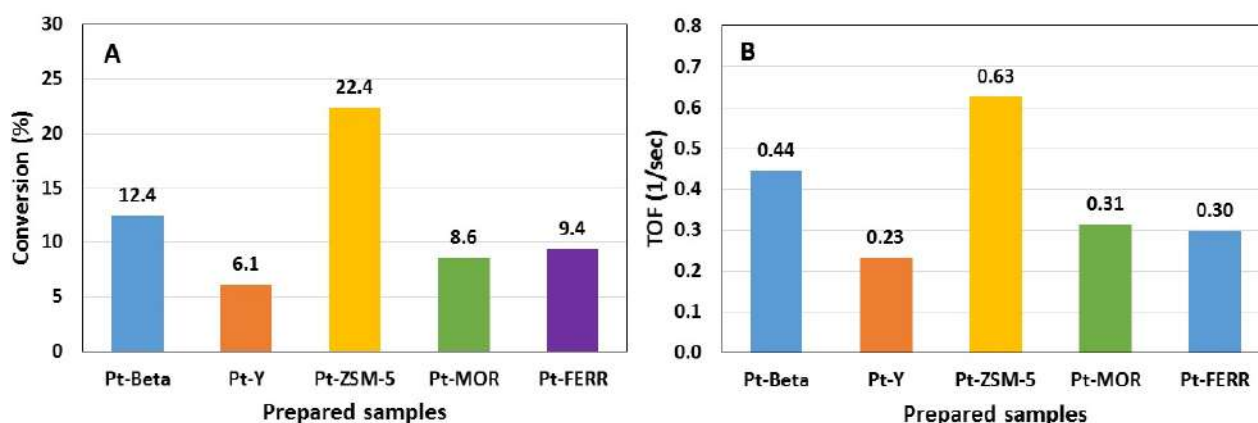
Figure 8. (**A**) The obtained conversion (%) of cyclohexene over Pt-incorporated zeolite materials (Beta, Y, ZSM-5, MOR, and FERR). (**B**) The corresponding TOF.

To have a fair comparison between the supports, the amount of Pt must be normalized, and hence the TOF s^{-1} is the correct parameter for comparison rather than conversion rate. Several parameters can affect the behavior of support, such as the geometrical configuration, texture properties, hydrophobicity, presence of contamination, and/or adsorption behavior. Moreover, the applied zeolites samples were ZSM-5, Y and Beta with three-dimensional pore systems, while MOR and FERR have two-dimensional pore systems. Therefore, it was expected that ZSM-5, Y and Beta would exhibit the highest activity, which was correct to a great extent. It was also expected that MOR and FERR would exhibit the minimum activity due to the small pore size, hindering the accessibility of cyclohexene to the Pt active sites in addition to the two-dimensional pore systems in both supports. The comparison between ZSM-5, Y and Beta (the three-dimensional pore system) also shows that ZSM-5 is the only support which contains alumina in the framework, which might improve the adsorption of the reactants.

The hydrogenation reaction over Pt-ZSM-5 was successfully performed under room temperature and, therefore, the study was extended to run the reaction under elevated temperatures up to 60 °C. The aim of this study was to calculate the kinetics of the hydrogenation reaction in addition to the activation energy calculation. The conversion % of cyclohexene over Pt-ZSM-5 at different reaction temperatures is plotted in Figure 9. The obtained results showed a typical improvement in the catalytic performance when the reaction temperature was increased. The conversion of cyclohexene reached 100% over Pt-ZSM-5 at 50 °C after 45 min, and at 60 °C after 35 min. Moreover, Pt-ZSM-5 did not suffer from thermal deterioration, and the structure of ZSM-5 was maintained and did not collapse as a result of applying 5 atm pressure and 60 °C temperature.
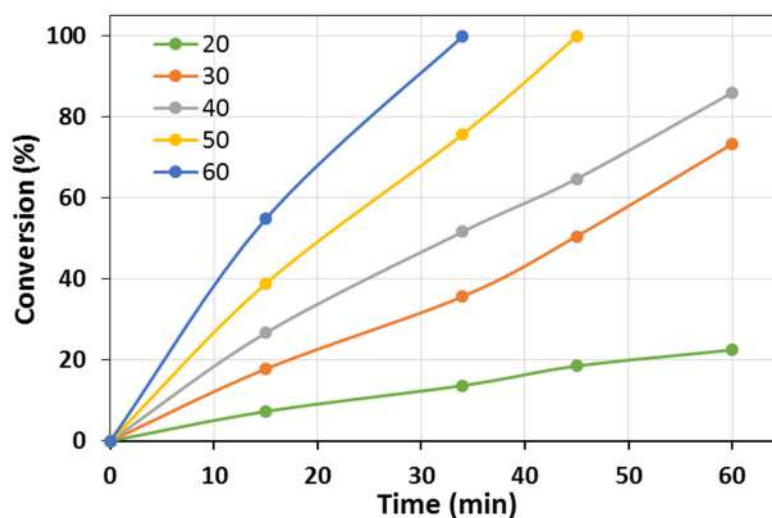
Figure 9. The conversion % profiles of cyclohexene over Pt-ZSM-5 at different temperatures as a function of the applied reaction time.

In order to identify the order of the hydrogenation reaction of cyclohexene over Pt-ZSM-5, several kinetic models were investigated. According to the literature [33], the zero-order reaction model was the most commonly used model to calculate the rate constants [K] of cyclohexene hydrogenation at various applied temperatures [34]. In this model, the concentration of cyclohexene is plotted against reaction time to obtain a straight line with a slope = −K.

The zero-order kinetic model of cyclohexene conversion over Pt-ZSM-5 at different reaction temperatures is plotted in Figure 10. The figure shows that all obtained conversion data are perfectly fit with the model, and the coefficient of determination (R2) values in both graphs (ten data sets) are greater than 0.984. It is also observed that the rate constants increased with the increase in applied reaction temperature, and the maximum value was 0.0072 mol/min Pt-ZEM-5 at 60 °C.
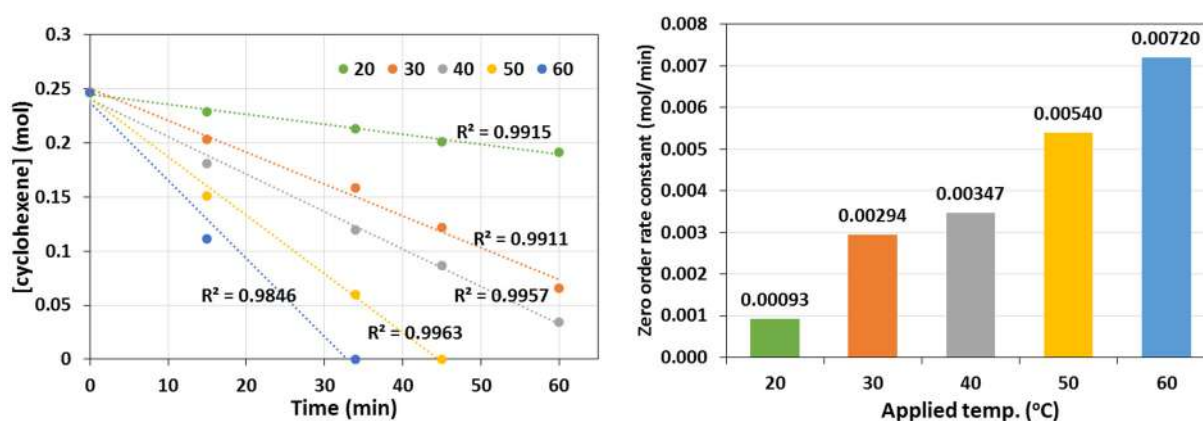

Figure 10. (**Left**) panel: The zero-order kinetic model for the hydrogenation of cyclohexene over Pt-ZSM-5 at different reaction temperatures. (**Right**) panel: comparison between the calculated zero-order rate constants.

To calculate the activation energy of the applied reaction, the Arrhenius equation was applied in which the plot of ln(K) against $1/T$ (kelven^{-1}) should give a straight line with a slope equal to $-Ea/R$, where R is the universal gas constant (Figure 11). The calculated activation energy (Ea) was 88.95 KJ/mol for Pt-ZSM-5.
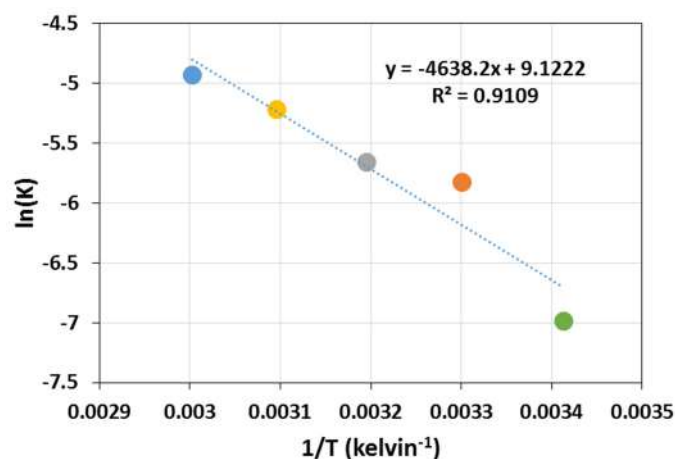
Figure 11. Arrhenius plot to calculate the activation energy (Ea) for Pt-ZSM-5 catalyst.

Furthermore, to confirm the exothermic nature of the hydrogenation reaction, the change in the reactor temperature was measured (Figure 12) for the Pt-ZSM-5 catalyst. It is clear that the reactor temperature is increasing as an indication of the exothermic nature of the hydrogenation reaction.
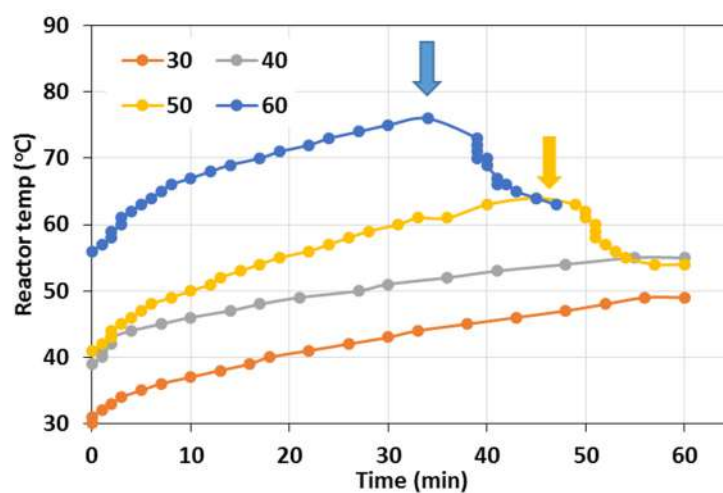

Figure 12. Change in the reactor temperature during the hydrogenation of cyclohexene over Pt-ZSM-5. Arrows are pointing to the 100% conversion of cyclohexene.

The reusability of the Pt-ZSM-5 was investigated by performing four consecutive runs using the same catalytic sample without any treatment, and a fifth run after thermal treatment at 300 °C for 180 min. The obtained results expressed by the conversion % of cyclohexene of the different runs are plotted in Figure 13. It is obvious that the Pt-ZSM-5 sample was able to activate the five runs at a good efficiency. Without treatment, the activity of Pt-ZSM-5 was reduced by 10% after four runs compared to a fresh sample. This is most likely due to the accumulation of organic species onto the surface of the catalysts, while after thermal treatment, only 7.1% loss in activity was obtained. This result clearly shows that Pt-ZSM-5 exhibited good stability after five runs.
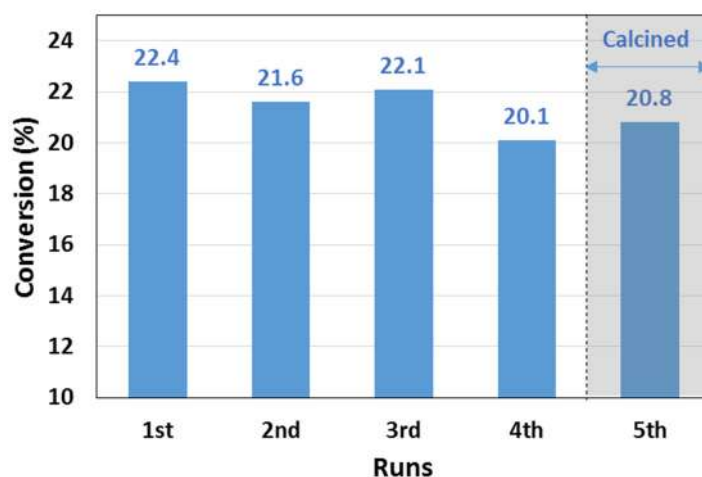
Figure 13. The cyclohexene conversion % over the same samples of Pt-ZSM-5 for four consecutive runs without treatment and one run after thermal treatment (calcination).

4. Conclusions

The current study presents—for the first time—a systematic comparison between the effects of five different zeolite supports on the catalytic performance of Pt nanoparticles in a hydrogenation reaction. Pt nanoparticles were incorporated into five different zeolites (HY, Beta, mordenite, ZSM-5, and ferrierite) using only water in a wet impregnation procedure. The incorporation efficiency differs from one sample to another. The zeolites which contained only silica, such as Beta and HY, exhibited the poorest incorporation efficiency (58% of Pt was incorporated into the zeolite framework). On the other hand, ZSM-5, which contains aluminum, exhibited the best incorporation efficiency (76%). The characterization data confirmed the presence of Pt nanoparticles with a size ranging from 5 to 10 nm. The five different catalysts were applied to activate the hydrogenation of the cyclohexene reaction at room temperature. Pt-ZSM-5 exhibited the best catalytic performance in which 22.4% conversion was achieved, while Pt-MOR and Pt-FERR exhibited the lowest activity (no more than 10% was obtained). This can be related to the three-dimensional framework of ZSM support which offers high accessibility to/from the Pt active sites. Moreover, the presence of Al^{3+} centers in ZSM-5 most likely facilitates the adsorption of the substrates onto the surface of the solid catalyst. The obtained activity at different temperatures fit perfectly with the zero-order kinetic model and the activation energy was calculated. Pt-ZSM-5 catalyzed five different reactions without significant loss in activity.

Data Availability Statement: The data presented in this study are available on request from the corresponding author. The data are not publicly available due to privacy issues.

Conflicts of Interest: The authors have no competing interest to declare that are relevant to the content of this article.

References

1. Stanislaus, A.; Cooper, B.H. Aromatic hydrogenation catalysis: A review. *Catal. Rev. Sci. Eng.* **1994**, *36*, 75–123. [CrossRef]
2. Stoffels, M.A.; Klauck, F.J.R.; Hamadi, T.; Glorius, F.; Leker, J. Technology trends of catalysts in hydrogenation reactions: A patent landscape analysis. *Adv. Synth. Catal.* **2020**, *362*, 1258–1274. [CrossRef] [PubMed]

3. McGlynn, S.E.; Glass, J.B.; Johnson-Finn, K.; Klein, F.; Sanden, S.A.; Schrenk, M.O.; Ueno, Y.; Vitale-Brovarone, A. Hydrogenation reactions of carbon on Earth: Linking methane, margarine, and life. *Am. Mineral.* **2020**, *105*, 599–608. [CrossRef]

4. Lee, Y.; Park, H.; Han, J.; Lee, J. Economically-feasible production of a nylon monomer using RANEY® catalysts. *React. Chem. Eng.* **2021**, *6*, 225–234. [CrossRef]

5. Spiccia, N.D.; Border, E.; Illesinghe, J.; Jackson, W.R.; Robinson, A.J. Preparation of a nylon-11 precursor from renewable canola oil. *Synthesis* **2013**, *45*, 1683–1688.

6. Jourdant, A.; González-Zamora, E.; Zhu, J. Wilkinson's catalyst catalyzed selective hydrogenation of olefin in the presence of an aromatic nitro function: A remarkable solvent effect. *J. Org. Chem.* **2002**, *67*, 3163–3164. [CrossRef]

7. Fouilloux, P. The nature of raney nickel, its adsorbed hydrogen and its catalytic activity for hydrogenation reactions. *Appl. Catal.* **1983**, *8*, 1–42. [CrossRef]

8. Teschner, D.; Révay, Z.; Borsodi, J.; Hävecker, M.; Knop-Gericke, A.; Schlögl, R.; Milroy, D.; Jackson, S.D.; Torres, D.; Sautet, P. Understanding palladium hydrogenation catalysts: When the nature of the reactive molecule controls the nature of the catalyst active phase. *Angew. Chem.* **2008**, *120*, 9414–9418. [CrossRef]

9. Bratlie, K.M.; Lee, H.; Komvopoulos, K.; Yang, P.; Somorjai, G.A. Platinum nanoparticle shape effects on benzene hydrogenation selectivity. *Nano Lett.* **2007**, *7*, 3097–3101. [CrossRef]

10. Etayo, P.; Vidal-Ferran, A. Rhodium-catalysed asymmetric hydrogenation as a valuable synthetic tool for the preparation of chiral drugs. *Chem. Soc. Rev.* **2013**, *42*, 728–754. [CrossRef]

11. El Sayed, S.; Bordet, A.; Weidenthaler, C.; Hetaba, W.; Luska, K.L.; Leitner, W. Selective hydrogenation of benzofurans using ruthenium nanoparticles in Lewis acid-modified ruthenium-supported ionic liquid phases. *ACS Catal.* **2020**, *10*, 2124–2130. [CrossRef]

12. Alhanash, A.M.; Alqahtani, F.A.; Aldalbahi, A.; Rahaman, M.; Benaissa, M.; Hamdy, M.S. The hydrogenation of cycloalkenes over direct-synthetized well-defined zero-valent Pt nanoparticles incorporated TUD-1 mesoporous material. *Inorg. Chem. Commun.* **2021**, *127*, 108545. [CrossRef]

13. Benaissa, M.; Alhanash, A.M.; Mubarak, A.T.; Eissa, M.; Sahlabji, T.; Hamdy, M.S. Solvent-free hydrogenation of cyclohexene over Rh-TUD-1 at ambient conditions. *RSC Adv.* **2018**, *8*, 34370–34373. [CrossRef] [PubMed]

14. Alhanash, A.M.; Atran, A.A.; Eissa, M.; Benaissa, M.; Hamdy, M.S. Liquid Phase Hydrogenation of MIBK over M/CsPW (M = Ag, Ru, Pt, and Pd). *Catalysts* **2019**, *9*, 47. [CrossRef]

15. Chen, H.; Sun, J. Selective hydrogenation of phenol for cyclohexanone: A review. *J. Ind. Eng. Chem.* **2021**, *94*, 78–91. [CrossRef]

16. Chen, L.-H.; Sun, M.; Wang, Z.; Yang, W.; Xie, Z.; Su, B. Hierarchically structured zeolites: From design to application. *Chem. Rev.* **2020**, *120*, 11194–11294. [CrossRef]

17. Dusselier, M.; Davis, M.E. Small-pore zeolites: Synthesis and catalysis. *Chem. Rev.* **2018**, *118*, 5265–5329. [CrossRef]

18. Bogdanov, B.; Georgiev, D.; Angelova, K.; Yaneva, K. Natural zeolites: Clinoptilolite. *Rev. Nat. Math. Sci.* **2009**, *4*, 6–11.

19. Vermeiren, W.; Gilson, J.-P. Impact of zeolites on the petroleum and petrochemical industry. *Top. Catal.* **2009**, *52*, 1131–1161. [CrossRef]

20. Sidhpuria, K.B.; Patel, H.A.; Parikh, P.A.; Bahadur, P.; Bajaj, H.C.; Jasra, R.V. Rhodium nanoparticles intercalated into montmorillonite for hydrogenation of aromatic compounds in the presence of thiophene. *Appl. Clay Sci.* **2009**, *42*, 386–390. [CrossRef]

21. Liu, H.; Jiang, T.; Han, B.; Liang, S.; Zhou, Y. Selective phenol hydrogenation to cyclohexanone over a dual supported Pd–Lewis acid catalyst. *Science* **2009**, *326*, 1250–1252. [CrossRef]

22. Horáček, J.; Šťávová, G.; Kelbichová, V.; Kubička, D. Zeolite-Beta-supported platinum catalysts for hydrogenation/hydrodeoxygenation of pyrolysis oil model compounds. *Catal. Today* **2013**, *204*, 38–45. [CrossRef]

23. Wang, J.; Li, Q.; Yao, J. The effect of metal–acid balance in Pt-loading dealuminated Y zeolite catalysts on the hydrogenation of benzene. *Appl. Catal. A Gen.* **1999**, *184*, 181–188. [CrossRef]

24. Wang, L.; Zhang, J.; Yi, X.; Zheng, A.; Deng, F.; Chen, C.; Ji, Y.; Liu, F.; Meng, X.; Xiao, F.S. Mesoporous ZSM-5 zeolite-supported Ru nanoparticles as highly efficient catalysts for upgrading phenolic biomolecules. *ACS Catal.* **2015**, *5*, 2727–2734. [CrossRef]

25. Aboul-Fotouh, S.M. Cyclohexene Reactivity Using Catalysts Containing Pt, Re and PtRe Supported on Na-and H-Mordenite. *J. Chin. Chem. Soc.* **2003**, *50*, 1151–1158. [CrossRef]

26. Baerlocher, C.; McCusker, L.B.; Olson, D.H. *Atlas of Zeolite Framework Types*; Elsevier: Amsterdam, The Netherlands, 2007.

27. Qin, H.; Qian, X.; Meng, T.; Lin, Y.; Ma, Z. $Pt/MO_x/SiO_2$, $Pt/MO_x/TiO_2$, and $Pt/MO_x/Al_2O_3$ Catalysts for CO Oxidation. *Catalysts* **2015**, *5*, 606–633. [CrossRef]

28. Wang, C.; Wu, C. Electrical sensing properties of silica aerogel thin films to humidity. *Thin Solid Films* **2006**, *496*, 658–664. [CrossRef]

29. Wu, R.; Sun, Y.; Lin, C.; Chen, H.; Chavali, M. Composite of TiO_2 nanowires and Nafion as humidity sensor material. *Sens. Actuators B Chem.* **2006**, *115*, 198–204. [CrossRef]

30. Shamzhy, M.; Opanasenko, M.; Concepción, P.; Martínez, A. New trends in tailoring active sites in zeolite-based catalysts. *Chem. Soc. Rev.* **2019**, *48*, 1095–1149. [CrossRef]

31. Ye, G.; Sun, Y.; Guo, Z.; Zhu, K.; Liu, H.; Zhou, X.; Coppens, M. Effects of zeolite particle size and internal grain boundaries on Pt/Beta catalyzed isomerization of n-pentane. *J. Catal.* **2018**, *360*, 152–159. [CrossRef]

32. Tamizhdurai, P. Isomerization of hydrocarbons over Pt supported on micro-mesoporous ZSM-5. *Polyhedron* **2018**, *154*, 314–324. [CrossRef]

33. Singh, U.K.; Vannice, M.A. Kinetics of liquid-phase hydrogenation reactions over supported metal catalysts—A review. *Appl. Catal. A Gen.* **2001**, *213*, 1–24. [CrossRef]

34. Li, G.; Zhao, Z.; Mou, T.; Tan, Q.; Wang, B.; Resasco, D. Experimental and computational kinetics study of the liquid-phase hydrogenation of CC and CO bonds. *J. Catal.* **2021**, *404*, 771–785. [CrossRef]